About Journal

The University of Sistan and Baluchestan entered into strategic partnership with Iranian Association of Electrical and Electronic Engineers (IAEEE) to publish the **International Journal of Industrial Electronics Control and Optimization (IECO)**. The IECO is a refereed international journal which presents to the international scientific community important results of work in these fields, whether in the form of modeling simulation, analysis, fundamental research, development, application, design or real-time implementation. The scope of IECO is broad, encompassing all aspects of Industrial Electronics, Control and Optimization.

Note: International Journal of Industrial Electronics, Control and Optimization (IECO) has qualified to **ACADEMIC RESEARCH JOURNAL (ELMI-PAJOHESHI)** status certified by the ministry of Science, Research and Technology of Iran (No. 231566/3/18 dated 1396/10/09), and is published by the University of Sistan and Baluchestan through a formal partnership (No. 952/2/1500 dated 1395/11/04) with Iranian Association of Electrical and electronic Engineers (IAEEE) in order to develop scientific and research cooperation.

Aims and Scope

International Journal of Industrial Electronics, Control and Optimization (IECO) is a Peer reviewed journal of advanced and state-of-the-art in the science and engineering of Industrial Electronics, Control and Optimization. Its Scope encompasses the applications of Industrial Electronics, power systems, control, optimization and computational intelligence for the enhancement of industrial and manufacturing system and processes. The scope of the journal include the following:

I. Industrial Electronics

- *Low and high power converters*
- *Renewable energy*
- *Drive control techniques*
- *Techniques for advanced power semiconductor devices*
- *Power quality and utility applications*
- *Communications*
- *Flexible AC Transmission Systems (FACTS)*
- *Control in power electronics*
- *Electromagnetic and thermal performance of electronic power converters*
- *Motion control, robotics, sensors and actuators*
- *Fault detection and diagnosis*
- *Power systems*
- *Factory automation, communication, and computer networks*

II. Control

- *Adaptive control*
- *Control of process systems*
- *Control theory*
- *Data processing*
- *Design of control systems*
- *Hybrid systems*
- *Identification and observation*
- *Intelligent systems*
- *Model-predictive control*
- *Optimal control*
- *Robust control*
- *Fractional order systems*

III. Optimization

- *Ant Colony*
- *Chaos Theory*
- *Evolutionary Computing*
- *Fuzzy Computing*
- *Hybrid Methods*
- *Immunological Computing*
- *Neuro Computing*

- *Particle Swarm*
- *Probabilistic Computing*
- *Rough Sets*
- *Wavelet*

International Journal of Industrial Electronics, Control and Optimization © 2022 IECO
Vol. 5, No. 2, pp. 109-121, April 2022

Maximizing Electric Vehicles Owners Profit Considering Optimal Charging and Discharging Management in Distribution Networks Using Dynamic Programming

Ali Masoudi[1], Mohsen Simab[2,†], Hamidreza Akbari[3], Seyed Amin Saeed[4] , Tahereh Daemi[5]

[1, 3, 4, 5] Department of Electrical Engineering, Yazd branch, Islamic Azad University, Yazd, Iran
[2,†] Department of Electrical Engineering, Islamic Azad University, Marvdasht branch, Marvdasht, Iran

ABSTRACT

With an increasing penetration rate of electric vehicles in distribution networks, it is becoming vital to schedule their battery charging/discharging to maintain the network balance and increase the vehicle owners' profit. Electric vehicles are now considered one of the most important and accessible sources of revenue for their owners since they can be connected to the grid (V2G) as a power source during peak hours. As such, while flattening the power profile, they can improve the voltage drop across the grid buses. If charging/discharging of the vehicles is scheduled irregularly, the power drawn from the phases will become unbalanced, which can cause global outages and impair system stability in addition to increasing the harmonic volume and decreasing power quality. The present paper uses dynamic programming to reduce operating costs and enhance the profits of vehicle owners who participate in the V2G program. This optimization algorithm eliminates the undesirable paths leading to unconventional responses in the search space, which will greatly increase the speed and accuracy by which the optimal response is achieved. This model, along with multi-part tariffs on electricity prices, can lead to the more active participation of vehicle owners and help improve the power quality indices of the electrical parameters of the grid. The proposed method is simulated on a sample distribution network, and the case studies conducted prove the validity of the proposed algorithm.

Article Info

Research Article

Keywords:

Dynamic programming, Electric Vehicles, Optimization, Unbalancing

Article History:

Received 2021-10-13

Accepted 2022-02-24

I. INTRODUCTION

Nowadays, the widespread entry of electric vehicles (EVs) into the market has created an inseparable link between the two industries of electricity and transportation. The electricity industry must be prepared enough to embrace such changes from now on – changes that can either turn into a challenge for the electricity industry, in case of mismanagement and improper planning, or an opportunity, if a proper implementation framework is in place. The concept, which is interpreted as connecting the vehicle to the grid or V2G in short in today's scientific literature, is nothing but a win-win collaboration between the field of transportation and electricity supply, the optimal implementation of which requires to embed a new piece called electric vehicles in the complicated puzzle of the electricity industry [1-2]. EVs can store electricity in their batteries during off-peak hours when electricity is cheap and deliver it to the grid during peak hours when electricity prices are high. When looking at EVs parked and connected to the grid as sources of service, one enters into the V2G discussion [3]. In other words, V2G means using the battery capacity of EVs as an electric energy saver to provide electrical power or ancillary services to the power grid. Moreover, one of the other relevant parameters of

[†]**Corresponding Author:** msimab@miau.ac.ir
Tel: +98-7143311150, Faculty of Electrical and Computer Engineering, Islamic Azad University, Marvdasht branch, Marvdasht, Iran

V2G is the control of the state of charge (SOC), whose impact on vehicle load management is examined here.

In addition to participating in electricity markets, V2G can also be used to play a complementary role in production from renewable resources. This means that fluctuations in the output power of power generation units such as wind and photovoltaic can be compensated by energy storage in batteries of EVs. The V2G required to stabilize solar power for peak power and wind power for base load is calculated in [4]. According to [5], four V2G-related markets include base load, peak, spinning reserve, and frequency regulation. The authors argue that V2G is unsuitable for base load, but it can be used for peak under certain conditions. It is competitive for the spinning reserve and highly competitive for regulation purposes. In the view of [6], V2G has two types, one-way and two-way. In the one-way type, the power direction is always from the grid to the vehicle, but in the two-way type, it is possible to inject the vehicle power into the grid. In other studies such as [7], V2G only refers to the second type, and the first type is called G2V.

The participation mode suggested by [8] for EVs in the electricity market in the V2G discussion is in such a way that EVs are in the charging phase at non-peak times, e.g., at night, and their aggregator contributes to amending the load curve. During the day and when the vehicles are parked, their aggregator can participate as a source in the regulatory market and can also be applied to reduce the peak. Reference [9] has studied the suitability of EVs for different markets in California and presented Table 1 in this regard. The applications mentioned for V2G in [9] include smoothing the power produced by wind farms and promoting short-term voltage stability.

TABLE I
VEHICLE OWNER'S POTENTIAL ANNUAL NET PROFIT FROM V2G IN CALIFORNIA ($) [1]

	Peak power ($)	Spinning reserve ($)	Frequency Regulation ($)
Battery Electric Vehicle	267	720	3162
Fuel Cell Electric Vehicle	-50 loss to 1226	2430 to 2685	2984 to 811
Hybrid Electric Vehicle	322	1581	-759 loss

Reference [10] has also emphasized the utilization of EVs and V2G to enhance the use of wind energy and has argued that the electricity, transportation, and heating industries can be scheduled in an integrated manner. According to the International Energy Agency, published in 2019, over the next 25 years, global energy demand will grow by 80%. A significant part of this energy is consumed in transportation, which is, on the other hand, one of the most important sources of production and emission of greenhouse gases [11]. One way to reduce the negative impact of battery charging on these vehicles is to manage their charging so that they are not charged simultaneously. Therefore, this reference has conducted research indicating that the peaks and valleys of the power curve can be flattened according to the habits of the American people in using their EVs. Studies on drivers' behavior have shown that their vehicles are parked for about 22 hours a day [12]. The energy in the batteries of EVs remains unused during this long parking time, so if they can be connected to the grid in a V2G manner, the energy stored in their batteries can be used to provide ancillary services, such as reducing peak power and spinning reserve [13].

The problems caused by the increased penetration rate of EVs in the grid are mostly related to the lack of control over the charger power of EVs and the lack of proper coordination between vehicles. Various research studies have been conducted on the regulation of EVs to adjust grid load, which are reviewed below. To increase the penetration factor of EVs, the starting time of the vehicle battery charging to the grid low-load intervals is shifted in [14]. To do this, it is assumed that there is a smart context between the grid and the vehicles in which the vehicles are aware of the energy price of the grid at any given time (Fig. 1). Vehicle owners also decide to charge their vehicle battery in less expensive hours. The grid can also prevent vehicle batteries from being charged during the network's peak load period.

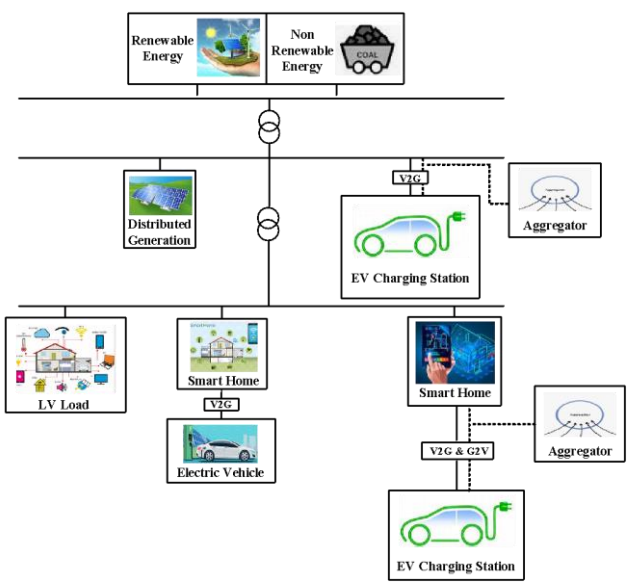

Fig. 1: The structure of a microgrid equipped with renewable resources and EV charging stations.

In addition to charging the batteries, the battery discharging state is also considered in [15] so that if the

vehicles connected to the grid have some energy in their batteries at the moment of connection, some vehicles can supply a part of their energy through the above-mentioned vehicles, which will ultimately reduce the energy loss. In this reference, the charging time of most vehicles is shifted to the lower load intervals. In [16], the optimal charging time of vehicles is obtained according to the grid load conditions and voltage profile, and the charging of vehicles is shifted to the low-load intervals of the grid. In this reference, in addition to determining the starting point of charging, the battery charging power is also controlled. In [17], a real-time load regulation method is presented in which EVs are charged in compliance with the priority of other vehicles at any time step. These studies have been carried out to solve the problems of increased energy demand in the grid peak load, for which the charging time of vehicles is generally shifted to the grid low-load intervals.

The present paper proposes a method based on dynamic programing that, in addition to a higher speed in finding the optimal response for battery scheduling of EVs, can identify insignificant paths during optimization and be careful not to pass them. Therefore, multi-stage dynamic programing is transformed into dynamic programing with a progressive approach in which the ways to reach from the zero stage to the final stage are modeled according to the vehicle battery charging state. Therefore, many non-optimal responses that are clearly identified before solving are removed from the search space, and the set of possible responses turns into a much smaller and convex space.

II. Optimal Charging and Discharging Formulation

The problem of charging several EVs in the grid, along with its technical and economic constraints, leads to the optimization of the following function:

$$cost(x^1, x^2, \dots, x^J) \quad ; \quad x^i \epsilon \theta^i \quad i = \{1, 2, \dots, N\} \tag{1}$$

where *cost (x)* is an objective function encompassing the power consumption parameters of the electric vehicle N in conditions *ix*. The power consumption or injection function of PEVs is defined by vector (2).

$$x^i = \left[x_1^i, x_2^i, \dots, x_k^i, \dots, x_{K^i}^i\right] \tag{2}$$

Set θi also defines all possible consumption or power injection modes for the 1st vehicle according to the following constraints. Given that the charger type is also important in this problem, regardless of its technology, the range of power exchanged between the PEV and the grid can be expressed by equation (3).

$$-\underline{p}^i < x_k^i < \underline{p}^i \quad \forall k \epsilon \{1, \dots, K^i\}, \forall i \epsilon \{1, 2, \dots, J\} \tag{3}$$

where $\underline{p}^i$ is the maximum nominal power of the charger used. The battery charging state must always remain within the permissible operating range. So, we will have:

$$\underline{SOC}^i < SOC_0^i + \tau \sum_{r=1}^{k} x_r^i < \underline{SOC}^i \tag{4}$$

τ is the length of the time steps and $\underline{SOC}^i$ and $\underline{SOC}^i$ are the minimum and maximum SOC, respectively. Therefore, the desirable SOC can be calculated by Equation (5), which is the same as the final charging of the vehicle battery. Of course, Equation (6) can also complement the formulation of the problem in cases where the charger type is not known.

$$SOC_{desired}^i = SOC_0^i + \tau \sum_{r=1}^{k} x_r^i \quad \forall i \epsilon \{1, 2, \dots, J\} \tag{5}$$

$$SOC_{desired}^i \leq SOC_0^i + \tau \sum_{r=1}^{k} x_r^i \leq SOC \tag{6}$$

III. Problem Solving by Dynamic Programing

In mathematics and optimization science, dynamic programing is an efficient way to solve a set of problems using the two characteristics of overlapping and optimal infrastructure sub-problems. In this method, like the division and solution method, the main problem is solved by combining the answers of the sub-problems, but the difference between the two methods is that in the division and solution method, the target problem is divided into a number of independent sub-problems and each one is solved separately. In the end, the answers are combined. But, in dynamic programing, the problems should not be completely independent, meaning that the sub-problems themselves have common constraints. These common sub-problems, although derived from separate paths, have the same answer in both cases and do not need to be recalculated. Therefore, in dynamic programing, the answers to these sub-problems are stored in a table or matrix so that they can be re-accessed. This difference may seem very simple and negligible, but in practice, problem-solving time is significantly reduced with this very simple solution. In general, problem-solving by the dynamic programing method is very similar to the inductive problem-solving method because, just like induction, in dynamic programing, the problem is divided into smaller problems but similar to the main problem, and the answer to the main problem is obtained by assuming the answer to these smaller problems. Finally, a step must be achieved whose answer could be easily calculated although a kind of induction is usually used to prove its accuracy. Dynamic programing is commonly applied to solve optimization and counting problems, including the arrival and departure times of EVs. The general model of the system under optimization is expressed using equation (7):

$$x_{k+1} = f_k(x_k, u_k, \xi_k) \quad k = 0, 1, \dots, T-1 \tag{7}$$

where k is a discrete interval time and f_k is a function that represents the model of the whole system. It models the state of the system in interval k, and u_k also shows the control and decision-making of system variables in passing from x_k to x_{k+1}. Furthermore, parameter ξ_k represents a random variable used for optimization. Therefore, the predicted value of the function with respect to the combined random variables included in the income function can be represented using equation (8).

$$Z = E\left(\sum_{k=0}^{T-1} \Phi(x_k, u_k, \xi_k) + \Phi_T(x_k)\right) \tag{8}$$

where E represents the mean or expectation function and Φ models the target cost function in interval k, which depends on the system state and the random variable. Using the control law of acceptable paths, ψ can be defined to be a mapping from x_k to u_k, in such a way that:

$$\psi = \{\Omega_0, \Omega_1, \dots, \Omega_{T-1}\} \quad \Omega_k(x_k) = u_k \tag{9}$$

$$u_k \in \Gamma_k(x_k) \subset \hat{\Gamma}_k \tag{10}$$

The set Γ_k includes all possible states for decisions of the control variable in interval k, and $\Gamma_k(x_k)$ is a non-empty subset of Γ_k that depends on the current state of the system. Therefore, we will have $x_k \in \Pi_k$ where the set Π_k contains all the states of the system in interval k.

Assume that the initial state of the system x_0 and the initial conditions of the control law, i.e. $\psi = \{\Omega_0, \Omega_1, \dots, \Omega_{N-1}\}$, exist, so the expected final cost of the system will be:

$$Z_\psi(x_0) = E\left(\sum_{k=0}^{T-1} \Phi(x_k, \Omega_k(x_k), \xi_k) + \Phi_T(x_k)\right) \tag{11}$$

where N is a set of acceptable paths in control theory. Therefore, the final function under optimization can be defined as follows:

$$Z_{\psi^*}(x_0) = Z^*(x_0) = \{Z_\psi(x_0)\} \tag{12}$$

where $\psi*$ is the optimal control and $Z^*(x_0)$ denotes its optimal cost.

Fig. 2 illustrates a dynamic programing problem-solving diagram with a multi-step approach, while Fig. 3 shows dynamic programing with a progressive approach. The difference between the two approaches is that in multi-step methods, there is a path from all nodes of the current stage to the nodes of the next stage, and this path includes all possible scenarios. This slows down the optimization performance. In dynamic programing with a progressive approach, it is possible to eliminate impossible states or states that clearly do not have the optimal response in those nodes (or paths) by using restrictive constraints that are applied to the system. Therefore, the routes passing from the current node to the next step node are not necessarily available.

To solve the problem of optimizing the charging and discharging time of EVs in the power grid, the most important parameter that is considered can be written, regardless of the system noise, as follows:

$$SOC_{k+1} = SOC_k + \Delta t\, p_k \tag{13}$$

The $\hat{\Gamma}_k$ set can be defined as the output powers of the batteries shown in equation (14).

$$-p_{max} < p_k < p_{max} \quad \forall\, k \epsilon \{0, 1, \dots, T-1\} \tag{14}$$

According to Fig. 4, to indicate how to optimize the charging/discharging schedule of vehicles using dynamic programing, the permissible interval of battery charging state is expressed by equation (15) as follows:

$$SOC_k^{min} < SOC_k < SOC_k^{max} \tag{15}$$

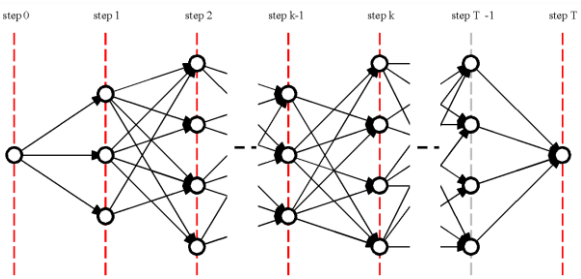

Fig. 2: Dynamic programing block diagram with a multi-stage approach.

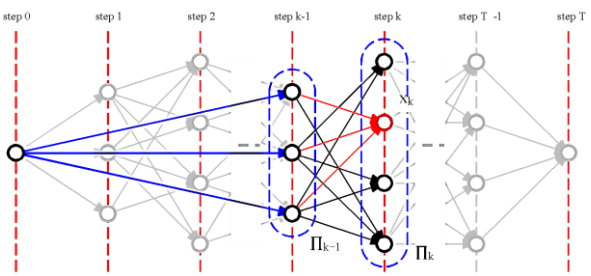

Fig. 3: Dynamic programing block diagram with a progressive approach.

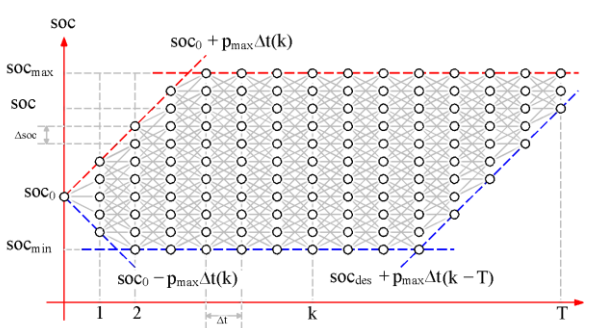

Fig. 4: Dynamic programing diagram in optimizing battery charging/discharging.

The parameters SOC_k^{min} and SOC_k^{max} are defined in terms of k in the form of equations (16) and (17):

$$SOC_k^{min} = \{SOC^{min}, SOC_0 - P_{max}\Delta t(k), SOC_{desired} + p_{max}\Delta t(k-T)\} \quad (16)$$

$$SOC_k^{max} = \{SOC^{max}, SOC_0 + P_{max}\Delta t(k)\} \quad (17)$$

According to Fig. 4, it is noteworthy that SOC_k^{min} and SOC_k^{max} do not depend only on the upper and lower limits of the battery charging rate but also on the maximum power drawn from the battery for charging/discharging. On the other hand, we have $\Gamma_k(SOC_k) \subset \hat{\Gamma}_k$, which depends on the state variations of the SOC_k variable. Therefore, considering the application of the dynamic programing method in this problem, we will have the following equation for the time $k-1$.

$$\frac{SOC_k - SOC_k^{max}}{\Delta t} < p_{k-1} < \frac{SOC_k - SOC_k^{min}}{\Delta t} \quad (18)$$

Then, the diagram block presented in Fig. 4 should be updated to Fig. 5 to achieve the progressive state.

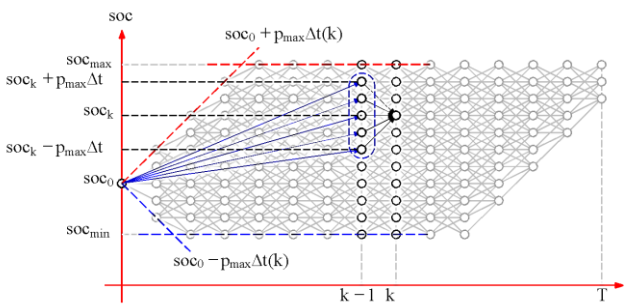

Fig. 5: Dynamic programing diagram with a progressive approach.

IV. Solution Algorithm

If the generating capacity of the vehicles directed towards the power aggregator is introduced using equation (19), then the total cost function can be approximated based on the grid load by equation (20).

$$P^i = [p_1^i, p_2^i, \dots, p_k^i, \dots, p_T^i] \quad (19)$$

$$G_i(P^i, P^{-i}) = -\sum_{k=1}^{T} \left(\left(p_k^i + \sum_{j=1, j\neq i}^{N} (p_k^j + l_k) \right) - L_{mean} \right)^2 \quad (20)$$

where L_{mean} is the average grid load and determined using equation (21).

$$L_{man} = \frac{\frac{1}{\Delta t}\sum_{i=1}^{N} (SOC_{desired}^i - SOC_0^i) + \sum_{k=1}^{T} l_k}{T} \quad (21)$$

Moreover, the power set of each vehicle, as an important actor, in supplying the grid load will be:

$$P^{-i} = [P^1, P^2, \dots, P^{i-1}, P^{i+1}, \dots, P^N] \quad (22)$$

In order to simplify the cost function, we can write:

$$L_k^{-i} = -\sum_{j=1, j\neq i}^{N} (p_k^j - l_k) + L_{mean} \quad (23)$$

Which results in:

$$G_i(P^i, P^{-i}) = -\sum_{k=1}^{T} \left(p_k^i - L_k^{-i}\right)^2 \quad (24)$$

The optimal power is denoted by P^{i*}. Fig. 6 displays the flowchart of the proposed optimization algorithm. Therefore, the general problem-solving process will be as follows. First, the grid information, including the balanced and unbalanced loads as well as the number of EVs in the grid, is identified. Also, the grid demand rate, the temporal priority of vehicle charging, the voltage range of grid feeders, etc. are defined as input variables at this stage.

In the next step, V2G and G2V algorithms are introduced to the vehicles so that each vehicle can determine how to enter and depart according to the price of upstream electricity. The information of each vehicle is then sent to the ISO.

Afterward, the SOC of each vehicle is evaluated. According to the dynamic programing method, if the SOC is less than the minimum or more than the maximum, the charging or discharging process is stopped, and the load limit for vehicles is set. According to the imbalance rate and grid losses, the distance that each vehicle can travel could be calculated.

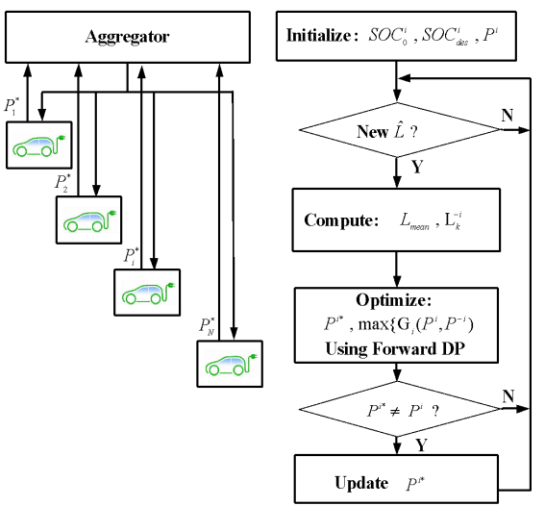

Fig.6: Optimization algorithm flowchart.

In the final stage, each vehicle that is connected to the upstream grid enters the load distribution, and the permissible ranges for the voltage of the feeders and the active and reactive power flowing on the grid lines are evaluated. This process is updated again after each vehicle is connected to or disconnected from the network. If the grid constraints are not observed during the G2V process, the vehicle connected to the grid and the other vehicles waiting to be charged will be shifted to the next interval.

Progressive load distribution methods have widely been used in distribution load calculations due to their high speed and little need for computer memory, as well as their good convergence characteristics. The general algorithm here

consists of two basic steps, including backward sweep and forward sweep, which are repeated until convergence is achieved. These methods are divided into three categories of sum current method, power sum method, and impedance sum method.

The general steps of the algorithm are as follows:

1) backward sweep: Starting from the end bus and moving towards the slack bus, the branch powers are calculated.

$$S_n = S_i + \sum_{m \epsilon M} S_m + Loss_n \quad (25)$$

where S_n is the branch power n, S_i indicates the power injected into the load connected to the node *i*, *M* is the sum of the branches connected to branch *n* in node *i*, S_m represents the power of branch *m* and $Loss_n$ is the losses of branch *n*, which are zero in the first iteration.

2) Forward sweep: Starting from the branches connected to the slack bus and moving towards the end branches, the currents in the bus of the sending branch n (j) and the voltages in the bus of the receiving branch (n), i, are calculated.

$$I_n = (\frac{S_n}{V^j})^*$$
$$V^i = V^j - Z_n * I_n \quad (26)$$
$$Loss_n = -(V^i - V^j) * I_n^*$$

3) Voltage mismatch calculation: After the two above-mentioned steps were completed in each iteration, the voltage mismatch is calculated for all buses:

$$\Delta V^{i(k)} = \left|V^{i(k)}\right| - \left|V^{i(k-1)}\right| \quad (27)$$

where k is the number of iterations. If each of the ΔV_i values is greater than the convergence criterion, steps 1 and 2 are repeated until convergence is achieved.

EV units that are included in the model as a PQ bus in the form of a negative load are controlled. That is, it is enough to reduce the amount of active and reactive power produced by the EV from the power consumption of the bus and do the load distribution. However, to include the distributed production units that are controlled as a PV bus, additional processes are needed to solve the load distribution. A compensation technique is used to control PV nodes. The basic idea of this method is that in order to obtain the voltage in a PV node, it is necessary to determine the correct amount of reactive current injection generated by the unit. For this purpose, in each PV bus, the constants for the generator are determined, i.e., the actual power output (P) and the voltage range (V). Then, this bus is considered a PQ bus in the load distribution algorithm. After the load distribution is converged, the optimal response is achieved using the voltage control sensitivity matrix and the reactive power control constraint in the PV bus.

The voltage variance index, which is known to indicate the improvement of the voltage profile, will also, be equal to:

$$f_v = \sum_{ni=1}^{n_n} (V_{ni} - V_{rated})^2 \quad (28)$$

Also for the voltage stability index we have:

$$SI_{(n_i)} = |V_{mi}|^4 - 4[P_{ni}(ni)R_{ni} + Q_{ni}(ni)X_{ni}]|V_{mi}|^2 - 4[P_{ni}(ni)R_{ni} + Q_{ni}(ni)X_{ni}]^2 \quad (29)$$

In addition, for the (current) load balance index we have:

$$f_{unbl} = \sum_{i=1}^{m} \left(\frac{I_{ni}}{I_{nj\cdot avg}}\right)^2 \quad (30)$$

$$I_{nj.avg} = \frac{1}{m}\sum_{j=1}^{m} I_{nj} \quad (31)$$

In which the current I_{ni} must always be close to I_{nj} so that the imbalance is eliminated.

V. SIMULATION

In order to validate the proposed method, three different case studies are presented in this paper, which are described below.

A. *Case Study 1*

In this case study, it is assumed that the electricity tariff is two-part, so the profit from the sale of battery power to the grid in the V2G state is directly related to the amount of charge in the batteries. It is assumed that four EVs shown in Fig. 7 are connected to the network and to buses 2, 4, 5, and 8. The initial charge of the batteries, their capacity, and other vehicle specifications are presented in Table (2).

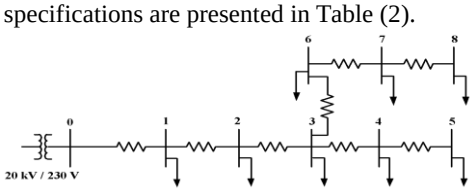

Fig. 7: Distribution grid considered in the case study 1.

Table II

CHARACTERISTICS OF THE MICROGRID IN CASE STUDY 1

Parameter	Value
Effective system voltage	230 (rms)
Line frequency	50 Hz
No. of connected buses	(5, 8, 4,2)
Battery capacity	(15, 15,16,20) kWh
Initial charge rate	(5, 8,3/2, 6/4) kWh
Final charge rate	(12, 15,15,17) kWh

As shown in Figures 8(a) and (b), the load profile becomes flatter when the vehicles are discharged. Since the single-part tariff has been considered to be 2 USD/kWh during all hours of the day, the payment cost will be:

$$cost_{single\ tarrif} = \sum_{j=1}^{N_{car}} P^j \times \pi^j \qquad (32)$$

According to the diagram and after simplification, we will have:

$$cost_{single\ tarrif} = 36.40^{kWh} \times 2^{\$/kWh} = 72.8\ \$ \qquad (33)$$

Figures 9(a) and (b) also illustrate the diagrams of voltage-bus profiles of the grid and battery output power of vehicles, respectively. In the two-part tariff, we consider the price of electricity at 15 to 33 hours to be \$2.8 and at the remaining hours to be \$2. In this case, the amount paid to the distribution company is equal to \$54.72 according to the diagrams in Fig. 10 and Equation (25), which has resulted in a saving of \$18.08. The amount of profit also increases correspondingly. The diagrams in Fig. 11 also show the voltage profile of the main buses and the output power of the vehicle batteries. Compared to the single-part tariff, it can be seen that the bus voltages have been improved.

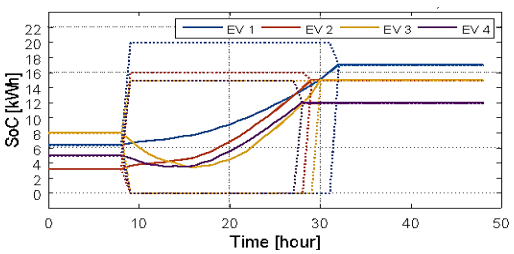

(a)

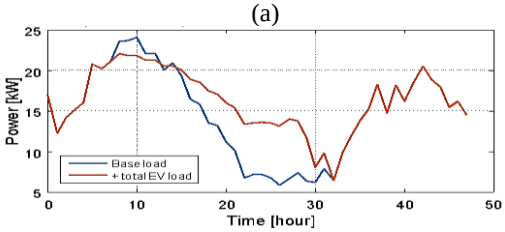

(b)

Fig. 8: Single-part tariff; a) SOC diagram, b) load profile

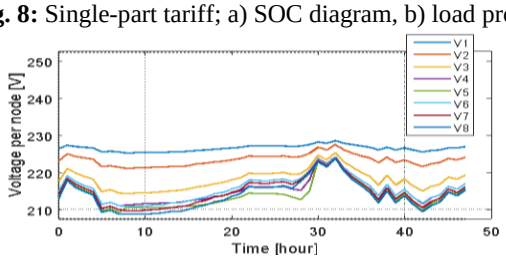

(a)

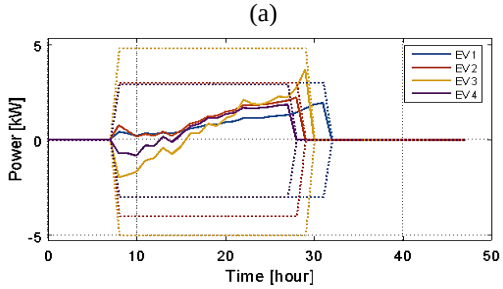

(b)

Fig. 9: Single-part tariff; a) Voltage profile, b) Battery output power

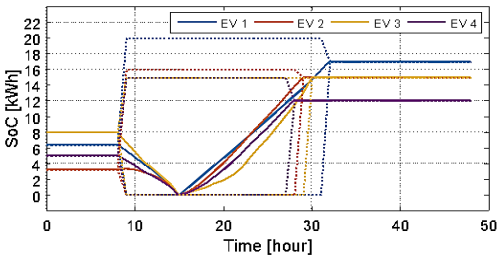

(a)

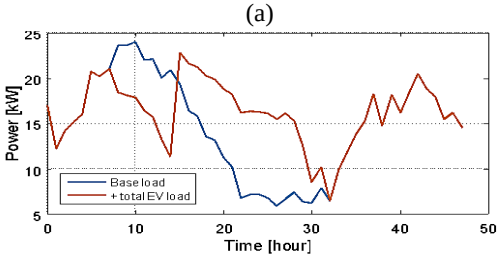

(b)

Fig. 10: Two-part tariff; a) SOC diagram, b) load profile

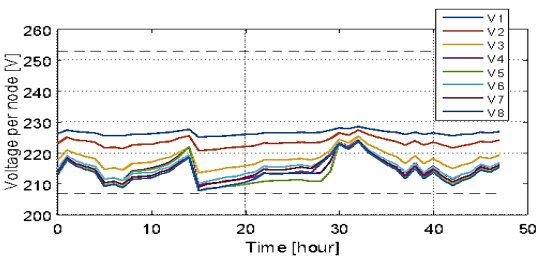

(a)

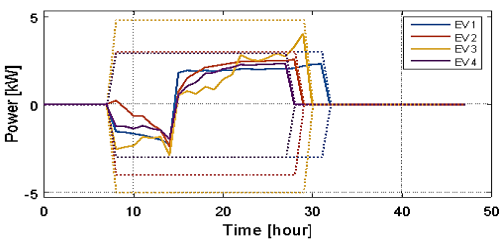

(b)

Fig. 11: Two-part tariff; a) Voltage profile, b) Output power of batteries

B. Case Study 2

In order to investigate the imbalance in the distribution network and to see how to balance it by the optimal management of vehicle battery charging/discharging, the power drawn from all three phases of the distribution system is investigated in this case study. Since the distribution systems in different feeders might be unbalanced and this imbalance may disturb the load balance, this study assumes that the power required for each vehicle battery is unequal (which is, of course, the case in practice) [18]. If the imbalance index of the main voltage is defined by equation (34), it is possible to drastically reduce the amount of imbalance by introducing a conversion function (35) so that the voltage of the negative and positive sequences gets very close to each other.

$$V_{unb} = \left|\frac{V^{-}_{PEV,k}}{V^{+}_{PEV,k}}\right| * 100 \quad (34)$$

$$OF = \{(V_{unb})\} \quad (35)$$

where parameters $V^{-}_{PEV,k}$ and $V^{+}_{PEV,k}$ are introduced by equations (36) and (37), respectively.

$$V^{-}_{PEV,k} = \frac{1}{3}\left(V^{a}_{PEV,k} + \beta V^{b}_{PEV,k} + \beta^2 V^{c}_{PEV,k}\right) \quad (36)$$

$$V^{+}_{PEV,k} = \frac{1}{3}\left(V^{a}_{PEV,k} + \beta \hat{} V^{b}_{PEV,k} + \beta V^{c}_{PEV,k}\right) \quad (37)$$

Parameter β is equal to $1\angle 2\pi 3$ which is extracted from the Fortescue matrix [19]. Considering the above equations and integrating them in the dynamic programing, the active and reactive power consumption of vehicles in each bus can be seen in the diagrams in Fig .12.

Before connecting the vehicles to the circuit, the imbalance in the power of all three phases is drawn with the lines, but with proper charging and discharging management of the vehicles (the dashed line), the imbalance is practically eliminated and the power of each of the three phases becomes roughly balanced [20]. The active and reactive diagrams drawn from all three phases are illustrated in Fig .12, in which they are shown with bold lines.

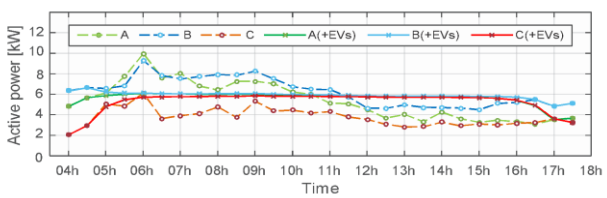

(a)

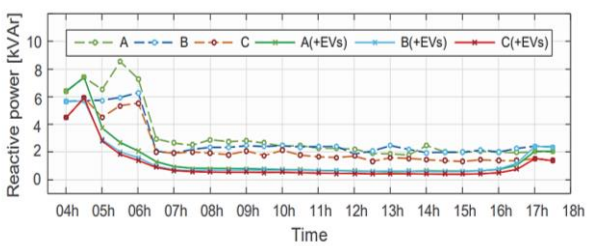

(b)

Fig. 12: Investigation of balancing the power drawn from all three phases in the distribution grid; a) Active power, b) Reactive power

C. Case Study 3

In this case study, it is assumed that five EVs are individually connected to the grid for six hours and charged. If the vehicles are connected to the grid irregularly, the diagram shown in Fig. 13 indicates that the load profile will also have large oscillations asymmetrically. This proves the importance of how the use of EVs is scheduled so that the load profile that is to be provided by the grid could exhibit the maximum flatness. The power consumption diagram of vehicles that are connected to the balanced distribution grid in a regular manner and with the same power is shown in Fig.14.

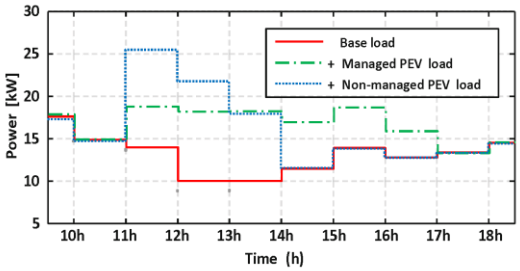

Fig. 13: Comparison of vehicle power consumption in managed/unmanaged charging states

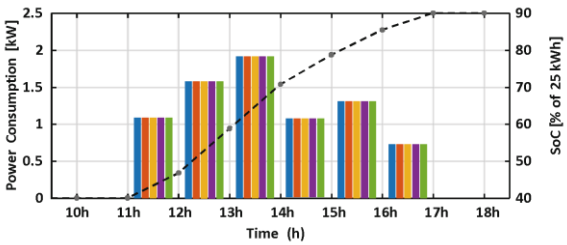

Fig. 14: Power consumption of each vehicle in the managed charging state with its SOC

D. *Case Study 4*

In this section, which is the continuation of the case study 3, it is assumed that the penetration rate of vehicles in the distribution grid is changed. Therefore, four different cases are evaluated below. It is noteworthy that the reliability indices have fully been described in [21-22].

1) The system without any vehicles

In this scenario, the grid is at a resting state and there is no PHEV. Therefore, active and reactive power control, as well as voltage and frequency rate control is performed only by the upstream operator, and consumers are not involved in the price. In this case, unsupplied energy may increase at peak load and reduce the grid reliability. Load response sources are not used here either.

2) PHEVs are on the grid but their charging is not managed:

In this scenario, the vehicles are connected to the grid, but their charging process is not managed, and each vehicle can get power from the grid at any time. This can cause a voltage drop at peak load because the vehicles are connected to the grid like extra loads in this scenario and the grid control is extremely difficult. This scenario shows the negative impact of using EVs.

3) Charging of PHEVs is managed (vehicles do not have returning storage source)

In this scenario, EVs are connected to the grid and are charged, but they do not deliver energy to the grid. Their only advantage for the grid is the reduction of pollutants and the reduction in the use of fossil fuels. In this case, the vehicles are charged in a managed manner (at low load) and are not connected to the grid during peak load.

4) Both managed charging and V2G scenario are applied (vehicles have returning storage source)

At this stage, in addition to the fact that charging of the vehicles is scheduled, the unused energy discharge of their batteries is also managed in the grid during production shortage. This scenario indicates the positive impact of using EVs.

5) Evaluation of Results

Comparing the results of cases 3 and 4 with case 2 shows that scheduled charging not only has a less negative effect than uncontrolled charging but also improves grid reliability. Unmanaged charging reduces reliability by 92%. PHEVs act as storage systems in the V2G state, thereby improving system reliability by 19%.

The results also suggest that the reliability indices are significantly affected by the unmanaged charge of PHEVs. Because the penetration of PHEVs into the smart grid is significantly increased, the grid reliability will sharply reduce if the proper charge management strategy is not implemented. In addition, the results show that the LOEE index (Loss of Energy Expected) is reduced by about 2.5% in the unmanaged charging state and also when charging the electric vehicle is only possible at home (during holidays). Using a managed charging strategy, especially in the V2G state and when charging scheduling is applied at home or work, the LOEE index is improved by about 2.92%. The results of comparing the above cases show that by implementing the proposed charge management methods, PHEV risks for grid reliability can be turned into an opportunity to improve it. With a managed charging strategy in case 3, the problems caused by load demand for charging PHEVs can be controlled. In the V2G strategy mentioned in case 4, the LOEE index and EENS (Energy Expected Not Supplied) are reduced compared to case 1 where there is no PHEV on the grid.

To evaluate the proper performance of the smart grid, the sensitivity analysis of important parameters such as charging level and penetration rate of PHEVs in the LOEE index was performed whose results are illustrated in Figures (15) to (17). These figures exhibit the changes in the LOEE index in relation to the level changes in charge and penetration rate of PHEVs in cases 2, 3, and 4. In the LOEE, sensitivity analysis was conducted for charging level factors (CLF) and PHEV penetration factors (PPF). CLF and PPF are multiplied by the current values of the charging level and the penetration level of electric vehicles, respectively. Then, the reliability indices are calculated, so it is possible to examine the importance of the charging level and the penetration level of PHEVs on the reliability parameters. The LOEE sensitivity in the unmanaged charging scenario for PPF and CLF changes is also shown in Fig.15.

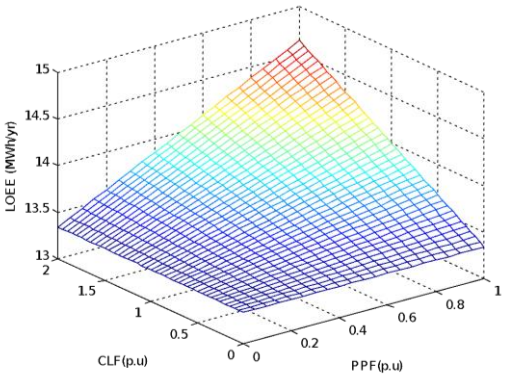

Fig. 15: LOEE index sensitivity based on CLF and PPF in the case 1.

As illustrated in Fig. 15, in the unmanaged charging scenario of PHEVs, as the penetration level of EVs (increased PPF) and their charging level (increased CLF) are increased, the LOEE index also rises. The system reliability decreases with an increase in the number of PHEVs whose charging has not been managed. The results also indicate that the charging level parameter increases the negative impacts of unmanaged charging of PHEVs. According to the results of sensitivity analysis, the worst grid reliability situation in the unmanaged charging of electric vehicles scenario occurs at the fast charging level and at maximum penetration of EVs. The results of case 1 (the scenario of unmanaged charging of EVs) suggest that changing the penetration of PHEVs and charging level have a similar effect. In electrical networks where it is not possible to use advanced communication and information technologies, the charging level of EVs can be reduced to improve system reliability. The LOEE changes in terms of large CLF changes and PPF (between 0 and 2) are shown in Fig. 16.

According to the results in Fig. 16, in the unmanaged charging scenario, when the EVs are charged with the maximum charging level, the grid reliability is drastically reduced. Fig. 16 shows the result of LOEE sensitivity analysis with respect to PPT and CLF changes in the V2G scenario. The load demand and production curves on a critical day in both the unmanaged charging scenario and the V2G scenario are compared. In the critical situation, the two main feeder transformers of the grid have been out of the circuit. In this situation, in the case of unmanaged charging, the load and production diagrams are shown in Fig. 17, and the load and production diagrams of an IEEE 34-bus grid in the V2G scenario are displayed in Fig. 18.

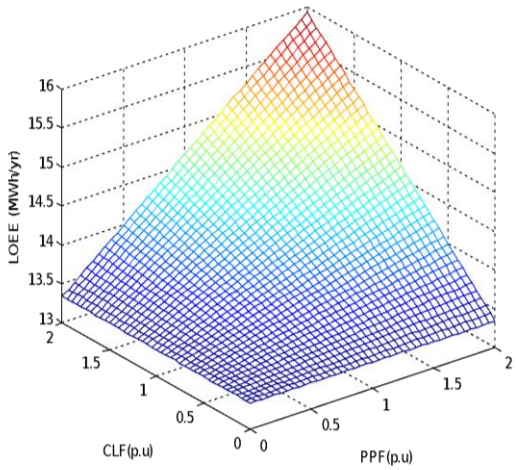

Fig. 16: Sensitivity of the LOEE index based on CLF and PPF in case 1 in a wide range of changes.

Therefore, it can be argued that the use of EVs can have favorable and unfavorable impacts on the grid, which requires strong management to operate it. In addition to increasing system losses, unmanaged vehicle charging also raises operating costs and reduces network reliability. SOC management is one of the most important operating parameters of the problem that can clearly affect network performance. Finally, Table (3) compares the proposed method with the existing methods. It is observed that in the proposed method, both the voltage imbalance index is lower than that of the other methods and the range of SOC changes is increased.

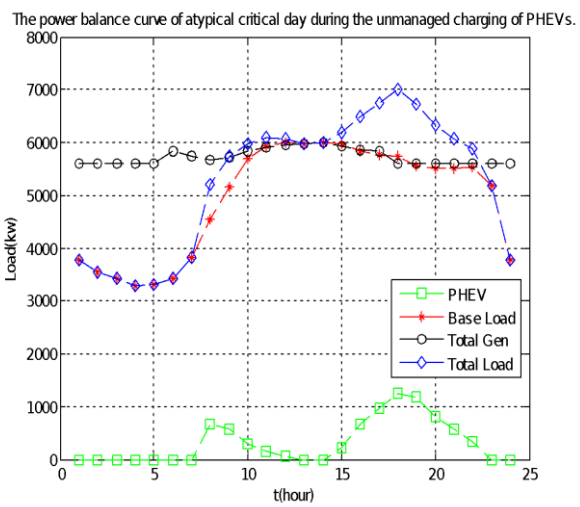

Fig. 17: Load supply in unmanaged charging state

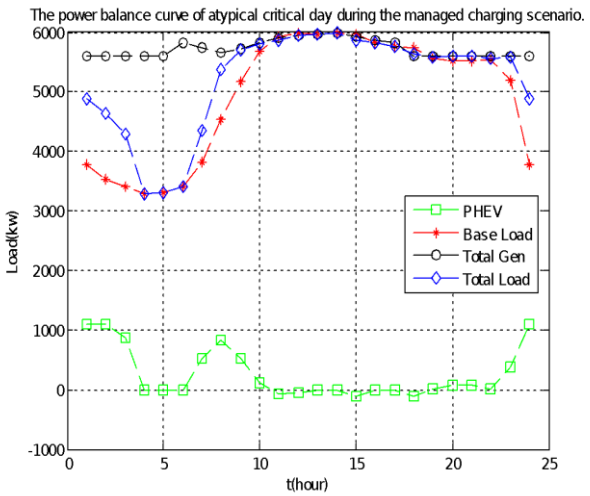

Fig. 18: Load supply in the managed charging state

Table III

COMPARISON OF THE PROPOSED METHOD WITH CONVENTIONAL METHODS

Method	Profit rate in scenario 1	SOC range	Voltage imbalance index
[5]	$ 16.236	(20-80)%	1.9%
[7]	$ 16.562	(20-85)%	1.8%
[17]	$ 18.105	(25-85)%	1.9%
Proposed method	$ 18.723	(15-90)%	1.5%

VI. CONCLUSION

In this paper, optimal scheduling to set the appropriate connecting time of EVs to a low-voltage distribution network has been presented. Since supplying peak load during peak for the distribution network is usually associated with many problems, EVs can help the network during these hours and flatten the load profile by injecting extra power.

According to the case studies conducted here, it is concluded that the two-price tariff benefits vehicle owners more and increases their participation in improving network voltage drops. An optimal vehicle charging and discharging schedule can also eliminate imbalances in the distribution network and act as reactive power control devices. When the charging/discharging of vehicles is not managed, fluctuations in the grid power profile increase, which can be considered a threat to grid security. Hence, all the problems mentioned can be reduced to a minimum level by using dynamic programming with a progressive approach.

TABLE IV
NOMENCLATURE

Variable	Explanations
x^i	Terms of operation EVs
θ^i	The set of all power injection or absorption by EVs
N	Number of EVs
i	EV number i
$\underline{p}$	Maximum Generation of EVs
SOC_0^i	Initial SOC
$\underline{SOC^i}$	Maximum SOC
$\underline{SOC^i}$	Minimum SOC
τ	Length of sampling time steps
$SOC_{desired}^i$	Desired SOC
f_k	The whole system modeling function
ξ_k	Positive random variable
$E(x)$	Mean function
Φ	Cost of f_k function
ψ	A mapping of x_k too u_k
$\hat{\Gamma}_k$	All the possible states for control variable decisions
$\Gamma_k(x_k)$	An non-empty subset of $\hat{\Gamma}_k$
Π_k	All the system states in k interval
Z	Expected value for the objective function
ψ^*	Optimal control
$Z^*(x_0)$	ψ^* cost
L_{mean}	Network average load
P^{i*}	Optimal powers
$V_{PEV,k}^-$	Negative sequence voltage of vehicles
$V_{PEV,k}^+$	Positive sequence voltage of vehicles
S_n	Power of branch *n*
S_i	Power injected to the bus *i*
M	set of branches connected to branch *n* in bus *i*
$Loss_n$	Losses of branch n
$P_{ni}(ni)$	Active power between n and i buses
$Q_{ni}(ni)$	Reactive power between n and i buses
R_{ni}	Line resistance between bus n and bust i
X_{ni}	Line reactance between bus n and bus i
I_{nj}	Current of the line between bus *n* and bus *i*
$I_{nj.avg}$	Average current of the line between bus *n* and bus *i*

REFERENCES

[1] R. Iacobucci, B. McLellan, and T. Tezuka, "Optimization of shared autonomous electric vehicles operations with charge scheduling and vehicle-to-grid," *Transportation Research Part C: Emerging Technologies*, vol. 100, pp. 34–52, Mar. 2019.

[2] H. Soltani Gohari, K. Abbaszadeh, and J. Gholami Gorji, "A Controllable Bidirectional Rectifier for EV Home Charging Station with G2H/G2VH/V2H/V2G Functions," *International Journal of Industrial Electronics Control and Optimization*, vol. 4, no. 1, pp. 99-113, 2021.

[3] M. Ramzanzadeh, M. Jafari Nokandi, T. Barforoushi, and J. Saebi, "Security-Constrained Unit Commitment in the Presence of Demand Response Programs and Electric Vehicles," *International Journal of Industrial Electronics Control and Optimization*, vol. 3, no. 3, pp. 313-326, 2020.

[4] L. Yao, Z. Damiran, and W. H. Lim, "Optimal Charging and Discharging Scheduling for Electric Vehicles in a Parking Station with Photovoltaic System and Energy Storage System," *Energies*, vol. 10, no. 4, p. 550, Apr. 2017.

[5] Y. Cao, L. Huang, Y. Li, K. Jermsittiparsert, H. Ahmadi-Nezamabad, and S. Nojavan, "Optimal scheduling of electric vehicles aggregator under market price uncertainty using robust optimization technique," *International Journal of Electrical Power & Energy Systems*, vol. 117, p. 105628, May 2020.

[6] Y. Zheng, S. Niu, Y. Shang, Z. Shao, and L. Jian, "Integrating plug-in electric vehicles into power grids: A comprehensive review on power interaction mode, scheduling methodology and mathematical foundation," *Renewable and Sustainable Energy Reviews*, vol. 112, no. 1, pp. 424-439, 2019.

[7] H. Ahmadi-Nezamabad, M. Zand, A. Alizadeh, M. Vosoogh, and S. Nojavan, "Multi-objective optimization based robust scheduling of electric vehicles aggregator," *Sustainable Cities and Society*, vol. 47, p. 101494, May 2019.

[8] A. Triviño-Cabrera, J. A. Aguado, and S. de la Torre, "Joint routing and scheduling for electric vehicles in smart grids with V2G," *Energy*, vol. 175, pp. 113–122, May 2019.

[9] C. Goebel and D. S. Callaway, "Using ICT-Controlled Plug-in Electric Vehicles to Supply Grid Regulation in California at Different Renewable Integration Levels," in *IEEE Transactions on Smart Grid*, vol. 4, no. 2, pp. 729-740, June 2013.

[10] Z. Wang, P. Jochem, and W. Fichtner, "A scenario-based stochastic optimization model for charging scheduling of electric vehicles under uncertainties of vehicle availability and charging demand," *Journal of*

Cleaner Production, vol. 254, p. 119886, May 2020.

[11] M.-W. Tian, S.-R. Yan, X.-X. Tian, M. Kazemi, S. Nojavan, and K. Jermsittiparsert, "Risk-involved stochastic scheduling of plug-in electric vehicles aggregator in day-ahead and reserve markets using downside risk constraints method," *Sustainable Cities and Society*, vol. 55, p. 102051, Apr. 2020.

[12] M. U. Javed, N. Javaid, A. Aldegheishem, N. Alrajeh, M. Tahir, and M. Ramzan, "Scheduling Charging of Electric Vehicles in a Secured Manner by Emphasizing Cost Minimization Using Blockchain Technology and IPFS," *Sustainability*, vol. 12, no. 12, p. 5151, Jun. 2020.

[13] A. González-Garrido, A. Thingvad, H. Gaztañaga, and M. Marinelli, "Full-scale electric vehicles penetration in the Danish Island of Bornholm—Optimal scheduling and battery degradation under driving constraints," *Journal of Energy Storage*, vol. 23, pp. 381–391, Jun. 2019.

[14] Y. Luo, G. Feng, S. Wan, S. Zhang, V. Li, and W. Kong, "Charging scheduling strategy for different electric vehicles with optimization for convenience of drivers, performance of transport system and distribution network," *Energy*, vol. 194, p. 116807, Mar. 2020.

[15] J. Su, T. T. Lie, and R. Zamora, "A rolling horizon scheduling of aggregated electric vehicles charging under the electricity exchange market," *Applied Energy*, vol. 275, p. 115406, Oct. 2020.

[16] E. Hadian, H. Akbari, M. Farzinfar, and S. Saeed, "Optimal Charging/Discharging Control of Electric Vehicle Charging Station Considering Grid Resiliency," *International Journal of Industrial Electronics Control and Optimization*, vol. 4, no. 4, pp. 453-464, 2021.

[17] S. Seyyedeh Barhagh, M. Abapour, and B. Mohammadi-Ivatloo, "Optimal scheduling of electric vehicles and photovoltaic systems in residential complexes under real-time pricing mechanism," *Journal of Cleaner Production*, vol. 246, p. 119041, Feb. 2020.

[18] C. Sabillon-Antunez, O. D. Melgar-Dominguez, J. F. Franco, M. Lavorato and M. J. Rider, "Volt-VAr Control and Energy Storage Device Operation to Improve the Electric Vehicle Charging Coordination in Unbalanced Distribution Networks," in *IEEE Transactions on Sustainable Energy*, vol. 8, no. 4, pp. 1560-1570, Oct. 2017.

[19] M. R. Islam, H. Lu, M. J. Hossain, and L. Li, "Mitigating unbalance using distributed network reconfiguration techniques in distributed power generation grids with services for electric vehicles: A review," *Journal of Cleaner Production*, vol. 239, p. 117932, Dec. 2019.

[20] A. HossienPour, and A. Khajeh, "Determining Optimal Value of Pole Arc to Pole Pitch Ratio in order to Increasing Average Torque and Decreasing Unbalance Magnetic Force in Hybrid Electrical Vehicle, " *International Journal of Industrial Electronics Control and Optimization*, vol. 4, no. 4, pp. 445-451, 2021.

[21] C. Singh, Panida Jirutitijaroen, and J. Mitra, *Electric power grid reliability evaluation : models and methods*. Chichester: Wiley Blackwell, 2019.

[22] B. W. Tuinema, *Probabilistic reliability analysis of power systems : a student's introduction*. Cham, Switzerland Springer, 2020.

Ali Masoudi was born at Eqlid, Iran, at 1974. He received the B.sc. degree at electrical engineering at Islamic Azad University, Khomeyni Shahr Branch, Khomeyni Shahr, Iran at 2009 and the M.sc. at Islamic Azad University, Mehriz Branch Mehriz, Iran at 2015. He is currently working towards his PhD degree in the Islamic Azad University, Yazd Branch. Yazd, Iran. He is currently working as Exploitation Manager at Fars Electricity Distribution Company, Shiraz, Iran since 2000. His main research interests include analysis and design of electrical machines, power electronics and renewable energies.

Mohsen Simab received his BSc degree in Electrical Engineering from Amir Kabir University, Tehran, Iran in 2003 and obtained the MSc and PhD degrees from Tarbiat Modares University, Tehran, Iran, 2005, and 2011, respectively. He is an Assistant Professor in power systems at the Department of Electrical Engineering, Marvdasht Branch, Islamic Azad University, Marvdasht, Iran. His main research interests are electric distribution regulation, power system operation, and power system reliability.

HamidReza Akbari was born in Yazd, Iran, in 1980. He received the B.Sc. and M.Sc. degrees in electrical engineering from the Amirkabir University of Technology, Tehran, Iran, in 2001 and 2004, respectively, and the Ph.D. degree in electrical engineering from Islamic Azad University, Science and Research Branch, Tehran, in 2011. He is currently working as an Assistant Professor of Electrical Engineering with Islamic Azad University, Yazd Branch. His main research interests include analysis and design of electrical machines, power electronics and renewable energies.

Seyed Amin Saied received the M.Sc. and Ph.D. degrees in electrical engineering from the K. N. Toosi University of Technology, Tehran, Iran, in 2006 and 2012, respectively. He is currently with the Department of Electrical Engineering, Yazd Branch, Islamic Azad University, Yazd, Iran. His main research interests include the design and modeling of electrical machines, and electrical parameter estimation of electrical machines.

Tahere Daemi was born in Iran, in 1979. She received the B.Sc degree in 2002 from Yazd university, the M.S degree in 2005 Shiraz University and Ph.D degree in 2012 from Isfahan University of Technology. Currently, she is an Assistant Professor of electrical engineering department in Islamic Azad University, Yazd Branch, Iran. Her major field of study is reliability and security analysis, renewable energy resources, energy management with application of data mining and Bayesian Networks in power systems.

IECO

This page intentionally left blank.

International Journal of Industrial Electronics, Control and Optimization © 2022 IECO
Vol. 5, No. 2, pp. 123-132, April (2022)

An Enhanced Distributed State Feedback for Secondary Control in an Islanded Microgrid

Morteza Alizadeh[1], Hossein Askarian.A[2†], Alireza Bakhshai[3] , Naser Khodabakhshi-Javinani[4]

[1,2] Department of Electrical Engineering, Amirkabir University of Technology
[3] Department of Electrical and Computer Engineering, Queen's University Kingston, ON, Canada
[4] Electrical and Computer Engineering Department, Yadegar-e-Imam Khomeini (RAH) Shahre Rey Branch, Islamic Azad University, Tehran, Iran.

ABSTRACT

This paper applies a new state feedback control to a distributed secondary voltage and frequency control in an islanded microgrid. The problem is focused on the output consensus of the multi-agent systems, which is converted to a first-order dynamic system. The inverter-based distributed generations play as agents in the proposed control strategy. It is assumed that the distributed generators communicate through a communication network modeled by a directed graph (digraph). The distributed output consensus is used to design the secondary controllers. Such innovative controllers synchronize distributed generators' output voltages and frequencies to their reference values by a novel state feedback approach. Compared to the existing consensus protocols, the proposed method provides a different innovative solution to the secondary voltage and frequency control of microgrids, which has a better response in case of communication failures. Finally, extensive and comparative simulations have been presented to verify the validity of the proposed control strategy and the system performance.

Article Info

Research Article

Keywords:

Distributed cooperative control, Islanded microgrid, State feedback control, Secondary voltage control, Secondary frequency control

Article History:

Received 2021-12-26
Accepted 2022-02-20

I. INTRODUCTION

Microgrids (MGs), consisting of distributed generators (DGs), loads, energy storages, power converters, LC filters, and output connectors, has recently been introduced and used to decrease the energy problems. Conventionally, MG can be operated in grid-connected, off-grid, or so-called islanded mode. MGs will change the traditional power generation structure and thus bring up new control challenges for the safe and efficient operation of the power system [1-5]. When islanded, voltage and frequency control of MGs become very important. In the well-known hierarchical control structure of MGs, secondary control restores voltage and frequency deviations caused by the primary control level to their reference values [6, 7]. Generally speaking, the secondary control uses a centralized structure that is required to send all the information of the DGs to a central control unit via a communication network system [8-11]. Information centralization provides reliability and security concerns. Also, centralized controllers have low-performance responses to plug-and-play and communication failures [9]. Moreover, the centralized methods do not satisfy accurate power-sharing [9].

In order to overcome the weaknesses mentioned above, several studies have suggested the so-called distributed secondary voltage and frequency control based on multi-agent systems [12-14]. Unlike a central controller, the distributed one works with a one-way communication network, and the agents only use their information and the information obtained from their just immediate neighbors. Therefore, the complex communication network of the centralized controllers is ignored. In particular, the upfront costs of communication infrastructure are decreased in distributed control approach. Moreover, in spite of the fact that centralized control has the

†**Corresponding Author**: askarian@aut.ac.ir
Tel: +98-2164543370, Fax: +98-2164543370, Electrical Engineering Department, Amirkabir University of Technology, Tehran, Iran

low plug-and-play capability, poor scalability, and weak response to communication failures, the distributed controller better handles the plugging out/in of any DGs and works more reliable in conditions of different communication failure. It is also worth noting that distributed control has persistent operation against time-varying communication graph topologies. In summary, all advantages of distributed controllers lead to efficient information sharing and allow the operator to make faster decisions.

As mentioned before, the secondary control's main aim is to restore the voltage and frequency of islanded MGs to their nominal references values. Also, a distributed approach is considered in the secondary control to share active power accurately when two or more DGs are working in parallel. Recently, researchers have shown an increased interest in distributed secondary voltage and frequency and active power-sharing control in AC microgrids [12-24]. Unlike frequency, a global variable in a microgrid, voltage is a local variable. Three different scenarios can be considered for voltage restoration through distributed secondary control in MGs, by (i) average voltage consensus in the whole MG [12, 13], (ii) accurate voltage consensus in the output of the voltage-controlled voltage source inverters (VSIs) [14, 15], or (iii) accurate voltage consensus in some specific busses in the MG [16]. Moreover, various distributed secondary control consider some limitations. For instance, in [17], the distributed secondary control (DSC) is utilized to implement a coordinated framework for multiple DGs grouped dynamically through smart switches in a microgrid. A DSC scheme is considered in [18] for a hybrid microgrid to control only the load voltage. Another DSC is provided by [19] to restore frequency and share active power in an AC microgrid with mobile emergency resources (MERs) during a specified time. DSC approach is also considered under sensor and actuator faults [20, 21], switching topologies [22], and variable time-delayed communications [23] or fixed-time delays [24].

Up to now, previous studies in the area of distributed secondary voltage and frequency control have examined initial cooperative consensus protocol. However, a novelty in the choice of consensus protocol has not been found in the literature. All the researches mentioned above have used conventional distributed control to restore voltage and frequency to their reference values and share active power accurately. However, in this paper, we enhanced the conventional DSC through an auxiliary part based on state information to improve the performance of the control protocol, such as accelerating the convergence speed and improving transient response. The proposed approach has a better performance than the conventional DSC approach in the presence of different power disturbances and communication failures.

In this paper, a new cooperative control based on state feedback control for a multi-agent system is considered to solve the secondary voltage and frequency control problem in an

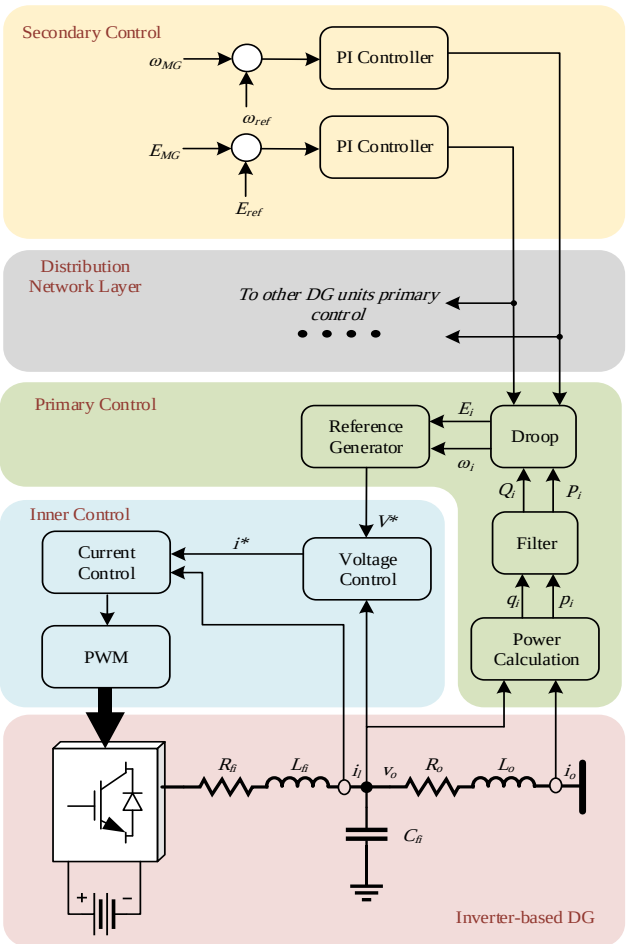

Fig. 1. Schematic diagram of an inverter-based DG with its three control levels

islanded MG. The problem is converted to a single integrator dynamic system to design a simple controller. It is considered that the multi-agent system is fully distributed, and all agents only use their information and information from their immediate neighbors. Simulations are performed to investigate all the implementation mentioned above concerns of distributed control. The proposed method is compared with the classical consensus protocol, and simulation results show that our method performs better, particularly in the presence of system and communication disturbances compared to the classical protocols.

The rest of this paper is organized as follows: Section II provides a brief review of the hierarchical structure of MG control. Section III presents a brief graph-theoretic preliminary and explains the problem statement. A novel output consensus with state feedback control is offered in Section IV. Section V and VI discuss problem formulation of distributed voltage and frequency control for an islanded MG, respectively. Section VII introduces the MG test system with four inverter-based DGs as a multi-agent system. Simulation studies and results analysis

are provided in Section VIII, and finally, the conclusions are drawn in Section IX.

II. Hierarchical Structure of MG Control

In this section, the conventional hierarchical structure of MG control is reviewed. This control structure consists of four levels, including inner loop (zero), primary, secondary, and tertiary control levels responsible for processing, adjusting, monitoring, and optimizing system variables, respectively. Since the aim of this paper is to control secondary voltage and frequency in an islanded MG, the tertiary control level is not taken into consideration. For a detailed explanation, see [8, 25]. Fig. 1 shows an inverter-based DG schematic diagram with three control levels. The electrical network includes a dc power source, a three-leg dc-ac inverter, an LC filter, and an RL output connector. In the following, each control level of the hierarchical control structure is discussed.

A. Inner Loop Control (Zero Level)

In this control level, the power is generated by using voltage-controlled voltage source inverters (VSIs), which are connected to an islanded MG, or current-controlled VSIs, which are connected to a grid-connected MG. As shown in Fig. 1, voltage-controlled VSIs consist of an inner current loop and an external voltage loop to stabilize the current and voltage and provide sufficient damping. While current-controlled VSIs are equipped with an inner current loop and a phase-locked loop to keep the synchronization with the grid. In the islanded mode of operation, a reference voltage is generated by the upper control layer as a primary control level.

B. Primary Control

The droop control method is employed when two or more VSIs are connected in parallel to eliminate circulating currents and share active and reactive powers between converters. Generally speaking, the droop control method provides operating frequency and reference voltage magnitude for the voltage control loop according to the active and reactive power of inverter-based DG, respectively. For inductive lines, the droop control functions of *i-th* DG can be defined as follows [6, 8, 25]

$$\omega_i = \omega^* - P_i m_p \tag{1}$$

$$E_i = E^* - Q_i n_q \tag{2}$$

Where: ω^* and E^* are frequency reference and voltage magnitude, P_i and Q_i are measured active and reactive powers of *i-th* DG, and. m_p and n_q are droop coefficients that are selected according to active and reactive power ratings. The primary control of the proposed VSI is shown in Fig. 1.

C. Secondary Control Level

Voltage and frequency deviations caused by the primary control level can be compensated via the secondary control level. If the load or generation changes in MGs, secondary control guarantees the zero error of voltage and frequency fluctuations. In order to compensate voltage and frequency deviations, we should measure the voltage and frequency at the point of common coupling (PCC), $\omega_{MG,}$ and E_{MG}, and compare them with their references, ω_{ref}, and E_{ref}. Then, the error values passed through the compensators are sent to all DG's primary control levels via communication links. The proportional-integral (PI) type controller shown in Fig. 1, as a common controller to restore voltage and frequency, can be obtained as follows [8]

$$\Delta\omega = k_{p\omega}(\omega_{ref} - \omega_{MG}) + k_{i\omega}\int(\omega_{ref} - \omega_{MG}) \tag{3}$$

$$\Delta E = k_{pE}(E_{ref} - E_{MG}) + k_{iE}\int(E_{ref} - E_{MG}) \tag{4}$$

Where: $k_{p\omega}$, $k_{i\omega}$, $k_{pE,}$ and k_{iE} are PI controller parameters. Conventionally, this controller can be implemented as a centralized secondary controller. However, as mentioned before, low reliability, complex communication network, and weak performance are significant drawbacks of the secondary centralized control approach.

III. Preliminary of Graph-Theoretic and Problem Statement

A. Graph Theory

The communication network of the multi-agent system can be displayed by using a directed graph (digraph) $\mathcal{G}= (V, E, A)$ of order n with the set of nodes $V=\{v_1, v_2, \ldots, v_n\}$, edges (arcs) $E \subseteq V \times V$, and *adjacency matrix* $A=\left[a_{ij}\right] \in \mathbb{R}^{n\times n}$. We assume the graph is simple, i.e., no self-loops and no multiple edges between two identical pairs of nodes. The node v_k represents the k_{th} agent, and the arc (v_i, v_j) shows the information flows and means the agent j is the neighbor of agent i. The number of its neighbor defines the *degree* of a node. Letting d_i be the degree of node v_i, then the *degree matrix* of a graph $\mathcal{G}$, $D \in \mathbb{R}^{n\times n}$, is given by D, $diag(d)$, $d = \left[d_1, \ldots, d_n\right]^T$. Besides, we assume a_{ij} is positive ($a_{ij} > 0$) if $(v_i, v_j) \in E$, *and* $a_{ij} = 0$ otherwise. The *Laplacian matrix*, L, associated with the graph $\mathcal{G}$, can be defined as $L_{ii} = \sum_{j\neq i} a_{ij}$ and $L_{ij} = -a_{ij}$, $j \neq i$ where $L\mathbf{1}_n = 0$. A sequence of successive edges in the form of $\{(v_i,v_k), (v_k,v_l), \ldots, (v_m,v_j)\}$ is considered as a direct path from node i to node j. A compact form can represent the Laplacian matrix as $L = D - A$. A directed graph is said to have or contain a directed *spanning tree* if a root node exists that has a direct path from that node to every other node in the graph. [26].

B. Problem Statement

We use a multi-agent with n followers and one leader in this paper. Consider n identical linear-space of the followers as:

$$\begin{aligned} \dot{x}_i(t) &= Ax_i(t) + Bu_i(t), \\ y_i(t) &= Cx_i(t), \qquad i = 1, 2, \ldots, n, \end{aligned} \tag{5}$$

With state vectors $x_i \in \mathbb{R}^n$, control input $u_i \in \mathbb{R}^p$, and output vector $y_i \in \mathbb{R}^q$. It is assumed that the matrix pairs (A, B) and (A, C) are controllable and observable,

respectively. Moreover, it is supposed that all followers have at least one neighbor. The leader, denoted as 0, generates the reference signal, which can be viewed as the following form:

$$\begin{aligned} \dot{x}_0(t) &= Mx_0(t), \\ y_0(t) &= Nx_0(t), \end{aligned} \tag{6}$$

Where: $x_0 \in \mathbb{R}^n$ and $y_0 \in \mathbb{R}^q$ are state and output leader, respectively. Also, it is assumed that the matrix pair (M, N) is observable. Moreover, suppose that the leader receives no information from any follower.

Assumption 1 For the followers in (5), there exist solution pairs (T_i, U_i) for $i = 1, 2, \ldots, n$ as we have

$$\begin{aligned} T_i M &= A T_i + B U_i \\ CP_i &= N. \end{aligned} \tag{7}$$

Also, we define the output error for each follower as follows

$$e_i(t) = y_i(t) - y_0(t), \qquad i = 1, 2, \ldots, n \tag{8}$$

Here, in this paper, we have a control object of developing a distributed cooperative controller to solve the consensus problem in a multi-agent system which obtains the output error $e \to 0$ as $t \to \infty$ for any initial condition.

IV. Output Consensus with State Feedback Control

In this section, the consensus problem of the multi-agent system is solved by designing state feedback in contrast with the classical consensus protocols. In order to reach output consensus, a distributed protocol for the system (5) and the leader (6) is given as in [27]

$$\begin{aligned} \dot{h}_i(t) &= Mh_i(t) + F[\sum_{j=1}^{n} a_{ij}(h_j(t) - h_i(t)) \\ &\quad + b_i(x_0(t) - h_i(t))], \\ u_i(t) &= K_1 x_i(t) + K_2 h_i(t), \qquad i = 1, 2, ..., n, \end{aligned} \tag{9}$$

Where: $h_i(t)$ is an auxiliary state of the controller $F \in \mathbb{R}^{p \times n}$, is called the coupling gain, and $K_1, K_2 \in \mathbb{R}^{p \times n}$ are the controller feedback gains to be determined. a_{ij} is the (i, j) - entry of the adjacency matrix associated with the $\mathcal{G}$ and b_i is called the pinning gain.

Theorem 1: Suppose that assumption 1 holds. The consensus problem of a multi-agent system of followers in (5) and the leader in (6) can be solved by the control protocol in (9) if the following two conditions are satisfied:

(1) $F = \sigma P$, where σ is a positive constant such that $\sigma\lambda_{\min} > 1$ where $\lambda_{\min}$ is the minimum eigenvalue of $L+b$ and the positive matrix P is a solution of the following Ricatti equation

$$PM + M^T P - 2P^2 < 0. \tag{10}$$

(2) K_1 and K_2 can be determined such that $A + BK_1$ is Hurwitz, and $K_2 = U_i - K_1 T_i$ where (T_i, U_i) is the solution of (7).

Proof: Let $x = col(x_1, x_2, \ldots, x_n)$ and $h = col(h_1, h_2, \ldots, h_n)$. Considering (5) and (8), the overall closed-loop network dynamics can be obtained in the following form

$$\begin{aligned} \dot{x}_i(t) &= (A + BK_1)x_i(t) + BK_2 h_i(t), \\ \dot{h}_i(t) &= Mh_i(t) + F[\sum_{j=1}^{n} a_{ij}(h_j(t) - h_i(t)) \\ &\quad + b_i(x_0(t) - h_i(t))]. \end{aligned} \tag{11}$$

The compact form of a closed-loop system can be written as

$$\begin{aligned} \dot{x}(t) &= (A + BK_1)x(t) + BK_2 h(t), \\ \dot{h}_i(t) &= (I_n \otimes M - (L+b) \otimes F)h(t) + ((L+b) \otimes F)\zeta_0(t), \end{aligned} \tag{12}$$

Where: $b = diag(b_1, b_2, \ldots, b_n)$ and $\zeta_0(t) = 1_n \otimes x_0(t)$.

By defining $\tilde{x}(t) = [x^T(t), h^T(t)]^T$, (12) can be rewritten as the following form

$$\dot{\tilde{x}}(t) = \tilde{A}\tilde{x}(t) + \tilde{B}\zeta_0(t), \tag{13}$$

Where: $A + BK$ is Hurwitz. Hence, the matrix $\tilde{A}$ is Hurwitz, if and only if $I_n \otimes M - (L+b) \otimes F$ is Hurwitz. Since $L+b$ is a symmetric matrix, we define an orthogonal matrix U such that

$$U(L+b)U^T = Q = diag(\lambda_1, \lambda_2, \ldots, \lambda_n), \tag{14}$$

Where: λ_i, $i = 1, 2, \ldots, n$, is the eigenvalue of the $L+b$ and the matrix U satisfies $UU^T = I_n$. Therefore, from (14) we can write:

$$\begin{aligned} & I_n \otimes M - (L+b) \otimes F \\ &= I_n \otimes M - (L+b) \otimes \tau P \\ &= (U^T \otimes I_n)(I_n \otimes M - Q \otimes \tau P)(U \otimes I_n) \\ &= (U^T \otimes I_n)diag(M - \lambda_1 \tau P, M - \lambda_2 \tau P, \ldots \\ &\quad , M - \lambda_n \tau P)(U \otimes I_n) \\ &\le (U^T \otimes I_n)diag(M - P, M - P, \ldots, M - P)(U \otimes I_n) \end{aligned} \tag{15}$$

Then, it concludes from (10) that:

$$PM + M^T P - 2P^2 = P(M-P) + (M-P)^T P < 0 \tag{16}$$

(16) together with (15) achieves $I_n \otimes M - (L+b) \otimes F$ which is Hurwitz. Therefore, it can be obtained that the matrix $\tilde{A}$ is Hurwitz, and the overall closed-loop system in (11) is asymptotically stable.

At the next step, we will prove that the output error $e_i(t)$ in (9) will converge to zero $t \to \infty$. Consider $\dot{\tilde{x}}_i(t) = \dot{x}_i - T_i \dot{x}_0(t)$, then we can write

$$\begin{aligned} \dot{\tilde{x}}_i(t) &= \dot{x}_i - T_i \dot{x}_0(t) \\ &= Ax_i(t) + B(K_1 x_i(t) + K_2 h_i(t)) - T_i(Mx_0(t)) \\ &= (A + BK_1)x_i(t) + BK_2 h_i(t) - T_i M x_0(t) \end{aligned} \tag{17}$$

From (8) and $K_2 = U_i - K_1 T_i$, (17) can be written in the form of (18)

$$\begin{aligned} \dot{\tilde{x}}_i(t) &= (A + BK_1)x_i(t) + (BU_i - BK_1 T_i)h_i(t) \\ &\quad - (AT_i + BU_i)x_0(t) \\ &= (A + BK_1)\tilde{x}_i(t) + BK_2(h_i(t) - x_0(t)) \end{aligned} \tag{18}$$

It is easy to see that if $A+BK_1$ is Hurwitz, then $\lim_{t\to\infty}\tilde{x}_i(t)=0$

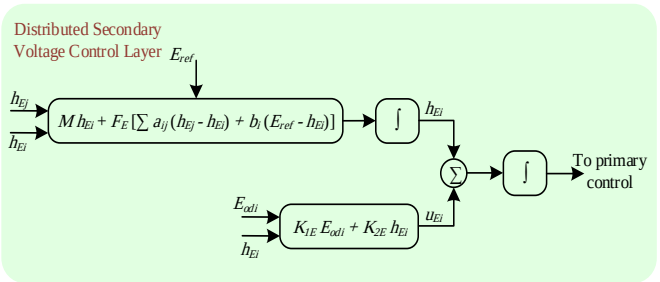

Fig. 2. The block diagram of the state feedback distributed secondary voltage control

. For the output error, we can derive (19)

$$\begin{aligned}\lim_{t\to\infty}e_i(t)&=\lim_{t\to\infty}(y_i(t)-y_0(t))\\&=\lim_{t\to\infty}(Cx_i(t)-Nx_0(t))\\&=\lim_{t\to\infty}(Cx_i(t)-CT_ix_0(t))\\&=\lim_{t\to\infty}C(x_i(t)-T_ix_0(t))\\&=\lim_{t\to\infty}C\tilde{x}_i(t)=0\end{aligned}\tag{19}$$

Which indicates the output error $e_i(t)\to 0$ as $t\to\infty$ for any initial condition. Therefore, the output consensus of the multi-agent followers (5) and the leader (6) is achieved by the protocol introduced in (8). This completes the proof.

V. Distributed State Feedback for Secondary Voltage Control

In this section, an output consensus controller, based on the state feedback, is designed to solve the secondary voltage synchronization in an islanded MG. It is important to note that the dynamics of voltage and current controllers are overlooked in this study. This assumption is possible because their dynamics are much faster than the droop and power controllers. To do so, (2) can be rewritten in *dq* reference frame as

$$\begin{aligned}E_{odi}&=U_n-n_{qi}Q_i\\E_{oqi}&=0\end{aligned}\tag{20}$$

By differentiating the top equation in (20) we have (21).

$$\dot{U}_n=\dot{E}_{odi}+n_{qi}\dot{Q}_i\triangleq u_{Ei}\tag{21}$$

Where: u_{Ei} is defined as an ancillary control. By employing (21) to a microgrid with *n* DGs the secondary voltage control of a microgrid can be changed to the consensus problem with first-order dynamics of the linear multi-agent system as follows:

$$\dot{E}_{odi}=u_{Ei},\quad i=1,2,...,n\tag{22}$$

In order to solve the synchronization problem, it is assumed that DGs can communicate with each other over the prescribed graph $\mathcal{G}$ in section 3. All nodes of graph $\mathcal{G}$ have scalar single-integrator dynamics according to (22). It is worth noting that the protocol is fully distributed because each DG needs its own information and its neighbors under a low-band width communication network layer. In order to reach the output consensus of secondary voltage in an islanded MG, the following state feedback distributed consensus algorithm and the control inputs u_{Ei} are considered, as described in (9) by (23):

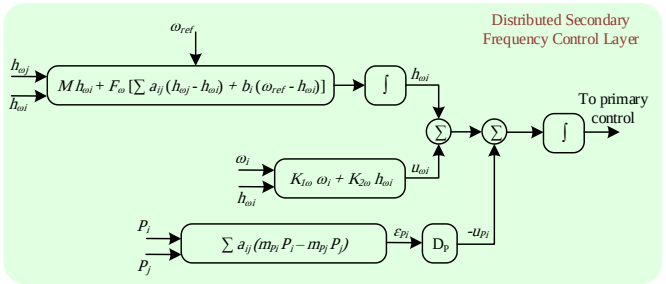

Fig. 3. The block diagram of the state feedback distributed secondary frequency control

$$\begin{aligned}\dot{h}_{Ei}&=M_Eh_{Ei}+F_E(\sum_{j=1}^{n}a_{ij}(h_{Ej}-h_{Ei})+b_i(E_{ref}-h_{Ei}))\\u_{Ei}&=K_{1E}E_{odi}+K_{2E}h_{Ei},\qquad i=1,2,...,n\end{aligned}\tag{23}$$

The block diagram of the proposed distributed secondary voltage control based on state feedback consensus algorithm is shown in Fig. 2.

VI. Distributed State Feedback for Secondary Frequency Control

In this section, a distributed cooperative control based on state feedback control selects proper control inputs to synchronize the frequency of DGs, to the reference frequency, i.e. 50 Hz in this study. As the previous section, differentiating from (1) yields

$$\dot{\omega}_n=\dot{\omega}_i+m_{Pi}\dot{P}\triangleq u_{\omega i}\tag{24}$$

Where (24) determines the feedback linearization method providing the following dynamic linear multi-agent system.

$$\dot{\omega}_i=u_{\omega i},\qquad i=1,2,...,n\tag{25}$$

We define state feedback distributed consensus algorithm the same as in (23), and the control inputs $u_{\omega i}$ for the frequency control are as follows

$$\begin{aligned}\dot{h}_{\omega i}&=M_\omega h_{\omega i}+F_\omega(\sum_{j=1}^{n}a_{ij}(h_{\omega j}-h_{\omega i})+b_i(\omega_{ref}-h_{\omega i}))\\u_{\omega i}&=K_{1\omega}\omega_i+K_{2\omega}h_{\omega i},\qquad i=1,2,...,n\end{aligned}\tag{26}$$

As discussed in the previous section, the proposed control strategy provides the synchronization of all DG units' frequency to the reference value. According to (24), we can write (27).

$$\omega_i^*=\int(u_{\omega i}+m_{Pi}\dot{P})dt\tag{27}$$

Despite the fact that the term $n_{Qi}\dot{Q}_i$ in (21) is ineffective in voltage control in MGs, when frequency control is applied the active powers of DGs in an MG match (28).

$$\frac{P_j}{P_i}=\frac{m_{Pi}}{m_{Pj}}\tag{28}$$

In order to satisfy (28), another distributed cooperative consensus control for the term $m_{Pi}\dot{P}_i$ is supposed to ensure the accuracy of active power-sharing. Therefore, an auxiliary

control u_{pi} is considered for the single-integrator and linear multi-agent system as follows:

$$m_{Pi}\dot{P}_i = u_{Pi}, \qquad i = 1, 2, ..., n \tag{29}$$

We consider a classical distributed cooperative consensus in order to synchronize the active powers of DGs with the same droop coefficients. By employing the local neighborhood tracking error of active powers ε_{Pi} and the auxiliary control u_{Pi} can be obtained as (30).

$$\begin{aligned} \varepsilon_{Pi} &= \sum_{j\in n} a_{ij}(m_{Pi}P_i - m_{Pj}P_j) \\ u_{Pi} &= -D_P\varepsilon_{Pi} \end{aligned} \tag{30}$$

In spite of (23) and (26) there is no second phrase in (30). Therefore, from Theorem 1 in [26], it can be realized that active powers with the same droop coefficients have to consensus with each other to ensure the active power sharing accuracy (i.e. $m_{Pk}P_k \rightarrow m_{Pi}P_i$).

Fig. 3 shows the complete block diagram of the proposed model based on a distributed secondary frequency control for both leader and follower DGs.

VII. System Under Study

To evaluate the detailed analysis of the proposed state feedback distributed secondary voltage and frequency with the accurate active power-sharing, we have simulated a 380 V, 50 Hz islanded MG [14], as shown in Fig. 4, under the sequence of events in the MATLAB/SimPowerSystems software environment. The test system consists of four inverter-based DGs, three lines, and two loads. The lines and loads are modeled as series RL branches and constant real and reactive power, respectively. Table 1 gives the DGs, loads, and lines parameters of the MG test system. Also, the corresponding voltage and current controller parameters and droop coefficients are shown in Table 1. It is considered that DGs of MG are connected to each other through a directed graph communication network, as depicted in Fig. 5.

TABLE 1.
PARAMETERS OF THE MG TEST SYSTEM

Line 1 & 3	$R_{L1,3}$	0.23 Ω	Load 1	P_{load1}	12 kW
	$L_{L1,3}$	0.318 mH		Q_{load1}	12 kVAr
Line 2	R_{L2}	0.35 Ω	Load 3	P_{load3}	15.3 kW
	L_{L2}	1.847 mH		Q_{load3}	7.6 kVAr
DG 1 & 2	m_P	9.4×10^{-5}	DG 3 & 4	m_P	12.5×10^{-5}
	n_Q	1.3×10^{-3}		n_Q	1.5×10^{-3}
	L_{f1},	0.35 mH		L_{f3}, L_{f4}	0.35 mH
	R_{f1},	0.03 Ω		R_{f3}, R_{f4}	0.03 Ω
	C_f	50 μF		C_f	50 μF
	K_{PV}	0.1		K_{PV}	0.05
	K_{IV}	420		K_{IV}	390
	K_{PC}	15		K_{PC}	10.5
	K_{IC}	20000		K_{IC}	16000

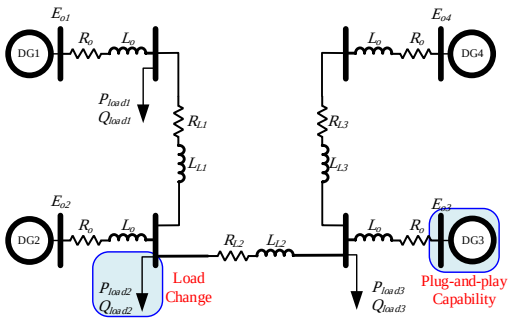

Fig. 4. The MG test system under study

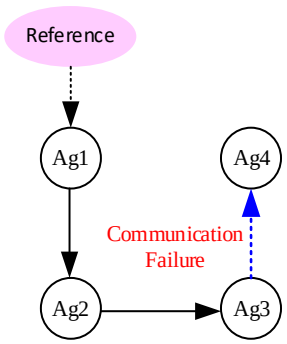

Fig. 5. Graph topology of the MG test system

VIII. Discussion on Simulation Results

From (22) and (25), for the single-integrator dynamics, $A = 0, B = 1$ and as the leader dynamic is scalar in both voltage and frequency control, then it is concluded that in (6) that we have, $M = 0, N = 1$. According to the directed graph topology shown in Fig. 5, the matrix $L+b$ can be determined as follows:

$$L + b = \begin{bmatrix} 2 & 0 & 1 & 1 \\ 0 & 1 & -1 & 0 \\ 0 & 0 & 1 & -1 \\ 0 & 0 & 0 & 0 \end{bmatrix}$$

The minimum positive eigenvalue of the proposed matrix $\lambda_{\min} = 1$. Therefore, the first condition in Theorem 1 is satisfied by choosing $\sigma > 1$. Therefore, under condition (1) of *Theorem 1*, the Ricatti equation in (10) satisfies for any value of P, and from condition (2), it is deduced that for K_1, and K_2 we must have $K_1 < 0, and\ K_2 = -K_1$. Simulation results consist of three parts. At the first step, the controller performance is discussed, and, in another step, we investigate the controller gains impact on the speed convergence. Finally, we compare the proposed consensus protocol with the classic one presented in [14].

A. Controller Performance

For the simulations of this part, we choose $K_{1E} = -60$, $K_{1\omega} = -30$, $F_E = 90$, $F_\omega = 50$ and $D_P = 70$, in order to have acceptable performance for the proposed controllers. Figs. 6 (a),

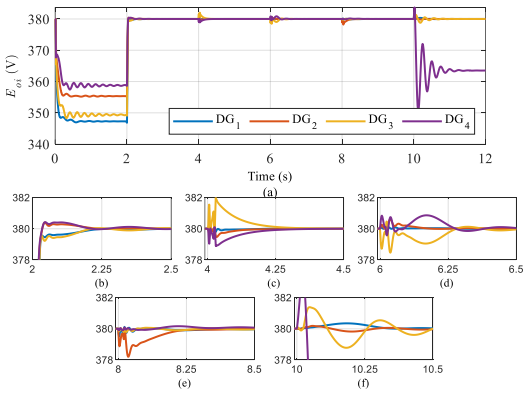

Fig. 6. DG output voltages with the proposed controller (a) Overall trajectory (b)- (f) Magnified trajectories

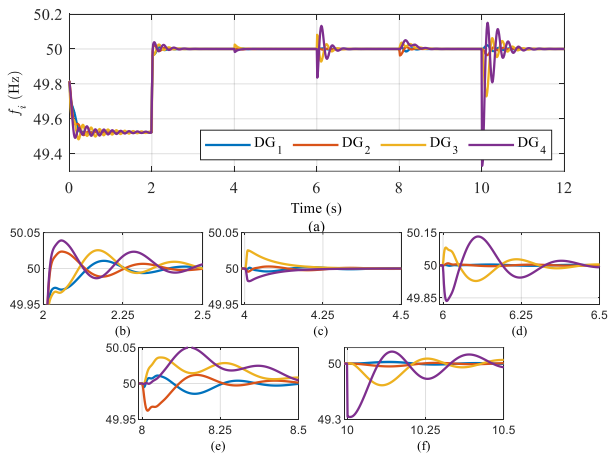

Fig. 7. DG frequencies with the proposed controller (a) Overall trajectory (b)- (f) Magnified trajectories

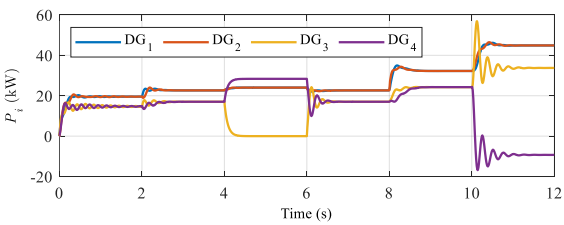

Fig. 8. DG active powers with the proposed controller

(b), and (c) show the output voltage, frequency, and active power of DGs, respectively, while distributed secondary voltage and frequency are activated. At t = 0 s, only the primary control as discussed in section II is applied, and the secondary control is intentionally deactivated. As Figs. 6 (a) and (b) show, the DGs output voltage and the MG frequency stray from the reference values because of DGs droop controllers. In order to restore the output voltage of DGs and MG frequency, the state feedback distributed cooperative controls for secondary voltage and frequency control, as explained in sections V and VI, is applied at t = 2 s, under the communication network shown in Fig. 5. It is shown that by applying the proposed distributed control, both voltage and frequency are rapidly restored to their reference values for all DGs. In the following, at t = 4 s, for examining the plug-and-play capability, DG3 is plugged out from the MG and, at t = 6, is reconnected to the MG. As shown in the zoomed Figs. 6 (c), (d) and 5 (c), and (d), both voltage and frequency have some acceptable fluctuations and restore to their reference values in finite-time (less than 1 sec). After that, at t = 8 s, the *load2* with P = 12 kW and Q = 12 kVAr is applied to the MG. Again, Fig 6 and 7 (e) show that the deviations of both voltage and frequency are damped in finite-time (less than 1 sec). Finally, at t = 8 s, the communication link between DG3 and DG4, as shown in Fig. 5 in the dashed line, is failed. The simulation results as depicted in zoomed pictures Fig. 6 and 7 (f) show that the proposed consensus protocol synchronizes voltage and frequency of three DGs to the reference values in finite-time, and the DG4 voltage is reduced to the 364.3 V because it separates from the graph topology. Since the frequency is a global parameter the DG4 frequency holds at 50 Hz. Also, Fig. 8 displays the active power of four DGs with the proposed consensus controller. Simulation results show that accurate active power-sharing is achieved by the proposed controller.

B. Controller Gains Effect

To investigate the effect of controller gains on the dynamic response of the outputs, we consider three different sets of values for K_{1E}, K_{2E}, $K_{1\omega}$ and $K_{2\omega}$. The effect of different controller gains on the dynamic response of the output error as in (8) for voltage and frequency of DG2, i.e., e_{E3} and $e_{\omega 3}$, is depicted in Fig. 9 (a) and (b), respectively. According to the simulation results, there is a clear trend of increase in the convergence speed with the growth of control gains in output error of voltage, as shown in Fig. 9 (a). Also, from Fig. 9 (b), it is clear that the frequency output error for the $K_{1\omega} = -10$ (the blue chart) has the slowest convergence compared with the one with $K_{1\omega} = -120$ (the red chart). From Figs. 9, it is clear that for the higher values of the controller gains, there is no significant development in speed convergence and dynamic response.

C. Controller Performance Compared with [14]

In this subsection, the proposed controller is compared with the classical consensus protocol proposed in [14]. As previously noticed in the introduction, the classical consensus protocol performance is not evaluated in existing studies. Since the proposed protocol is applied in the homogenous single-integrator systems as shown in (22), (25), and (29), which is the same as in [14], we compare the proposed controller with the one presented in [14]. In order to study the performance of both controllers, we select the output voltage and the frequency of DG3, as depicted in Fig. 10 and Fig. 11, respectively. The gain controllers are chosen as both controllers have almost the same response at t = *2*, i.e., the time that secondary distributed control is applied. Simulation results in Fig. 10 show that the proposed consensus protocol rapidly reaches consensus and, especially,

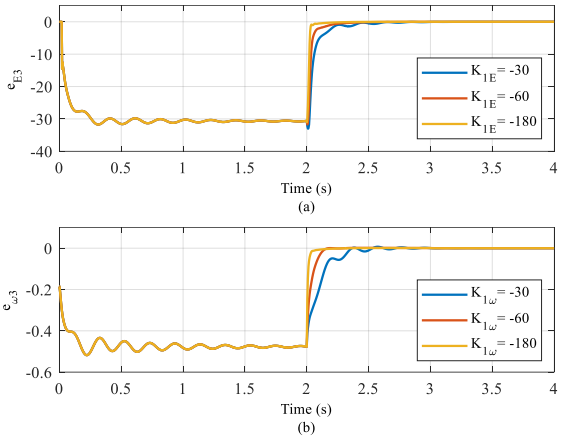

Fig. 9. Output error of DG3 for (a) Voltage (b) Frequency

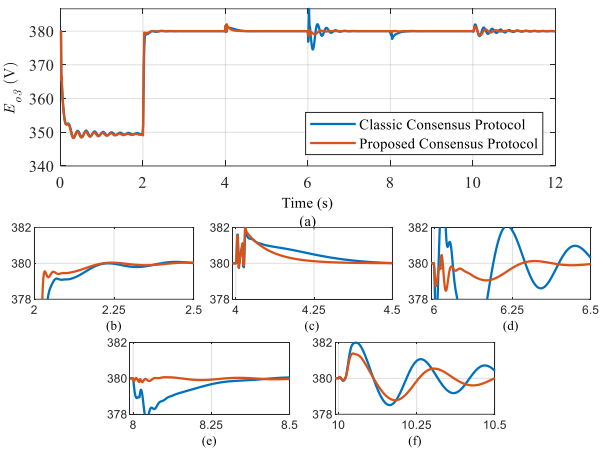

Fig. 10. Comparison between the proposed and the classical

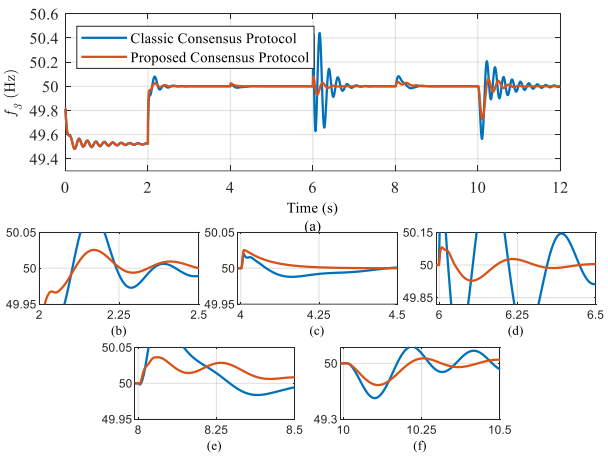

Fig. 11. Comparison between the proposed and the classical consensus protocols in [14] for the frequency of DG3 (a) Overall trajectory (b)- (f) Magnified trajectories

in plug-and-play and load changes has more robust performance than the classical protocol presented in [14].

Fig. 11 shows the frequency of DG3 with the proposed consensus protocol compared with the classical protocol studied in [14]. As seen from Fig. 9 it is clear that our protocol has a better response in comparison to the classical consensus protocol. Again, in particular, in plug-and-play capability, load changes, and communication failure, the proposed protocol has a more appropriate response.

IX. Conclusions

New state feedback distributed voltage and frequency of an islanded MG is proposed in this paper. The MG is considered with DGs that can communicate through a communication graph topology. The secondary voltage and frequency problem is converted to a simple single integrator consensus problem with a scalar controller gain by feedback linearization. Two state feedback distributed consensus algorithms for output voltage frequency and one classical distributed cooperative consensus protocols in [14] for the output voltage of DG3 (a) Overall trajectory (b)- (f) Magnified trajectories approach for output real power demonstrate active power-sharing among DGs. Despite a centralized control structure, the proposed controller only works with the information of some neighbors' DGs. The designed controller is very simple and has not been proposed or investigated for secondary voltage and frequency control of MGs before. A number of simulation studies were carried out in MATLAB/SimPowerSystems to show the effectiveness of the controller. Simulation results show that the prescribed state feedback control strategy has a significant performance in restoring voltage and frequency to their reference values and has the ability to change the convergence speed directly by adjusting the controller gains.

References

[1] R. H. Lasseter, "Microgrids," in *2002 IEEE Power Engineering Society Winter Meeting. Conference Proceedings (Cat. No. 02CH37309)*, 2002, vol. 1, pp. 305-308: IEEE.

[2] R. H. Lasseter, "Smart distribution: Coupled microgrids," *Proceedings of the IEEE*, vol. 99, no. 6, pp. 1074-1082, 2011.

[3] "Microgrids and active distribution networks," *The institution of Engineering Technology*, 2009.

[4] F. Katiraei, R. Iravani, N. Hatziargyriou, and A. Dimeas, "Microgrids management," *IEEE power energy magazine*, vol. 6, no. 3, pp. 54-65, 2008.

[5] E. Hossain, E. Kabalci, R. Bayindir, R. Perez, and Management, "Microgrid testbeds around the world: State of art," *Energy Conversion*, vol. 86, pp. 132-153, 2014.

[6] A. Bidram and A. Davoudi, "Hierarchical structure of microgrids control system," *IEEE Transactions on Smart Grid*, vol. 3, no. 4, pp. 1963-1976, 2012.

[7] J. M. Guerrero, M. Chandorkar, T.-L. Lee, and P. C. Loh, "Advanced control architectures for intelligent microgrids—Part I: Decentralized and hierarchical control," *IEEE Transactions on Industrial Electronics*, vol. 60, no. 4, pp. 1254-1262, 2012.

[8] J. M. Guerrero, J. C. Vasquez, J. Matas, L. G. De Vicuña, and M. Castilla, "Hierarchical control of droop-controlled AC and DC microgrids—A general approach toward standardization,"

IEEE Transactions on industrial electronics, vol. 58, no. 1, pp. 158-172, 2010.

[9] T. Morstyn, B. Hredzak, and V. G. Agelidis, "Control strategies for microgrids with distributed energy storage systems: An overview," *IEEE Transactions on Smart Grid*, vol. 9, no. 4, pp. 3652-3666, 2016.

[10] A. Mehrizi-Sani and R. Iravani, "Potential-function based control of a microgrid in islanded and grid-connected modes," *IEEE Transactions on Power Systems*, vol. 25, no. 4, pp. 1883-1891, 2010.

[11] C. Yang *et al.*, "Dynamic event-triggered robust secondary frequency control for islanded AC microgrid," *Applied energy*, vol. 242, pp. 821-836, 2019.

[12] Q. Shafiee, J. M. Guerrero, and J. C. Vasquez, "Distributed secondary control for islanded microgrids—A novel approach," *IEEE Transactions on power electronics*, vol. 29, no. 2, pp. 1018-1031, 2013.

[13] J. W. Simpson-Porco, Q. Shafiee, F. Dörfler, J. C. Vasquez, J. M. Guerrero, and F. Bullo, "Secondary frequency and voltage control of islanded microgrids via distributed averaging," *IEEE Transactions on Industrial Electronics*, vol. 62, no. 11, pp. 7025-7038, 2015.

[14] A. Bidram, A. Davoudi, F. L. Lewis, and Z. Qu, "Secondary control of microgrids based on distributed cooperative control of multi-agent systems," *IET Generation, Transmission Distribution*, vol. 7, no. 8, pp. 822-831, 2013.

[15] N. M. Dehkordi, N. Sadati, and M. Hamzeh, "Fully distributed cooperative secondary frequency and voltage control of islanded microgrids," *IEEE Transactions on Energy Conversion*, vol. 32, no. 2, pp. 675-685, 2016.

[16] G. Lou, W. Gu, W. Sheng, X. Song, and F. Gao, "Distributed model predictive secondary voltage control of islanded microgrids with feedback linearization," *IEEE Access*, vol. 6, pp. 50169-50178, 2018.

[17] Y. Du, X. Lu, J. Wang, and S. Lukic, "Distributed secondary control strategy for microgrid operation with dynamic boundaries," *IEEE Transactions on Smart Grid*, vol. 10, no. 5, pp. 5269-5282, 2018.

[18] Y. Jafarian, A. Karimi, and H. Bevrani, "Secondary voltage control in a hybrid microgrid," *International Journal of Industrial Electronics Control and Optimization*, vol. 2, no. 3, pp. 221-232, 2019.

[19] Q. Zhou, M. Shahidehpour, M. Yan, X. Wu, A. Alabdulwahab, and A. Abusorrah, "Distributed secondary control for islanded microgrids with mobile emergency resources," *IEEE Transactions on Power Systems*, vol. 35, no. 2, pp. 1389-1399, 2019.

[20] A. Afshari, M. Karrari, H. R. Baghaee, and G. B. Gharehpetian, "Distributed fault-tolerant voltage/frequency synchronization in autonomous AC microgrids," *IEEE Transactions on Power Systems*, vol. 35, no. 5, pp. 3774-3789, 2020.

[21] B. N. Alhasnawi, B. H. Jasim, and B. E. Sedhom, "Distributed secondary consensus fault tolerant control method for voltage and frequency restoration and power sharing control in multi-agent microgrid," *International Journal of Electrical Power & Energy Systems*, vol. 133, p. 107251, 2021.

[22] M. Raeispour, H. Atrianfar, H. R. Baghaee, and G. B. Gharehpetian, "Distributed LMI-based control of heterogeneous microgrids considering fixed time-delays and switching topologies," *IET Renewable Power Generation*, vol. 14, no. 12, pp. 2068-2078, 2020.

[23] Y. Du, H. Tu, H. Yu, and S. Lukic, "Accurate consensus-based distributed averaging with variable time delay in support of distributed secondary control algorithms," *IEEE Transactions on Smart Grid*, vol. 11, no. 4, pp. 2918-2928, 2020.

[24] S. Ullah, L. Khan, I. Sami, and N. Ullah, "Consensus-based delay-tolerant distributed secondary control strategy for droop controlled AC microgrids," *IEEE Access*, vol. 9, pp. 6033-6049, 2021.

[25] O. Palizban and K. Kauhaniemi, "Hierarchical control structure in microgrids with distributed generation: Island and grid-connected mode," *Renewable Sustainable Energy Reviews*, vol. 44, pp. 797-813, 2015.

[26] F. L. Lewis, H. Zhang, K. Hengster-Movric, and A. Das, *Cooperative control of multi-agent systems: optimal and adaptive design approaches*. Springer Science & Business Media, 2013.

[27] T. Han, Z.-H. Guan, B. Xiao, J. Wu, and X. Chen, "Distributed output consensus of heterogeneous multi-agent systems via an output regulation approach," *Neurocomputing*, 2019.

Morteza Alizadeh received the B.S and M.S degrees in electrical engineering from the Islamic Azad University and the University of Birjand, Birjand, Iran, respectively. Currently, he is working toward a Ph.D. degree in electrical engineering with the Amirkabir University of Technology, Tehran, Iran. His research interests include microgrid, distributed control systems in microgrids, power system control, and power system.

H. Askarian Abyaneh (SM'09) was born in Abyaneh, Iran. He received the Ph.D. degree in electrical power system engineering from the University of Manchester Institute of Science and Technology, Manchester, U.K., in 1988. Currently, he is a Professor with the Department of Electrical Engineering, Amirkabir University of Technology (AUT), Tehran, Iran. His research interests are relay protection, power quality, restructuring, and deregulation in power systems.

Alireza Bakhshai (Fellow, IEEE) received the B.Sc. and M.Sc. degrees from the Isfahan University of Technology, Isfahan, Iran, in 1984 and 1986, respectively, and the Ph.D. degree from Concordia University, Montreal, QC, Canada, in 1997, all in electrical engineering. He is currently a Faculty Member with the Department of Electrical and Computer Engineering, Queen's University and a Licensed Professional Engineer (P. Eng.) in Ontario. From 1986 to 1993 and from 1998 to 2004, he was a Faculty Member with the

Department of Electrical and Computer Engineering, Isfahan University of Technology. His research interests include high power electronics, distributed energy generation and conversion, microgrid and smart grid systems, and advanced control theories applied to power electronics converters.

N. Khodabakhshi-Javinani received a Ph.D. degree in Electrical Engineering from Amirkabir University of Technology (AUT). He is currently an Assistant Professor with the Electrical and Computer Engineering Department, Yadegar-e-Imam Khomeini (RAH) Shahre Rey Branch, Islamic Azad University, Tehran, Iran, and a Senior Research Associate with the Power System Protection, Amirkabir University of Technology, Tehran, Iran. Dr. Khodabakhshi-Javinani has a scientific cooperation with Prof. M.Abedi and Prof. H.Askarian A. His current research interests include Power System Protection, Monitoring, Operation, Control, and Signal Processing.

International Journal of Industrial Electronics, Control and Optimization © 2022 IECO
Vol. 5, No. 2, pp.133-142, April (2022)

Leader-Follower Formation Control of Uncertain USV Networks Under Stochastic Disturbances

Ali Azarbahram[1], Naser Pariz[2,†], Mohammad-Bagher Naghibi-Sistani[3], Reihaneh Kardehi Moghaddam[4]

[1,2,3] Department of Electrical Engineering, Faculty of Engineering, Ferdowsi University of Mashhad, Mashhad, Iran.
[4] Department of Electrical Engineering, Mashhad Branch, Islamic Azad University, Mashhad, Iran

ABSTRACT

The robust adaptive leader-follower formation control of uncertain unmanned surface vehicles (USVs) under stochastic disturbances is studied in this paper. The additive noises are considered in the kinematics that stands for the un-modeled dynamic. The disturbances induced by wind, waves and ocean currents are also separated into stochastic and deterministic components. A comprehensive model for each agent is then derived by stochastic differential equations including standard Wiener processes. Thus, the problem definition is more challenging since both the environmental disturbances and kinematics states are defined by stochastic differential equations. Quartic Lyapunov functions synthesis, dynamic surface control (DSC) technique, the projection algorithm, and neural networks (NNs) are employed to guarantee that all the tracking errors converge to a ball centered at the origin in probability. Finally, the simulation experiments quantify the effectiveness of proposed approach.

Article Info

Research Article

Keywords:

Dynamic Surface Control (DSC), Formation Control, Robust Adaptive Control, Stochastic Nonlinear Systems, Unmanned Surface Vehicles (USVs)

Article History:

Received 2021-04-04

Accepted 2021-12-28

I. INTRODUCTION

The control of nonlinear systems has been among the hot topics in the past decades [1]. The control and stability analysis of cooperative nonlinear agents has been given considerable attention in the past several years such as in formation control of robot agents [2], synchronization (consensus) of multiple robots [3], and etc. Among these approaches, the formation of agents leads to maintaining a desired configuration between the neighboring systems [4], [5]. The leader-follower formation control of USVs was studied in several works (see for example, [5], [6]).

The stability analysis of nonlinear control systems has led to different controlling architectures and schemes such as sliding mode control (SMC) [7], feedback linearization [8], [9], backstepping [1], and etc. An adaptive robust tracking controller based on backstepping method is presented for uncertain electrically-driven robotic manipulators in the framework of voltage control strategy in [10]. The *explosion of complexity* for the backstepping approach was resolved using dynamic surface control (DSC) method in [11] for deterministic cases. The DCS approach is utilized for deterministic types of nonlinear systems [12], [13] and different classes of stochastic nonlinear systems [14]–[16].

On the other hand, the existence of stochastic environmental loads highlights the importane of analyzing the stability of nonlinear stochastic systems [17]–[19] and correlated stochastic agents [20], [21]. We have to note that the distructive effects of environmnetal loads on the performance of marine vehicles is necessary to be considered in practice [22]. The platoon and leader-follower formation of multiple USVs are investigated in [4] and [5], respectively. Time

† **Corresponding Author:** n-pariz@um.ac.ir
Tel: +98-5138806051, Fax: +98-5138806051,
Faculty of Engineering, Ferdowsi University of Mashhad (FUM), Mashhad, 9177948974, Iran.

varying external disturbances are considered and compensated in [4], [5]. Nevertheless, these environmental loads are deterministic. We have to note that ocean loads contain stochastic components in practice [23]. An ocean vehicle is supposed to track a reference trajectory under stochastic exogenous disturbances in [24]. A backstepping path-tracking method is investigated in [25] under stochastic loads. Although [24] and [25] have investigated the effects of stochastic disturbances, a single path tracking vehicle is only addressed. In [20], the formation is achieved among the agnent. In earlier problem formulations for formation control of MASs the kinematics is considered deterministic [20]. To be precise, even in stochastic problem formulations, the kinematics is considered deterministic. More understandably, uncertain states and un-modeled dynamics in all the existing literature for the kinematics are ignored, which makes a control design inapplicable in practice.

The main contributions of the proposed approach in this paper are listed below:

- Compared to existing results, the kinematics in our proposed approach is described by ordinary stochastic differential equations.
- The proposed architecture in this paper considers both state uncertainty and stochastic exogenous loads denoted by standard Wiener process.

The remaining paper is organized as follows. The first section gives the preliminaries. Section two, studies the formation control architecture. In Section four, the effectiveness of the implementation is investiagateds. Finally, Section five concludes the paper.

II. PREPARATORY WORK

The used notation in this paper is reported in Table I.

TABLE I.
USED NOTATION

$\mathbb{R}$	The sets of real numbers
$\mathbb{R}^N$	The sets of real *N*-vectors
$\mathbb{R}^{N\times N}$	The sets of real $N\times N$ matrices
$\|x\|$	The absolute value of $x\in\mathbb{R}$
$\|\|\mathbf{x}\|\|$	The 2-norm of a given vector $\mathbf{x}$
$\|\|\mathbf{x}\|\|_{\mathrm{p}}$	The p-norm of a given vector $\mathbf{x}$
$diag(\bullet)$	A diagonal matrix of its argument
$\mathbf{I}$	The identity matrix of appropriate dimensions
$(\bullet)^{\mathcal{T}}$	The transpose operation on vectors or matrices
$\mathrm{Tr}(\bullet)$	The trace of a given matrix
$\mathcal{C}\mathrm{ov}(\bullet)$	The covariance matrix of its arguments
$\mathcal{C}\mathrm{ol}(\bullet)$	The column spaces of its arguments
$\mathcal{R}\mathrm{ow}(\bullet)$	The row spaces of its arguments
$\mathbf{x}\circ\mathbf{x}$	The Hadamard production
$\lambda_m(\bullet)$	the minimum eigenvalue of its arguments
$\lambda_M(\bullet)$	the maximum eigenvalue of its arguments

A. Preliminaries

Neural Networks: In order to approximate the continuous function $g(\mathbf{Z}):\mathbb{R}^q\rightarrow\mathbb{R}$, RBF neural networks is utilized as

$$g_{\mathrm{nn}}(\mathbf{Z}) = \mathbf{W}^{\mathcal{T}}\mathcal{S}(\mathbf{Z}). \tag{1}$$

The networks node number and input dimension are denoted by $l>1$ and q, respectively. Therefore, $\mathbf{Z}\in\mathbb{R}^q$ is the input vector and the weight vector is indicated by $\mathbf{W}=[w_1,w_2,\ldots,w_l]^{\mathcal{T}}$. The elements of basis function vector $\mathcal{S}(\mathbf{Z})=[s_1(\mathbf{Z}),s_2(\mathbf{Z}),\ldots,s_l(\mathbf{Z})]^{\mathcal{T}}$ is chosen as Gaussian functions of the form

$$s_i(\mathbf{Z}) = \exp\left[-\frac{(\mathbf{Z}-\varkappa_i)^{\mathcal{T}}(\mathbf{Z}-\varkappa_i)}{\eta_i^2}\right] \quad ,i=1,2,\ldots,l, \tag{2}$$

where $\varkappa_i=[\varkappa_{i1},\varkappa_{i2},\ldots,\varkappa_{iq}]^{\mathcal{T}}$ is the center of receptive field, and η_i is the width of Gaussian function. The RBF neural networks approximate almost any function $g(\mathbf{Z})$ with sufficiently large number of nodes l over a compact set $\Omega_{\mathbf{Z}}$ to arbitrary any accuracy $\epsilon>0$ as

$$g(\mathbf{Z}) = \mathbf{W}^{*\mathcal{T}}\mathcal{S}(\mathbf{Z})+\delta(\mathbf{Z}),\ \forall z\in\Omega_{\mathbf{Z}}\subset\mathbb{R}^q, \tag{3}$$

where $\mathbf{W}^*$ is the ideal constant weight vector and defined as

$$\mathbf{W}^* = \arg\min_{\mathbf{W}\in\mathbb{R}^l}\left\{\sup_{\mathbf{Z}\in\Omega_{\mathbf{Z}}}|g(\mathbf{Z})-\mathbf{W}^{\mathcal{T}}\mathcal{S}(\mathbf{Z})|\right\}, \tag{4}$$

and $\delta(\mathbf{Z})$ is the approximation error which satisfies $|\delta(\mathbf{Z})|\leq\epsilon$.

Definition 1 [26]: The projection algorithm over two arguments ϖ and $\hat{\varrho}$ is denoted by $\mathcal{J}(\varpi,\hat{\varrho})$ and defined as

$$\begin{cases}\mathcal{J}(\varpi,\hat{\varrho})=(1-\Omega(\hat{\varrho}))\varpi:\Omega(\hat{\varrho})>0\,\&\,\bar{\Omega}(\hat{\varrho})\varpi>0,\\ \mathcal{J}(\varpi,\hat{\varrho})=\varpi:\Omega(\hat{\varrho})>0\ \&\bar{\Omega}(\hat{\varrho})\varpi\leq 0,\\ \mathcal{J}(\varpi,\hat{\varrho})=\varpi:\Omega(\hat{\varrho})\leq 0,\end{cases} \tag{5}$$

with

$$\Omega(\hat{\varrho})=\frac{\|\hat{\varrho}\|^2-\varrho_M^2}{\kappa^2+2\kappa\varrho_M},\ \bar{\Omega}(\hat{\varrho})=\frac{\partial\Omega(\hat{\varrho})}{\partial\hat{\varrho}} \tag{6}$$

where κ is a small positive constant and $\|\varrho\|\leq\varrho_M$.

The projection algorithm is such that if

$$\dot{\hat{\varrho}}=\Gamma\mathcal{J}(\varpi,\hat{\varrho})$$

For some positive symmetric positive definite matrix Γ and $\|\hat{\varrho}(t_0)\|\leq\varrho_M$ then

$a)\ \hat{\varrho}(t) \le \varrho_M + \kappa, \quad t_0 \le t \le \infty,$

$b)\ \mathcal{J}(\varpi, \hat{\varrho}) \quad is\ continuous,$

$c)\ \| \mathcal{J}(\varpi, \hat{\varrho}) \| \le \| \varpi \|,$

$d)\ \tilde{\varrho}^T \mathcal{J}(\varpi, \hat{\varrho}) \ge \tilde{\varrho}^T \varpi, \ \tilde{\varrho} = \varrho - \hat{\varrho}$

Young's Inequality [1]: For any vector set $(\mathbf{k}, \mathbf{m}) \in \mathbb{R}^n$, the following inequality holds

$$\mathbf{k}^{\mathrm{T}}\mathbf{m} \le \frac{\varepsilon^p}{p}\|\mathbf{k}\|^p + \frac{1}{q\varepsilon^q}\|\mathbf{m}\|^q, \tag{7}$$

where $\varepsilon > 0$, $p > 1, q > 1$, and $(p-1)(q-1) = 1$.

B. Stochastic dynamics

The dynamics of a particular stochastic nonlinear system is described by [24]

$$\mathrm{d}\mathbf{x} = \mathbf{h}(\mathbf{x}, t)\mathrm{d}t + \mathbf{G}(\mathbf{x}, t)\mathbf{\Lambda}(t)\mathrm{d}\mathbf{w} \tag{8}$$

where $\mathbf{x} \in \mathbb{R}^n$ is the system state. $\mathbf{w}$ is an independent standard Wiener process of dimension r. $\mathbf{h} : \mathbb{R}^n \times \mathbb{R}_+ \to \mathbb{R}^n$ and $\mathbf{G} : \mathbb{R}^n \times \mathbb{R}_+ \to \mathbb{R}^{n \times r}$ are locally bounded and Lipschitz continuous in $\mathbf{x} \in \mathbb{R}^n$. $\mathbf{\Lambda}(t) : \mathbb{R}_+ \to \mathbb{R}^{r \times r}$ is nonnegative definite and Borel measurable for all $t \in \mathbb{R}_+$ and also bounded.

Lemma 1 [27]: Let a C^2 function $\mathcal{V}(\mathbf{x}(t))$ is defined over the stochastic system (8). Then the infinite generator $\mathcal{L}\mathcal{V}(\mathbf{x}(t))$ is derived as

$$\mathcal{L}\mathcal{V}(\mathbf{x}(t)) = (\frac{\partial \mathcal{V}}{\partial \mathbf{x}})^{\mathrm{T}}\mathbf{h}(\mathbf{x}, t) + \frac{1}{2}\mathrm{Tr}\big(\mathbf{\Lambda}^{\mathrm{T}}(t)\mathbf{G}^{\mathrm{T}}(\mathbf{x}, t)\frac{\partial^2 \mathcal{V}}{\partial \mathbf{x}^{\mathrm{T}} \partial \mathbf{x}}\mathbf{G}(\mathbf{x}, t)\mathbf{\Lambda}(t)\big). \tag{9}$$

Lemma 2 [28]: Suppose that a C^2 function $\mathcal{V}(\mathbf{x}(t)) : \mathbb{R}^n \to \mathbb{R}_+$ is defined. If there exist class K_∞ functions $\varsigma_1(\bullet)$ and $\varsigma_2(\bullet)$, constant c, and a Borel measurable increasing function $\varsigma_3(\bullet)$ such that $\forall \mathbf{x}(t) \in \mathbb{R}^n$ and $\forall t \ge t_0 \ge 0$, we have

$$\begin{cases} \varsigma_1(\|\mathbf{x}(t)\|) \le \mathcal{V}(\mathbf{x}(t)) \le \varsigma_2(\|\mathbf{x}(t)\|), \\ \mathcal{L}\mathcal{V}(\mathbf{x}(t)) \le -c\mathcal{V}(\mathbf{x}(t)) + \varsigma_3(\|\mathbf{\Lambda}(t)\mathbf{\Lambda}^{\mathrm{T}}(t)\|), \end{cases} \tag{10}$$

then there exists a unique strong solution of the system (8) for each $\mathbf{x}(t_0) \in \mathbb{R}^n$ which satisfies

$$\mathbf{E}[\mathcal{V}(\mathbf{x}(t))] \le \exp(-c(t-t_0))\mathcal{V}(\mathbf{x}(t_0)) + \frac{1}{c}\varsigma_3(\sup_{t_0 \le \tau \le t}\|\mathbf{\Lambda}(\tau)\mathbf{\Lambda}^{\mathrm{T}}(\tau)\|). \tag{11}$$

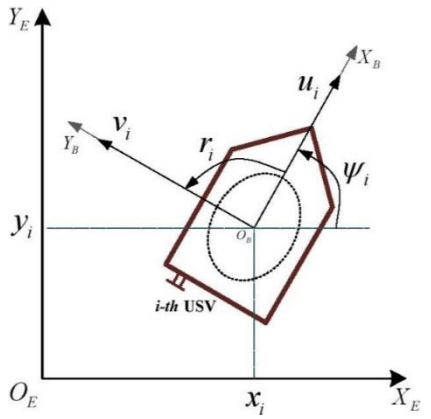

Fig. 1: The schematic motion behavior of i-th hypothetical USV.

C. Problem Statement

The motion of each agent is depicted in Fig. 1. The kinematics of one particular agent is described by

$$\begin{cases} dx_i = (u_i \cos(\psi_i) - v_i \sin(\psi_i))dt + g_{x_i}dw, \\ dy_i = (u_i \sin(\psi_i) + v_i \cos(\psi_i))dt + g_{y_i}dw, \\ d\psi_i = r_i dt + g_{\psi_i}dw, \end{cases} \tag{12}$$

where w denotes a one-dimensional standard Wiener process defined on a complete probability space. Furthermore, $g_{x_i} : \mathbb{R} \to \mathbb{R}$, $g_{y_i} : \mathbb{R} \to \mathbb{R}$ and $g_{\psi_i} : \mathbb{R} \to \mathbb{R}$ are smooth unknown nonlinear functions of $\mathbf{\eta}_i$ with zero initial conditions where $\mathbf{\eta}_i = [x_i, y_i, \psi_i]^T$.

With $\mathbf{v}_i = [u_i, v_i, r_i]^T$, the kinetics of i-th USV agent is usually derived using Lagrangian mechanics represented by

$$\begin{aligned} d\mathbf{v}_i = \mathbf{M}_i^{-1}[&-C_i(\mathbf{v}_i)\mathbf{v}_i - D_i(\mathbf{v}_i)[\mathbf{v}_i + \mathbf{v}_c] \\ &- \mathbf{M}_A\dot{\mathbf{v}}_r + \phi_i(\mathbf{\eta}_i, \mathbf{v}_i)\xi_i + \mathbf{\tau}_{\mathrm{wd}} + \mathbf{\tau}_{\mathrm{wv}} + \mathbf{\tau}_i]dt, \end{aligned} \tag{13}$$

where $\mathbf{M}_i$ is the vehicle inertia matrix as

$$\mathbf{M}_i = \begin{bmatrix} m - X_{\dot{u}} & 0 & 0 \\ 0 & m - Y_{\dot{v}} & mx_g - Y_{\dot{r}} \\ 0 & mx_g - N_{\dot{v}} & I_z - N_{\dot{r}} \end{bmatrix}. \tag{14}$$

$\mathbf{M}_A$ is added mass inertia matrix. The control input is $\mathbf{\tau}_i = [\tau_{i,1}, \tau_{i,2}, \tau_{i,3}]^T$. The total Coriolis matrix is $C_i(\mathbf{v}_i)$ with

$$C_i(\mathbf{v}_i) = \begin{bmatrix} 0 & 0 & C_{i13} \\ 0 & 0 & C_{i23} \\ -C_{i13} & -C_{i23} & 0 \end{bmatrix} \tag{15}$$

The damping matrix $D_i(\mathbf{v}_i)$ is

$$D_i(\mathbf{v}_i) = \begin{bmatrix} -X_u - X_{|u|u}|\bar{u}| - X_{uuu}\bar{u}^2 & 0 & 0 \\ 0 & -Y_v - Y_{|\bar{v}|v}|\bar{v}| & -Y_r \\ 0 & -N_v - N_{|\bar{v}|v}|\bar{v}| & 0 \end{bmatrix} \tag{16}$$

Note that here, $C_{i13} = -(m - Y_{\dot{v}})v - (mx_g - Y_{\dot{r}})r$, $C_{i23} = (m - X_{\dot{u}})u$, $\bar{u} = u - \bar{\bar{u}}_c$, $\bar{v} = v - \bar{\bar{v}}_c$ and $\bar{r} = r$.

$\boldsymbol{\xi}_i = \left[Y_{|r_i|v_i}, Y_{|v_i|r_i}, Y_{|r_i|r_i}, N_{|r_i|v_i}, N_{r_i}, N_{|v_i|r_i}, N_{|r_i|r_i}, b_{1i}, b_{2i}, b_{3i}\right]^{\mathcal{T}}$ is also a constant uncertain parameter vector and $\phi_i(\boldsymbol{\eta}_i, \mathbf{v}_i)$ is described by

$$\phi_i(\boldsymbol{\eta}_i, \mathbf{v}_i) = \begin{bmatrix} 0 & 0 & 0 & 0 & 0 & 0 & 0 & \cos(\psi_i) & \sin(\psi_i) & 0 \\ |r_i|v_i & |v_i|r_i & |r_i|r_i & 0 & 0 & 0 & 0 & -\sin(\psi_i) & \cos(\psi_i) & 0 \\ 0 & 0 & 0 & |r_i|v_i & r_i & |v_i|r_i & |r_i|r_i & 0 & 0 & 1 \end{bmatrix} \quad (17)$$

The relative velocity vector is $\mathbf{v}_r = \mathbf{v} - \mathbf{v}_c$, where $\mathbf{v}_c = [u_c, v_c, r_c]^{\mathcal{T}}$ is the sea current velocity. Let $\hat{s}$ and $\breve{s}$ be the deterministic and stochastic elements of s, respectively. Then, one has $\boldsymbol{\tau}_{\text{wd}} = \hat{\boldsymbol{\tau}}_{\text{wd}} + \breve{\boldsymbol{\tau}}_{\text{wd}}$, $\boldsymbol{\tau}_{\text{wv}} = \hat{\boldsymbol{\tau}}_{\text{wv}} + \breve{\boldsymbol{\tau}}_{\text{wv}}$, $\mathbf{v}_c = \hat{\mathbf{v}}_c + \breve{\mathbf{v}}_c$, and $\dot{\mathbf{v}}_c = \dot{\hat{\mathbf{v}}}_c + \dot{\breve{\mathbf{v}}}_c$. Accordingly, one has

$$\mathbf{M}_A \dot{\mathbf{v}}_r = \mathbf{M}_A(\dot{\mathbf{v}} - \dot{\mathbf{v}}_c) = \mathbf{M}_A(\dot{\mathbf{v}} - \dot{\hat{\mathbf{v}}}_c - \dot{\breve{\mathbf{v}}}_c). \quad (18)$$

Therefore, by defining $\mathbf{M}_t = \mathbf{M} - \mathbf{M}_A$, the stochastic kinetics of i-th USV agent is derived as

$$d\mathbf{v}_i = [\mathbf{g}_i + \mathbf{G}_i \mathbf{Y}_i + \phi_i(\boldsymbol{\eta}_i, \mathbf{v}_i)\boldsymbol{\xi}_i + \boldsymbol{\tau}_i^*]dt + [\mathbf{G}_i \boldsymbol{\Lambda}_i]d\mathbf{w}, \quad (19)$$

where $\mathbf{w}$ is a 6-dimensional Wiener standard process vector and

$$\begin{cases} \boldsymbol{\tau}_i^* = \mathbf{M}_t^{-1}\boldsymbol{\tau}_i, \\ \mathbf{g}_i = \mathbf{M}_t^{-1}(-C_i(\mathbf{v}_i)\mathbf{v}_i - D_i(\mathbf{v}_i)\mathbf{v}_i), \\ \mathbf{G}_i = \mathbf{M}_t^{-1}\mathcal{R}\text{ow}(D_i(\mathbf{v}_i), \mathbf{I}_3), \\ \mathbf{Y}_i = \mathcal{C}\text{ol}(\hat{\mathbf{v}}_c, \mathbf{M}_A\dot{\hat{\mathbf{v}}}_c + \hat{\boldsymbol{\tau}}_{\text{wd}} + \hat{\boldsymbol{\tau}}_{\text{wv}}). \end{cases} \quad (20)$$

Furthermore, $\boldsymbol{\Lambda}_i = \text{diag}(\boldsymbol{\Lambda}_{1i}, \boldsymbol{\Lambda}_{2i})$, with

$$\begin{cases} \boldsymbol{\Lambda}_{1i} = \mathcal{C}\text{ov}(\breve{\mathbf{v}}_c), \\ \boldsymbol{\Lambda}_{2i} = \mathcal{C}\text{ov}(\mathbf{M}_A\dot{\breve{\mathbf{v}}}_c + \breve{\boldsymbol{\tau}}_{\text{wd}} + \breve{\boldsymbol{\tau}}_{\text{wv}}). \end{cases} \quad (21)$$

III. Main Results

The following assumptions hold true.

Assumption 1: The reference signal is deterministic, bounded, and also satisfies $\boldsymbol{\eta}_0 \in C^2$

Assumption 2: There exists a predefined preceding USV i-1 associated with agent i.

Assumption 3: The vectors $\mathbf{Y}_i$, $\boldsymbol{\xi}_i$ and covariance matrix $\boldsymbol{\Lambda}_i(t)$ are all bounded, i.e., for $\mathrm{Y}_i^{\mathbf{M}}$, $\xi_i^{\mathbf{M}}$, and $\Lambda_i^{\mathbf{M}}$, one has

$$\| \mathbf{Y}_i \| \le \mathrm{Y}_i^{\mathbf{M}}, \| \boldsymbol{\xi}_i \| \le \boldsymbol{\xi}_i^{\mathbf{M}}, \| \boldsymbol{\Lambda}_i \boldsymbol{\Lambda}_i^{\mathcal{T}} \|_\infty \le \Lambda_i^{\mathbf{M}}. \quad (22)$$

D. Leader-follower formation control design

Consider again the team of N fully actuated USVs described in (12) and (19). The schematic of two agents is shown in Fig. 2.

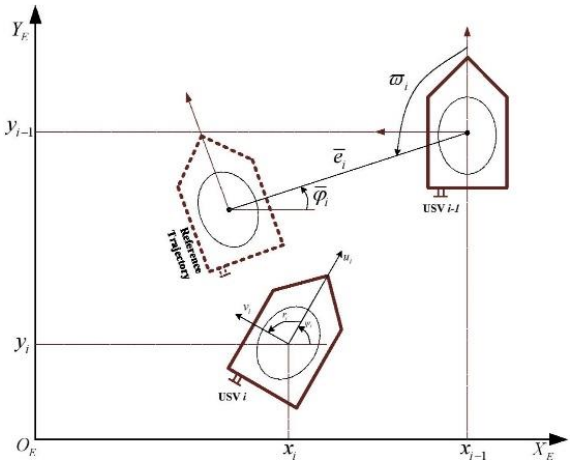

Fig. 2: The schematic of two hypothetical agents.

A desired predetermined reference trajectory $\boldsymbol{\eta}_0 = [x_0, y_0, \psi_0]^{\mathcal{T}}$ is accessible by the leading USV of the team. In this configuration, each follower is the leader for another agent. More precisely, each two consecutive USVs act as a pair of leader-follower. According to Fig. 2, the reference trajectory to be followed by the i-th vehicle is determined by USV i-1, which is shifted longitudinally and circularly by predefined parameters $\bar{e}_i$ and ϖ_i, respectively, and then rotated relatively through $\bar{\varphi}_i$. These predetermined formation parameters can be either time-invariant or time-varying.

The reference trajectories for the i-th follower agent in x, y, and ψ directions are described as

$$\begin{cases} x_{ri} = x_{i-1} + \bar{e}_i[\cos(\psi_{i-1})\cos(\varpi_i) - \sin(\psi_{i-1})\sin(\varpi_i)], \\ y_{ri} = y_{i-1} + \bar{e}_i[\sin(\psi_{i-1})\cos(\varpi_i) + \cos(\psi_{i-1})\sin(\varpi_i)], \\ \psi_{ri} = \psi_{i-1} + \bar{\varphi}_i, \end{cases} \quad (23)$$

We define the leader-follower formation errors as

$$s_{xi} = x_i - x_{ri},\ s_{yi} = y_i - y_{ri},\ s_{\psi i} = \psi_i - \psi_{ri}. \quad (24)$$

Then according to Lemma 1, we have

$$\begin{aligned} ds_{xi} &= [u_i\cos(\psi_i) - v_i\sin(\psi_i) - \bar{x}_{i-1} + f_{x_i}]dt + \bar{g}_{x_i}dw_i, \\ ds_{yi} &= [u_i\sin(\psi_i) + v_i\cos(\psi_i) - \bar{y}_{i-1} + f_{y_i}]dt + \bar{g}_{y_i}dw_i, \\ ds_{\psi_i} &= [r_i - \bar{\psi}_{i-1}]dt + \bar{g}_{\psi_i}dw_i, \end{aligned} \quad (25)$$

where

$$\begin{cases} \bar{x}_{i-1} = u_{i-1}\cos(\psi_{i-1}) - v_{i-1}\sin(\psi_{i-1}) \\ \quad -\bar{e}_i r_{i-1}[\cos(\varpi_i)\sin(\psi_{i-1}) + \sin(\varpi_i)\cos(\psi_{i-1})], \\ \bar{y}_{i-1} = u_{i-1}\sin(\psi_{i-1}) + v_{i-1}\cos(\psi_{i-1}) \\ \quad -\bar{e}_i r_{i-1}[\cos(\varpi_i)\cos(\psi_{i-1}) - \sin(\varpi_i)\sin(\psi_{i-1})], \\ \bar{\psi}_{i-1} = r_{i-1} \end{cases} \quad (26)$$

and

$$f_{x_i} = 0.5\bar{e}_i g_{\psi_{i-1}}^2 [\cos(\varpi_i)\cos(\psi_{i-1}) - \sin(\varpi_i)\sin(\psi_{i-1})],$$
$$f_{y_i} = 0.5\bar{e}_i g_{\psi_{i-1}}^2 [\cos(\varpi_i)\sin(\psi_{i-1}) + \sin(\varpi_i)\cos(\psi_{i-1})] \quad (27)$$

Additionally

$$\bar{g}_{x_i} = \bar{e}_i g_{\psi_{i-1}} [\cos(\varpi_i)\sin(\psi_{i-1}) + \sin(\varpi_i)\cos(\psi_{i-1})] + g_{x_i} - g_{x_{i-1}},$$
$$\bar{g}_{y_i} = \bar{e}_i g_{\psi_{i-1}} [\sin(\varpi_i)\sin(\psi_{i-1}) - \cos(\varpi_i)\cos(\psi_{i-1})] + g_{y_i} - g_{y_{i-1}}, \quad (28)$$
$$\bar{g}_{\psi_i} = g_{\psi_i} - g_{\psi_{i-1}}$$

Step I:

Let

$$\begin{cases} \boldsymbol{\zeta}_i = \mathbf{v}_i - \boldsymbol{\alpha}_i^f, \\ \boldsymbol{\chi}_i = \boldsymbol{\alpha}_i^f - \boldsymbol{\alpha}_i. \end{cases} \quad (29)$$

A Lyapunov function candidate is selected as

$$\mathcal{V}_{0,i} = \frac{1}{4}s_{xi}^4 + \frac{1}{4}s_{yi}^4 + \frac{1}{4}s_{\psi i}^4. \quad (30)$$

By employing Lemma 1, we have

$$\begin{aligned} \mathcal{L}\mathcal{V}_{0,i} &= s_{xi}^3[\alpha_{1i}\cos(\psi_i) - \alpha_{2i}\sin(\psi_i) - \bar{x}_{i-1} + f_{1i}(\bullet)] \\ &+ s_{yi}^3[\alpha_{1i}\sin(\psi_i) + \alpha_{2i}\cos(\psi_i) - \bar{y}_{i-1} + f_{2i}(\bullet)] \\ &+ s_{\psi i}^3[\alpha_{3i} - \bar{\psi}_{i-1} + f_{3i}(\bullet)] + \boldsymbol{\zeta}_i^{\mathcal{T}}\mathbf{E}_i + \boldsymbol{\chi}_i^{\mathcal{T}}\mathbf{E}_i \\ &- \frac{3}{4}s_{xi}^4\left(1 + 2\left(\frac{\beta_{1i}^2 + \beta_{2i}^2}{\beta_{1i}^2\beta_{2i}^2}\right)\| h_{1i}^* \|^4\right) + \frac{3}{2}s_{xi}^2\bar{g}_{x_i}^2 \\ &- \frac{3}{4}s_{yi}^4\left(1 + 2\left(\frac{\beta_{1i}^2 + \beta_{2i}^2}{\beta_{1i}^2\beta_{2i}^2}\right)\| h_{1i}^* \|^4\right) + \frac{3}{2}s_{yi}^2\bar{g}_{y_i}^2 \\ &- \frac{3}{4}s_{\psi i}^4\left(1 + \frac{1}{\beta_{3i}^2}\| h_{2i}^* \|^4\right) + \frac{3}{2}s_{\psi i}^2\bar{g}_{\psi_i}^2, \end{aligned} \quad (31)$$

where $\mathbf{E}_i = [\mathcal{E}_{1i}, \mathcal{E}_{2i}, \mathcal{E}_{3i}]^{\mathcal{T}}$, with

$$\begin{cases} \mathrm{E}_{1i} = s_{xi}^3\cos(\psi_i) + s_{yi}^3\sin(\psi_i), \\ \mathrm{E}_{2i} = s_{yi}^3\cos(\psi_i) - s_{xi}^3\sin(\psi_i), \\ \mathrm{E}_{3i} = s_{\psi i}^3 \end{cases} \quad (32)$$

with unknown smooth nonlinear functions $h_{1i}^*(s_{xi})$, $h_{2i}^*(s_{yi})$, and $h_{3i}^*(s_{\psi i})$ to be introduced later. Moreover, we have the following unknown continuous functions

$$\begin{aligned} f_{1i}(\bullet) &= \frac{3}{4}s_{xi}\left(1 + 2\left(\frac{\beta_{1i}^2 + \beta_{2i}^2}{\beta_{1i}^2\beta_{2i}^2}\right)\| h_{1i}^* \|^4 + \frac{1}{l_{1i}^2}\| \bar{g}_{x_i} \|^4\right) + f_{x_i}, \\ f_{2i}(\bullet) &= \frac{3}{4}s_{yi}\left(1 + 2\left(\frac{\beta_{1i}^2 + \beta_{2i}^2}{\beta_{1i}^2\beta_{2i}^2}\right)\| h_{2i}^* \|^4 + \frac{1}{l_{2i}^2}\| \bar{g}_{y_i} \|^4\right) + f_{y_i}, \\ f_{3i}(\bullet) &= \frac{3}{4}s_{\psi i}\left(1 + \frac{1}{\beta_{3i}^2}\| h_{3i}^* \|^4 + \frac{1}{l_{3i}^2}\| \bar{g}_{\psi_i} \|^4\right) \end{aligned} \quad (33)$$

One has

$$\begin{cases} \frac{3}{2}s_{xi}^2\bar{g}_{x_i}^2 \le \frac{3}{4l_{1i}^2}s_{xi}^4\| \bar{g}_{x_i} \|^4 + \frac{3}{4}l_{1i}^2, \\ \frac{3}{2}s_{yi}^2\bar{g}_{y_i}^2 \le \frac{3}{4l_{2i}^2}s_{yi}^4\| \bar{g}_{y_i} \|^4 + \frac{3}{4}l_{2i}^2, \\ \frac{3}{2}s_{\psi i}^2\bar{g}_{\psi_i}^2 \le \frac{3}{4l_{3i}^2}s_{\psi i}^4\| \bar{g}_{\psi_i} \|^4 + \frac{3}{4}l_{3i}^2. \end{cases} \quad (34)$$

Define the approximation errors $\tilde{\Theta}_{1i}$, $\tilde{\Theta}_{2i}$, and $\tilde{\Theta}_{3i}$. Then, we have

$$\begin{cases} s_{xi}^3 f_{1i} \le \frac{s_{xi}^6}{2a_{1i}^2}\mathcal{S}_{1i}^{\mathcal{T}}\mathcal{S}_{1i}\Theta_{1i}^* + \frac{1}{2}a_{1i}^2 + \frac{3}{4}s_{xi}^4 + \frac{1}{4}\epsilon_{1i}^{*4}, \\ s_{yi}^3 f_{2i} \le \frac{s_{yi}^6}{2a_{2i}^2}\mathcal{S}_{2i}^{\mathcal{T}}\mathcal{S}_{2i}\Theta_{2i}^* + \frac{1}{2}a_{2i}^2 + \frac{3}{4}s_{yi}^4 + \frac{1}{4}\epsilon_{2i}^{*4}, \\ s_{\psi i}^3 f_{3i} \le \frac{s_{\psi i}^6}{2a_{3i}^2}\mathcal{S}_{3i}^{\mathcal{T}}\mathcal{S}_{3i}\Theta_{2i}^* + \frac{1}{2}a_{3i}^2 + \frac{3}{4}s_{\psi i}^4 + \frac{1}{4}\epsilon_{3i}^{*4}, \end{cases} \quad (35)$$

By expanding the Lyapunov function candidate in (30) one has

$$\mathcal{V}_{1,i} = \mathcal{V}_{0,i} + \frac{1}{2\gamma_{1i}}\tilde{\Theta}_{1i}^2 + \frac{1}{2\gamma_{2i}}\tilde{\Theta}_{2i}^2 + \frac{1}{2\gamma_{3i}}\tilde{\Theta}_{3i}^2, \quad (36)$$

which, results in

$$\mathcal{L}\mathcal{V}_{1,i} = \mathcal{L}\mathcal{V}_{0,i} - \frac{1}{\gamma_{1i}}\tilde{\Theta}_{1i}\dot{\hat{\Theta}}_{1i} - \frac{1}{\gamma_{2i}}\tilde{\Theta}_{2i}\dot{\hat{\Theta}}_{2i} - \frac{1}{\gamma_{3i}}\tilde{\Theta}_{3i}\dot{\hat{\Theta}}_{3i}. \quad (37)$$

The virtual control laws α_{1i}, α_{2i}, and α_{3i} are then designed as

$$\begin{aligned} \alpha_{1i} &= [-\mathcal{K}_{xi}s_{xi} - \frac{1}{2a_{1i}^2}s_{xi}^3\mathcal{S}_{1i}^{\mathcal{T}}\mathcal{S}_{1i}\hat{\Theta}_{1i} + \bar{x}_{i-1}]\cos(\psi_i) \\ &+ [-\mathcal{K}_{yi}s_{yi} - \frac{1}{2a_{2i}^2}s_{yi}^3\mathcal{S}_{2i}^{\mathcal{T}}\mathcal{S}_{2i}\hat{\Theta}_{2i} + \bar{y}_{i-1}]\sin(\psi_i), \\ \alpha_{2i} &= [\mathcal{K}_{xi}s_{xi} + \frac{1}{2a_{1i}^2}s_{xi}^3\mathcal{S}_{1i}^{\mathcal{T}}\mathcal{S}_{1i}\hat{\Theta}_{1i} - \bar{x}_{i-1}]\sin(\psi_i) \\ &- [\mathcal{K}_{yi}s_{yi} + \frac{1}{2a_{2i}^2}s_{yi}^3\mathcal{S}_{2i}^{\mathcal{T}}\mathcal{S}_{2i}\hat{\Theta}_{2i} - \bar{y}_{i-1}]\cos(\psi_i), \\ \alpha_{3i} &= -\mathcal{K}_{\psi i}s_{\psi i} - \frac{1}{2a_{3i}^2}s_{\psi i}^3\mathcal{S}_{3i}^{\mathcal{T}}\mathcal{S}_{3i}\hat{\Theta}_{3i} + \bar{\psi}_{i-1}, \end{aligned} \quad (38)$$

where $\mathcal{K}_{xi}, \mathcal{K}_{yi}, \mathcal{K}_{\psi i}, i = 1, \ldots, N$, are control gains. We design

$$\begin{cases} \dot{\hat{\Theta}}_{1i} = \frac{\gamma_{1i}}{2a_{1i}^2}s_{xi}^6\mathcal{S}_{1i}^{\mathcal{T}}\mathcal{S}_{1i} - \gamma_{1i}\sigma_{1i}\hat{\Theta}_{1i}, \\ \dot{\hat{\Theta}}_{2i} = \frac{\gamma_{2i}}{2a_{2i}^2}s_{yi}^6\mathcal{S}_{2i}^{\mathcal{T}}\mathcal{S}_{2i} - \gamma_{2i}\sigma_{2i}\hat{\Theta}_{2i}, \\ \dot{\hat{\Theta}}_{3i} = \frac{\gamma_{3i}}{2a_{3i}^2}s_{\psi i}^6\mathcal{S}_{3i}^{\mathcal{T}}\mathcal{S}_{3i} - \gamma_{3i}\sigma_{3i}\hat{\Theta}_{3i}. \end{cases} \quad (39)$$

By taking all the aforementioned into account, (37) leads to

$$\begin{aligned}\mathcal{L}\mathcal{V}_{1,i} \le & -\mathcal{K}_{xi}s_{xi}^4 - \mathcal{K}_{yi}s_{yi}^4 - \mathcal{K}_{\psi i}s_{\psi i}^4 - \frac{1}{2}\sigma_{1i}\tilde{\Theta}_{1i}^2 - \frac{1}{2}\sigma_{2i}\tilde{\Theta}_{2i}^2 \\ & -\frac{1}{2}\sigma_{3i}\tilde{\Theta}_{3i}^2 + \zeta_i^{\mathcal{T}}\mathbf{E}_i - \frac{3}{2}s_{xi}^4\left(\frac{\beta_{1i}^2+\beta_{2i}^2}{\beta_{1i}^2\beta_{2i}^2}\right)\| h_{1i}^* \|^4 + \boldsymbol{\chi}_i^{\mathcal{T}}\mathbf{E}_i \\ & -\frac{3}{2}s_{yi}^4\left(\frac{\beta_{1i}^2+\beta_{2i}^2}{\beta_{1i}^2\beta_{2i}^2}\right)\| h_{1i}^* \|^4 - \frac{3}{4}s_{\psi i}^4\frac{1}{\beta_{3i}^2}\| h_{2i}^* \|^4 + \frac{1}{2}a_{1i}^2 \\ & +\frac{1}{4}\epsilon_{1i}^{*4} + \frac{1}{2}a_{2i}^2 + \frac{1}{4}\epsilon_{2i}^{*4} + \frac{1}{2}a_{3i}^2 + \frac{1}{4}\epsilon_{3i}^{*4} + \frac{3}{4}l_{1i}^2 + \frac{3}{4}l_{2i}^2 \\ & +\frac{3}{4}l_{3i}^2 + \frac{1}{2}\sigma_{1i}\Theta_{1i}^{*2} + \frac{1}{2}\sigma_{2i}\Theta_{2i}^{*2} + \frac{1}{2}\sigma_{3i}\Theta_{3i}^{*2}\end{aligned} \tag{40}$$

Consider the first-order filter $\boldsymbol{\mu}_i\dot{\boldsymbol{\alpha}}_i^f + \boldsymbol{\alpha}_i^f = \boldsymbol{\alpha}_i$ such that $\boldsymbol{\alpha}_i^f(0) = \boldsymbol{\alpha}_i(0)$. Then for $q = 1,2,3,$ we have

$$\begin{cases} d\chi_{qi} = [\dfrac{-\chi_{qi}}{\mu_{qi}} - \mathcal{B}_{qi}(\bullet)]dt - \mathcal{C}_{qi}(\bullet)dw, \\ d\alpha_{qi}^f = \dfrac{-\chi_{qi}}{\mu_{qi}}, \end{cases} \tag{41}$$

where $\mathcal{B}_{1i}$ and $\mathcal{B}_{2i}$ are functions of $\bar{\boldsymbol{\eta}}_{i-1}$, $\dot{\bar{\boldsymbol{\eta}}}_{i-1}$, $\ddot{\bar{\boldsymbol{\eta}}}_{i-1}$, s_{xi}, s_{yi}, χ_{1i}, χ_{2i}, ζ_{1i}, ζ_{2i}, $\tilde{\Theta}_{1i}$, and $\tilde{\Theta}_{2i}$. The arguments of $\mathcal{B}_{3i}$ on the other hand are $\bar{\boldsymbol{\eta}}_{i-1}$, $\dot{\bar{\boldsymbol{\eta}}}_{i-1}$, $\ddot{\bar{\boldsymbol{\eta}}}_{i-1}$, $s_{\psi i}$, χ_{3i}, ζ_{3i}, and $\tilde{\Theta}_{3i}$. Note that $\bar{\boldsymbol{\eta}}_{i-1} = [\bar{x}_{i-1}, \bar{y}_{i-1}, \bar{\psi}_{i-1}]^{\mathcal{T}}$. Furthermore, we have

$$\begin{cases} \mathcal{C}_{1i} = \dfrac{\partial\alpha_{1i}}{\partial s_{xi}}h_{1i} + \dfrac{\partial\alpha_{1i}}{\partial s_{yi}}h_{2i},\ \mathcal{C}_{2i} = \dfrac{\partial\alpha_{2i}}{\partial s_{xi}}h_{1i} + \dfrac{\partial\alpha_{2i}}{\partial s_{yi}}h_{2i}, \\ \mathcal{C}_{3i} = \dfrac{\partial\alpha_{3i}}{\partial s_{\psi i}}h_{3i}. \end{cases} \tag{42}$$

We can write, $h_{1i} = s_{xi}h_{1i}^*$, $h_{2i} = s_{yi}h_{2i}^*$, and $h_{3i} = s_{\psi i}h_{3i}^*$. The Lyapunov function candidate is expanded to give

$$\mathcal{V}_{2,i} = \mathcal{V}_{1,i} + \sum_{j=1}^{3}\frac{1}{4}\chi_{ji}^4, \tag{43}$$

which yields in

$$\mathcal{L}\mathcal{V}_{2,i} = \mathcal{L}\mathcal{V}_{1,i} + \sum_{j=1}^{3}\chi_{ji}^3[\frac{-\chi_{ji}}{\mu_{ji}} - \mathcal{B}_{ji}(\bullet)] + \sum_{j=1}^{3}\frac{3}{2}\chi_{ji}^2\| \mathcal{C}_{ji} \|^2. \tag{44}$$

One has

$$\begin{aligned}\frac{3}{2}\chi_{1i}^2\| \mathcal{C}_{1i} \|^2 \le & \frac{3}{2\beta_{1i}^2}(s_{xi}^4\| h_{1i}^* \|^4 + s_{yi}^4\| h_{2i}^* \|^4)\| ^4) \\ & +\frac{3}{2}\beta_{1i}^2\chi_{1i}^4[(\frac{\partial\alpha_{1i}}{\partial s_{xi}})^4 + (\frac{\partial\alpha_{1i}}{\partial s_{yi}})^4],\end{aligned} \tag{45}$$

$$\begin{aligned}\frac{3}{2}\chi_{2i}^2\| \mathcal{C}_{2i} \|^2 \le & \frac{3}{2\beta_{2i}^2}(s_{xi}^4\| h_{1i}^* \|^4 + s_{yi}^4\| h_{2i}^* \|^4) \\ & +\frac{3}{2}\beta_{2i}^2\chi_{2i}^4[(\frac{\partial\alpha_{2i}}{\partial s_{xi}})^4 + (\frac{\partial\alpha_{2i}}{\partial s_{yi}})^4],\end{aligned}$$

$$\frac{3}{2}\chi_{3i}^2\| \mathcal{C}_{3i} \|^2 \le \frac{3}{4}\beta_{3i}^2\chi_{3i}^4(\frac{\partial\alpha_{3i}}{\partial s_{\psi i}})^4 + \frac{3}{4\beta_{3i}^2}s_{\psi i}^4\| h_{3i}^* \|^4.$$

We have

$$\begin{aligned}\mathcal{L}\mathcal{V}_{2,i} \le & -\mathcal{K}_{xi}s_{xi}^4 - \mathcal{K}_{yi}s_{yi}^4 - \mathcal{K}_{\psi i}s_{\psi i}^4 - \frac{1}{2}\sigma_{1i}\tilde{\Theta}_{1i}^2 \\ & -\frac{1}{2}\sigma_{2i}\tilde{\Theta}_{2i}^2 - \frac{1}{2}\sigma_{3i}\tilde{\Theta}_{3i}^2 + \zeta_i^{\mathcal{T}}\mathbf{E}_i + \boldsymbol{\chi}_i^{\mathcal{T}}\mathbf{E}_i \\ & -\sum_{j=1}^{3}\frac{\chi_{ji}^4}{\mu_{ji}} + \sum_{j=1}^{3}\frac{1}{4\beta_{4i}^4}\mathcal{B}_{qi}^4(\bullet) + \sum_{j=1}^{3}\frac{3}{4}\beta_{4i}^{\frac{4}{3}}\chi_{ji}^4 \\ & +\mathbb{A}_i + \frac{1}{2}a_{1i}^2 + \frac{1}{4}\epsilon_{1i}^{*4} + \frac{1}{2}a_{2i}^2 + \frac{1}{4}\epsilon_{2i}^{*4} \\ & +\frac{1}{2}a_{3i}^2 + \frac{1}{4}\epsilon_{3i}^{*4} + \frac{3}{4}l_{1i}^2 + \frac{3}{4}l_{2i}^2 + \frac{3}{4}l_{3i}^2 \\ & +\frac{1}{2}\sigma_{1i}\Theta_{1i}^{*2} + \frac{1}{2}\sigma_{2i}\Theta_{2i}^{*2} + \frac{1}{2}\sigma_{3i}\Theta_{3i}^{*2}.\end{aligned} \tag{46}$$

with

$$\begin{aligned}\mathbb{A}_i = & \frac{3}{2}\beta_{1i}^2\chi_{1i}^4[(\frac{\partial\alpha_{1i}}{\partial s_{xi}})^4 + (\frac{\partial\alpha_{1i}}{\partial s_{yi}})^4] \\ & +\frac{3}{2}\beta_{2i}^2\chi_{2i}^4[(\frac{\partial\alpha_{2i}}{\partial s_{xi}})^4 + (\frac{\partial\alpha_{2i}}{\partial s_{yi}})^4] \\ & +\frac{3}{4}\beta_{3i}^2\chi_{3i}^4(\frac{\partial\alpha_{3i}}{\partial s_{\psi i}})^4\end{aligned} \tag{47}$$

This completes the first step of designing the leader-follower formation control approach.

Step II:

From (19) and (29), one obtains that

$$d\zeta_i = [\mathbf{g}_i + \mathbf{G}_i\mathbf{Y}_i + \phi_i(\boldsymbol{\eta}_i, \mathbf{v}_i)\xi_i + \boldsymbol{\tau}_i^* + \boldsymbol{\mu}_i^{-1}\boldsymbol{\chi}_i]dt + [\mathbf{G}_i\boldsymbol{\Lambda}_i]d\mathbf{w}. \tag{48}$$

Define $\mathbf{Y}_i = \mathrm{Y}_i^* - \mathbf{Y}_i$, $\tilde{\xi}_i = \xi_i^* - \hat{\xi}_i$, and $\tilde{\delta}_i = \| \boldsymbol{\Lambda}_i\boldsymbol{\Lambda}_i^{\mathcal{T}} \|_\infty^2 - \hat{\delta}_i$, $i = 1,\ldots,N$.

Then, expand the Lyapunov function to

$$\mathcal{V}_{3,i} = \mathcal{V}_{2,i} + \frac{1}{4}\| \zeta_i \|_4^4 + \frac{1}{2}\mathbf{Y}_i^{\mathcal{T}}\Gamma_{1i}^{-1}\mathbf{Y}_i + \frac{1}{2}\tilde{\xi}_i^{\mathcal{T}}\Gamma_{2i}^{-1}\tilde{\xi}_i + \frac{1}{2\gamma_{3i}}\tilde{\delta}_i^2. \tag{49}$$

where Γ_{1i} and Γ_{2i} are symmetric positive definite design matrices and $\gamma_{3i}, i = 1,\ldots,N$ are positive constants. Hence

$$\begin{aligned}\mathcal{LV}_{3,i} \le{}& \mathcal{LV}_{2,i} + \zeta_i^{\mathcal{T}} \circ |\zeta_i^2|^{\mathcal{T}} [\mathbf{g}_i + \mathbf{G}_i \mathbf{Y}_i \\ &+ \phi_i(\boldsymbol{\eta}_i, \boldsymbol{\nu}_i)\xi_i + \boldsymbol{\tau}_i^* + \boldsymbol{\mu}_i^{-1}\boldsymbol{\chi}_i] \\ &+ \frac{1}{2}\mathrm{Tr}\{\boldsymbol{\Lambda}_i^{\mathcal{T}} \mathbf{G}_i^{\mathcal{T}} \frac{\partial^2(\bullet)}{\partial \zeta_i^{\mathrm{T}} \partial \zeta_i} \mathbf{G}_i \boldsymbol{\Lambda}_i\} - \mathbf{Y}_i^{\mathcal{T}} \Gamma_{1i}^{-1} \dot{\mathbf{Y}}_i \\ &- \tilde{\xi}_i^{\mathcal{T}} \Gamma_{2i}^{-1} \dot{\hat{\xi}}_i - \frac{1}{\gamma_{3i}} \tilde{\delta}_i \dot{\hat{\delta}}_i,\end{aligned} \tag{50}$$

where

$$\frac{\partial^2(\bullet)}{\partial \zeta_i^{\mathrm{T}} \partial \zeta_i} = \mathrm{diag}(3\zeta_{1i}^2, 3\zeta_{2i}^2, 3\zeta_{3i}^2),\ i = 1,\ldots,N$$

By Young's inequality, one obtains

$$\zeta_i^{\mathcal{T}} \mathbf{E}_i \le \frac{1}{2}\beta_{5i}^4 \| \zeta_i \|_4^4 + \frac{3}{2}\bar{\beta}_{5i}^{3} s_{xi}^4 + \frac{3}{2}\beta_{5i}^{-3} s_{yi}^4 + \frac{3}{4}\bar{\beta}_{5i}^{3} s_{\psi i}^4, \tag{51}$$

and

$$\boldsymbol{\chi}_i^{\mathcal{T}} \mathbf{E}_i \le \frac{1}{2}\beta_{7i}^4 \sum_{j=1}^{3} \chi_{ji}^4 + \frac{3}{2}\bar{\beta}_{7i}^{3} s_{xi}^4 + \frac{3}{2}\beta_{7i}^{-3} s_{yi}^4 + \frac{3}{4}\bar{\beta}_{7i}^{3} s_{\psi i}^4. \tag{52}$$

Furthermore, the following holds true

$$\begin{aligned}&\frac{1}{2}\mathrm{Tr}\{\boldsymbol{\Lambda}_i^{\mathcal{T}} \mathbf{G}_i^{\mathcal{T}} \frac{\partial^2(\bullet)}{\partial \zeta_i^{\mathrm{T}} \partial \zeta_i} \mathbf{G}_i \boldsymbol{\Lambda}_i\} \\ &\qquad \le 3\beta_{6i} \| \mathbf{G}_i \|^4 \| \zeta_i \|^4 \| \boldsymbol{\Lambda}_i \boldsymbol{\Lambda}_i^{\mathcal{T}} \|_\infty^2 + \frac{3}{4\beta_{6i}}.\end{aligned} \tag{53}$$

As a matter of fact, $\| \zeta_i \|_2 \le \sqrt{n} \| \zeta_i \|_4$. In this problem formulation n is equal to three. Then,

$$\begin{aligned}\mathcal{LV}_{3,i} \le{}& \mathcal{LV}_{2,i} + \zeta_i^{\mathcal{T}} \circ |\zeta_i^2|^{\mathcal{T}} [\mathbf{g}_i + \mathbf{G}_i \mathbf{Y}_i \\ &+ \phi_i(\boldsymbol{\eta}_i, \boldsymbol{\nu}_i)\hat{\xi}_i + \boldsymbol{\tau}_i^* + \boldsymbol{\mu}_i^{-1}\boldsymbol{\chi}_i] \\ &+ \zeta_i^{\mathcal{T}} \circ |\zeta_i^2|^{\mathcal{T}} \mathbf{G}_i \mathbf{Y}_i + \zeta_i^{\mathcal{T}} \circ |\zeta_i^2|^{\mathcal{T}} \phi_i(\boldsymbol{\eta}_i, \boldsymbol{\nu}_i)\tilde{\xi}_i \\ &+ \frac{27}{2}\beta_{6i} \| \mathbf{G}_i \|^4 \| \zeta_i \|_4^4 (\tilde{\delta}_i + \hat{\delta}_i) - \mathbf{Y}_i^{\mathcal{T}} \Gamma_{1i}^{-1} \dot{\mathbf{Y}}_i \\ &- \tilde{\xi}_i^{\mathcal{T}} \Gamma_{2i}^{-1} \dot{\hat{\xi}}_i - \frac{1}{\gamma_{3i}} \tilde{\delta}_i \dot{\hat{\delta}}_i + \frac{3}{8\beta_{6i}}.\end{aligned} \tag{54}$$

We know that

$$\frac{27}{2}\beta_{6i} \| \mathbf{G}_i \|^4 \| \zeta_i \|_4^4 \hat{\delta}_i = \zeta_i^{\mathcal{T}} \circ |\zeta_i^2|^{\mathcal{T}} (\frac{27}{2}\beta_{6i} \hat{\delta}_i \| \mathbf{G}_i \|^4 \zeta_i) \tag{55}$$

Now we choose the control law as

$$\begin{aligned}\boldsymbol{\tau}_i^* = -(&\mathcal{K}_i + \frac{27}{2}\beta_{6i}\hat{\delta}_i \| \mathbf{G}_i \|^4)\zeta_i - \phi_i(\boldsymbol{\eta}_i, \boldsymbol{\nu}_i)\hat{\xi}_i \\ &- \mathbf{G}_i \mathbf{Y}_i - \mathbf{g}_i - \boldsymbol{\mu}_i^{-1}\boldsymbol{\chi}_i,\end{aligned} \tag{56}$$

where $\mathcal{K}_i$, $i = 1,\ldots,N$ are control gain matrices. The following are also derived

$$\begin{cases}\dot{\mathbf{Y}}_i = \Gamma_{1i} \mathcal{J}(\mathbf{G}_i^{\mathcal{T}} (\zeta_i \circ |\zeta_i^2|), \mathbf{Y}_i), \\ \dot{\hat{\xi}}_i = \Gamma_{2i} \mathcal{J}(\phi_i^{\mathcal{T}} (\zeta_i \circ |\zeta_i^2|), \hat{\xi}_i), \\ \dot{\hat{\delta}}_i = \gamma_{3i} \mathcal{J}(\frac{27}{2}\beta_{6i} \| \mathbf{G}_i \|^4 \| \zeta_i \|_4^4, \hat{\delta}_i).\end{cases} \tag{57}$$

By taking the aforementioned equations into account, we have

$$\begin{aligned}\mathcal{LV}_{3,i} \le{}& [-\mathcal{K}_{xi} + \frac{3}{2}(\bar{\beta}_{5i}^{3} + \bar{\beta}_{7i}^{3})]s_{xi}^4 - \frac{1}{2}\sigma_{1i}\tilde{\Theta}_{1i}^2 - \frac{1}{2}\sigma_{2i}\tilde{\Theta}_{2i}^2 \\ &+ [-\mathcal{K}_{yi} + \frac{3}{2}(\bar{\beta}_{5i}^{3} + \bar{\beta}_{7i}^{3})]s_{yi}^4 - \frac{1}{2}\sigma_{3i}\tilde{\Theta}_{3i}^2 + \sum_{j=1}^{3} \frac{1}{4\beta_{4i}^4} \mathcal{B}_{qi}^4(\bullet) \\ &+ [-\mathcal{K}_{\psi i} + \frac{3}{4}(\bar{\beta}_{5i}^{3} + \bar{\beta}_{7i}^{3})]s_{\psi i}^4 + [-\frac{1}{\mu_{1i}} + \frac{1}{4}(3\bar{\beta}_{4i}^{3} + \beta_{7i}^4)]\chi_{1i}^4 \\ &+ [-\frac{1}{\mu_{2i}} + \frac{1}{4}(3\bar{\beta}_{4i}^{3} + \beta_{7i}^4)]\chi_{2i}^4 + \frac{3}{8\beta_{6i}} + \mathbb{A}_i + \frac{1}{2}\sigma_{1i}\Theta_{1i}^{*2} \\ &+ [-\frac{1}{\mu_{3i}} + \frac{1}{4}(3\bar{\beta}_{4i}^{3} + \beta_{7i}^4)]\chi_{3i}^4 + [-\lambda_m(\mathcal{K}_i) + \frac{1}{4}\beta_{5i}^4] \| \zeta_i \|_4^4 \\ &+ \frac{1}{2}\sigma_{2i}\Theta_{2i}^{*2} + \frac{1}{2}\sigma_{3i}\Theta_{3i}^{*2} + \frac{1}{2}a_{1i}^2 + \frac{1}{4}\epsilon_{1i}^{*4} + \frac{1}{2}a_{2i}^2 + \frac{1}{4}\epsilon_{2i}^{*4} \\ &+ \frac{1}{2}a_{3i}^2 + \frac{1}{4}\epsilon_{3i}^{*4} + \frac{3}{4}l_{1i}^2 + \frac{3}{4}l_{2i}^2 + \frac{3}{4}l_{3i}^2.\end{aligned} \tag{58}$$

Consider the compact sets

$$\Omega_{di} = \{ \| \bar{\boldsymbol{\eta}}_{i-1} \|^2 + \| \dot{\bar{\boldsymbol{\eta}}}_{i-1} \|^2 + \| \ddot{\bar{\boldsymbol{\eta}}}_{i-1} \|^2 \le B_{di} \}$$

and

$$\begin{aligned}\Omega_i = \{&| s_{xi} |^2 + | s_{yi} |^2 + | s_{\psi i} |^2 + \| \zeta_i \|^2 + \| \boldsymbol{\chi}_i \|^2 \\ &+ | \tilde{\Theta}_{1i} |^2 + | \tilde{\Theta}_{2i} |^2 + | \tilde{\Theta}_{3i} |^2 + \| \mathbf{Y}_i \|^2 \\ &+ \| \tilde{\xi}_i \|^2 + \| \tilde{\delta}_i \|^2 \le 2\iota_i\}\end{aligned}$$

with positive constants B_{di} and ι_i for $i = 1,\ldots,N$. We know that all the variables of functions $\mathcal{B}_{qi}(\bullet) q = 1,2,3$ are bounded in $\Omega_{di} \times \Omega_i$, which indicates that $|\mathcal{B}_{qi}(\bullet)| \le \bar{b}_i$. With similar lines of reasoning, one concludes that $|(\frac{\partial \alpha_{1i}}{\partial s_{xi}})^4 + (\frac{\partial \alpha_{1i}}{\partial s_{yi}})^4| \le a_{1i}$, $|(\frac{\partial \alpha_{2i}}{\partial s_{xi}})^4 + (\frac{\partial \alpha_{2i}}{\partial s_{yi}})^4| \le a_{2i}$ and $|(\frac{\partial \alpha_{3i}}{\partial s_{\psi i}})^4| \le a_{3i}$.

Theorem 1: By considering Assumptions 1-3, consider a team of N USVs seeking to follow a reference signal and keep a predefined formation among themselves under stochastic exogenous disturbances as described in uncertain dynamics (12) and (19). Choose the parameters such that Ξ_{qi}, $q = 1,2,\ldots,7$ and $i = 1,\ldots,N$ are strictly positive where,

$$\begin{cases}\Xi_{1i}=\mathcal{K}_{xi}-\frac{3}{2}(\beta_{5i}^{\frac{-4}{3}}+\beta_{7i}^{\frac{-4}{3}}),\ \Xi_{2i}=\mathcal{K}_{yi}-\frac{3}{2}(\beta_{5i}^{\frac{-4}{3}}+\beta_{7i}^{\frac{-4}{3}}),\\ \Xi_{3i}=\mathcal{K}_{\psi i}-\frac{3}{4}(\beta_{5i}^{\frac{-4}{3}}+\beta_{7i}^{\frac{-4}{3}}),\ \Xi_{4i}=\frac{1}{\mu_{1i}}-\frac{1}{4}(3\beta_{4i}^{\frac{4}{3}}+\beta_{7i}^{4})-\frac{3}{2}\beta_{1i}^{2}a_{1i},\\ \Xi_{5i}=\frac{1}{\mu_{2i}}-\frac{1}{4}(3\beta_{4i}^{\frac{4}{3}}+\beta_{7i}^{4})-\frac{3}{2}\beta_{2i}^{2}a_{2i},\\ \Xi_{6i}=\frac{1}{\mu_{3i}}-\frac{1}{4}(3\beta_{4i}^{\frac{4}{3}}+\beta_{7i}^{4})-\frac{3}{4}\beta_{3i}^{2}a_{3i},\\ \Xi_{7i}=\lambda_m(\mathcal{K}_i)-\frac{1}{4}\beta_{5i}^{4}\end{cases}$$

Then, design the virtual inputs (38), the adaptive rules (39), and the actual control signal (56) alongside with update laws using the projection algorithm in (57). Finally, by applying the control signal $\boldsymbol{\tau}_i = \mathbf{M}_t\boldsymbol{\tau}_i^*$ to the i-th physical system, all the tracking errors, i.e.,

$$\mathbf{X_{ei}} = \mathcal{C}ol(s_{xi}, s_{yi}, s_{\psi i}, \tilde{\Theta}_{1i}, \tilde{\Theta}_{2i}, \tilde{\Theta}_{3i}, \chi_{1i}, \chi_{2i}, \chi_{3i}, \zeta_i)$$

converge to a ball centered at the origin in probability.

Proof: The following holds true

$$\begin{aligned}\mathcal{L}\mathcal{V}_{3,i} \le{}& \mathcal{L}\mathcal{V}_{2,i}+[-\lambda_m(\mathcal{K}_i)+\frac{1}{4}\beta_{5i}^{4}]\|\zeta_i\|_4^4\\ &+\frac{3}{8\beta_{6i}}\pm\frac{1}{2\gamma_{3i}}\tilde{\delta}_i^2\pm\frac{1}{2}\tilde{\mathbf{Y}}_i^{\mathcal{T}}\Gamma_{1i}^{-1}\tilde{\mathbf{Y}}_i\pm\frac{1}{2}\tilde{\boldsymbol{\xi}}_i^{\mathcal{T}}\Gamma_{2i}^{-1}\tilde{\boldsymbol{\xi}}_i,\end{aligned} \tag{59}$$

which results in

$$\mathcal{L}\mathcal{V}_{3,i} \le -\frac{c_{1i}}{c_{2i}}\mathcal{V}_{3,i}+c_{3i}. \tag{60}$$

The positive constants c_{1i}, c_{2i} and c_{3i}, $i=1,\ldots,N$ are specified as

$$\begin{cases}c_{1i}=\min\{4\Xi_{1i},4\Xi_{2i},4\Xi_{3i},4\Xi_{4i},4\Xi_{5i},4\Xi_{6i},\\ \qquad 4\Xi_{7i},\sigma_{1i},\sigma_{2i},\sigma_{3i},\lambda_m(\Gamma_{1i}),\lambda_m(\Gamma_{2i}),\frac{1}{2\gamma_{3i}}\},\\ c_{2i}=\max\{\frac{1}{4},\lambda_M(\Gamma_{1i}),\lambda_M(\Gamma_{2i}),\frac{1}{2\gamma_{3i}}\},\\ c_{3i}=\Xi_{8i}+\frac{1}{2}\lambda_M(\Gamma_{1i}^{-1})(2\Upsilon_i^{\mathbf{M}}+\kappa)^2\\ \qquad+\frac{1}{2}\lambda_M(\Gamma_{2i}^{-1})(2\xi_i^{\mathbf{M}}+\kappa)^2+\frac{1}{2\gamma_{3i}}(2\Lambda_i^{\mathbf{M}}+\kappa)^2.\end{cases} \tag{61}$$

where κ is defined in Definition 1, and

$$\begin{aligned}\Xi_{8i}={}&\frac{1}{2}a_{1i}^2+\frac{1}{4}\epsilon_{1i}^{*4}+\frac{1}{2}a_{2i}^2+\frac{1}{4}\epsilon_{2i}^{*4}+\frac{1}{2}a_{3i}^2+\frac{1}{4}\epsilon_{3i}^{*4}\\ &+\frac{3}{4}l_{1i}^2+\frac{3}{4}l_{2i}^2+\frac{3}{4}l_{3i}^2+\frac{1}{2}\sigma_{1i}\Theta_{1i}^{*2}+\frac{1}{2}\sigma_{2i}\Theta_{2i}^{*2}\\ &+\frac{1}{2}\sigma_{3i}\Theta_{3i}^{*2}+\frac{3}{8\beta_{6i}}+\frac{3}{4\beta_{4i}^4}\bar{b}_i^4.\end{aligned} \tag{62}$$

Then according to Lemma 1, the closed loop system consisting has a strong solution. By applying Lemma 2 to (60), an exponential convergence of the expectation of the tracking errors to $c_{3i}c_{2i}/c_{1i}$ is achieved. Then,

$$\mathbf{E}[\mathcal{V}_{3,i}(\mathbf{X_{ei}}(t))] \le \exp(-c(t-t_0))\mathcal{V}_{3,i}(\mathbf{X_{ei}}(t_0))+\frac{c_{3i}c_{2i}}{c_{1i}} \quad \text{and}$$

therefore,

$$\mathbf{E}[\|\mathbf{X_{ei}}(t)\|] \le [\|\mathbf{X_{ei}}(t_0)\|^4\exp(-\frac{c_{1i}}{c_{2i}}(t-t_0))+\frac{4c_{3i}c_{2i}}{c_{1i}}]^{\frac{1}{4}}. \tag{63}$$

This completes the proof. ■

IV. SIMULATION RESULTS

The simulations are performed on a vigilant networked group of $N=3$ USVs seeking for the platoon formation among themselves. In platoon configuration, $\varpi_i=\pi$ and $\bar{\varphi}_i=0$. Consider the stochastic dynamics of a USV group as described in (12) and (19). A desired reference trajectory is defined as

$$\begin{cases}\boldsymbol{\eta}_0=[1.2t,0,0]^{\mathcal{T}} & t\le t_c\\ \boldsymbol{\eta}_0=[1.2t+60\sin t',60(1-\cos t'),t']^{\mathcal{T}} & t>t_c\end{cases}$$

where, $t_c=100$ and $t'=0.02(t-t_c)$. The desired distance is $\bar{e}_i=5$. The USV agents are stationary positioned at $\boldsymbol{\eta}_1=[0,5,0]^{\mathcal{T}}$, $\boldsymbol{\eta}_2=[0,10,0]^{\mathcal{T}}$, $\boldsymbol{\eta}_3=[0,15,0]^{\mathcal{T}}$.

The design parameters are also chosen as $\Gamma_{1i}=2\mathbf{I}_6$, $\Gamma_{1i}=2\mathbf{I}_{10}$, $\gamma_{3i}=1.5$, $\mathcal{K}_{xi}=10$, $\mathcal{K}_{yi}=12$, $\mathcal{K}_{\psi i}=8$, $\mathcal{K}_i=\text{diag}(9,9,6)$. The simulation is performed for $t=400$ sec with a sample time of $T_s=0.001$ sec.

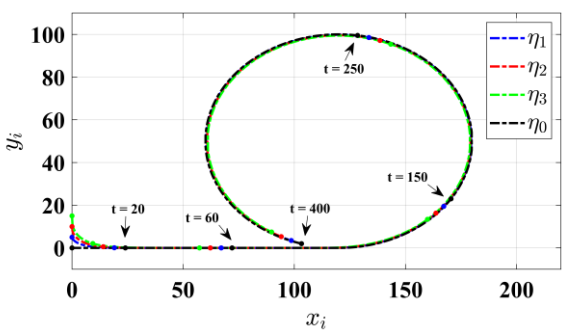

Fig. 3: The formation tracking of USV agents.

The uncertain functions are $g_{x_i}=x_i^2\ln(x_i^2+2)$, $g_{y_i}=y_i^2\sin(y_i)$, $g_{\psi_i}=0.5\psi_i^2\cos(\psi_i)$. All other dynamical system parameters are taken from [29] including the system matrices. Additionally, the covariance matrices $\boldsymbol{\Lambda}_{1i}$ and $\boldsymbol{\Lambda}_{2i}$

are chosen such that $\| \mathbf{\Lambda}_i \mathbf{\Lambda}_i^{\mathcal{T}} \|_\infty = 40$. The Neural Networks inputs are $\mathbf{Z}_{1i} = [x_i, x_{ri}]^{\mathrm{T}}$, $\mathbf{Z}_{2i} = [y_i, y_{ri}]^{\mathrm{T}}$, and $\mathbf{Z}_{3i} = [\psi_i, \psi_{ri}]^{\mathrm{T}}$. The centers of the NN are evenly spaced on $[-1.5,1.5]\times[-1.5,1.5]$, $[-1.5,1.5]\times[-1.5,1.5]$ and $[-0.5,0.5]\times[-0.5,0.5]$, respectively. The results are shown in Fig. 3 -Fig. 6. In Fig. 3, the tracking performance of USV agents is shown for the whole simulation time including four distinct time instants, $t = 20$, $t = 60$, $t = 150$, $t = 250$, and $t = 400$. The control inputs are also shown in Fig. 4 – Fig. 6.

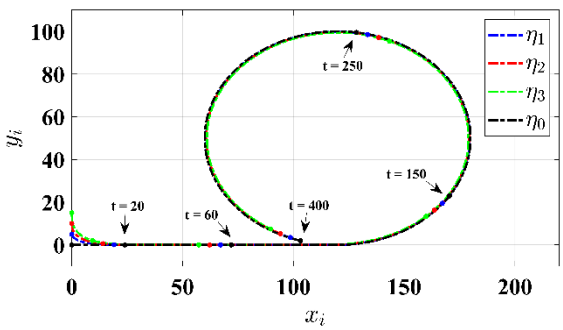

Fig. 3: The formation tracking of USV agents.

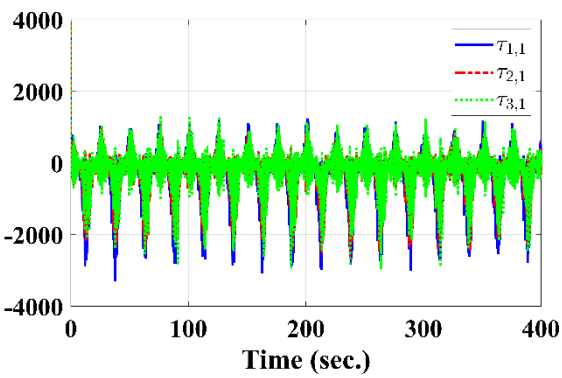

Fig. 4: The Control inputs $\tau_{i,1}$.

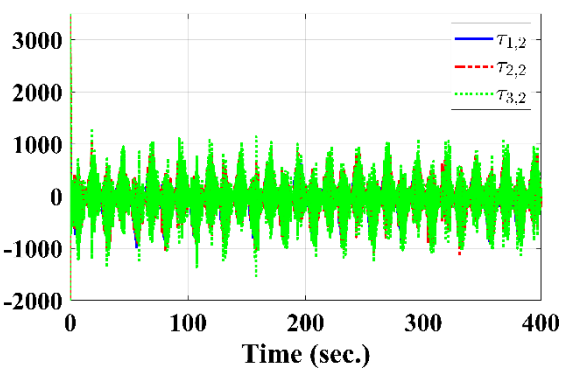

Fig. 5: The Control inputs $\tau_{i,2}$.

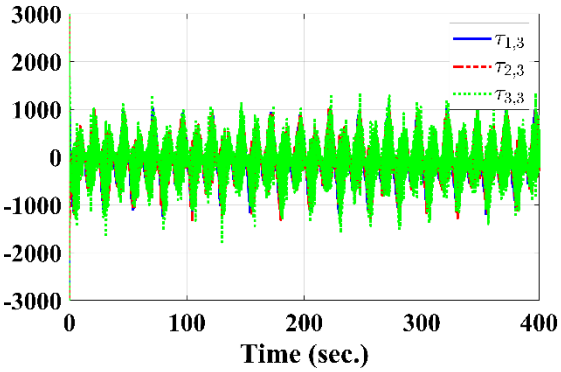

Fig. 6: The Control inputs $\tau_{i,3}$.

V. Conclusion

We studied the robust adaptive leader-follower formation of USVs under stochastic exogenous disturbances. The environmental disturbances were separated into distinguished stochastic and deterministic parts. A comprehensive model for each USV agent was then derived by stochastic differential equations. All the tracking errors are proved to converge to a ball centered at the origin in probability.

References

[1] M. Krstic, I. Kanellakopoulos, and V. Petar, *Nonlinear and adaptive control design*. Wiley New York, 1995.

[2] K.-K. Oh, M.-C. Park, and H.-S. Ahn, "A survey of multi-agent formation control," *Automatica*, vol. 53, pp. 424–440, Mar. 2015, doi: 10.1016/j.automatica.2014.10.022.

[3] J. Qin, Q. Ma, Y. Shi, and L. Wang, "Recent Advances in Consensus of Multi-Agent Systems: A Brief Survey," *IEEE Trans. Ind. Electron.*, vol. 64, no. 6, pp. 4972–4983, Jun. 2017, doi: 10.1109/TIE.2016.2636810.

[4] S.-L. Dai, S. He, H. Lin, and C. Wang, "Platoon formation control with prescribed performance guarantees for USVs," *IEEE Trans. Ind. Electron.*, vol. 65, no. 5, pp. 4237–4246, 2017.

[5] S. He, M. Wang, S.-L. Dai, and F. Luo, "Leader–follower formation control of USVs with prescribed performance and collision avoidance," *IEEE Trans. Ind. Inform.*, vol. 15, no. 1, pp. 572–581, 2018.

[6] X. Jin, "Fault tolerant finite-time leader–follower formation control for autonomous surface vessels with LOS range and angle constraints," *Automatica*, vol. 68, pp. 228–236, 2016.

[7] V. I. Utkin, *Sliding Modes in Control and Optimization*. Springer Science & Business Media, 2013.

[8] L. Hunt, Renjeng Su, and G. Meyer, "Global transformations of nonlinear systems," *IEEE Trans. Autom. Control*, vol. 28, no. 1, pp. 24–31, Jan. 1983, doi: 10.1109/TAC.1983.1103137.

[9] A. Isidori, *Nonlinear control systems*. Springer Science & Business Media, 2013.

[10] J. Keighobadi and M. M. Fateh, "Adaptive Robust Tracking Control Based on Backstepping Method for Uncertain Robotic Manipulators Including Motor Dynamics," *Int. J. Ind. Electron. Control Optim.*, vol. 4, no. 1, pp. 13–22, Jan.

2021, doi: 10.22111/ieco.2020.31792.1213.
[11] D. Swaroop, J. K. Hedrick, P. P. Yip, and J. C. Gerdes, "Dynamic surface control for a class of nonlinear systems," *IEEE Trans. Autom. Control*, vol. 45, no. 10, pp. 1893–1899, Oct. 2000, doi: 10.1109/TAC.2000.880994.
[12] Q. Su and M. Wan, "Adaptive Neural Dynamic Surface Output Feedback Control for Nonlinear Full States Constrained Systems," *IEEE Access*, vol. 8, pp. 131590–131600, 2020, doi: 10.1109/ACCESS.2020.3010027.
[13] K. Li and Y. Li, "Adaptive Fuzzy Finite-time Dynamic Surface Control for High-order Nonlinear System with Output Constraints," *Int. J. Control Autom. Syst.*, vol. 19, no. 1, pp. 112–123, Jan. 2021, doi: 10.1007/s12555-019-0986-4.
[14] Y. Gao and S. Tong, "Composite adaptive fuzzy output feedback dynamic surface control design for stochastic large-scale nonlinear systems with unknown dead zone," *Neurocomputing*, vol. 175, pp. 55–64, 2016.
[15] Z. Yu, S. Li, and F. Li, "Observer-based adaptive neural dynamic surface control for a class of non-strict-feedback stochastic nonlinear systems," *Int. J. Syst. Sci.*, vol. 47, no. 1, pp. 194–208, Jan. 2016, doi: 10.1080/00207721.2015.1043364.
[16] M. Xia and T. Zhang, "Adaptive neural dynamic surface control for full state constrained stochastic nonlinear systems with unmodeled dynamics," *J. Frankl. Inst.*, vol. 356, no. 1, pp. 129–146, Jan. 2019, doi: 10.1016/j.jfranklin.2018.10.011.
[17] F. Wang, B. Chen, Y. Sun, Y. Gao, and C. Lin, "Finite-Time Fuzzy Control of Stochastic Nonlinear Systems," *IEEE Trans. Cybern.*, vol. 50, no. 6, pp. 2617–2626, Jun. 2020, doi: 10.1109/TCYB.2019.2925573.
[18] H. Wang, P. X. Liu, J. Bao, X.-J. Xie, and S. Li, "Adaptive Neural Output-Feedback Decentralized Control for Large-Scale Nonlinear Systems With Stochastic Disturbances," *IEEE Trans. Neural Netw. Learn. Syst.*, vol. 31, no. 3, pp. 972–983, Mar. 2020, doi: 10.1109/TNNLS.2019.2912082.
[19] Z. Zhu, Y. Pan, Q. Zhou, and C. Lu, "Event-Triggered Adaptive Fuzzy Control for Stochastic Nonlinear Systems with Unmeasured States and Unknown Backlash-Like Hysteresis," *IEEE Trans. Fuzzy Syst.*, pp. 1–1, 2020, doi: 10.1109/TFUZZ.2020.2973950.
[20] G. Wen, C. L. P. Chen, and Y. Liu, "Formation Control With Obstacle Avoidance for a Class of Stochastic Multiagent Systems," *IEEE Trans. Ind. Electron.*, vol. 65, no. 7, pp. 5847–5855, Jul. 2018, doi: 10.1109/TIE.2017.2782229.
[21] X. You, C.-C. Hua, H.-N. Yu, and X.-P. Guan, "Leader-following consensus for high-order stochastic multi-agent systems via dynamic output feedback control," *Automatica*, vol. 107, pp. 418–424, Sep. 2019, doi: 10.1016/j.automatica.2019.06.006.
[22] R. Cui, L. Chen, C. Yang, and M. Chen, "Extended state observer-based integral sliding mode control for an underwater robot with unknown disturbances and uncertain nonlinearities," *IEEE Trans. Ind. Electron.*, vol. 64, no. 8, pp. 6785–6795, 2017.
[23] A. Naess and T. Moan, *Stochastic dynamics of marine structures*. Cambridge University Press, 2013.
[24] K. D. Do, "Control of fully actuated ocean vehicles under stochastic environmental loads in three dimensional space," *Ocean Eng.*, vol. 99, pp. 34–43, 2015.
[25] K. D. Do, "Global robust adaptive path-tracking control of underactuated ships under stochastic disturbances," *Ocean Eng.*, vol. 111, pp. 267–278, Jan. 2016, doi: 10.1016/j.oceaneng.2015.10.038.
[26] J.-B. Pomet and L. Praly, "Adaptive nonlinear regulation: Estimation from the Lyapunov equation," *IEEE Trans. Autom. Control*, vol. 37, no. 6, pp. 729–740, 1992.
[27] I. Karatzas and S. Shreve, *Brownian Motion and Stochastic Calculus*. Springer, 2014.
[28] H. Deng, M. Krstic, and R. J. Williams, "Stabilization of stochastic nonlinear systems driven by noise of unknown covariance," *IEEE Trans. Autom. Control*, vol. 46, no. 8, pp. 1237–1253, 2001.
[29] R. Skjetne, T. I. Fossen, and P. V. Kokotović, "Adaptive maneuvering, with experiments, for a model ship in a marine control laboratory," *Automatica*, vol. 41, no. 2, pp. 289–298, Feb. 2005, doi: 10.1016/j.automatica.2004.10.006.

Ali Azarbahram graduated from IAU, Kerman, Iran, in 2012. He received the M.Sc. degree from Tarbiat Modares University, Tehran, Iran, 2015. His research interests include power systems control, control of large-scale and multi-agent systems, nonlinear and adaptive control, sensor networks control.

Naser Pariz received the B.S. and M.Sc degree in Electrical Engineering from Ferdowsi University of Mashhad, Iran, in 1988 and 1991 respectively. He received his Ph.D. from the Department of Electrical Engineering at Ferdowsi University of Mashhad in 2001. He is a Professor at Ferdowsi University. His research interests are nonlinear and control systems.

Mohammad-BagherNaghibi-Sistan received the B.S. degree in electronics from the University of Tehran, Tehran, Iran, in 1991, the M.S. degree at control engineering from the University of Tehran, Tehran, Iran, in 1995, and the Ph.D. degree in control engineering from the Ferdowsi University of Mashhad, Iran, in 2005. He currently is Associate Professor at the Department of Electrical Engineering and Biomedical Engineering, Ferdowsi University of Mashhad. His research interests include reinforcement learning, soft computing, optimal control, multi- agent systems, and machine learning. He has published over 70 journal and conference papers.

Reihaneh Kardehi Moghaddam received the Ph.D. degree in control engineering from the Ferdowsi University of Mashhad, Iran in 2010. She is an associate professor of Azad University electrical and computer engineering department. Her favorite field of research is optimization of extracted power from renewable energy sources, nonlinear fractional order sliding mode controllers and intelligent optimization methods. So far, she has supervised 4 doctoral dissertations and more than 45 master's dissertations in the mentioned research fields. She is the Author of more than 70 articles which have been cited more than 100 times so far.

International Journal of Industrial Electronics, Control and Optimization © 2022 IECO
Vol. 5, No. 2, pp. 143-151, April (2022)

Design and Implementation of a Novel Wind Turbine-PMSG for Marine and Domestic Water Purification Application

Hassan Zare[1, †], Alireza Nateghi[2], Hossein Asgharpour-Alamdari[3], Mohsen Latifi[4]

[1,3]Department of Electrical Engineering, Technical and Vocational University (TVU), Tehran, Iran.
[2]Faculty of Electrical and Computer Engineering, Shahid Sattari University of Aeronautical Engineering, Tehran, Iran.
[4]Faculty of Electrical and Computer Engineering, Islamic Azad University, Tehran, Iran.

ABSTRACT

The supply of purified water in marine and domestic applications, especially in remote areas regarding fossil fuels environmental pollutants, makes it hard to use conventional energy sources. Therefore, the present research seeks to construct a water purification system by using reverse osmosis technology supplied by a novel wind turbine driven with a permanent magnet synchronous generator. To reach this goal, an efficient high torque wind turbine was designed with new butterfly blades in which the lift and drag forces were determined along with creating twisting angles in blades. The blades were initially designed in SolidWorks software. Then, the computational fluid dynamics principles were simulated in the COMSOL5.2a environment by utilizing the k-ω pattern and multi-reference coordinate axis method. A laboratory prototype was implemented to verify the theoretical calculations, simulation analysis, and validity of the wind turbine. To ensure the sufficient capability of the system in worse situations, the performance of the turbine system at a low wind speed of 4 m/s was evaluated. The results showed that a maximum power factor of 0.29 was obtained, making the micro-turbine appropriate for both marine and domestic sweetener systems.

Article Info

Research Article
Keywords:
Desalination System, PMSG, Reverse Osmosis, Savonius, Wind Turbine.
Article History:
Received 2021-10-13
Accepted 2022-04-04

I. INTRODUCTION

Nowadays, access to adequate purified water is turning into a global issue given the growing expansion of human societies and industrial development [1]. On the other hand, increasing concern about generating electricity from fossil energy due to their depletion crisis and environmental pollutant emissions necessitated energy generation from renewable energy sources [2]. Among all sorts of emerging energies, wind power has a special place due to lower energy costs, high efficiency, easy access, and eco-friendliness, which has attracted the attention of many researchers and industrialists [3]. It is anticipated that by 2050, at least 12% of the world's electrical energy will be generated from wind. Wind turbines operate on the basis of a drag force like an open sail, and the wind force pushes the desired surface [4]. Savonius Rotor is a very simple example of the windmill based on the drag force [5]. These turbines move because the drag force in the open and concave regions of these rotors is much larger and more than that in the closed and convex regions. In these turbines, the drag force acts as a propulsion force to rotate the blades. Savonius turbines usually have two or three wind power absorption blades. The design of these turbines is such that the rotational speed is low, but a large torque is generated in each turning circle. Studies on the aerodynamic behavior of the Savonius blade to increase its efficiency have suggested that the height of the blade will be considered twice its diameter, the initial overlap ratio will be between 0.15 and 0.3, and the second overlap distance will be zero

[†]**Corresponding Author**: hszare@tvu.ac.ir
Tel: +98-1144730114, Technical and Vocational University
Department of Electrical Engineering, Technical and Vocational University (Tvu), Tehran, Iran

[1, 5]. Besides, analyzing the helix rotor in comparison with its power production, torque, start-up characteristics, and rotational speed with conventional Savonius and their work results show higher efficiency and easier startup compared to conventional Savonius [6]. In addition, an experimental study on the Savonius turbine found that with the increase in the speed coefficient of the blade tip, the efficiency of these turbines increased, and the turbine with an overlapping space β and a round at the ends of the plates had better performance than the turbine without them [7]. The advantages of Savonius turbines for domestic electricity generation and wind turbine efficiency at various speeds were studied in [8]. The position of blades against the wind was investigated by [9] in an experimental and numerical study on a small type Savonius wind turbine. Aerodynamic simulation of a Savonius micro-turbine was conducted in [10] to identify the suitable point for installing wind turbines on the roof of a solar building. The effects of the overlapping ratio on the performance of domestic wind turbines were examined both numerically and experimentally in [11] according to which the best overlap ratio for this rotor is 20%. Authors in [12] tested wind turbines for quantitative and qualitative drinking water production by using RO systems in Ghana. In [13], a sweetener system was designed using wind turbines for rural areas to facilitate maintenance and allow high cost savings. An RO system with a back and forth pump that needed about 2 kW of power was utilized. Similarly, in [14], a study was conducted on the use of RO desalinating systems in a concrete plant. In this research, a comparative study was carried out to evaluate electrical energy versus wind energy for use as an energy source in RO desalinating systems.

On the other hand, Nuclear Energy Agency and Energy Information Management's report considered the equalized cost of power generation technologies in different countries as well as mentioning wind power as one of the cheapest power generation options [15]. Accordingly, many interesting solutions have been proposed for using wind power. The feasibility of using a Savenius wind micro-turbine on the roof of residential buildings was investigated in [16]. Similarly, many studies have been carried out on the use of Sovenius wind turbines in various applications. But, technical optimization of these turbines and their use in power generation for desalinating have been neglected. Therefore, the present study investigates the optimization of the Sovenius blade regarding the economic analysis of its application for electricity generation for a desalinating system. On the scale of domestic water consumption, reverse osmosis (RO) water desalination systems can only be used with wind power and without the need for another source because the electricity they need can be supplied by a small wind turbine and in the low-speed wind condition. The first step in the construction and installation of these small wind turbines is to conduct feasibility studies to assess the technical, economic, and infrastructural feasibility of establishing a water purification system using wind energy on a specific site using wind turbines. The rest of the paper is structured as follows: Section II introduces comprehensive modeling of the proposed system, including conventional units, electrical components, and Permanent Magnet Synchronous Generator (PMSG), as well as mechanical parts. Additionally, the model proposed for designing blades for an RO system incorporating a wind turbine is implemented in this section considering a detailed comparison between research samples. Section III presents the numerical results and simulation analyses obtained from the computational software. Section IV reports the experimental results derived from mechanical and electrical tests. Finally, the conclusions are summarized in Section V.

II. Problem Description

A. Governing equations of the fluid flow

Equations governing the flow of incompressible fluids are called Navier-Stokes equations. Many models have been suggested to solve these equations under different fluid conditions, each of which is suitable for a particular situation and its particular conditions. The fundamental equations in the analysis of fluids are the two relationships of conservation of mass (Eq. 1) and the relation of momentum (Eq. 2). Since there is a fluid rotation in the analysis of wind turbines, the two resultants, which are named Coriolis and centrifugal acceleration, are entered into the momentum equation. The Coriolis acceleration is defined as $2\vec{\omega} \times \vec{V_r}$ and the centrifugal acceleration as $\vec{\omega} \times \vec{\omega} \times \vec{r}$ where r is the radial position of the rotation domain relative to the center, ω is the angular velocity of the spinning domain, Vr is the relative velocity, ρ is the static pressure, τ_r is the stress tensor, and F is the external forces subjected on the object [17].

$$\frac{\partial \rho}{\partial t} + \nabla . \rho \vec{V_r} = 0 \quad (1)$$

$$\frac{\partial}{\partial t}\left(\rho \vec{V_r}\right) + \nabla . \rho \vec{V_r} \vec{V_r}) + \rho\left(2\vec{\omega} \times \vec{V_r} + \vec{\omega} \times \vec{\omega} \times \vec{r}\right) = -\nabla \rho + \nabla \tau_r + \vec{F} \quad (2)$$

B. Standard method k-ω

To simulate two flow domains, including rotors and stators, a combination of two Cartesian and cylindrical

coordinates was used. The standard k-ω model whose relations are presented in the following equations was used to analyze the turbulent flow [3]. These relationships are related to Navier Stokes relations by the flow switching parameters. The k-ω method is a suitable precision method for analyzing turbulent flow and Reynolds stresses caused by it.

$$\rho(u.\nabla)k = \nabla[(\mu + \mu_T\sigma_k)\nabla k] + P_k - \beta_0\rho\omega k$$
$$\rho(u.\nabla)\omega = \nabla[(\mu + \mu_T\sigma_\omega)\nabla\omega] + \alpha\frac{\omega}{k}P_k - \rho\beta_0\omega^2 \quad (3)$$

$$\mu_T = \rho\frac{k}{\omega} \quad (4)$$

$$P_k = \mu_T[\frac{\nabla u}{\nabla u + (\nabla u)^T}] \quad (5)$$

C. Permanent Magnet Synchronous Generators

Permanent magnet synchronous generators (PMSGs) are kinds of synchronous generators that are connected to the system directly. However, higher reliability, efficiency, and power-to-weight ratio make them more attractive than other generators. Particularly, PMSGs are praised for direct drive, operating without a gearbox, slow rotation speed, and lack of rotor current. However, they still have some drawbacks. For example, they need an electromagnetic field with a flexible structure, which leads to high manufacturing and operation standards, and some temperature-related issues make them less applicable at wind farms.

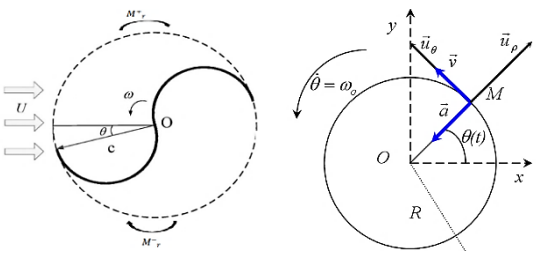

Fig. 1. The k-ω method for Sovenius wind turbine blade.

The high efficiency and low maintenance will reduce the cost, which is the most important concern to invest [18]. Further details about control systems, aggregation methods, and equivalent models for PMSG wind turbines are presented in [19]. Figure 2 describes the components of a PMSG system including the generator and grid side converters' controllers.

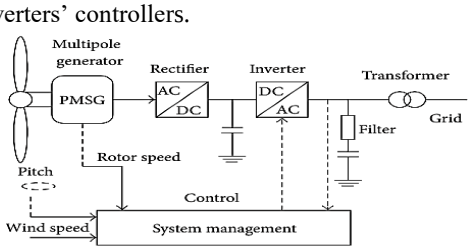

Fig. 2. A schematic of a wind turbine driven PMSG

Considering ρ as air density in kg/m^3, blade pitch angle (β), A_r as blade impact area in m^2, and wind speed in m/s (V_w), the power coefficient of the variable speed wind turbine (C_p), tip speed ratio (λ), and mechanical power (P_m) can be calculated as [2, 20]:

$$P_m = 0.5.\rho.A_r.V_w^3.C_p(\lambda,\beta) \quad (6)$$

$$C_p(\lambda,\beta) = 0.22 \times (\frac{116}{\gamma} - 0.4.\beta - 5).\exp(\frac{12.5}{\gamma}) \quad (7)$$

$$\frac{1}{\gamma} = \frac{1}{\gamma + 0.89} - \frac{0.035}{\beta^3 + 1} \quad (8)$$

$$\lambda = \frac{R.\omega}{V_w} \quad (9)$$

Further details and expressions are discussed in [21]. The relationship between mechanical power, torque, and wind speed can be established below:

$$T_m = \frac{P_m}{\omega} \quad (10)$$

Accordingly, the mechanical torque depends on the wind speed and regarding system states (6) to (10), the model of the wind turbine can be modeled. Hence, the Simulink platform of a wind turbine is shown in Fig. 3.

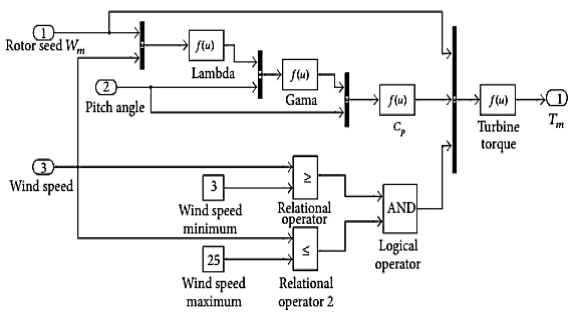

Fig. 3. The block diagram of the wind turbine aerodynamic.

The current equations for the generator with the help of a rotor-fixed rotating coordinate system can be calculated as follows:

$$\frac{di_{sd}}{dt} = -\frac{R_{sa}}{L_{sd}}i_{sd} + \omega_s\frac{L_{sq}}{L_{sd}}i_{sq} + \frac{1}{L_{sd}}u_{sd} \quad (11)$$

$$\frac{di_{sq}}{dt} = -\frac{R_{sa}}{L_{sq}}i_{sq} - \omega_s(\frac{L_{sd}}{L_{sq}}i_{sd} + \frac{1}{L_{sq}}\psi_p) + \frac{1}{L_{sq}}u_{sq} \quad (12)$$

Ultimately, the electromagnetic torque of the rotor is:

$$T_e = 1.5\frac{P}{2}\left[\psi_p i_{sq} + i_{sd}i_{sq}(L_{sd} - L_{sq})\right] \quad (13)$$

where i_{sd} and u_{sd} are the current and voltage of d-axis, respectively. Similarly, i_{sq} and u_{sq} are the q-axis current and voltage, L_{sd} and L_{sq} are the generator inductance, ω_s is the generator's electrical angular frequency, $\psi_p$represents the permanent flux, R_{sa} represents the stator's resistance, and finally, P is the number of the generator's poles.

D. Reverse osmosis water purification method

Reverse Osmosis (RO) is a filtration method with membrane technology that eliminates many types of large

molecules and ions from the solution by compressing the solution behind the membrane. As a result, the solvents remain on the side under pressure, and the pure solvent is allowed to pass to the other side. If a semi-permeable membrane is placed between two solutions with different concentrations, some of the solvent is transferred from one side of the membrane to the other. The natural direction of the solvent movement (i.e., from a higher chemical potential to lower chemical potential) is in such a way that the more concentrated solution is diluted. Pure water passes through the membrane and enters saline water. If the system is allowed to reach a balance, then the level of more concentrated saline water will rise upper than the level of pure water. This difference in the surface on both sides of the membrane is called osmotic pressure. By applying more mechanical pressure than osmotic pressure to saline water, water molecules are separated from the salt molecules and the water moves towards the pure water section, which is called "reverse osmosis".

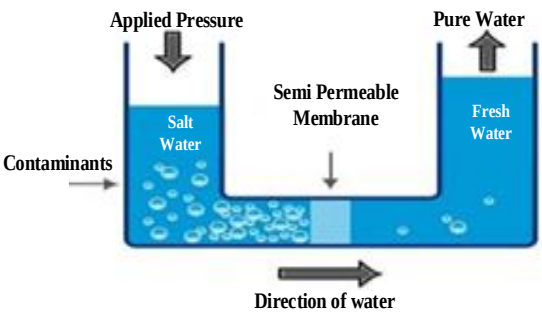

Fig. 4. Reverse Osmosis filtration overview.

E. Comparison between research samples

It is worth mentioning that the geometric and aerodynamic shape of the blade is the most important parameter in the operation of wind turbines, but limited research has been carried out in this field. Since one of the design goals in this research is to determine the effect of the aerodynamic shape of the blade on the efficiency and torque of wind turbines, a few examples of existing blades that have been investigated so far have been gathered in Fig. 5 and their properties have been investigated.

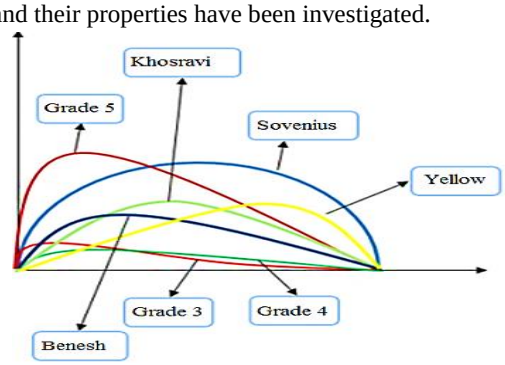

Fig. 5. Different geometric and aerodynamic shapes.

As can be seen, in all of these patterns, it has been tried to determine the effect of each of these parameters on turbine performance by increasing and decreasing the curvature of the blade. If the Benesh blade is considered a control blade, then the curvature of yellow, grade 3, and grade 4 patterns is lower and the curvature of Sovenius, Khosravi, and Grade 5 is higher than that of the Benesh blade [20]. Considering this point, the optimized turbine in this study has a higher power factor or better efficiency than the conventional Sovenius and Khosravi blades, but it has a lower power factor than the Benesh. Table I shows the lift (L_C) and drag coefficients (D_C) for several samples of turbine blades. It should be noted that in this table, Pc represents the center of pressure. As can be seen, the difference between the values of drag coefficients is not significant. On the other hand, the lift coefficients include a range of variables. Therefore, the most important factor in varying the efficiency of wind turbines of this type is the variation in the lift coefficient. For example, the conventional Sovenius turbine has the lowest lift coefficient and the lowest efficiency in the reports. Moreover, the length of the torque arm plays an important role in determining the efficiency of turbines, but not the most important factor, since the Benesh and conventional Savenius blades have the highest effective arm length, while they have the highest and lowest efficiency in the table, respectively.

TABLE I

THE COMPARISON OF POWER COEFFICIENTS AND DRAG AND LIFT FORCES OF DIFFERENT TURBINE BLADES.

Blade name	Dc	Cp,max	Cm,max	Pc (cm)	λmax	Lc
Grade 5	3.01	0.34	0.41	9.3	1.3	0.07
Grade 4	3.01	0.3	0.39	10.5	1.2	0.09
Grade 3	3	0.31	0.4	10.5	1.2	0.11
Benesh	3.01	0.37	0.34	11.9	1.2	0.08
Yellow	3.08	0.36	0.34	10.8	1.2	0.11
Khosravi	3.16	0.26	0.29	10.6	0.9	0.007
Sovenius	2.3	0.23	-	11.9	0.8	0.001

III. SIMULATION RESULTS

The equations mentioned for the wind turbine are solved by producing nodes in the control volume, the meshing method, and the quality of the produced meshes. Hence, three different models of turbines are designed, modeled, meshed, and analyzed in COMSOL software in this study. The specifications of this meshing are presented in Table II and the related meshing is illustrated in Fig. 6. In this study, the air fluid enters the computing region at a speed of 4 m/s. Either one of the two conditions can be used: input velocity and input flow, which do not have any difference as the fluid in the input has constant properties. The velocity input boundary conditions were used as well.

The output pressure boundary condition as zero we used, as well as the other walls, the floor and the ceiling of the computational area were determined by wall boundary conditions (see fig. 7).

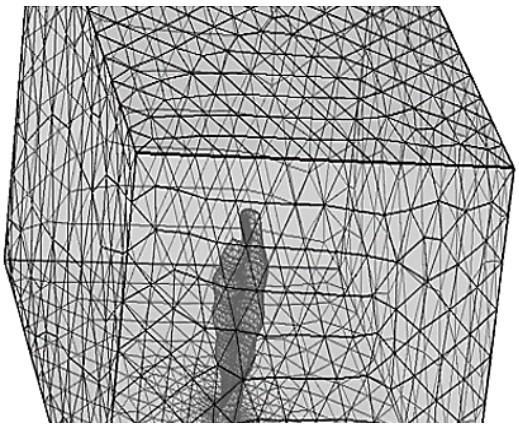

Fig. 6. The meshing of this study.

TABLE II
MESHING CHARACTERISTICS.

Mesh types	Mesh numbers
In apexes	**36497**
Pyramid	**165530**
Tetrahedral	**2201**
Hexagonal	**89634**
Foursquare	**440**
Triangular	**9434**
In boundary layer	**18000**
In edges	**14870**
Total meshes	**337706**
Mesh quality	**0.4276**

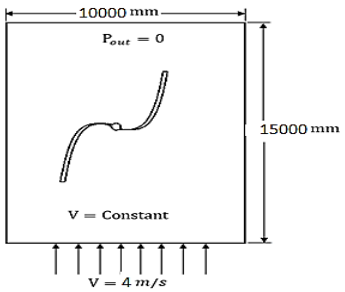

Fig. 7. Specific boundary conditions of this study.

According to the literature review, the potential of wind energy is calculated to be in the range of 900-1500 W/m^2. Therefore, the power of wind energy in the geographical regions of the country should be considered independently and regionally [20]. Hence, statistical methods, mathematical and computational relations, the amount of energy, and wind speed in different months are calculated in this research. For this purpose, daily and hourly statistics (eight times measured at three-hour intervals) for wind speed during the last 5 years of the synoptic meteorological station as presented in table III are used. Figure 8 shows the diagram of the pressure distribution on the simulated rotor surface, in which, according to the colors, the highest pressure on the turbine blade is at the rotor's edges and shows that with the flow of air into the airfoil-shaped blades, the airflow creates a lift force that causes the turbine to rotate. When the blades rotate 90° from the horizontal position, the blade profiles become completely tensile (preventer). The opening cup at the top causes the blade to rotate clockwise, while the downward cup is subjected to a preventing force, which is opposed to the blade rotation. In terms of blade shape, the purer torque is in the clockwise direction.

TABLE III
AVERAGE MONTHLY AND HOURLY WIND SPEED AND ITS PERCENTAGE VARIABILITY OF METEOROLOGICAL STATION

Month	Wind speed (m/s) for each time period								Average
	0:00	03:00	06:00	09:00	12:00	15:00	18:00	21:00	
Jan	0.419	0.516	0.968	2.258	2.451	1.032	0.968	0.367	**0.12**
Feb	0.414	0.517	1.517	3.034	2.759	1.448	0.379	0.62	**1.34**
Mar	0.903	1.226	2.645	3.064	3.742	1.839	2.194	1.129	**2.09**
Apr	1.4	1.034	1.433	1.533	2.967	2.933	1.633	0.7	**2.08**
May	0.161	0.193	2.323	2.870	4.032	4.355	1.806	1.097	**2.10**
Jun	1.733	1.433	3.133	4.3	4.161	3.933	3.333	1.633	**2.99**
Jul	1.419	0.839	2.163	3.064	2.741	3.258	2.645	2.387	**2.38**
Aug	1.290	0.516	3.161	2.548	2.129	4	1.156	1.354	**2.06**
Sep	0.5	0.433	1.933	2.333	2	0.533	0.3	0.667	**1.08**
Oct	0.451	0.580	1.516	2.129	1.580	0.935	0.419	0.516	**1**
Nov	0.433	0.433	0.366	1.5	1.833	0.548	1.516	0.733	**1.05**
Dec	0.545	0.387	1.193	1.645	1.064	0.345	0.419	0.741	**0.76**
$\bar{V}$	0.805	0.676	1.946	2.329	2.621	2.096	1.396	0.995	**1.67**
σ	0.52	0.38	0.95	0.8	0.97	1.5	0.98	0.57	**0.7**
C_v	64.5	55.5	48.9	34.7	37.3	71.9	70	57.4	**41.7**

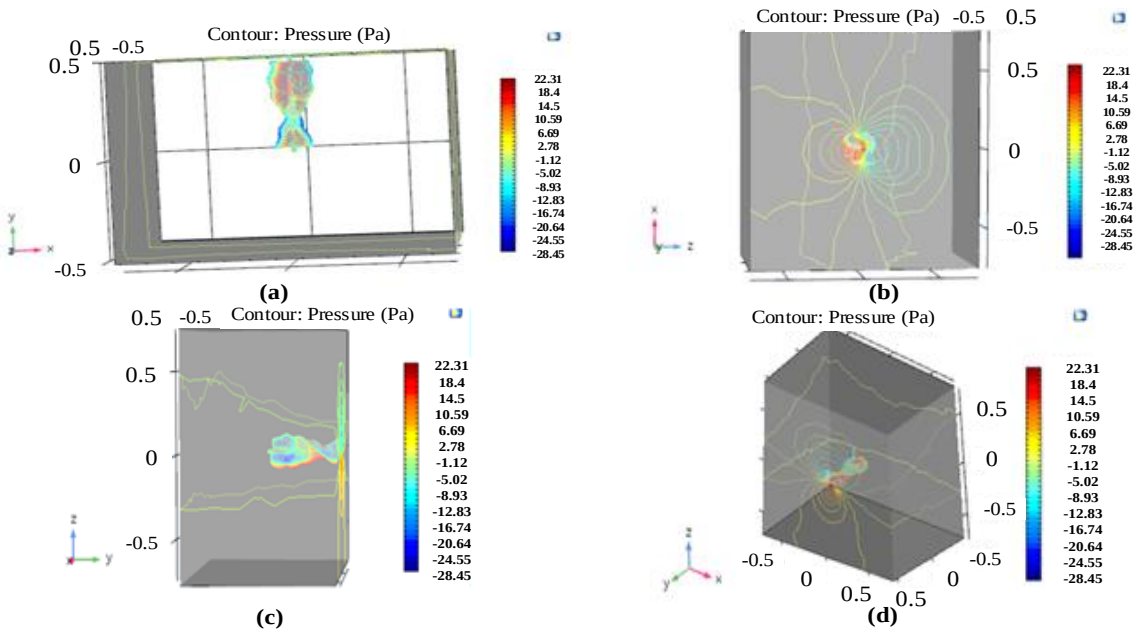

Fig. 8. Pressure distribution diagram **a**) in x-y, b) in x-z, c) in z-y and d) 3-dimensional

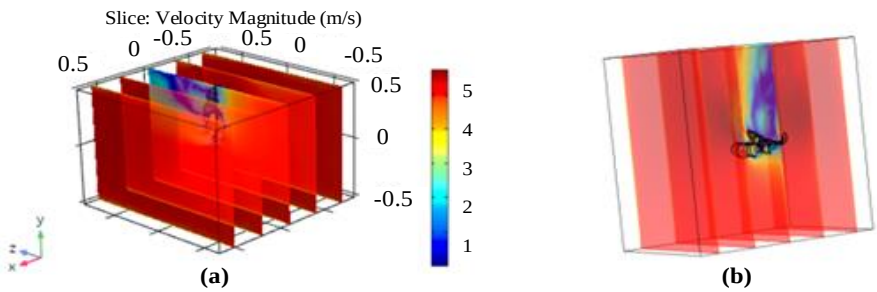

Fig. 9. Velocity distribution diagram a) of the turbine rotor and b) on the studying blade.

Since these two cups are connected by a middle portion, this causes the air to flow between the two blades and, as a result, reduces turbulence. Figure 9 shows the distribution of velocity on the turbine rotor and turbine blade, respectively. As seen in the figures, the maximum velocity is in the direction in which the wind hits the turbine rotor from ahead. To maximize the efficiency of the Sovenius rotor, the end plates should be used on both sides of the rotor. A part of the air fluid, after collision with the rotor, moves away from the rotor towards the rotor's edges so that the maximum momentum of the wind is not transmitted to the rotor and the efficiency decreases. The other thing is that the air fluid after colliding to the surface that faces wind rotation by 90° from the concave side moves upward and down the blade. In order to obtain the most momentum in its ideal state, this angle should increase to 180°. Figure 10 shows the power factor diagram based on the speed of the tip of the blade (m/s). The maximum power factor of 0.29 for the rotor's blade at the speed coefficient of 0.8 is obtained. Moreover, the lift and drag forces and the pressure center of the Sovenius blade at the Reynolds number range of 106 are obtained through simulations. Obtaining the center of pressure is necessary since the torque arm increases by increasing the distance between the pressure center and turbine center, thereby increasing the torque probability. Further simulation results are presented in Table IV. After determining the aerodynamic shape and the lift and drag forces, the torque f blades is obtained in a complete cycle using the CFD analysis.

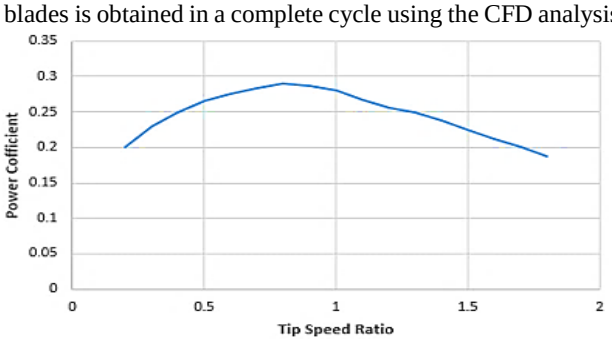

Fig. 10. PF diagram in terms of the tip of the blade speed (m/s).

TABLE IV

AERODYNAMIC CHARACTERISTICS OF THE ROTOR

Parameter	Magnitude
Drag coefficient	2.48
Lift coefficient	0.25
Center of pressure (cm)	12.72
Average torque (N. m)	22.27

Figure 11 indicates the torque subjected to the blades in a complete cycle. Accordingly, the maximum torque for the proposed turbine blades is 24.94 N.m, which is at 90°. To maximize the efficiency of the Sovenius rotor, the end plates should be used on both sides of the rotor. A part of the air fluid moves away from the rotor towards the rotor's edges after collision with the rotor so that the maximum momentum of the wind is not transmitted to the rotor, and thus, its efficiency decreases. To avoid this issue, it is necessary to use the end plates on the rotor. The other thing is that, similar to the previous section, the air fluid rotates 90° from the concave side after colliding with the surface in its ideal state and this angle should increase by 180°.

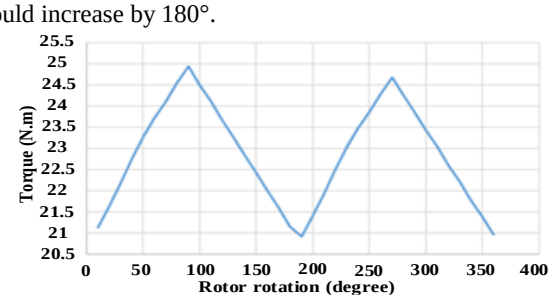

Fig. 11. The torque diagram subjected to the blade.

IV. EXPERIMENTAL RESULTS

The executive activity for blade metrology (metallurgical and mechanical properties) is obtained by comparing the strength and flexibility of the aluminum alloy sheets to other steel and foam sheets. As a result, aluminum alloy is chosen in this study. After that, regarding the design, each blade is divided into five equal parts. In this case, if a part of the blade is damaged, it can be easily replaced and the maintenance costs would be reduced. In the next step, these blades are cut by laser and then curved with a working roll that has a radius of 0.46 m for the turbine blade, which is less than the radius of conventional Savonius wind turbines. This feature results in a greater force and torque on the blades and greater power for the turbine. Then, by coupling the wind turbine and the generator, the proposed setup was structured. Moreover, the MRO1644 water desalination system is utilized in which the amount of sweetened water is 187 L/day. Due to the DC 30 w/hrs power demand of the device, a PWM rectifier was applied in. Accordingly, the properties of the test system are presented in Table V and the photo of the setup in the test environment including both the wind tunnel and suppling the water desalination system is illustrated in Fig. 12. As a result, the experimental results are summarized in Table VI, approving the sufficient perfomance of the system and satisfying the required power demand during every possible condition as considered during system design.

TABLE V

PROPERTIES OF THE LABORATORY PROTOTYPE

Name	Vertical Axis Wind Turbine
Started Wind Speed	1 m/s
Rated Wind Speed	10 m/s
Safe Wind Speed	45 m/s
Rated Voltage (DC)	12.24 v
Rated Power	100 watt
Max Power	150 watt
Rotor Diameter of Blades	0.48 m
Blades Height (m)	1 m (include generator 8 flange)
Blades Material	Aluminum Alloy
Generator	PMSG
Work Environment Temperature	-10 c^o ~ +40 c^o
Work Environment Humidity	Controller and inverter ≤ 80%
Product Assembly Weight (kg)	< 19 kg

a) b)

Fig. 12. The overview of the manufactured laboratory prototype for a) wind tunnel test and b) RO application.

TABLE VI

EXPERIMENTAL RESULTS OF THE PROPOSED STRUCTURE

Torque (N.m)	Power (watt)	Current (A)	Voltage (Volt)	Angular Speed (rad/sec)
5.94	19.62	1.8	10.9	200
7.30	36.5	2.5	14.6	300
6.54	43.21	2.9	14.9	400
7.42	61.6	4	15.4	500
8.30	83.04	4.8	17.3	600
8.38	97.24	5.2	18.7	700
8.65	115.05	5.9	19.5	800
8.39	125.86	6.2	20.3	900

V. CONCLUSION

This study aimed to design, simulate, and manufacture the rotor of wind turbine CH-50/butterfly type and use it as a power generator for a water desalinating system. To achieve this goal, the aerodynamic performance of this blade was first calculated by using computational fluid dynamics and performing 3D simulations. Both of the simulation results and analyses demonstrated 0.29 for the power coefficient of the rotor at a speed coefficient of 0.8. Also, the rotor has a torque of 24.94 N.m at 90 in a complete cycle. Comparing the two-dimensional analysis of simulations demonstrated

that the difference between the wide range values of lift and drag coefficients was not significant. The highest drag coefficient was for a blade that had a low lift factor. Therefore, the lift coefficient variations can be considered the most important factor in the efficiency variations of this turbine type. Besides, the length of the torque arm plays an important role in determining the efficiency of the turbines. At last, a prototype test setup was implemented and the various tests regarding the technical specifications of the desalination system were conducted. The results indicate that the amount of the generated power by the proposed setup can meet the demand of the desalination system, leading to providing 187 liters of purified water per day.

REFERENCE

[1] A. Khajeh & Z. Shabani, Adaptive gain scheduling control of doubly fed induction generator based wind turbines to improve fault ride through performance. *International Journal of Industrial Electronics, Control and Optimization*, 1(1), 61-70, 2018.

[2] R. Zeinali & M. Salehi, The Effect of Different Representations of Wind Turbines on the SSR Analysis in the Double Cage Induction Generator Based Wind Farm. *International Journal of Industrial Electronics, Control and Optimization*, 3(1), 69-80, 2020.

[3] H. Hajiabadi, M. Farshad & M. Shamsinejad, Multi-objective optimization and online control of switched reluctance generator for wind power application. *International Journal of Industrial Electronics Control and Optimization*, 4(1), 33-45, 2021.

[4] E. Jafari, coordinated operation of Wind Farms, Cascaded Hydro, Photo-voltaic and Pump-storage Units by WT-ANN-ICA Prediction Method. *International Journal of Industrial Electronics Control and Optimization*, 4(1), 127-139, 2021.

[5] J .L.Menet, N. Bourabaa, "Increase in the savonius rotor efficiency via α parametric investigation,", European Wind Energy conference & exhibition (pp. 22-25). Nov 2004.

[6] U.K. Saha, M.J.Rajkumar, "On the performance analysis of savonius rotor with twisted blades," *Renewable energy*, vol 31, pp: 1776-1788, 2006.

[7] N.H. Mahmoud, A.A. El-Haroun, E. Wahba, M.H. Nasef,, "An experimental study on improvement of Savonius rotor performance," *Alexandria Engineering Journal*, vol 51, pp:19–25, 2010.

[8] M. C. Percival, P. S. Leung, P. K. Datta, "The Development of a Vertical Turbine for Domestic Electricity Generation,", In European Wind Energy Conference (pp. 22-25). Nov, 2004.

[9] A. Abdlokadir, S.Golde. F.Alam. H. Maria, "Experimental and Computational Study of Micro Vertical Axis Wind Turbine," *IEF International Energy Congress*, vol 49, pp: 254-262, 2012.

[10] Saeed. Qodsi, M. Jamil, M. Layeqi, "Aerodynamic simulation of the wind turbine of Sovenius on the roof of the solar building of the Materials and Energy Research Center", *MSc Thesis, Iran Materials and Energy Research Institute*, 2014.

[11] Jaber Hossein Zadeh Geravi, Mehran Nosratollahi, Mostafa Mahmoudi, "Numerical and experimental study of the effect of coverage ratio on the performance of a domestic wind turbine," *Journal of Engineering and Energy Management*, 5(1), 54-53, 2015.

[12] Park, G. L., A. I. Schäfer, and B. S. Richards., "Potential of wind-powered renewable energy membrane systems for Ghana," Desalination 248.1-3, 169-176, 2009.

[13] Verma, Shivendra, Ramsingh Meena, and Anurag Mudgal., "A Cost-Effective Wind Power-Driven RO Plant for Treatment of Brackish Water," *Journal of Geoscience and Environment Protection* 3.10, 40, 2015.

[14] Alsairafi, A. A., and M. H. Al-Shehaima., "Wind Driven Reverse Osmosis Desalination for Concrete Factory Application in Kuwait," *Journal of Clean Energy Technologies* 4.2, 2016.

[15] Maeda, M., & Watts, D., "The unnoticed impact of long-term cost information on wind farms," economic value in the USA. –A real option analysis', Applied energy, 241, 540-547, 2019.

[16] Muhammad Yavari Foroushani, Mohammad Javad Mehrani, "The feasibility study of the use of Sovenius wind micro-turbine in roof of residential buildings in Tehran," *National Energy Conference, Islamic Azad University, Khomeini Shahr Branch*, 2015.

[17] Kaewchoothong, N., & Nuntadusit, C. Flow and Heat Transfer Behaviors in a Two-Pass Rotating Channel with Rib Turbulators using Computational Fluid Dynamics, Heat Transfer Engineering, 1-19. Feb 2022.

[18] O. Rabaza, D. G, M. J. Mercado-Vargas, D. Gómez-Lorente, O. Rabaza, and E. Alameda-Hernandez, "Aggregated models of PMSG wind farms," *Renew. Energy*, vol. 83, pp. 1287–1298, 2015.

[19] S. Das, & O. H. Gupta, Study and Simulation of a PMSG-Based Wind Turbine, Recent Advances in Power Electronics and Drives, Springer, pp. 37-46, 2021.

[20] H. Khosravi, M. Jamil, "Effect of aerodynamic, positioning and number of advanced Savonius rotor blades on efficiency and torque of wind turbine," *MSc Thesis, Iranian Institute of Materials and Energy*, 2011

[21] M.Prakash, & J. Young-Hoon, "Fuzzy Event-triggered Control for Back to Back Converter involved PMSG-based Wind Turbine Systems." IEEE Transactions on Fuzzy Systems, 2021.

Hassan Zare received his Ph.D. from Semnan University, Iran in 2018. He is currently an Assistant Professor with Technical and Vocational University (TVU), Tehran, Iran. His research interests include power system stability and control, electrical machines and drive, converters, and their application in renewable energy.

Alireza Nateghi was born in Tehran, Iran in 1969. He received his B.Sc. degree from the Sharif University of Technology, Tehran, Iran in 1999. He received his M.Sc. and Ph.D. degrees in Electrical Engineering from Shahid Beheshti University, Tehran, Iran in 2009. He joined the University of Shahid Sattari as an Assistant Professor in the Department of Electric Engineering, from 2010 to 2021. His current research interests include control of distributed energy resources and design and control of power electronic converters for microgrids**.**

Hossein Asgharpour-Alamdari received his Ph.D. from Semnan University, Iran in 2017. He is currently an Assistant Professor with Technical and Vocational University (TVU), Tehran, Iran. His research interests are power system stability and control, power system protection, electrical machines, and their application in renewable energy.

IECO
This page intentionally left blank.

International Journal of Industrial Electronics, Control and Optimization © 2022 IECO
Vol. 5, No. 2, pp. 153-165, April (2022)

A New Enhanced Droop Controller for Seamless Load Sharing in AC Microgrids in Presence of Wind Turbine and Photovoltaic Sources

Sadegh Shajari[1], Reza Keypour[2, †]

[1,2] Department of Electrical and Computer Engineering, Semnan University, Semnan, Iran

ABSTRACT

Load sharing, as an important challenge in microgrids (MGs), is realized commonly via a droop control method. Conventional droop control methods are not applicable in unpredictable renewable energy sources (RESs) like photovoltaic (PV) and wind turbines (WT) because their output power depends on the weather conditions and can be extracted only if these free sources are available. This paper considers two operating modes for these types of sources as Maximum Power Point Tracking (MPPT) and DC-link Voltage Control (DCLVC). These power sources usually operate in the MPPT mode unless the load of the MG drops to a lower level compared to the maximum power generation by RESs, in which case the sources switch to the DCLVC operating mode. This study proposed a method based on enhanced droop control, which helps RESs to choose their control mode locally without communication and share the demand of the AC MG with other dispatchable sources besides supplying its maximum power. The proposed method focused on supplying MG load from RESs as much as possible and simplicity in implementation. MG frequency helps the proposed controller to select its operation mode. Enhanced control for DC link voltage control is offered for inverter-based RESs. The validity of the proposed method is approved by simulations in the MATLAB/SIMULINK environment.

Article Info

Research Article

Keywords:

Droop Method, Load Sharing, Microgrid (MG), Photovoltaic (PV), Wind Turbine (WT)

Article History:

Received 2021-09-18

Accepted 2022-04-12

I. INTRODUCTION

Since greenhouse gas reduction has become an important environmental issue, renewable energy resources (RESs), such as wind and solar energy, have gained huge attention, especially in MGs [1], [2]. Integration of RESs and MGs requires power electronic interfaces [3], [4]. Hence, MGs comprise of RESs, energy storage systems, and power electronic interfaces. To share MG's load among parallel power electronic interfaces, suitable control methods should be applied to avoid circulating currents, especially in presence of RESs [5] – [7].

In the future, many countries around the world are likely to experience high penetration levels of WT and PV as RESs, to not only reduce greenhouse gas emissions but also utilize an interesting economic alternative in areas with abundant wind or solar radiation. The integration of high penetration levels of WT and PV into MGs may require new approaches and solutions [8], [9]. Due to the intermittency effect and renewable characteristics, WT and PV units can operate in either MPPT or DCLVC mode, while other dispatchable sources have the linear droop characteristic.

Basically, the first solution is to employ a central controller, that is why the authors in [10] propose a central controller to control the PV output power in an MG. Supplying unbalanced load via the combination of PV and battery energy storage system in [11] and [12] is another example indicating an effort to control RESs via a central controller. High bandwidth is critical for central controllers in an MG. The costs of high bandwidth infrastructure besides noise and network security make the central controller an undesirable option and weakness of the mentioned papers. That is the reason researchers tend to use local controllers.

[†]**Corresponding Author**: rkeypour@semnan.ac.ir
Tel: +98-2331532724, Fax: +98-31532699, Semnan University
Faculty of Electrical and Computer Engineering, Semnan University, Semnan, Iran

Although the increase in the RESs penetration in MGs is intended and desirable, DC MGs are preferred because of their less complexity. That is why authors in [13] and [14] apply a voltage droop control to a DC MG. In [15], an integrated PV and battery energy storage are controlled based on the voltage of a DC MG. Also, the authors in [16] propose the supervisory control for a combination of PV and WT along with a battery energy storage device for a DC MG. Although the mentioned literature proposes a control method for RESs in DC MGs, dispatchable sources besides RESs do not share the load with each other. Hence not involving load sharing in the study is a disadvantage of their methods. In [17], a decentralized control method based on the V-I droop concept is proposed for multiple PV sources, where the objective is to regulate the DC bus in a DC MG. Despite the fact that power sharing among PV sources has been carried out in some studies, PV sources cannot operate in the MPPT mode, unless a DC MG is in connected grid connected mode and that is the weakness of the study.

Some authors tried to control RESs in AC MGs, where the droop control method was used to control PV sources to improve the MG voltage at the fundamental frequency [18]. In another study, a control method is proposed for a PV source so that it could operate in grid-connected or standalone mode, but load sharing in presence of RESs is not discussed because multi-source MGs were discarded [19]. Load-sharing in the studies is still not addressed, which is the weakness of the above studies. Most papers addressing the load sharing in AC MGs are focused on dispatchable sources while neglecting RESs [20] – [22]. Due to intermittent characteristics of RESs, load sharing of the proposed paper does not have the capability of controlling RESs. There are few studies that discuss the effects of RESs on load sharing. In [23], autonomous control strategies are proposed for PV and battery units operating in a droop-controlled islanded MG based on PV. Authors in [24] present a local controller for a single PV source to share its power and a dispatchable source power, in which the intermittent effect of RESs is considered in the AC MG. Nonetheless, it can be used only for MGs with a single PV source. References [25] and [26] introduce a decentralized controller for load sharing of a hybrid PV/Battery source based on switching between different operating modes. Yet, due to switching between numerous modes, an unpleasant transient is inevitable and it is the foible of the method. Considering the mentioned studies, further investigation is required to analyze the load sharing in intermittent RESs, especially in WTs of AC MGs.

The present study proposed a decentralized controller to select the operating mode of the RESs based on local measurements and a droop method. MG frequency is used as a switching criterion between operation modes. The proposed controller helps RESs to extract the maximum power and supply the MGs in the MPPT mode. During low load conditions, the DCLVC mode is activated in the RESs to control DC link voltage in RESs and, while other dispatchable sources provide their minimum power, RESs share MG's load among each other, and power curtailment might occur if it is necessary. A comprehensive controller is proposed for DC link voltage control in PV and WT sources. It has the responsibility for determining the amount of power curtailment according to the voltage level of the DC link voltage. The power curtailment method varies according to the type of source.

The organization of the paper is as follows. The primary control and proposed decentralized controller are explained in sections II and III, respectively. Simulation results are provided in section IV, and the last section presents the conclusions.

II. PRIMARY CONTROL

Various types of power sources are connected to MGs. They may operate in stand-alone or grid-connected mode. Fig. 1 shows that power sources, such as PVs, WTs, or battery energy storage devices, are connected to MG by DC/AC power electronics interfaces in a sample structure of the MG. Voltage Source Inverter (VSI) and Current Source Inverter (CSI) are usually used as DC/AC interfaces between the source and the MG. Thanks to the ride-through and power quality advantages, VSIs have gained more attention in MGs applications [27], [28].

Current control loops, voltage control loop, virtual impedance loop, and droop control of VSI primary control are depicted in Fig. 2. The voltage control loop is responsible for voltage stability, especially in RESs-based MGs. Current control is in charge of continuous current injection with eliminated harmonics, especially in low-order harmonics. Current tracking must have a high bandwidth because it should provide a faster response than the voltage control; otherwise, any voltage disturbance can lead to an increase in the current THD and result in instability [29].

The proportional integral (PI) controller is the most widely used controller in inverter controls, but the proportional resonant (PR) controller is becoming more popular because of its faster dynamic response, higher gain at the fundamental frequency, and less harmonic components, especially in low-order harmonics.

The frequency and amplitude of the reference voltage are calculated based on frequency-active power and amplitude–reactive power relationships in the droop control method. Virtual impedance is added to make up the line impedance effect and reduce the dependency of active power and reactive power to voltage, and frequency, respectively [30]. Secondary control is responsible for the compensation of primary control deviation [31].

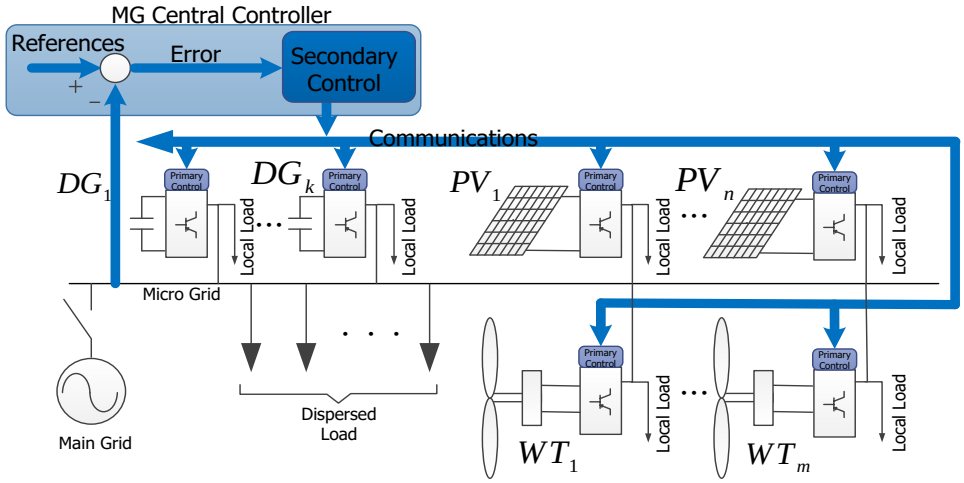

Fig. 1. Structure of an MG

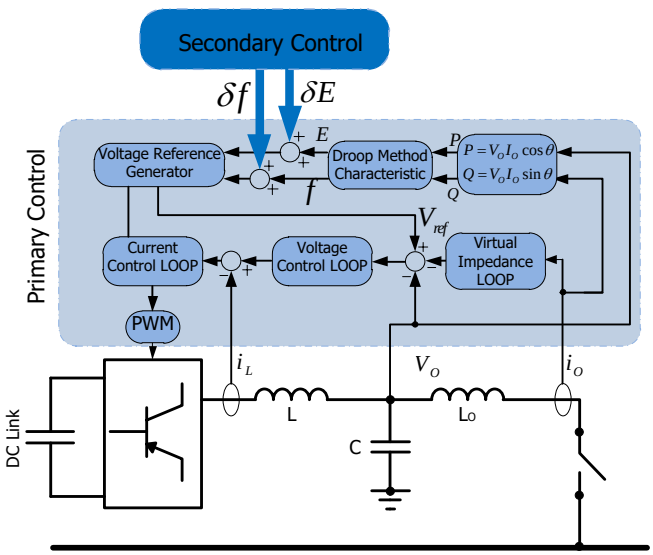

Fig. 2. Control of a DG source in an MG

III. PROPOSED METHOD

The sample AC MG depicted in Fig. 3 is used for the study. As Fig. 3 shows, the considered AC MG consists of 'm' number of WT sources, 'k' number of battery energy storage sources and 'n' number of PV sources. PV sources are connected to the AC MG through a DC/DC converter and a DC/AC inverter. The DC/DC converter is responsible for the maximum power point tracking. The DC/AC inverter is used in the WT. The MG load is converted to an integrated single load.

Load sharing in the sample MG is usually performed by the droop control method, which is described by the following equations:

$$\begin{aligned} \omega_{PVi} &= \omega^{*}_{PVi} - D_{PVi}(s)P_{PVi} \qquad 0 \le i \le n \\ \omega_{WTj} &= \omega^{*}_{WTj} - D_{WTj}(s)P_{WTj} \qquad 0 \le j \le m \\ \omega_{h} &= \omega^{*}_{h} - D_{h}(s)P_{h} \qquad 0 \le h \le k \end{aligned} \tag{1}$$

where, ω^{*}_{PVi}, ω^{*}_{WTj}, and ω^{*}_{h} are angular frequency references and D_{PVi}, D_{WTj} and D_{h} represent frequency droop coefficients.

$$\begin{aligned} E_{PVi} &= E^{*}_{PVi} - D_{Q-PVi}(s)Q_{PVi} \qquad 0 \le i \le n \\ E_{WTj} &= E^{*}_{WTj} - D_{Q-WTj}(s)Q_{WTj} \qquad 0 \le j \le m \\ E_{h} &= E^{*}_{h} - D_{Q-h}(s)Q_{h} \qquad 0 \le h \le k \end{aligned} \tag{2}$$

where, E^{*}_{PVi}, E^{*}_{WTj} and E^{*}_{h} show voltage references, and $D_{Q-PVi)}$, D_{Q-WTj} and D_{Q-h} denote voltage droop coefficients.

The conventional droop method should be developed to be applicable to renewable intermittent sources like PVs or WTs. Hence, a new method is proposed here, with two operating modes as illustrated in Fig. 4 (a). Two control modes, one corresponding to the droop section of the curve and the other one corresponding to the vertical section of the curve in Fig 4. While the system frequency remains between f_{DS} and f_{min}, renewable intermittent sources which may be PV sources or WTs track the maximum power and deliver it to the MG and operate in the MPPT mode (vertical section). As shown in Fig. 4 (a), the maximum power can be changed according to the weather variations and the remaining load shares among dispatchable sources. When the frequency of the MG increases to a higher level compared to f_{DS}, dispatchable sources deliver their minimum power due to the load decrease, and intermittent sources share the load among each other based on a droop characteristic, which depends on the maximum extractable power of each available source according to the droop section of Fig. 4.

Fig. 5 depicts different operating modes of the proposed method in the sample AC MG with two PV sources, one WT source, and one dispatchable source. At State 1, each source delivers its maximum available power to the MG. Decreasing the load in this mode leads to a power decrease in the dispatchable source while renewable intermittent sources still operate at the maximum power point (MPP). When frequency reaches f_{DS} and the MG operates at State 2, the dispatchable source operates at its minimum power mode and RESs are in charge of supplying the load. Increasing the frequency to State 3 leads to power curtailment in RESs and the DCLVC is activated in RESs to properly decrease their output power. At State 3, RESs share the load of the MG among each other using a new droop characteristic based on the maximum available power of each source.

Since the proposed characteristic includes both MPPT and DCLVC modes, each part should be covered in a separate section.

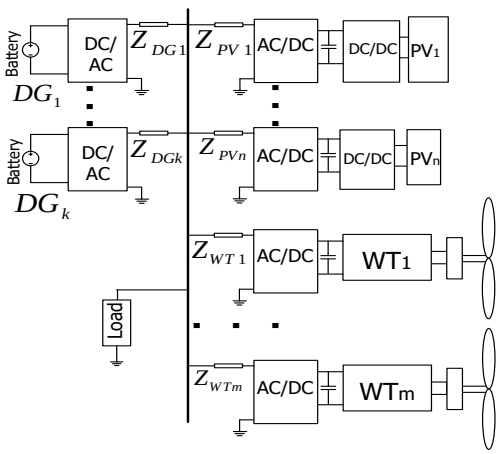

Fig. 3. Configuration of the system under study

A. *Maximum Power Point Tracking Control Mode*

This mode is an important mode [32], [33] and RESs track their maximum power points and frequency of the MG is lower than f_{DS}. Thus, the active power equation should be modified as follows:

$$\begin{aligned}\omega_{PVi} &= \omega^*_{PVi-New} - D_{PVi}(s)P_{PVi}\\ \omega_{WTj} &= \omega^*_{WTj-New} - D_{WTj}(s)P_{WTj}\\ \omega_h &= \omega^*_h - D_h(s)P_h\end{aligned} \tag{3}$$

Where, $\omega^*_{PVi-New}$ and $\omega^*_{WTj-New}$ are new angular frequency references obtained from Equ. (4):

$$\begin{aligned}\omega^*_{PVi-New} &= \omega^*_{PVi} + \frac{D_{PVi}(s)}{S}\left(P_{Max-PVi} - P_{PVi}\right)\\ \omega^*_{WTj-New} &= \omega^*_{WTj} + \frac{D_{WTj}(s)}{S}\left(P_{Max-WTj} - P_{WTj}\right)\end{aligned} \tag{4}$$

Equ. (4) helps RESs to deliver their maximum power to the MG with updating character.

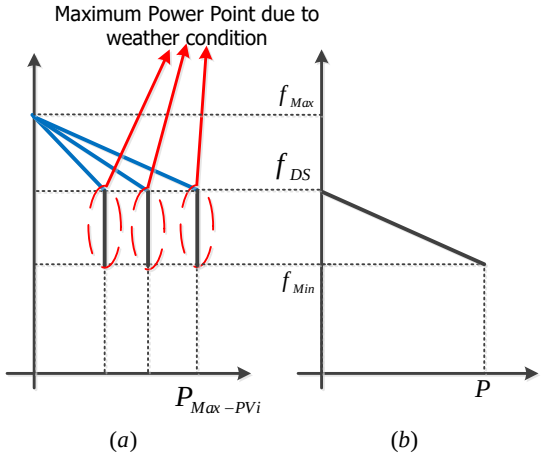

Fig. 4. The proposed characteristic for an intermittent renewable source (a) beside a conventional droop (b)

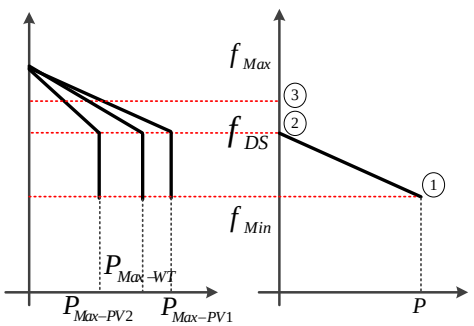

Fig. 5. Operation of the proposed method in different states

Active power and phase angle relationships are similar in all sources. The relationship between the active power of inverter 'i' belonging to the PV source and its phase angle is given by Eq. (5) [33]:

$$\begin{aligned}\left(\delta_{PVi} - \delta_{com}\right) &= \int\left(\omega_{PVi} - \omega_{com}\right)dt\\ P_{PVi} &= \frac{E_{PVi}V_{com}\sin\left(\delta_{PVi} - \delta_{com}\right)}{X_{PVi}}\end{aligned} \tag{5}$$

Where, E_{PVi} is the output voltage magnitude of the *i*th inverter V_{com} is the common bus voltage magnitude, and assuming inductive impedance of line, X_{PVi} is the connection inductance.

Small signal analysis is necessary for the adjustment of control parameters. Linearization of Equs. (3) - (5) at a single operating point leads to:

$$\begin{cases}\Delta\omega_h = \Delta\omega^*_h - D_{h(S)}\Delta P_h\\ \Delta\omega_{PVi} = \Delta\omega^*_{PVi-New} + \dfrac{D_{PVi(S)}}{S}\left(\Delta P_{Max-PVi} - \Delta P_{PVi}\right)\\ -D_{PVi(S)}\left(\Delta P_{PVi}\right)\\ \Delta\omega_{WTj} = \Delta\omega^*_{WTj-New} + \dfrac{D_{WTj(S)}}{S}\left(\Delta P_{Max-WTj} - \Delta P_{WTj}\right)\\ -D_{WTj(S)}\left(\Delta P_{WTj}\right)\end{cases} \tag{6}$$

$$\begin{cases} (\Delta\delta_h - \Delta\delta_{com}) = \int (\Delta\omega_h - \Delta\omega_{com})dt \\ (\Delta\delta_{PVi} - \Delta\delta_{com}) = \int (\Delta\omega_{PVi} - \Delta\omega_{com})dt \\ (\Delta\delta_{WTj} - \Delta\delta_{com}) = \int (\Delta\omega_{WTj} - \Delta\omega_{com})dt \end{cases} \quad (7)$$

$$\begin{cases} \Delta P_h = G_h (\Delta\delta_h - \Delta\delta_{com}) \\ \Delta P_{PVi} = G_{PVi} (\Delta\delta_{PVi} - \Delta\delta_{com}) \\ \Delta P_{WTj} = G_{WTj} (\Delta\delta_{WTj} - \Delta\delta_{com}) \end{cases} \quad (8)$$

$$G_h = \frac{E_h^i V_{com}^i \cos(\delta_h^i - \delta_{com}^i)}{X_h}$$

$$G_{PVi} = \frac{E_{PVi}^i V_{com}^i \cos(\delta_{PVi}^i - \delta_{com}^i)}{X_{PVi}} \quad (9)$$

$$G_{WTj} = \frac{E_{WTj}^i V_{com}^i \cos(\delta_{WTj}^i - \delta_{com}^i)}{X_{WTj}}$$

The control block diagram for RESs and the dispatchable source is illustrated in Fig. 6. As the small signal model of all RESs is similar, small signal model of one PV source is depicted as an example. A low-pass filter with a cut-off frequency of 0.2 Hz is considered in the control block of all sources. The filter is represented by $G_{LPF(S)}$, and a PI controller is used for droop control as represented in Equ. (11) [30]:

$$G_{LPF(S)} = \frac{1}{1+\tau_p S} \quad (10)$$

$$D_h, D_{PVi}, D_{WTj} = \frac{K_{pP} S + K_{iP}}{S} \quad (11)$$

According to Ref. [27], the characteristic equation can be extracted from Fig. 6. In Fig. 7 root locus of the model is depicted. As all the three poles stay on the left side, the stability of the proposed method is confirmed. The conventional voltage-reactive power droop is applied to the reactive power control [30].

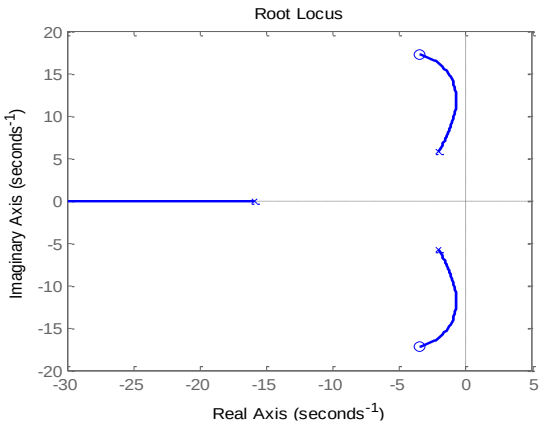

Fig. 7. Root locus for small signal analysis in MPPT mo

B. DC-link Voltage Control Mode

When the load of the MG decreases to a lower level compared to the total maximum power of the RESs and dispatchable sources operate in a minimum power state, power curtailment is inevitable in RESs. The DC-link voltage will increase beyond its permissible maximum voltage due to the difference between the injected power to the DC-link and extracted power from it. Hence, RESs should switch from the MPPT mode to the DCLVC mode to control the DC-link voltage by controlling the power injected into the DC-link.

As there are two types of RESs in this study, two types of a controller are proposed for the DC-link voltage control of PV and WT units, as shown in Figs. 8 and 9. These two controllers operate similarly but with minor differences. In both of them, the difference between the DC-link voltage and the permissible maximum voltage passes through the saturation block. If the difference value is positive, the saturation block saturates the output at zero, and the voltage controller for DC/DC converter in PV source or pitch

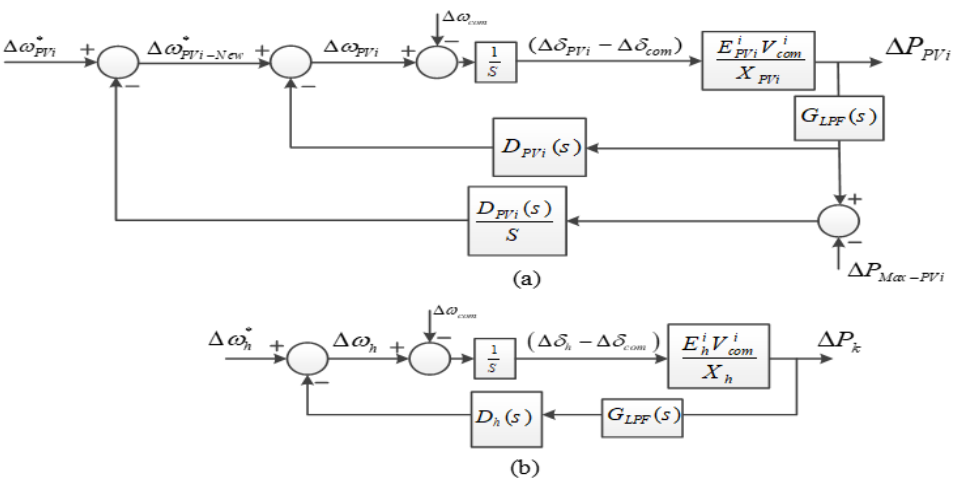

Fig. 6. Small signal model of the active power control in the MPPT mode (a) active power control controller in of RESs, and (b) active power control of the dispatchable source

WT source works to seek maximum power. When the difference value is negative, the output of the compensators, which are PI controllers, will be added to the output of the MPPT controller or the pitch angle controller. Therefore, the output of the DC/DC converter or the pitch angle controller does not track the maximum power and is changed to fix the DC-link voltage at the permissible maximum voltage.

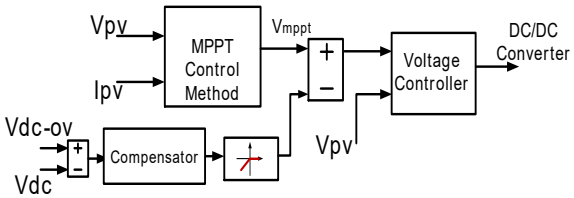

Fig. 8. Block diagram of the DC/DC converter control

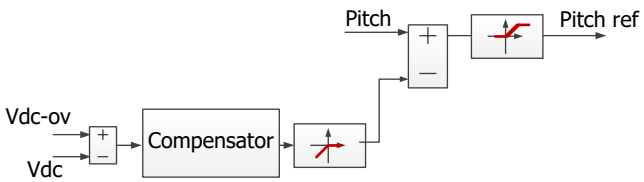

Fig. 9. Block diagram of the AC/DC rectifier control of the WT

As power curtailment is happening in this state and power is shared among RESs based on the new droop control, the droop equation for RESs changes as follows:

$$\omega_{PVi} = \omega^{*}_{PVi} - D_{PVi-New} P_{PVi}$$
$$\omega_{WTj} = \omega^{*}_{WTj} - D_{WTj-New} P_{WTj} \quad (13)$$

New droop coefficients can be calculated by Equ. (14).

$$D_{PVi-New} = \frac{f_{\max} - f_{DS}}{P_{Max-PVi}}$$
$$D_{WTj-New} = \frac{f_{\max} - f_{DS}}{P_{Max-WTj}} \quad (14)$$

Similar to the previous section, small signal can be obtained. This is shown in Fig. 10 for the PV as an example.

C. Mode Detection

Fig. 11 shows how the proposed controller works locally and chooses its control mode for the PV source. The control method for WT is the same. According to Fig. 4, f_{DS} is a border between two operating modes. Equation (15) shows the calculation of f_{DS} for an MG. Thus, when the system frequency is higher than f_{DS}, the proposed controller locally chooses the DCLVC mode and if it is lower than f_{DS}, the MPPT mode is selected. Consequently, the system frequency passes through two saturation blocks with inverse operation modes and the outputs are multiplied by the reference voltage values. Finally, the sum of multipliers outputs produces reference voltage. Therefore, when the frequency of the MG is lower than f_{DS} , the reference voltage is the product of the MPPT mode, else it will be the product of the DCLVC mode.

$$f_{DS} = \frac{Dispatchable\ \ Power(f_{Max} - f_{Min})}{Dispatchable\ \ Power + Renewable\ \ Power} + f_{Min} \quad (15)$$

IV. Simulation Results

Simulation of the proposed method is performed in the MATLAB/Simulink environment to show its validity. Fig. 12 illustrates the sample AC MG, in which two PV sources, one WT source, and one dispatchable source are used for simulation purposes. The WT consists of an induction generator, a gearbox, and a wind turbine all interconnected. As Matlab Simulink environment is used for simulation, the default model of wind turbine beside some modifications from [8] and [9] are used for modeling the wind turbine. The maximum power of PV sources below 1000 W/m^2 irradiation is shown in Table I. Method of [34] and [35] is used for PV power extraction. The Maximum power of the WT source below 10 m/s wind speed and zero pitch angle is provided in Table I. An LC filter at the output of the inverter is connected to all sources. Control parameters for all sources are provided in Table I. Common parameters for all sources have the same values. The load of the MG load is varied in a way that all operating modes can be achieved. The maximum and minimum frequencies of the MG are 50.1 Hz and 49.9 Hz, respectively. Hence, f_{DS} is roughly 49.96 Hz in the MG with the power in Table I.

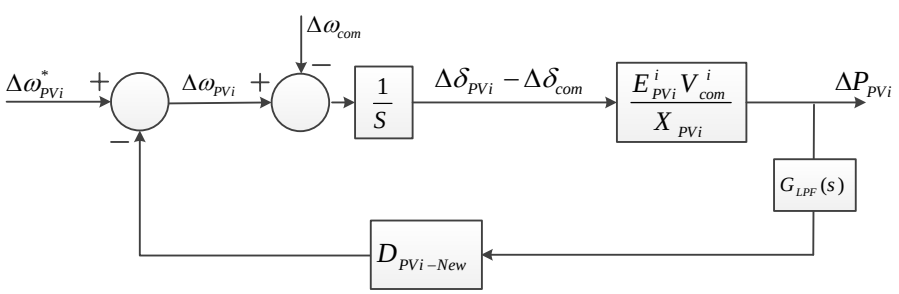

Fig. 10. Small signal model for active power control in the DC-link voltage control mode for the RESs.

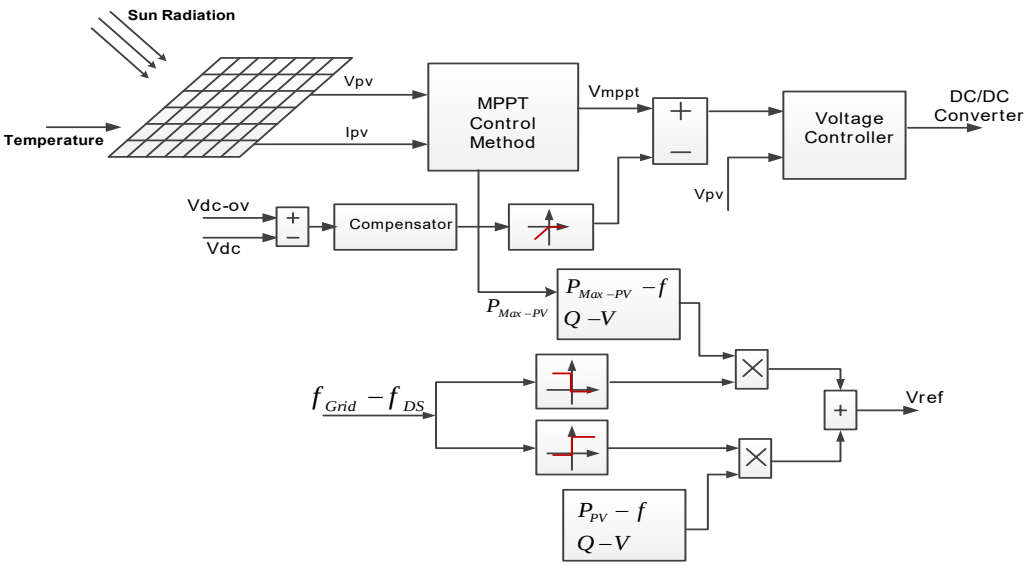

Fig. 11. The proposed control method

Simulations under different situations are performed. Changes in the load and weather conditions are investigated in the first and second simulations, respectively. The first simulation starts under 1000 $\frac{W}{m^2}$ irradiance for PV sources, 10 $\frac{m}{s}$ wind speed for the WT source, and the MG load equal to 3400 W. Then the MG load decreases two times; in the first case, the load reaches 3100 W at t = 5 s (section 2 in Fig. 13) and in the second case, it decreases to 2200 W at t = 10 s (section 3 in Fig. 13). In the next step, the MG load increases and reaches 2600 W at t = 30 s (section 4 in Fig. 13).

As expected, when the MG load is 3400 W, the frequency drops below f_{DS} and all RESs deliver maximum reachable power to the MG and the remaining load is supplied by the dispatchable source, which is shown in section 1 in Fig. 13 and Fig. 14. At t = 5 s, the MG load decreases and the frequency increases to a higher level to become almost equal to f_{DS} . Therefore, the dispatchable source power decreases to its minimum power state, while RESs still deliver maximum power to the MG. More decrease in the MG load leads to more increase in the MG frequency. Thus it is expected that the frequency increases to a higher level compared to f_{DS} and RESs change the control mode from the MPPT to the DCLVC mode, and power curtailment happens. Section 3 of Fig 13 illustrates the proposed controller reaches the predetermined goals and load sharing during DCLVC mode is properly performed. Fig 15 shows the DC-link voltage for RESs. Different maximum permissible voltages are considered for each source to check each source separately. According to Fig. 13 and Fig. 15, RESs share the load between each other in a very proper manner and the DC-link voltage is kept constant at permissible maximum voltage. The DC-link voltage variation of PV1 and PV2 is similar and the controller response is very fast. However, in the case of the WT, it is much slower because of mechanical mechanism dynamics. The controller changes the pitch angle and due to a higher time constant and a slower response of the pitch control system, the variations in the DC-link voltage in the WT are much slower compared to those of PV sources.

Table I
SIMULATION PARAMETERS

Type	Symbol	Quantity	Value
Electrical Parameter	V_{MG}	MG voltage	311 V
	f	MG frequency	50 Hz
	V_{DC}	DC voltage	650 V
	$P_{Max-PV1}$	PV1 Maximum Power	1.4 kW
	$P_{Max-PV2}$	PV2 Maximum Power	0.7 kW
	P_{Max-WT}	WT Maximum Power	1 kW
	$P_{Max-Dispatch}$	Dispatchable Source Maximum Power	1.35 kW
	C	Filter Capacitance	25 μf
	L	Filter Inductance	1.8 mH
	L_O	Output Impedance	1.8 mH
Inner Loops	K_{pI}	Current proportional term	0.35
	K_{iI}	Current Integral term	200
	K_{pV}	Voltage proportional term	0.35
	K_{iV}	Voltage integral term	400
Droop Control	K_{pP}	Active power droop coefficient	0.00001 ($^{Rad}/_{W}$
	K_{iP}	Active power droop Integral term	0.0008 ($^{Rad}/_{W.s}$
	K_{pQ}	Reactive power droop coefficient	0.16($^{V}/_{Var}$)
	R_V	Virtual Resistance	1 Ω
	L_V	Virtual Inductance	4 mH

At t=30 s, the MG load increases and makes the MG frequency decrease but it is still higher than f_{DS}, therefore DCLVC is ON and power curtailment happens again. Due to a sudden increase in the output power, the DC-link voltage

experiences a sudden decrease but power from RESs compensate for the changes, and the DC-link voltage returns to its previous state immediately.

As the controller has online maximum power tracking, it should have the ability to respond to any changes in weather conditions. So, in the second simulation case, irradiance and wind speed changes are considered to examine the response of the proposed controller.

In the second simulation, the MG load is kept constant and irradiance for the PV1 is decreased from 1000 $\frac{W}{m^2}$ to 500 $\frac{W}{m^2}$ at t = 10 s, then it is increased to 1000 $\frac{W}{m^2}$ at t = 20 s. Wind speed change occurs at t = 30 s and t = 40 s for the WT. At t = 30 s, wind speed is decreased from 10 $\frac{m}{s}$ to 8 $\frac{m}{s}$ and at t = 40 s it becomes 10 $\frac{m}{s}$. Fig. 16 shows active power variation of all sources while the MG load is 3400 W and kept constant while weather conditions are changed for some of the RESs. As depicted in section 2 of Fig. 16, when irradiance changes from 1000 $\frac{W}{m^2}$ to 500 $\frac{W}{m^2}$ for PV1, as expected the MPPT controller finds a new maximum power, and the output power of PV1 decreases to 50 percent of its nominal power. While other RESs deliver their maximum power, the dispatchable source has the free capacity to compensate for differences between the MG load and the generation. So, the output power of the dispatchable source increases to make up the difference. When irradiance increases to 1000 $\frac{W}{m^2}$ at t = 20 s in section 3 of Fig. 16, the MPPT of PV1 changes its operating point to a previous state, and as it is predictable the output power of PV1 increases to its nominal power, hence the dispatchable source power drops to its previous state. The response of the WT to a decrease in the wind speed is shown in section 4 of Fig. 16, in which the wind speed decreases to 8 $\frac{m}{s}$ at t = 30 s. It can be guessed that the dispatchable source takes the responsibility for the generation and load difference by increasing its output power. As depicted in section 4 of Fig.16, the dispatchable source makes up the difference. Section 5 shows the return to the previous state when the wind speed increases and the dispatchable source power decreases to its initial state. Figs. 17 and 18 show the frequency of the MG and variations in DC-link voltages of all RESs. Although irradiance or wind speed has been changed during the second simulation, the power injected into the DC-link and power extracted from DC- link was almost equal during weather changes for all RESs. Hence, the DC-link voltage did not experience much variation due to weather changes. MG voltage variation due to weather change is illustrated in Fig. 19. As shown in Fig. 19, changes in solar radiation or wind speed, which are accompanied by changes in the output power of REVs, cause changes in the MG voltage. Of course, the performance of the reactive power controller, which is responsible for the MG voltage control, is quite satisfactory and has a good speed to power changes.

load sharing with the conventional droop method is performed in Fig. 20 to compare with the proposed controller operation. Weather variation is the same as Fig. 16. As depicted in Fig 20, load sharing performed very well but the dispatchable source share is increased compared to Fig. 16. Hence extracting power from RESs is decreased and RESs do not work at MPPT under any circumstances. As previously mentioned, the conventional droop method is not suitable for use with RESs.

In order to check the effectiveness of the proposed method, simultaneous change in load variation and weather change is applied. At t=15 s load decreased from 3400W to 3000W and sun radiation for PV1 decreased to 500 $\frac{W}{m^2}$ from 1000 $\frac{W}{m^2}$. Again at t=30 s load decreased to 2300W and wind speed from 10 $\frac{m}{s}$ reduced to 8$\frac{m}{s}$. Fig. 21 shows that even in the simultaneous change of load and weather, the proposed controller properly shares the MG load among sources and insists on supplying load from RESs by helping them to work in MPPT mode.

V. CONCLUSION

This study shows that the proposed controller is applicable in renewable inverter-based sources with the DC-link voltage. It helps RESs to select their control mode locally using the MG frequency. Thus, the communication link can be omitted or lower bandwidth communication with much less cost can be used instead. Any decrease in dependency on communication will increase the reliability of the system and reduce the noise influence on the operation of the controller.

Due to insist of the proposed method on consuming maximum reachable power of renewable source unless MG is in low load condition and cannot absorb the power, greenhouse gas emission reduces and penetration of renewable sources such as PV and WT in AC MG grows.

Simulation results show that the operating mode is identified very well with the help of local measurements and the response of RESs to the MG load changes is very fast. Usage of the proposed method with PV and WT confirms that the proposed method is capable of matching with different types of RESs and the maximum power point tracking method.

It is recommended to consider battery state of charge or DC link voltage level in power sharing during DCLVC mode for future work. RESs with a low level of DC link voltage can absorb power and act as a load during low load conditions and power curtailment can be reduced. It helps to use more renewable power. Load management can be investigated in future work when MG's available power is less than MG demand.

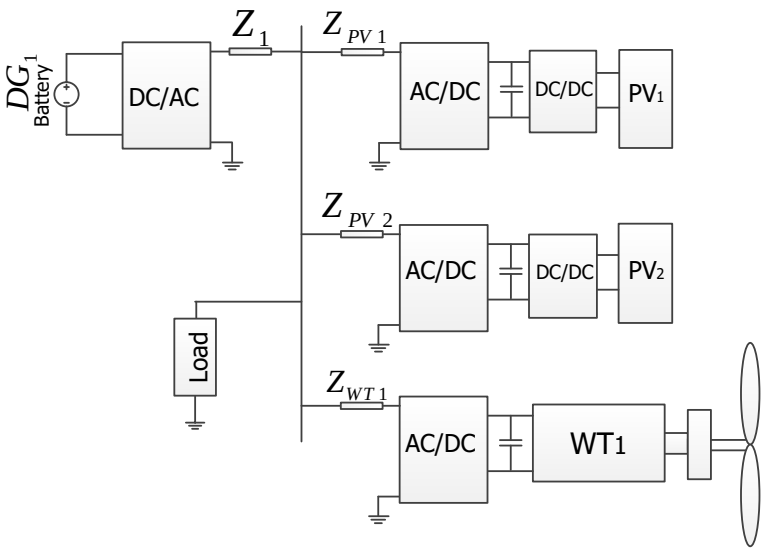

Fig. 12. A sample AC MG with three RESs and one dispatchable source used in simulations

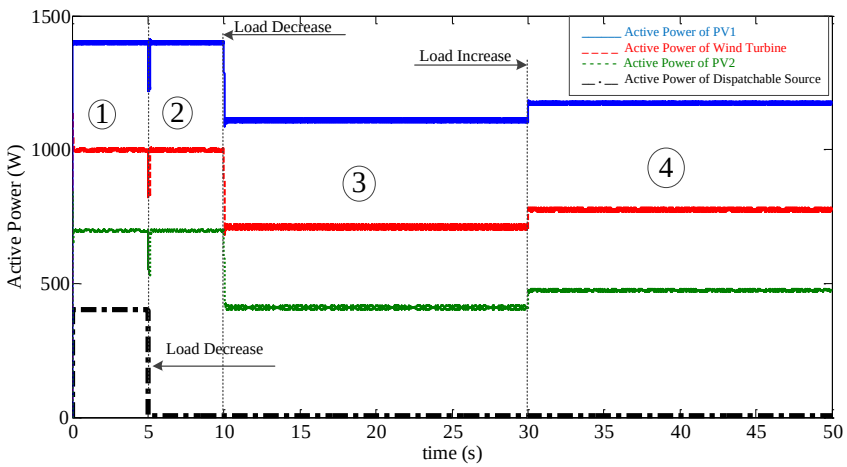

Fig 13. Active power variations according to load change

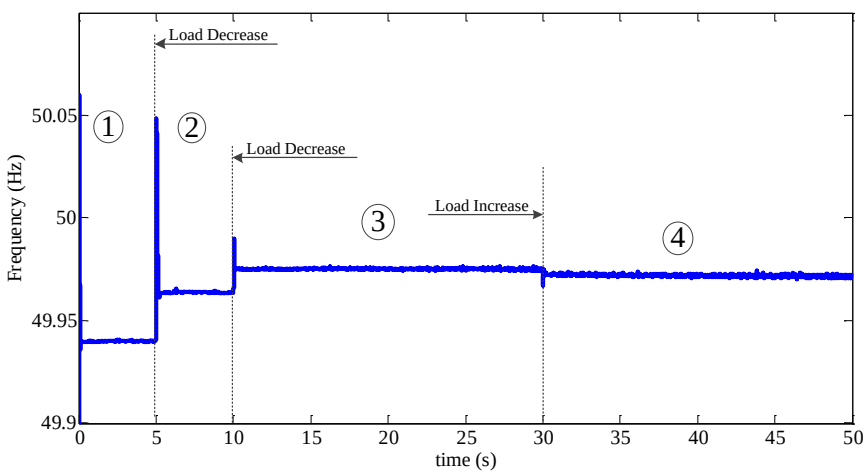

Fig. 14. Frequency variations according to load changes

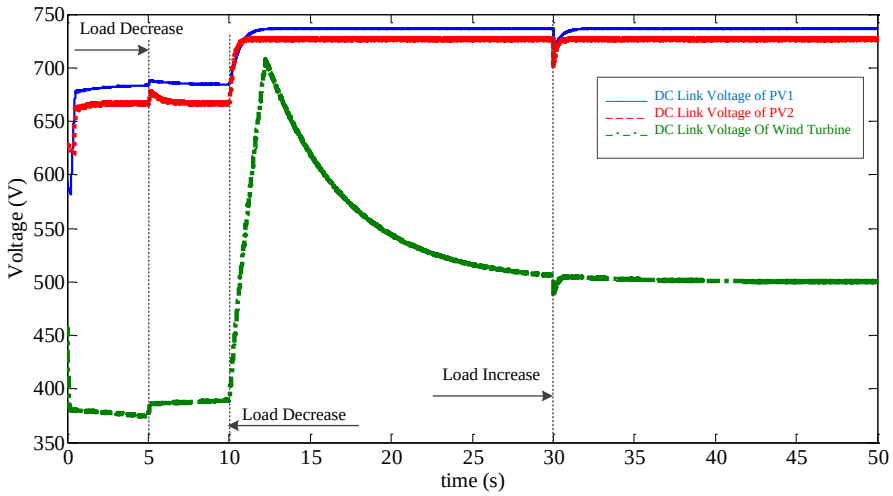

Fig. 15. DC-link voltage variations according to load changes

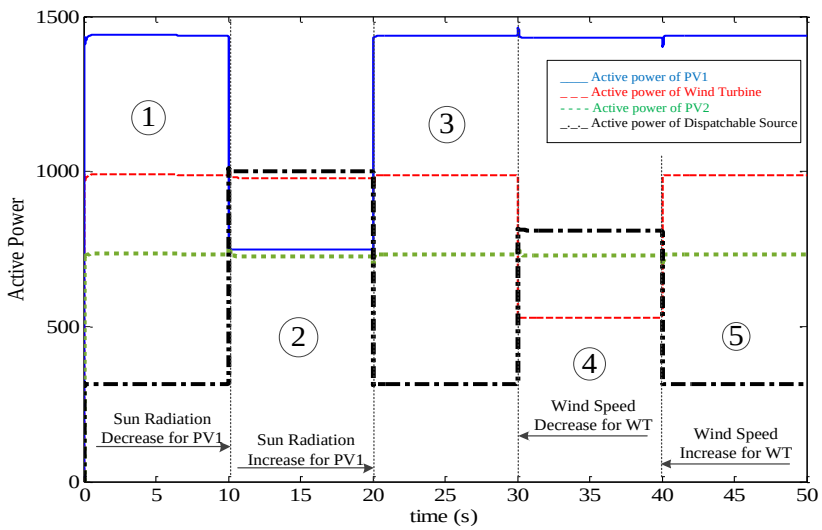

Fig 16. Active power variations according to weather changes

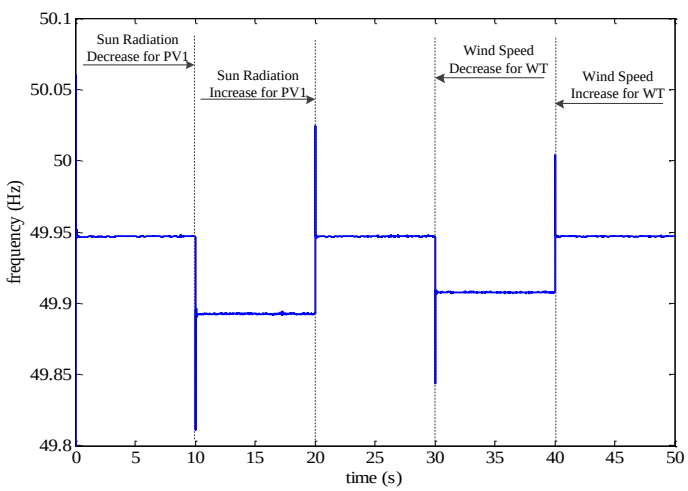

Fig. 17. Frequency variations according to weather changes

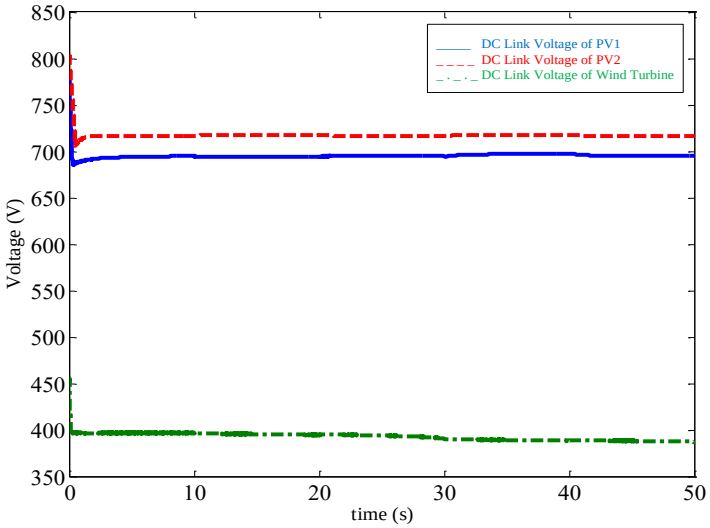

Fig. 18. DC-link voltage variations according to weather changes

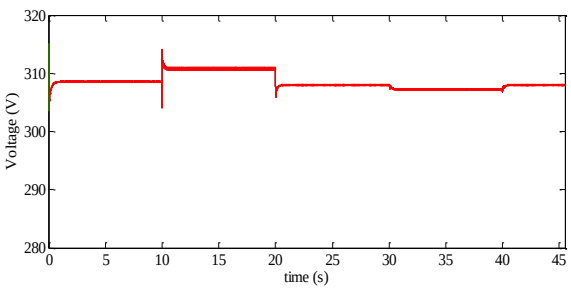

Fig. 19. MG voltage variations according to weather changes

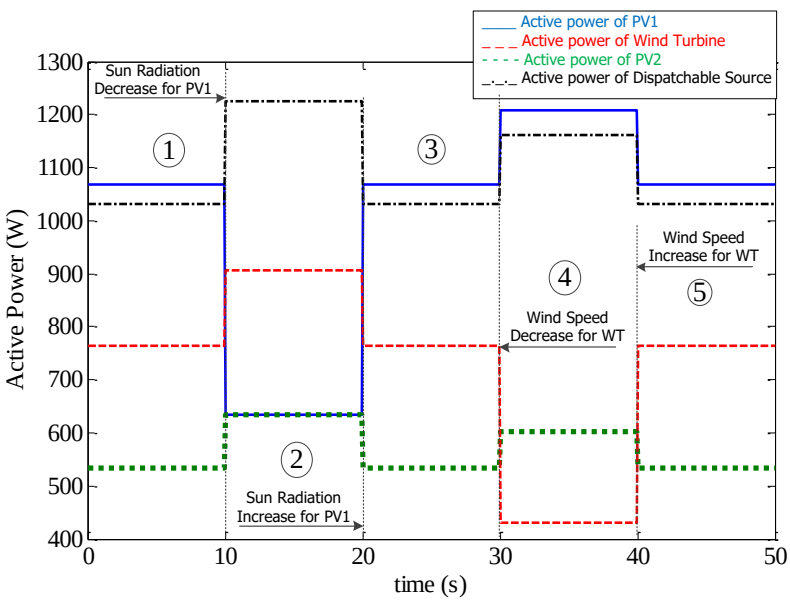

Fig 20. Active power variations according to weather changes with conventional droop controller

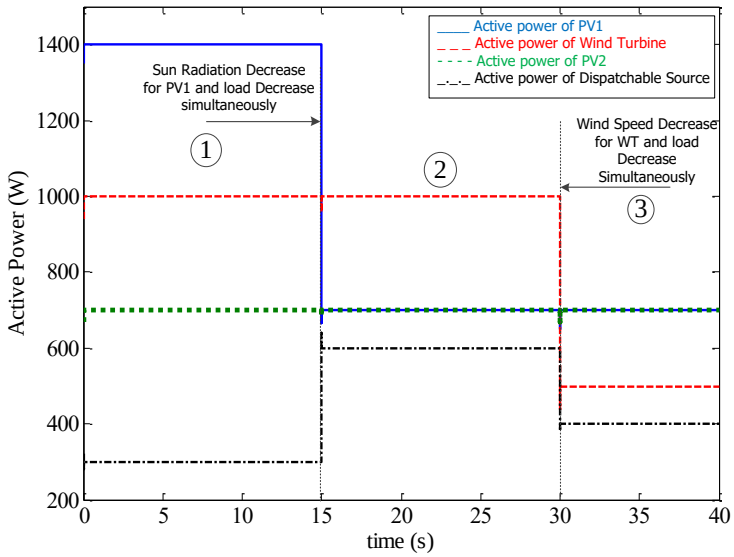

Fig 21. Active power variations according to weather changes and load change simultaneously with proposed droop controller

REFERENCES

[1] C. Bustos, D. Watts and H. Ren, "MicroGrid Operation and Design Optimization With Synthetic Wins and Solar Resources," *IEEE Latin AMERICA TRANSACTIONS*, vol. 10, no. 2, pp. 1550-1562, March 2012.

[2] M. Ahmadi kamarposhti, "Optimal Control of Islanded Micro grid Using Particle Swarm Optimization Algorithm," *International Journal of Industrial Electronics, Control and Optimization (IECO)*, vol. 1, no. 1, pp. 53-60, 2018.

[3] N. Duić and M. da Graça Carvalho, "Increasing renewable energy sources in island energy supply: case study Porto Santo," *RENEWABLE AND SUSTANABLE ENERGY REVIEWS*, vol. 8, no. 4, p. 383–399, August 2004.

[4] J. M. Guerrero, J. C. Vasquez, J. Matas, L. G. d. Vicuña and M. Castilla, "Hierarchical Control of Droop-Controlled AC and DC Microgrids—A General Approach Toward Standardization," *IEEE TRANSACTIONS ON INDUSTRIAL ELECTRONICS*, vol. 58, no. 1, pp. 158-172, JANUARY 2011.

[5] J. C. Vasquez, J. M. Guerrero, M. Savaghebi, J. Eloy-Garcia and R. Teodorescu, "Modeling, Analysis, and Design of Stationary-Reference-Frame Droop-Controlled Parallel Three-Phase Voltage Source Inverters," *IEEE TRANSACTIONS ON INDUSTRIAL ELECTRONICS*, vol. 60, no. 4, pp. 1271-1280, April 2013.

[6] U. Borup, F. Blaabjerg and P. N. Enjeti, "Sharing of Nonlinear Load in Parallel-Connected Three-Phase Converters," *IEEE TRANSACTIONS ON INDUSTRY APPLICATIONS*, vol. 37, no. 6, pp. 1817-1823, November/December 2001.

[7] J. M. Guerrero, L. Hang and J. Uceda, "Control of Distributed Uninterruptible Power Supply Systems," *IEEE TRANSACTIONS ON INDUSTRIAL ELECTRONICS*, vol. 55, no. 8, pp. 2845-2859, AUGUST 2008.

[8] M. R. Patel, Wind and Solar Power System, Second ed., Tylor @ Francis, 2021.

[9] T. Ackermann, Wind Power in Power Systems, 1st ed., Stockholm: John Wiley & Sons Ltd, 2004.

[10] Y. Yang, F. Blaabjerg and H. Wang, "Constant power generation of photovoltaic systems considering the distributed grid capacity," in *IEEE APPLIED POWER ELECTRONICS CONFERENCE AND EXPOSITION*, 2014.

[11] R. Noroozian, M. Abedi, G. Gharehpetian and S. Hosseini, "Combined operation of DC isolated distribution and PV systems for supplying unbalanced AC loads," *RENEWABLE ENERGY*, vol. 34, no. 3, p. 899–908, March 2009.

[12] X. Liu, P. Wang and P. C. Loh, "Optimal coordination control for stand-alone PV system with nonlinear load," in *IPEC 2010 Conference Proceedings*, Singapore, 2010.

[13] Y. Liu, X. Zhuang, Q. Zhang, M. Arslan and H. Guo, "A novel droop control method based on virtual frequency in DC microgrid," *INTERNATIONAL JOURNAL OF ELECTRICAL POWER & ENERGY SYSTEMS*, vol. 119, 2020.

[14] R. Babazadeh-Dizaji, M. Hamzeh and A. Hekmati, "A frequency-based economical-sharing strategy for low-voltage DC microgrids," *INTERNATIONAL JOURNAL OF ELECTRICAL POWER & ENERGY SYSTEMS*, vol. 118, 2020.

[15] N. Eghtedarpour and E. Farjah, "Control strategy for distributed integration of photovoltaic and energy storage systems in DC micro-grids," *RENEWABLE ENERGY*, vol. 45, pp. 96-110, September 2012.

[16] T. Dragicevi, J. M. Guerrero, J. C. Vasquez and D. Skrlec, "Supervisory Control of an Adaptive-Droop Regulated DC Microgrid With Battery Management Capability," *IEEE TRANSACTIONS ON POWER ELECTRONICS*, vol. 29, no. 2, pp. 695 - 706, FEBRUARY 2014.

[17] H. Cai, J. Xiang and W. Wei, "Decentralized Coordination

Control of Multiple Photovoltaic Sources for DC Bus Voltage Regulating and Power Sharing," *IEEE TRANSACTION ON INDUSTRIAL ELECTRONICS*, vol. 65, no. 7, pp. 5606-5610, 2018.

[18] R. Mastromauro, M. Liserre, A. Dell'Aquila, J. Guerrero and J. Vasquez, "Droop control of a multifunctional PV inverter," in *IEEE INTERNATIONAL SYMPOSIUM ON INDUSTRIAL ELECTRONICS (ISIE)*, Cambridge, 2008.

[19] C. Trujillo Rodriguez, D. Velasco de la Fuente, G. Garcera, E. Figueres and J. Guacaneme Moreno, "Reconfigurable Control Scheme for a PV Microinverter Working in Both Grid-Connected and Island Modes," *IEEE TRANSACTION ON INDUSTRIAL ELECTRONICS*, vol. 60, no. 4, pp. 1582-1595, April 2013.

[20] X. Wang, F. Blaabjerg and Z. Chen, "Autonomous control of inverter-interfaced Distributed Generation units for harmonic current filtering and resonance damping in an islanded microgrid," *IEEE TRANSACTIONS ON INDUSTRY APPLICATIONS*, vol. 50, no. 1, pp. 452-461, JANUARY/FEBRUARY 2014.

[21] T. L. Vandoorn, B. Renders, L. Degroote, B. Meersman and L. Vandevelde, "Active Load Control in Islanded Microgrids Based on the Grid Voltage," *IEEE TRANSACTION ON SMART GRID*, vol. 2, no. 1, pp. 139-151, March 2011.

[22] Y. W. Li and C.-N. Kao, "An Accurate Power Control Strategy for Power-Electronics-Interfaced Distributed Generation Units Operating in a Low-Voltage Multibus Microgrid," *IEEE TRANSACTIONS ON POWER ELECTRONICS*, vol. 24, no. 12, pp. 2977-2988, December 2009.

[23] H. Mahmood, D. Michaelson and J. Jiang, "Strategies for Independent Deployment and Autonomous Control of PV and Battery Units in Islanded Microgrids," *IEEE JOURNAL OF EMERGING AND SELECTED TOPICS IN POWER ELECTRONICS*, vol. 3, no. 3, pp. 742-755, 2015.

[24] S. Shajari and R. Keypour, "A novel seamless droop control method for load-sharing in photovoltaic-based AC microgrids," *JOURNAL OF RENEWABLE AND SUSTAINABLE ENERGY*, vol. 11, no. 1, pp. 1-12, 2019.

[25] Y. Karimi, H. Oraee, M. S. Golsorkhi and J. M. Guerrero, "Decentralized Method for Load Sharing and Power Management in a PV/Battery Hybrid Source Islanded Microgrid," *IEEE TRANSACTIONS ON POWER ELECTRONICS*, vol. 32, no. 5, pp. 3525-3535, 2017.

[26] Y. Karimi, H. Oraee and J. M. Guerrero, "Decentralized Method for Load Sharing and Power Management in a Hybrid Single/Three-Phase-Islanded Microgrid Consisting of Hybrid Source PV/Battery Units," *IEEE TRANSACTIONS ON POWER ELECTRONICS*, vol. 32, no. 8, pp. 6135-6144, 2017.

[27] J. M. Guerrero, J. C. Vásquez, J. Matas, M. Castilla and L. G. D. Vicuña, "Control Strategy for Flexible Microgrid Based on Parallel Line-Interactive UPS Systems," *IEEE TRANSACTION ON INDUSTRIAL ELECTRONICS*, vol. 56, no. 3, pp. 726-736, March 2009.

[28] R. Sedaghati and M. R. Shakarami, "A New Sliding Mode-based Power Sharing Control Method for Multiple Energy Sources in the Microgrid under Different Conditions," *International Journal of Industrial Electronics, Control and Optimization (IECO)*, vol. 2, no. 1, pp. 25-38, 2019.

[29] G. M. Azevedo, M. C. Cavalcanti, F. A. Neves, P. Rodriguez and J. Rocabert, "Performance improvement of the droop control for single-phase inverters," in *IEEE INTERNATIONAL SYMPOSIUM ON INDUSTRIAL ELECTRONICS (ISIE)*, 2011.

[30] Q. Shafiee, J. M. Guerrero and J. C. Vasquez, "Distributed Secondary Control for Islanded MicroGrids - A Novel Approach," *IEEE TRANSACTIONS ON POWER ELECTRONIC*, vol. 29, no. 2, pp. 1018-1031, Februry 2014.

[31] A. Bidram and A. Davoudi, "Hierarchical Structure of Microgrids Control System," *IEEE TRANSACTIONS ON SMART GRID*, vol. 3, no. 4, pp. 1963-1976, DECEMBER 2012.

[32] J. Farzaneh and A. Karsaz, "Application of Improved Salp Swarm Algorithm Based on MPPT for PV Systems under Partial Shading Conditions," *International Journal of Industrial Electronics, Control and Optimization (IECO)*, vol. 3, no. 4, pp. 407-414, 2020.

[33] M. Sedaghat, A. Siadatan and B. Taheri, "Photovoltaic system with sliding mode control for work on for maximum power point," *Computational Intelligence in Electrical Engineering*, vol. 9, no. 3, pp. 76-90, 2018.

[34] C. K. Sao and W. Lehn, "Autonomous load sharing of voltage source converters," *IEEE TRANSACTION ON POWER DELIVERY*, vol. 20, p. 1009–1016, April 2005.

[35] J. Farzaneh, R. Keypour and A. Karsaz, "A novel fast maximum power point tracking for a PV system using hybrid PSO-ANFIS algorithm under partial shading conditions," *International Journal of Industrial Electronics, Control and Optimization (IECO)*, vol. 2, no. 1, pp. 47-58, winter 2019.

Sadegh Shajari was born in Mazandaran, Iran, in 1986. He received the B.S. and M.S degrees from the Faculty of Electrical Engineering, K. N. Toosi University of Technology both in Electrical Power System Engineering, Tehran, Iran, in 2008 and 2010 respectively. His main fields of interest were power system and Renewable Energy. He is now perusing the Ph.D. degree in the department of Electrical Engineering at Semnan University of Technology. His main research interests include hierarchical control, networked control systems, power quality and renewable energy in MicroGrids.

Reza Keypour received his B.Sc. degree in electrical engineering from Shahid Beheshti University in 1997 and M.Sc. and Ph.D degrees from Tarbiat modares University, Tehran, Iran in 2000 and 2006, respectively. He is currently an Associate Professor with the Faculty of Electrical and Computer Engineering, Semnan University, Semnan, Iran. His research interests include power system operation and planning, microgrids and renewable energy.

IECO

This page intentionally left blank.

International Journal of Industrial Electronics, Control and Optimization IECO
Vol. 5, No. 2, pp.167-176, April (2022)

An Electrical Energy Regeneration Scheme for Energy Harvesting From a Vibration Absorption System in Tall Buildings

Mohammad A. Beladi Pour[1], Amir H. Abolmasoumi[2†], Mehdi Soleymani[3] , Mazdak Ebadi[4]

[1] Department of Mechatronics, Arak University, Arak, Iran,
[2,4] 1. Electrical Engineering Department, Arak University, Arak, Iran, Research Institute of Renewable Energy, Arak University, Arak, Iran,
[3] Department of Mechanical Engineering, Arak University, Arak, Iran,

ABSTRACT

Electrical energy regeneration and storage in a tall structure with the installed passive pendulum tuned mass and damper (PPTMD) is investigated. While the passive vibration absorbing system works as an energy harvesting device, an electrical system including an electric motor, power electronic converters, a battery charger and storage subsystem are designed in order to store the energy taken from the structure vibrations which may be resulted from various external disturbances such as wind or earthquakes. The whole 76-story structure and the relevant electrical energy regeneration system are modeled and simulated and the design scheme is implemented on a two-story reduced order lab structure equipped with PPTMD, the electronic circuit and the battery. A boost AC rectifier is designed and controlled to rectify the AC output voltage and is followed by a boost DC-DC converter as a battery charger for the Li-ion battery. A passivity-based controller (PC) and a sliding mode controller are designed for the rectifier and the battery charger, respectively. The simulation and the real test results demonstrate the efficient harvesting and storage of the energy extracted from the building.

Article Info

Research Article

Keywords:

Boost AC rectifier, Boost DC-DC converter, Energy regeneration Passivity-based control, Passive tuned mass damper Sliding mode control.

Article History:

Received 2022-01-31
Accepted 2020-05-20

I. INTRODUCTION

Recent architecture of buildings in modern cities of high population has moved towards tall structures with some movement flexibility [1,2] where the external disturnbance loads such as wind and seismic forces are potential treats to the stability of such structures. The emerging of structural control systems is a response to the urgent need of building stabilization [3,4]. There are several types of such systems reported in the literature such as passive-type [3,5] , the semi-active-type [6,7] and active-type solutions [8-12]. As the most commonly used and easy to implement solutions, passive-type systems include the simple methods such as the base isolation solution [13] and viscoelastic dampers solutions [14], or different kinds of the the vibration absorbing systems such as tuned mass dampers (TMDs) [15], tuned liquid column dampers (TLCDs) [16], and pendulum-based TMDs (PTMDs) [17,18], etc. All mentioned types of passive vibration absorber systems have as their objective the damping of the structural vibrations resulted from the external disturbances.

The passive-type vibration absorbing systems used for the structural control consume less amount of energy as compared to other systems such as the semi-active and active ones since they need no source of power for their operation. However, the

†Corresponding Author: a-abolmasoumi@araku.ac.ir
Tel: +98-32625620,
1. Electrical Engineering Department, Arak University, Arak, Iran,
2. Research Institute of Renewable Energy, Arak University, Arak, , Iran

energy of the vibration that is absorbed by the passive-type device, for example an installed pendulum, is completely dissipated. To harvest such otherwise-wasted energy from the building vibrations an energy conversion unit together with an especial design is needed. The recovered energy can be later utilized as the common utility electric power or be stored in the building emergency power storage system. Extracting of energy from vibrating systems has been previously studied in [19-22]. There are few studies regarding the energy regeneration in the passive structural systems. For example, in [23] the extraction of energy from through-building openings openings is investigated. Authors in [24] sduggest the extraction of the energy from the engineered cementitious composites by using the polyvinylidene fluoride piezo polymer. In [25] energy harvesting from a TMD system is studied. Also in [26] authors design a pendulum-based energy regenerating systems to provide the energy for the wireless sensor network installed in the structure when under seismic forces.

As the power generated by pendulum-based compensators is of oscillatory nature, to store such power there is a need to convert the power to a DC output with minimum fluctuations. In this paper, an scheme for restoring the power from the pendulum actuator is proposed and the electronic processing and control of such power to be finally stored in the battery system. To this aim a DC generator followed by an AC rectifier system is utilized in order to simultaneously rectify and convert the semi-AC voltage into amplified DC voltage prior to being boosted through the DC-DC converter. The AC rectifier unit includes a passivity-based PWM control (PC) which adjusts the output DC voltage. Afterwards, a boost DC-DC converter is responsible to enhance and tune the voltage and also acts as the battery charger system to adjust the fixed charging current according to the charging plan of the Li-ion battery. A sliding mode controller has been designed using the augmented nonlinear dynamic model of the battery to fix the battery charging current. There several application of sliding mode controllers on DC-DC converters (See for example [27-28] and the references therein). Here, a simple sliding mode controllers is designed based on the augmented dynamic model of the battery/converter to adjust the battery charging current.

The whole two-story structure and energy regeneration generator has been experimentally constructed and installed over a shake table. To have a better visibility of results the electronic processing and storage system including converters and batteries are simulated in Matlab Simulink and linked to the hardware to form a harware-in-loop test setup. The results show the effective implementation of the proposed scheme in regenerating the power from the PTMD actuator.

The novelty of this paper is threefold: (1) this paper presents a complete scheme for energy regeneration from PPTMD. The plan is a multi-stage energy regeneration scheme that has not been previously proposed. (2) A passivity-based control design for the AC rectifier system has been designed (3) a sliding mode controller has been designed for the boost DC-DC

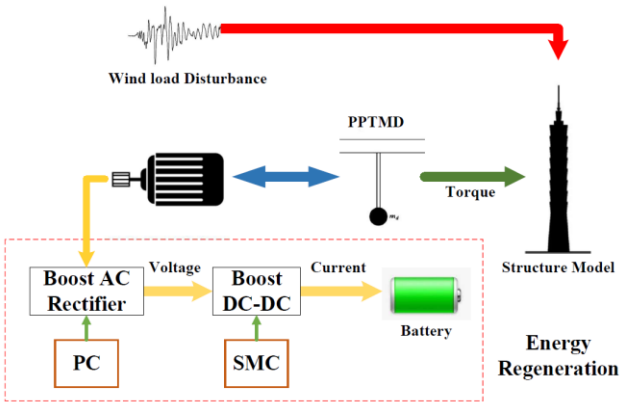

Fig. 1. The overall plan of energy regeneration from passively damped structure including PPTMD.

battery charger using the unified model of the converter/battery.

The rest of the paper is organized as follows: Section II firstly gives the basics on energy regeneration from a passively damped structure and then each component of the energy regeneration system is introduced in detail. The designed dynamic controllers are also discussed. Section IV represents the simulation and test results regarding the implementation of the regeneration system. Finallly, section V concludes the paper.

II. Energy Regeneration Scheme

The vibrations from different external forces such as wind and earthquake are devastating factors considered in the design and operation of tall buildings. Tuned mass-damper (TMD) systems are common devices which are employed to absorb the kinetic energy of the structure vibrations. In this study, a structure with an installed passive-pendulum-type TMD (PPTMD) is considered. The pendulum is usually installed on the upper floors where the most intense movements occur [17, 18]. In our energy regeneration scheme, an electric motor is coupled along the pendulum joint to transform the mechanical energy of the pendulum swings to the electrical energy. The outcome electric voltage is then rectified and converted to DC voltage. The electrical energy is finally stored in a Li-ion battery via a charger circuit. The described structure including the PPTMD, the electric motor and the power electronic circuit is shown in Figure 1.

The dynamic equations of the structure movements are described as ([29])

$$\mathbf{M}\ddot{\boldsymbol{x}}+\mathbf{C}\dot{\boldsymbol{x}}+\mathbf{K}\boldsymbol{x}=\left(-\mathbf{M}\{\mathbf{r}\}\{\ddot{u}_g\}\boldsymbol{or}\{\mathbf{E}\}\{f_w(t)\}\right) \quad (1)$$

in which $\boldsymbol{x}$ is the vector of the displacements. The centered masses of floors are represented as the following diagonal

matrix

$$\mathbf{M} = \begin{pmatrix} m_1 & \dots & 0 \\ \vdots & \ddots & \vdots \\ 0 & \dots & m_n \end{pmatrix} \quad (2)$$

and the stiffness matrix **K** is represented as

$$\mathbf{K} = \begin{pmatrix} k_1 + k_2 & 0 & 0 & \dots & 0 \\ -k_2 & \ddots & 0 & 0 & \vdots \\ \vdots & 0 & k_{ij} & 0 & 0 \\ 0 & 0 & 0 & \ddots & -k_n \\ 0 & \dots & 0 & 0 & k_n \end{pmatrix} \quad (3)$$

where k_i is the stiffness of the *i*-th floor. The damping matrix *C* in (1) is described as

$$\mathbf{C} = a_0\mathbf{M} + a_1 \quad (4)$$

where a_0 and a_1 are calculated in terms of stiffness of floors and the natural frequencies of the structure as

$$a_0 = \frac{2\xi w_1 w_3}{w_1 + w_3},\ a_1 = \frac{2\xi}{w_1 + w_3}$$

where w_1, w_2, w_3 are first three structural modes [29]. In (1), $\ddot{u}_g$ is the external disturbance acceleration and **r (**or **E)** is the disturbance excitation coefficient matrix and $f_w(t)$ is the wind force. The dynamic equation describing the pendulum swing is expressed as

$$\ddot{\theta} = -\left(\frac{g}{L_p}\right)\sin\theta - \frac{\ddot{x}_h}{ML_p^2} + \left(\frac{1}{ML_p^2}\right)T \quad (5)$$

where x_h is the top story displacement, g represents the gravity acceleration, L_p is the pendulum arm length, T is the outcome torque and θ is the swing angle. In case the pendulum axis is coupled with a generator shaft, the mechanical torque T contributes to the electrical energy production by the pendulum system which should be later processed to be stored in the battery. The length and mass of the pendulum is determined according to the natural frequency of the structure and its first modal mass [30]. Such energy is not currently harvested in the passively damped structures. In order to harvest and store such energy a generator system together with power electronic devices are employed. The complete diagram of energy regeneration has been depicted in Figure 1. As seen, the pendulum joint is coupled with a DC generator to transform the output mechanical power into an almost-AC electric power. The output voltage of the generator is rectified and regulated using an AC rectifier. The result is a DC voltage of desired magnitude. The output is then applied to a DC-DC boost converter that acts as a current charge controller for the battery. The resulting power is restored in Li-ion battery. In the following, different parts of the energy regeneration system together with the relevant control strategies are explained.

TABLE I
SPECIFICATIONS OF THE DC GENERATOR

Parameter	Unit	Simulated 76-story building	Two-story structure
Maximum Power	W	4500	12
Nominal Voltage	V	400	12
Nominal Current	Amp	10	1
Electric inductance (L)	μH	100.5	10
Electric resistance (Ra)	Ohm	3.5	1.1
Friction coefficient (B)	N.m.s	0.002	0.001
Moment of inertia (J)	Kg/m^2	0.001	0.01
Torque constant (K)	N.m/Amp	1.8	0.2

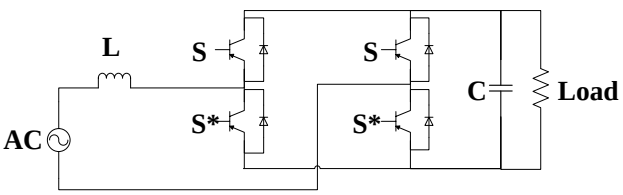

Fig. 2. Structure of the AC rectifier.

A. Electric DC Generator

The electric DC generator is coupled with the pendulum installed on the upper floor of the structure. The motor include a gearbox system to adjust the rotational speed and torque and is connected to the pendulum joint on the structure. The DC generator is of the permanent-magnet type. The specifications of the used DC electric motor for a 76-story and the one used for the reduced-order two-story lab structure in this study, are given in Table I.

B. AC Rectifier

The output voltage of the DC generator is almost AC while including contaminations of higher frequencies. It means that the voltage is of alternative nature as a result of the swing movements of the pendulum; however, it may include harmonics of different orders. In order to store the electric voltage extracted from the structural movements it is necessary to convert it into the DC voltage. Moreover, the magnitude of such voltage is usually low. It is because the output voltage depends on the rotational speed/frequency of the swing and such rotational speed is usually low. Such voltage will then undergo some processing by the power electronic circuits to be finally stored in the batteries. As each circuit causes some voltage loss, it is essential for the voltage magnitudes to be high enough before applying to the battery charger. Employing a gearbox system can slightly improve the voltage magnitude, however, it is still needed to provide a higher voltage. To obtain the regulated DC voltage from the input AC-like

voltage, using the conventional bridge rectifiers is not recommended. Instead, a boost AC rectifier can be used here that converts the voltage into DC and amplifies the magnitude at the same time. Boost rectifier or boost AC rectifier is a well-known interface circuit in power electronics. In some references it is also called the power factor correction (PFC) boost rectifier. Such circuit increases the power factor and reduces harmonic currents. As a result, the circuit is usually used for improving the power quality of power supplies. For general description on these circuits please refer to [31-34]. Here, the boost AC-DC circuit is used to convert the DC voltage to AC voltage and, in the same time amplify the magnitude of voltage. The circuit diagram of the used AC rectifier is depicted in Figure 2. The circuit includes four switches, a capacitor, and an inductor connected to the resistance load.

The dynamic equations of the single phase boost AC rectifier is given as follows ([35]):

$$\begin{aligned} L\frac{di}{dt} &= -uV + \bar{V}_{AC}, \\ C\frac{dV}{dt} &= ui - \frac{1}{R}V, \end{aligned} \tag{6}$$

where $\bar{V}_{AC} = E\sin(\omega_0\tau)$, is the ideal input AC voltage, i is the input current, V is the output DC voltage, u is the average duty-cycle of the PWM input applied to the switch gates, L is the inductance, R is the resistance, C is the capacitance and E is the AC voltage magnitude. Using the time-scale change $\tau = t/\sqrt{LC}$ defining the quality factor $Q = R\sqrt{C/L}$, and the normalized states $x_1 = (i/E)\sqrt{L/C}$, $x_2 = V/E$, the average state-space equations of the boost AC rectifier could be rewritten as follows:

$$\begin{cases} \dot{x}_1 = -ux_2 + V_{AC}, \\ \dot{x}_2 = ux_1 - \dfrac{x_2}{Q}, \end{cases} \tag{7}$$

where $V_{AC} = \sin(\omega_0\tau)$ could be the ideal normalized input. Here a passivity-based controller is designed to adjust the level of the output voltage. It is assumed that the desired state trajectory $x^*(\tau)$ also satisfies

$$\begin{aligned} \dot{x}_1^* &= -u^* x_1^* + V_{AC}, \\ \dot{x}_2^* &= u^* x_1^* - \frac{x_2^*}{Q}, \end{aligned} \tag{8}$$

By defining the state tracking error $e = x(\tau) - x^*(\tau)$ it can be easily shown that the error dynamics are obtained as

$$\begin{aligned} \dot{e}_1 &= -ue_2 - x_2^* e_u, \\ \dot{e}_2 &= ue_1 - \frac{e_2}{Q} + x_1^* e_u, \end{aligned} \tag{9}$$

where $e_u = u - u^*$. Now suppose that the control is designed such that $e_u = -\gamma\left(-x_2^* e_1 + x_1^* e_2\right)$ for some positive γ. Replacing to (9) results in

$$\begin{aligned} \dot{e}_1 &= -ue_2 + \gamma x_2^*\left(-x_2^* e_1 + x_1^* e_2\right), \\ \dot{e}_2 &= ue_1 - \frac{e_2}{Q} - \gamma x_1^*\left(-x_2^* e_1 + x_1^* e_2\right), \end{aligned} \tag{10}$$

Defining the error energy as $V = 0.5(e_1^2 + e_2^2)$ leads to

$$\begin{aligned} \dot{V} &= e_1\left[-ue_2 - \gamma(x_2^*)^2 e_1 + \gamma x_1^* x_2^* e_2\right] \\ &\quad + e_2\left[ue_1 - \frac{e_2}{Q} + \gamma x_1^* x_2^* e_1 - \gamma(x_1^*)^2 e_2\right] \\ &= -\gamma(x_2^*)^2 e_1^2 + 2\gamma x_1^* x_2^* e_1 e_2 - \gamma(x_1^*)^2 e_2^2 - \frac{e_2^2}{Q}. \end{aligned} \tag{11}$$

In order to have negative value for the Lyapunov time derivative the following inequality, referred to as dissipation matching condition, should hold:

$$\begin{bmatrix} \gamma(x_2^*)^2 & \gamma x_1^* x_2^* \\ \gamma x_1^* x_2^* & -\dfrac{1}{Q} - \gamma(x_1^*)^2 \end{bmatrix} > 0 \tag{12}$$

The controller is then calculated as

$$\begin{aligned} u &= u^* + \gamma\left[x_2^*\left(x_1 - x_1^*\right) - x_1^*\left(x_2 - x_2^*\right)\right] \\ &= u^* + \gamma\left(x_2^* x_1 - x_1^* x_2\right) \end{aligned} \tag{13}$$

It is needed to choose the desired state trajectory values x_1^* and x_2^* in calculation of control. If the total average energy of the system is $E = 0.5(x_1^2 + x_2^2)$ then the power is given by

$$\frac{dE}{dt} = x_1 V_{AC} - \frac{x_2^2}{Q}, \tag{14}$$

in which the first term is the input power and the second is the delivered power. In the balance condition the dc values of two terms are equal that gives

$$\left\langle \bar{x}_1 V_{AC} \right\rangle_{dc} = \left\langle \frac{\bar{x}_2^2}{Q} \right\rangle_{dc}. \tag{15}$$

The desired state trajectory values can be selected by considering (15). In an ideal case, the normalized output voltage x_2 converge to the steady state dc value V_d and the normalized AC current have the steady state $\bar{x}_1 = A\sin(\omega_0\tau)$. Setting also $V_{AC} = \sin(\omega_0\tau)$ we have

$$A = \frac{2V_d^2}{Q}, \tag{16}$$

Therefore, the steady state values $x_2^* = V_d$, $x_1^* = A\sin(\omega_0\tau)$ are appropriate choices. In (13) it is also needed to calculate u^* that can be obtained from (8) as

$$u^* = \frac{V_{AC} - \dot{x}_1^*}{x_2^*} \tag{17}$$

which in case of ideal AC input becomes

$$u^* = \frac{\sin(\omega_0\tau) - A\omega_0\cos(\omega_0\tau)}{V_d}. \quad (18)$$

Thus, as a summary, the PC can be designed as

$$u = u^*(\tau) + \gamma\left[x_2^* x_1 - x_1^* x_2\right],$$
$$u^* = \frac{\sin(\omega_0\tau) - A\omega_0\cos(\omega_0\tau)}{x_2^*}, \quad (19)$$
$$x_1^* = A\sin(\omega_0\tau),\ x_2^* = V_d,\ A = 2V_d^2/Q.$$

where V_d is the desired DC voltage ratio and γ is a positive design parameter to adjust the speed and damping of the transient response.

C. Battery Charging Circuit

The boost AC rectifier provides the regulated DC voltage with the desired magnitude. Such voltage level is determined by the battery specifications. However, the rectifier is not able to control the input current for charging the battery. Consequently, a charge controller circuit is needed to control the charging current. To this aim, a boost DC-DC converter is suggested as the battery charger. The application of DC-DC converter as the battery charger is studied by several researchers (see for example [36, 37] and the references therein). The circuit diagram of the boost DC-DC converter is shown in Figure 3. The output current of the boost DC-DC converter should be controlled for the goal of ensuring the efficient battery charge-time and its long-time health. The dynamic state-space equations of the boost DC-DC converter is described as follows:

$$L\frac{di}{dt} = -(1-u)V + V_{in},$$
$$C\frac{dV}{dt} = (1-u)i - i_{bat},$$
$$\frac{dSOC}{dt} = i_{bat},$$
$$i_{bat} = \frac{V - E_{oc}}{R_0}, E_{oc} \approx \alpha SOC + \beta, \quad (20)$$

where i is the input current, V is the output DC voltage, i_{bat} is the battery input current, $u \in [0,1]$ is the on-off input applied to the switch gate, SOC is the state of charge of the battery, E_{oc} is the open-circuit voltage of the battery, L is the inductance, R_0 is the battery internal resistance, and V_{in} is the input voltage. Also, parameters α, β are describing the dependency of the open-circuit voltage of the battery on its charging level. Here, this relationship is approximately assumed to be linear.

To regulate the charging current a sliding mode controller is designed using the unified dynamic model of the boost DC-DC and the battery. The sliding surface is defined as $S = i_{bat} - \bar{i}_{bat}$ in which $\bar{i}_{bat}$ is the desired charging current. The equivalent control u_{eq} is obtained by setting $\dot{S} = 0$. According to (20), this results in

TABLE II
SPECIFICATIONS OF THE BATTERY AND ELECTRONIC CIRCUITS

Device	Parameter	76-story structure	Two-story structure
Battery Cell	Rated capacity (Ah)	4500	0.018
	Internal resistance (Ohm)	400	1.777
	Nominal voltage (V)	10	3.2
AC Rectifier	Inductance (mH)	2	0.5
	Capacitance (μF)	1000	10
Boost DC-DC	Inductance (mH)	1	0.1
	Capacitance (μF)	4700	1000

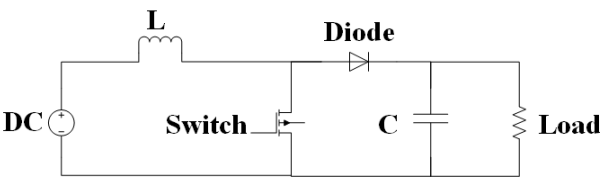

Fig. 3. Structure of the battery charging system.

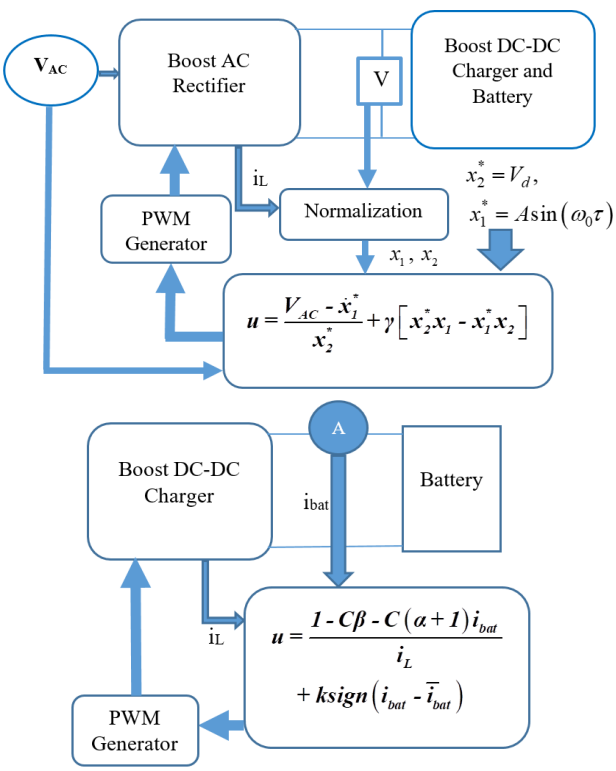

Fig. 4. A block diagram of control system.

$$u_{eq} = \frac{1 - C\beta - C(\alpha+1)i_{bat}}{i}. \quad (21)$$

The whole sliding mode control is then expressed as

$$u = u_{eq} + ksign(S) \quad (22)$$

The sliding gain k can be then chosen large enough to guarantee the stability of the sliding surface.

The specification of the required battery, and the component values of the boost AC rectifier and the boost DC-DC converter is given in Table II. The size of the battery-pack is determined using a serial-parallel cell arrangement. The implementation of the control methods are also shown in Figure 4.

III. Simulations and Test Results

To evaluate the implementation of the proposed energy regeneration scheme, the overall plan is simulated on two-story and 76-story buildings. Moreover, laboratory test results are taken from a two-story experimental lab structure that is constructed based on the reduced model of an eleven-story building. Since the level of the generated voltage at the terminal of the DC generator installed on the laboratory structure is too low to be processed in actual electronic circuits, a hardware-in-loop test system was used to interface the laboratory structure, the pendulum and the corresponding coupled generator with the LabVIEW software in the PC where the electronic circuits are simulated.

A. Simulation Results

A two-story and a 76-story building with the regeneration system are simulated. It should be noted that the first goal of PPTMD system is to reduce the oscillations of the structure under the effect of the external disturbances such as earthquake or wind. Thus, firstly the performance of the passive pendulum in the structure stabilization is demonstrated.

For the two-story building only the earthquake force is considered to be effective while for the 76-story building the wind effect has been simulated. For the simulated two-story building the parameters are as follows:

$$M=\begin{pmatrix}3.7769 & 0\\ 0 & 3.2372\end{pmatrix}, K=\begin{pmatrix}511.4320 & -322.1163\\ -322.1163 & 322.1163\end{pmatrix},$$

$$C=\begin{pmatrix}3.3703 & -1.3951\\ -1.3951 & 2.3853\end{pmatrix} \quad (23)$$

A pendulum with the length equal to 60 cm and the mass equal to 500g is used. To induce the structural movements, the data from *El Centro* earthquake has been utilized [38] whose acceleration profile is given in Figure 5. Also Figure 6 shows the time variations of the upper floor's displacement and velocity for the passively-damped structure compared to the undamped one. As seen, the passive pendulum system leads to a decrease in the structural movements. The effect of wind has been studied on a 76-story building. The wind force is calculated as

$$F=\frac{1}{2}\rho A_z^2 C_d V_{z,t}^2 \quad (24)$$

where $V_{z,t}$ is the wind speed, C_d is the aerodynamic drag coefficient, A_z is the effective area and ρ is the air density.

For 76-sotry building, a PPTMD system with the mass of 1000kg and the length of 2.5m is considered that is installed

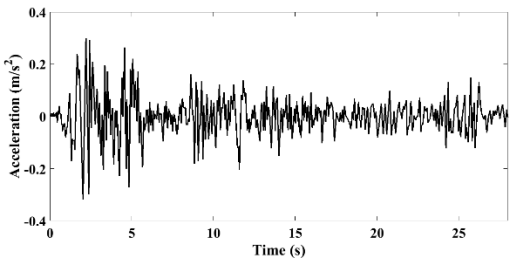

Fig. 5. El Centro earthquake acceleration profile used as the structure disturbance force [38].

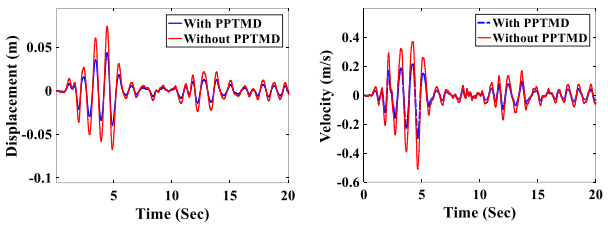

(a) (b)

Fig. 6. Upper floor's movements for the simulated two-story building (a) displacement (b) velocity.

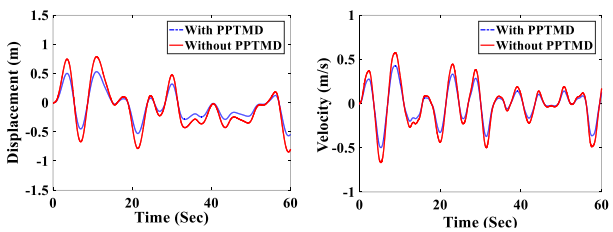

(a) (b)

Fig. 7. Top floor's movements for the simulated 76-story building (a) displacement (b) velocity.

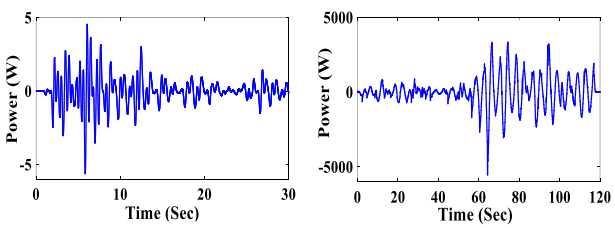

(a) (b)

Fig. 8. The active power damped by the PPTMD without energy regeneration for (a) simulated two-story building under earthquake (b) 76-story building under wind force.

on the upper floor. Figure 7 shows the top floor's displacement and velocity with and without PPTMD system which clearly shows the superiority of the PPTMD system in stabilizing the structural movements. The active powers damped by the PPTMD for both simulated structures are depicted in Figure 8. Such power may be utilized by conversion into the electrical power, processing and finally storing in the batteries. For the

76-story, however, the actual wind calculations are used.

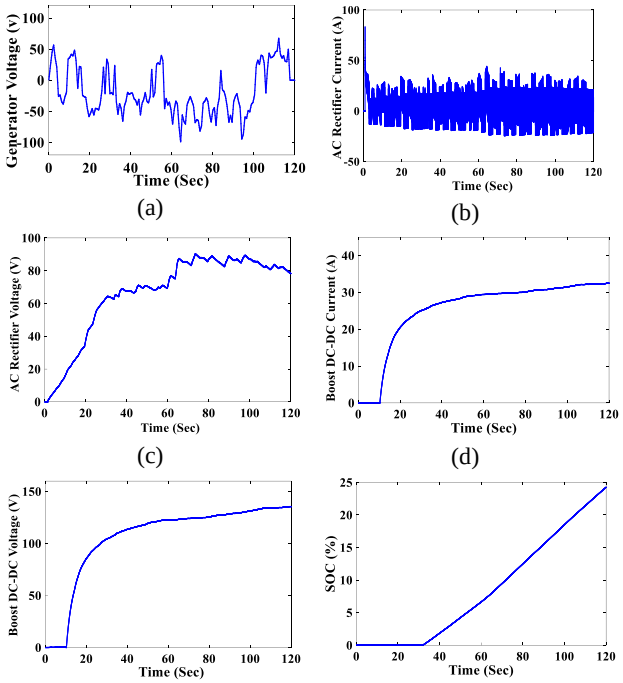

Fig. 9. Electrical signals at different stages of the power processing for the simulated 76-story building: (a) output voltage of the pendulum-coupled generator (b) input current of boost AC rectifier (c) output voltage of boost AC rectifier (d) input current to boost DC-DC converter (battery charger) (e) battery charger voltage (f) state of charge of the battery.

The electric voltages and currents at different stages of the power processing are shown in Figure 9 that demonstrates the satisfactory performance of the proposed plan. Figure 9(a) represents the voltage produced by the generator as a result of the movements of the pendulum installed on a 76-story building. In this case the pendulum absorbs the movements of the structure by the wind. The current of the boost AC rectifier is shown in Figure 9(b). The reasons for high frequency of the current is the assumption that in PC the input voltage is ideally sinusoidal signal with fixed frequency while it is not true for the case of 76-story building. PC makes use of the derivative of the voltage that may results in high frequency control input and the possible high frequency current. The effect of the SMC control on the DC-DC charger may also induce high frequencies on the boost AC rectifier.

Figure 9(c) shows the almost DC voltage as the output of the boost AC rectifier. The non-smooth DC voltage is again due to the non-sinusoidal voltage of the generator. However, this is fixed by the boost DC-DC charger as the current and voltage are almost DC (Figures 9(c) and 9(d)) and the state-of-charge is increasing with time with fixed current (Figure 9(f)).

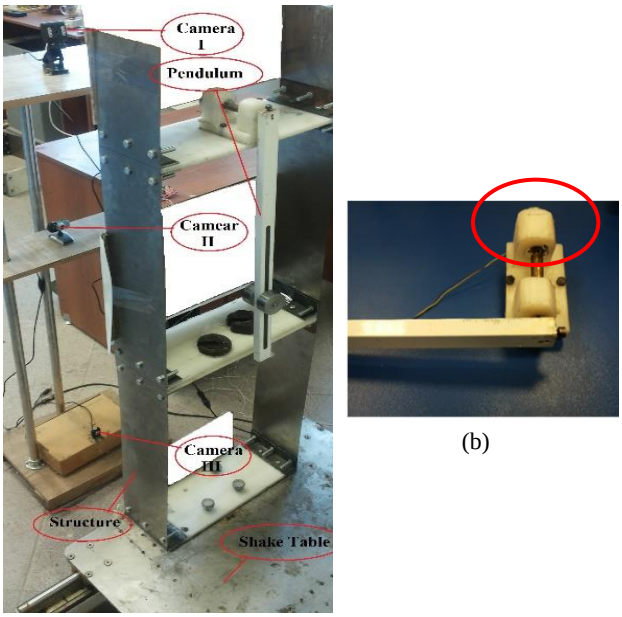

Fig. 10. The laboratory setup of the regenerative PPTMD: (a) The whole structure (b) the pendulum and the coupled generator.

B. Experimental Results

In addition to simulation of the proposed plan by using the modeling principles, the proposed energy regeneration scheme is implemented on a laboratory structure. The two-story structure, i.e. the reduced model of an 11-story building by mimicking its major natural frequencies, is installed on a single-axis laboratory shake table. The shake table is controlled using the LabVIEW software on the PC exchanging the data with an AC servo drive via data acquisition cards. The servo drive controls the the shake table to generate any desired acceleration profile. Previous researches has been carried out the tracking control of the shake table taking into account various sensoring/control issues (See for example [38-41]). The laboratory setup is shown in Figure 10. Three PC-connected cameras are measuring the displacement and velocity of movements at different structure floors. The pendulum with appropriately calculated length, material and weight is installed on the top floor. The structure is composed of flexible metal sheets whose length, weight and elasticity are precisely calculated to reflect a real 11-story building in terms of the main natural frequencies. The details of the laboratory structure designed is available in [7, 9]. Figure 11 shows the results taken from the implemented setup in which the two-story structure, pendulum and the generator are real laboratory equipment and the electronic circuits and the battery are simulated in LabVIEW software and two parts of system are connected via a hardware-in-loop system. As seen in Figure 11, in this case, the voltage is rectified to a smooth DC voltage by the boost AC rectifier (see Figure 11(c))

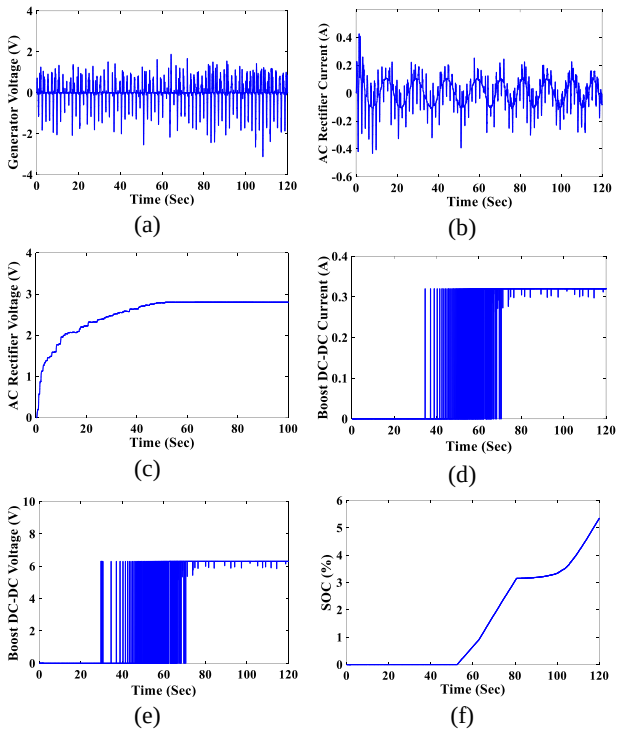

Fig. 11. Electric voltages at different stages of power processing for the laboratory test setup connected to the LabVIEW simulated electronic circuit and battery (a) output voltage of the pendulum-coupled (b) input current of boost AC rectifier (c) output voltage of boost AC rectifier (d) input current to boost DC-DC converter (battery charger (e) battery charger voltage (f) state of charge of the battery.

and the charging current is adjusted by the boost DC-DC charger (Figure 11(d)). The adjusted voltage and the increasing state-of-charge are also shown in Figures 11(e) and 11(f). The high frequency oscillations in the voltage and current is due to the intrinsic chattering caused by the SMC.

IV. Conclusions

An energy regeneration scheme for harvesting energy from a passive PTMD structural control system was proposed. The suggested plan includes a DC generator coupled with the damping pendulum. The output voltage produced by the electric motor was converted to a rectified DC by a boost AC rectifier that is controlled by a passivity-based control. A boost dc-dc converter is then utilized as the battery charger to guarantee the desired charging characteristics for the Li-ion battery. The boost charger is controlled by a sliding mode controller to address the nonlinear dynamics and model uncertainties of the converter and the battery. A 76-story building under wind force effect is simulated and the results show almost DC voltage as the output of the boost AC rectifier, DC output of the boost charger and the smooth charging current. Also the plan was experimentally implemented on a two-story laboratory structure mounted on a shake table. The electronic part was simulated within the PC using a hardware-in-loop system. The results from the experimental setup also verifies the efficiency of the proposed method in providing smooth DC output for the boost AC rectifier, and the desired charging characteristics for the battery charging system.

References

[1] M. M. Ali and K. S. Moon, "Structural developments in tall buildings: current trends and future prospects," *Architectural science review*, vol. 50, no. 3, pp. 205–223, 2007.

[2] Soong and B. Spencer Jr Reviewer, "Active structural control: theory and practice," *Journal of Engineering Mechanics*, vol. 118, no. 6, pp.1282–1285, 1992.

[3] B. Spencer Jr and S. Nagarajaiah, "State of the art of structural control," *Journal of structural engineering*, vol. 129, no. 7, pp. 845–856, 2003.

[4] B. Kavyashree, S. Patil, and V. S. Rao, "Review on vibration control in tall buildings: from the perspective of devices and applications," *International Journal of Dynamics and Control*, vol. 9, no. 3, pp.1316–1331, 2021.

[5] Parulekar and G. Reddy, "Passive response control systems for seismic response reduction: A state-of-the-art review," *International Journal of Structural Stability and Dynamics*, vol. 9, no. 01, pp. 151–177, 2009.

[6] M. D. Symans and M. C. Constantinou, "Semi-active control systems for seismic protection of structures: a state-of-the-art review," *Engineering structures*, vol. 21, no. 6, pp. 469–487, 1999.

[7] M. Soleymani, T. Asgari, and M. Sadeghi, "Design and implementation of a semi-active structural control system using shake table test," *Sharif Journal of Civil Engineering*, vol. 35, no.2.2, pp. 133–142, 2019.

[8] Korkmaz, "A review of active structural control: challenges for engineering informatics," *Computers & Structures*, vol. 89, no. 23-24,pp. 2113–2132, 2011.

[9] A. Khalatbarisoltani, M. Soleymani, and M. Khodadadi, "Online control of an active seismic system via reinforcement learning," *Structural Control and Health Monitoring*, vol. 26, no. 3, p. e2298, 2019.

[10] A. Preumont, Vibration control of active structures: an introduction. Springer, 2018, vol. 246.

[11] M. Soleymani, A. H. Abolmasoumi, H. Bahrami, A. Khalatbari-S, E. Khoshbin, and S. Sayahi, "Modified sliding mode control of aseismic active mass damper system considering model uncertainties and input time delay," *Journal of Vibration and Control*, vol. 24, no. 6,pp. 1051–1064, 2018.

[12] E. Khoshbin, A. H. Abolmasoumi, M. Soleymani, and A. Khalatbari, "Generalized active disturbance rejection control of structures under seismic disturbance considering time delays," *Structural Control and Health Monitoring*, vol. 25, no. 1, p. e2029, 2018.

[13] D. Botto and M. Umer, "A novel test rig to investigate under-platform damper dynamics," *Mechanical Systems and Signal Processing*, vol.100, pp. 344–359, 2018.

[14] S. Gong and Y. Zhou, "Experimental study and numerical simulationon a new type of viscoelastic damper with strong nonlinear characteristics," *Structural Control and Health*

Monitoring, vol. 24, no. 4, p.e1897, 2017.
[15] F. Rahimi, R. Aghayari, and B. Samali, "Application of tuned mass dampers for structural vibration control: a state-of-the-art review," *Civil Engineering Journal*, pp. 1622–1651, 2020.
[16] A. Di Matteo, T. Furtmuller, C. Adam, and A. Pirrotta, "Optimal design of tuned liquid column dampers for seismic response control of base-isolated structures," *Acta Mechanica*, vol. 229, no. 2, pp. 437–454, 2018.
[17] L. Wang, W. Shi, and Y. Zhou, "Study on self-adjustable variable pendulum tuned mass damper," *The Structural Design of Tall and Special Buildings*, vol. 28, no. 1, p. e1561, 2019.
[18] Wang, Liangkun, Weixing Shi, and Ying Zhou. "Study on self-adjustable variable pendulum tuned mass damper." *The Structural Design of Tall and Special Buildings*, vol. 28, no. 1, p e1561, 2019.
[19] H. S. Kim, J.-H. Kim, and J. Kim, "A review of piezoelectric energy harvesting based on vibration," *International journal of precision engineering and manufacturing*, vol. 12, no. 6, pp. 1129–1141, 2011.
[20] H. Wang, A. Jasim, and X. Chen, "Energy harvesting technologies in roadway and bridge for different applications–a comprehensive review," *Applied Energy*, vol. 212, pp. 1083–1094, 2018.
[21] H.-X. Zou, L.-C. Zhao, Q.-H. Gao, L. Zuo, F.-R. Liu, T. Tan, K.-X. Wei, and W.-M. Zhang, "Mechanical modulations for enhancing energy harvesting: Principles, methods and applications," *Applied Energy*, vol. 255, p. 113871, 2019.
[22] M. Gholikhani, H. Roshani, S. Dessouky, and A. Papagiannakis, "Acritical review of roadway energy harvesting technologies," *Applied Energy*, vol. 261, p. 114388, 2020.
[23] S. Hassanli, K. Chauhan, M. Zhao, and K. C. Kwok, "Application of through-building openings for wind energy harvesting in built environment," *Journal of Wind Engineering and Industrial Aerodynamics*, vol. 184, pp. 445–455, 2019.
[24] Y.-F. Su, R. R. Kotian, and N. Lu, "Energy harvesting potential of bendable concrete using polymer based piezoelectric generator," *Composites Part B: Engineering*, vol. 153, pp. 124–129, 2018.
[25] Y. Luo, H. Sun, X. Wang, L. Zuo, and N. Chen, "Wind induced vibration control and energy harvesting of electromagnetic resonant shunt tuned mass-damper-inerter for building structures," *Shock and Vibration*, vol. 2017, pp. 1-13. 2017.
[26] W. Shen, S. Zhu, H. Zhu, and Y.-l. Xu, "Electromagnetic energy harvesting from structural vibrations during earthquakes," *Smart structures and systems*, vol. 18, no. 3, pp. 449–470, 2016.
[27] G. Mohebalizadeh, H. Alipour, L. Mohammadian, and M. Sabahi, "An improved sliding mode controller for DC/DC boost converters used in EV battery chargers with robustness against the input voltage variations," International Journal of Industrial Electronics Control and Optimization, vol. 4, no. 2, p. 257-266, 2021.
[28] V. Utkin, "Sliding mode control of DC/DC converters," *Journal of the Franklin Institute*, vol. 350, no. 8, p. 2146-2165, 2013
[29] R. Clough and J. Penzien, "Dynamics of structures (3rd)," *Computers & Structures, Inc., California*, pp. 342–344, 2003.
[30] J. P. Den Hartog, *Mechanical vibrations*. Courier Corporation, 1985.
[31] D. Williams, "How the boost PFC converter circuit improves power quality," Available: https://www.allaboutcircuits.com/technical-articles/how-the-boost-pfc-converter-circuit-improves-power-quality/, 2016.
[32] J.C. Salmon, "Circuit topologies for single-phase voltage-doubler boost rectifiers," *IEEE Transactions on Power Electronics*, vol. 8, no. 4, p.521-529, 1993.
[33] J. Sastry, O. Ojo, and Z. Wu, "High-performance control of a boost AC–DC PWM rectifier/induction generator system," *IEEE transactions on industry applications*, vol. 42, no. 5, p.1146-1154, 2006.
[34] M. Monfard, M. Babaei, and S. Sharifi, "A z-source network integrated buck-boost PFC rectifier," International journal of industrial electronics control and optimization, vol. 2, no. 4, p.289-296, 2019.
[35] H. J. Sira-Ramirez, and S. O.Ramón, "Control design techniques in power electronics devices," Springer Science & Business Media, 2006.
[36] M. Feizi, R. Beiranvand, and M. Daneshfar, "An integrated high power self-equalized battery charger using a voltage multiplier and phase-shifted full-bridge DC-DC converter for lithium-ion batteries," International Journal of Industrial Electronics Control and Optimization, vol. 4, no. 2, p. 141-155, 2021.
[37] A. Taheri, and N. Asgari, "Sliding mode control of LLC resonant DC-DC converter for wide output voltage range in battery charging applications," International Journal of Industrial Electronics Control and Optimization, vol. 2, no. 2, p.127-136, 2019.
[38] P. Memarzadeh, M. Saadatpour, and M. Azhari, "Nonlinear dynamic response and ductility requirements of a typical steel plate shear wall subjected to El Centro earthquake," *Iranian Journal of Science and Technology Transaction B-Engineering*, vol. 34, no. B4, pp. 371-384, 2010.
[39] N. Rajabi, A. H. Abolmasoumi, and M. Soleymani, "Sliding mode trajectory tracking control of a ball-screw-driven shake table based on online state estimations using EKF/UKF," *Structural Control and Health Monitoring*, vol. 25, no. 4, p. e2133, 2018.
[40] M. Soleymani and A. H. Abolmasoumi, "Fuzzy-sliding mode supervisory control of an electric seismic shake table," *transformation*, p. 1, 2016.
[41] S. Sayahi, M. Hamidizadeh, H. Moradzadeh, M. Soleymani, and M. Rahmani, "Fuzzy control of a seismic shake table using a vision-based displacement measurement system." *Modares Mechanical Engineering*, vol. 14, no. 14, 2015.

Mohammad A. Beladi Pour was born in Gachsaran, Iran. He received his B.S. degree in Electrical Engineering majored in Control Engineering from Semnan University, Semnan, Iran in 2016 and his M.Sc. degree in Mechatronics from Arak University, Arak, Iran in 2018. From 2018 to 2019 he was collaboratingd with several knowledge-based enterprise companies. From 2020, he has worked as a researcher at Electronic Technology Institute, Shiraz, Iran. His Current research interests include nonlinear control, adaptive control, data driven methods, and machine vision systems.

Amir H. Abolmasoumi was born in Arak, Iran. He received his B.S. degree in control engineering from Tehran University, Tehran, Iran in 2005 and M.S. and Ph.D. degrees from Tarbiat Modares University, Tehran, Iran in 2008 and 2011, respectively. From then, he has been with the Electrical Engineering Department of Arak University, Arak, Iran. His main research interests include state estimation theory and applications in power and biological systems, Koopman operator theory, data-driven modeling, delay dynamic systems and structural control.

Mehdi Soleymani received his BSc, MSc, and PhD degrees from Iran University of Science and Technology (IUST) in 2000, 2003, and 2009 respectively. He was with Automotive Industry Research and Innovation Centre (AIRIC) of SAIPA Company as a senior test engineer from 2002 to 2004. He joined Arak University as an assistant professor of mechanical engineering and director of the system simulation and control laboratory in 2009. He has been with Arak University as an associate professor of mechanical engineering and mechatronics from 2015 up to the present. He joined Advanced Vehicle Engineering Centre (AVEC) of Cranfield University as a research fellow from 2018 to 2021. He is also an associate fellow of the higher education academy of UK. His research interest includes active vibration control of vehicular and structural systems, energy harvesting from vibration control systems in vehicles, tall buildings, and wind turbines, and design of control strategies and optimization algorithms for energy storage and energy management systems in hybrid electric, fuel cell, and electric vehicles.

Mazdak Ebadi was born in Booshehr, Iran. He received his B.S. degree in Electrical and Electronics Engineering from Shiraz University, Shiraz, Iran, in 2005, and his M.S. and Ph.D. degrees in Electrical Engineering from the Shahid Chamran University, Ahvaz, Iran, in 2008 and 2014, respectively. In 2014, he joined Arak University as an Assistant Professor in the School of Electrical and Electronics Engineering. His current research interests include Electrical Machinery, Power Inverters, DC-DC converters, and PWM converter/inverter systems.

International Journal of Industrial Electronics, Control and Optimization 2022 IECO
Vol. 5, No. 2, pp. 177-187, April (2022)

Design a PLL for Fractional Frequency Synthesizers using DDSM with Reduced Hardware

Leila Jahanpanah[1], Seyed Ali Sadatnoori[2,†], Iman Chaharmahali[3]

[1] Department of Electrical Engineering, Mahshahr Branch, Islamic Azad University, Mahshahr, Iran
[2] Department of Electrical Engineering, Shoushtar Branch, Islamic Azad University, Shoushtar, Iran
[3] Department of Electrical Engineering, Andimeshk Branch, Islamic Azad University, Andimeshk, Iran

ABSTRACT

Phase locked loop (PLL) circuits are widely used in fractional frequency synthesizers. In these synthesizers, fractional multiples of the reference frequency can be synthesized, so the reference frequency and the bandwidth of the loop can be increased. This frequency synthesizer is commonly used due to its flexibility and convenient frequency adjustment. In this paper, a PLL circuit of the transistor level is designed in which a hybrid digital sigma-delta modulator with reduced hardware is used. This Digital Delta-Sigma Modulator (DDSM) has four stages that have a lower noise level and power consumption than the conventional type. This PLL circuit has a third-order loop filter and a voltage-controlled oscillator of the NMOS type. In the PLL circuit, two counters are used in its feedback path. In the proposed divider, there is a dual divider P / P + 1 (in this case 5, 6) which divides its input signal by 5, 6 according to the control input. A design example for the PLL is provided. A third stage digital Delta-Sigma modulator with reduced hardware is also used to control these counters. This modulator has less power consumption than the conventional method and has less number of transistors by 85%.

Article Info

Research Article

Keywords:
Digital delta-sigma modulator, Fractional frequency synthesizers, Hybrid modulators, Phase locked loop, Spurious tones.

Article History:
Received 2022-01-02
Accepted 2022-05-11

I. INTRODUCTION

Frequency synthesizers are an important part of multi-frequency wireless transmitter / receiver circuits. The phase locked loop in the frequency synthesizer is primarily used as a local oscillator in wireless receivers, lowering the carrier frequency to the intermediate frequency (IF). Phase locked loop circuits are used for modulation phase and frequency modulation, clocked pulse recovery, communication noise prevention, frequency synthesizer, deflection prevention, edge detection and many other applications.

Phase locked loop (PLL) circuits are widely used in fractional frequency synthesizers. In these synthesizers, fractional multiples of the reference frequency can be synthesized, so the reference frequency and the bandwidth of the loop can be increased. This frequency synthesizer is commonly used due to its flexibility and convenient frequency adjustment.

Most frequency synthesizers use phase locked loop circuits. Each PLL circuit includes a phase comparator (PC), a low-pass filter (LPF), a charge pumping (CP), and a voltage-controlled oscillator (VCO). [1]

The blocked diagram of a PLL circuit is shown in Fig.1. A digital sigma-delta modulator is used to control the division ratio in the phase locked loop circuit. In Fig.1 X is the modulator input, N_0 is the correct division ratio and M is the modulator module. Therefore, the following relation is established in the fractional frequency synthesizer. Usually,

†**Corresponding Author:** a.sadatnoori@iau-shoushtar.ac.ir
Tel: +989166401872, University of Shoushtar Branch,
Faculty of Electrical Engineering, Islamic Azad University, Shoushtar Branch, Shoushtar, Iran

the modulus M is a multiple of two.

$$f_{out} = \left(N_0 + \frac{X}{M}\right).f_{ref} \quad (1)$$

where f_{ref} is the input frequency at the input to the phase comparator. In fractional frequency synthesizer architecture, both f_{out} and f_{ref} are integer multiples of f_s, where $f_s = \frac{f_{ref}}{M}$ is the channel spacing.

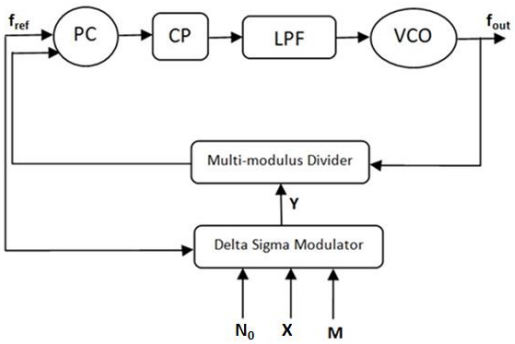

Fig.1: Blocked diagram of a PLL based fractional frequency synthesizer.

Digital Delta-Sigma modulators generally use two methods to increase the output period: Stochastic method and deterministic method.

The stochastic method uses a single-bit dither signal to randomize the output. This dither signal is either directly or filtered or effectively applied to the modulator input [2-6].

The deterministic method causes a change in the internal structure of the modulator to increase the periodicity of the output signal. Some of the deterministic methods used before are: Use the initial conditions for the first stage of the modulator [7], use the delay feedback path in each stage of the modulator [8-9], use the quantizer with the prime module [10], use the straight forward path to add the output of each stage to the next stage of the modulator [11].

Wang *et al.* [12] recommended a method for avoiding the development of spurs by substituting the sigma-delta modulator for a new type of digital quantizer and a charge pump offset incorporated with a sampled loop filter.

In [13-14], a solution is presented based on mixed-radix algebra, where the required ratio is formed by combining two and three different modulus. In [15-17], a novel method is proposed for applying periodic dither to a DDSM to obtain minimized spurious tones. The effects of adding the pseudorandom dither signal in different stages within the proposed Multi-stAge noise SHaping (MASH) modulator are expressed in a set of equations. In [18], the design of a new architecture of Continuous-Time (CT) MASH 2-2 (multi-stage noise shaping modulators) full feedforward Sigma-Delta (ΣΔ) modulator is presented. In [19], it is shown that applying a linear feedback shift register (LFSR) dither to a digital delta-sigma modulator (DDSM) cannot always increase its fundamental period.

The purpose of this paper is to introduce and design a new four stage Sigma-Delta modulator that has less hardware and power consumption than conventional methods. This modulator is used in a phase locked loop to properly adjust the division ratio of the modulator.

In the present work, we introduce hybrid DDSM 1-2-3-4 modulator architecture. In this method, the First Order Error Feedback Modulator (EFM1) in the first stage has a variable programmable modulus M_1 that is not a power of 2. The modulators in the second, third and four stages (M_2, M_3, and M_4, respectively) are the power of 2. The planning methodology relies on error masking [20-21]. Thus, the frequency synthesizer can produce the required frequency accurately without declining the performance and increasing hardware complexity. In this paper, a new phase locked loop circuit is designed which includes a third-order loop filter, a charge pump circuit, a voltage-controlled oscillator with the NMOS method, and a divider with two counters. The counters use the proposed digital Delta-Sigma modulator, which reduces hardware consumption.

The remainder of this paper is structured as follows: Section 2 describes the overall operation of the DDSM and summarizes related works. Section 3 describes the proposed hybrid modulator. The calculation of periodic length for hybrid MASH modulators is presented in Section 4. The parts of the phase locked loop circuit proposed in Section 5 are presented. Section 6 illustrates the design example and simulation results. Finally, conclusions are made in Section 7.

II. RELATED WORKS

Before presenting our plan methodology in detail, we first review a conventional MASH DDSM architecture. Here, a structure based on the error feedback modulator model (Fig.2) is considered. The signal v[n] is the sum of the digital words x[n] and s[n]. When v[n] is greater than M, the quantizer overflows and the output signal will be 1. In comparison, when v[n] is less than M, the quantizer does not overflow and y[n] will then be 0. Mathematically, we write:

$$y[n] = Q(v[n]) = \begin{cases} 0, & v[n] < M \\ 1, & v[n] \geq M \end{cases} \quad (2)$$

where M is the modulus of the quantizer and v[n] is the input to the quantizer [1].

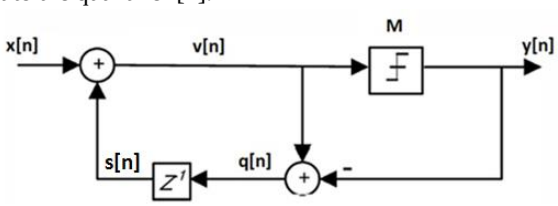

Fig.2: Blocked diagram of the first order error feedback modulator.

Fig.3 shows the blocked diagram of a classical l^{th} order

MASH DDSM comprising a cascade of l N-bit EFM1 blocks and a noise cancellation network.

The output of the classical MASH DDSMl can be expressed in the z-domain as [1]:

$$Y(z) = \frac{1}{M}.X(z) + (1 - z^{-1})^{l}.Q_{l}(z) \quad (3)$$

where $X(z)$ and $Q_l(z)$ are the z-transforms of the input and the quantizer noise introduced by stage l.

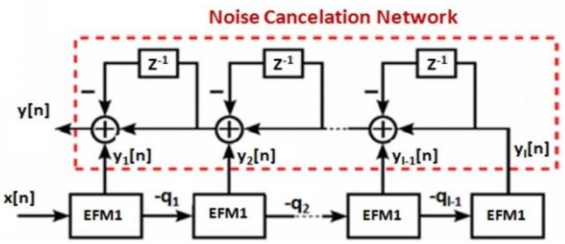

Fig.3: Blocked diagram of an l^{th} order MASH DDSM incorporating a cascade of EFM1s [1].

The structure of the HK-EFM1 (Hosseini and Kennedy EFM) used in the HK-MASH (Hosseini and Kennedy MASH) is illustrated in Fig.4. There is just one difference between this structure and the classical EFM1 in Fig.2; i.e., the existence of the feedback blocked az^{-1}. Here, a is a selected small integer to make (M−a) the maximum prime number below M. The cycle length of it is $(M - a)^{l} = (2^{N} - a)^{l}$, where l is the order of the modulator. Song and Park [11] proposed the modified MASH 1-1-1, as shown in Fig.5. The modified MASH structure cascades several first-order digital accumulators like the traditional MASH structure but has a supernumerary feedforward connection between two adjoining categories and increases the sequence period of quantization error.

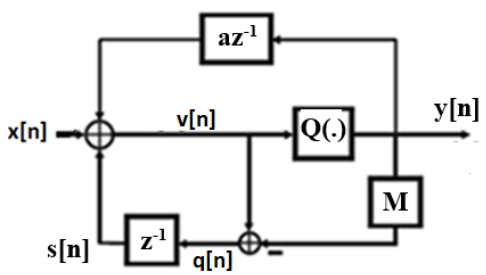

Fig.4: The modified EFM1 used in HK-MASH [10].

Le and Chen [23] presents a self-adaptive Sigma-Delta modulator, which offers opportunity to simplify the process of tuning parameters and further improve the noise performance.

Mazzaro and Kennedy [24] presents a Fractional-N Charge Pump (CP) PLL with a MASH 1-1-1 divider controller to exhibit pairs of spurious tones called “horn spurs”. Mai and Kennedy [25] describes a detailed analysis of the cause of wandering spur patterns in a MASH 1-1-1 DDSM-based fractional-N frequency synthesizer, supported by experimental measurements.

Shamsi proposes a new mismatch cancelation technique for quadrature delta-sigma modulators (QDSM). In this approach, a high speed and simple structure dynamic element matching (DEM) based on homogenization and time-division (HTD) is designed. [26]

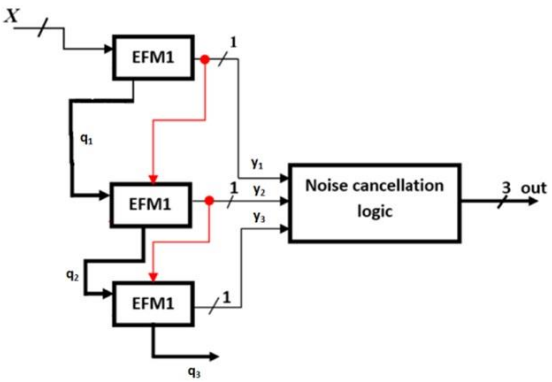

Fig.5: Blocked diagram of the modified MASH 1-1-1 proposed in Song and Park [11].

Mai et all presents two methods. It describes a 4.9-GHz 180-nm SiGe BiCMOS charge-pump phase-locked loop (CP-PLL) fractional-N frequency synthesizer platform with a divider controller that can function as: 1) a standard MASH 1-1-1; 2) a MASH 1-1-1 with high-amplitude dither; and 3) a MASH 1-1-1 with a modified third stage. [27]

Abdul and Nelakuditi presents the design and implementation of Charge Pump (CP) circuit to improve the mismatch in currents with good linearization in Low Voltage Fractional-N PLL suitable for RF applications. [28]

The Global System for Mobile communication (GSM) system is a time and frequency division system in which a carrier frequency and a time slot number characterize each physical channel.

Thus, in GSM 1800, the problem of synthesizing is considered an (f_{out}) output frequency of 1.80 GHz from a 13 MHz (f_{ref}) reference clocked. In this example, $f_{ref} = 13\ MHz, f_s = 200\ KHz, f_{out} = 1.80\ GHz$ yielding, $N_0 = 138$, and $X = 15123$, $M = 2^{15}$. In conventional MASH 1-1-1 based fractional frequency synthesizers having $M = 2^{15}$, the required division number can be approximated as follows:

$$f_{out} = \left(138 + \frac{15123}{2^{15}}\right).f_{ref} = 1.799999725\ GHz \quad (4)$$

Hence, a frequency offset is approximately 274.65 Hz.

The approximation noise can be reduced using a larger value of modulus M. Also, it correlates with increasing the word length of the modulator, hardware complexity, and power consumption.

III. THE PROPOSED HYBRID DIGITAL SIGMA DELTA MODULATOR

In this section, we introduce a novel structure for the

dithered MASH DDSM 1-2-3-4 that produces a long sequence period.

This paper attempts to reduce the hardware and power consumption of the fourth-order Digital Sigma-Delta Modulator and improve the noise level. Therefore, a fourth-order sigma-delta modulator with a high bit number is broken down into several smaller sigma-delta modulators with fewer bits. Then, the input of the fourth-order modulator is divided into four segments so that each part of it is subdivided into first, second, third, and fourth-order modulators. We call this modulator, which consists of 4 sub-sections, a hybrid modulator.

The hybrid modulator architecture is shown in Fig.6. In this architecture, instead of a single classical power-of-two modulus sigma-delta modulator in the fractional-N frequency synthesizer, we can use four modulators. The first stage modulator is a Variable Modulus EFM1 (VM-EFM1) and has a programmable modulus M_1 that is not a power of 2. The VM-EFM1 is shown in Fig.7. The modulator has two inputs: X is the input signal and M_1 is an optional modulus. By using the modulus M_1, we can change the quantizer accuracy. The output of the VM-EFM1 can be expressed in the z-domain as:

$$Y(z) = \frac{X(z)}{M_1} + (1 - z^{-1})^{-1}.Q(z) \quad (5)$$

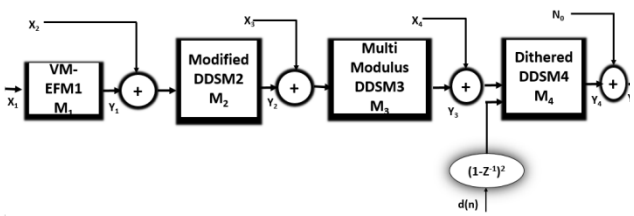

Fig.6: Blocked diagram of the hybrid modulator DDSM 1-2-3-4 used in fractional frequency synthesizer.

where X(z) and Q(z) are the z-transforms of the input and the quantization noise introduced by the VM-EFM1.In the fractional-frequency synthesizer, we can control the numerator and denominator of the fraction.

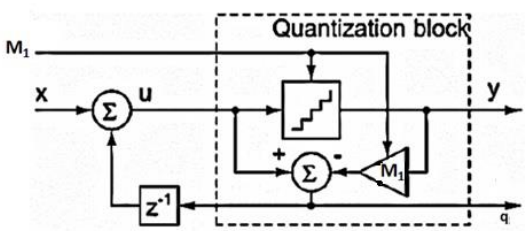

Fig.7: The variable modulus first order error feedback modulator (VM-EFM1) [7]

The second modulator in the hybrid structure is modified MASH 1-1, which has conventional modulo M_2. The cycle length in modified MASH 1-1 structure is ${M_2}^2$, where M_2 is the quantizer modulus in the classical DDSM.

The third modulator in the hybrid structure is multi-modulus MASH 1-1-1, which has conventional modulo M_3. The small positive integer a in the i^{th} stage of HK EFM1 is denoted as a_i. This value will be assumed different for each stage. The values of a_i are selected such that to make $\{M - a_1, M - a_2, \dots, M - a_l\}$ co-prime numbers to maximize the period. A few values of a_i are given in Table I. It is of note that to make the period independent of the input, $M - a_1$ is set as a prime number.

TABLE I

SOME VALUES OF A_I IN THIRD ORDER MASH 1-1-1.

Word Lengths (N)	a_1	a_2	a_3
4,6, 9, 10, 12	3	0	1
3, 5, 7	1	0	3
8	5	0	1
11	9	0	1

If the greatest common divisor of any two numbers is 1, they are co-prime numbers. A prime number is a number that has two divisors.

The fourth modulator in the hybrid proposed structure is dithered MASH 1-1-1-1, which a periodic LFSR dither input with a period N_d added to the third and fourth stages of MASH 1-1-1-1. Fig.8 presents an implementation of the second-order dither hybrid modulator.

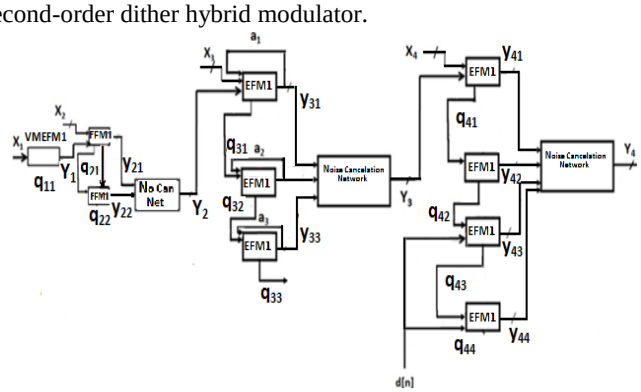

Fig.8: Implementation of the second order dither hybrid DDSM 1-2-3-4 modulator.

The output frequency (f_{out}) in the fractional frequency synthesizer is determined by:

$$f_{out} = (N_0 + \frac{X_4 + \frac{X_3 + \frac{X_2 + \frac{X_1}{M_1}}{M_2}}{M_3}}{M_4}).f_{ref} \quad (6)$$

In this case, the z-transforms y_1, y_2, y_3, y_4, and y_{out} are shown by:

$$Y_{out}(z) = N_0 + Y_4(z) \quad (7)$$

$$Y_4(z) = STF_4(z)(X_4 + Y_3(z)) + NTF_4(z)Q_4(z) \quad (8)$$

$$Y_3(z) = STF_3(z)(X_3 + Y_2(z)) + NTF_3(z)Q_3(z) \quad (9)$$

$$Y_2(z) = STF_2(z)(X_2 + Y_1(z)) + NTF_2(z)Q_2(z) \quad (10)$$

$$Y_1(z) = STF_1(z).X_1 + NTF_1(z)Q_1(z) \quad (11)$$

where STF_1, STF_2, STF_3, STF_4, NTF_1, NTF_2, NTF_3, and NTF_4 are the signal and error transfer functions of first, second, third and fourth stage modulators, respectively, and $Q_1(z)$, $Q_2(z)$, $Q_3(z)$, and $Q_4(z)$ are the quantization

error signals introduced by the first, second, third, and fourth sigma-delta modulators, respectively. X_1, X_2, X_3, and X_4 are the integer inputs of the VM-EFM1, modified MASH 1-1, multi-modulus MASH 1-1-1, and second-order dithered MASH 1-1-1-1in the hybrid architecture, respectively. Hence, the final output y_{out} can be attained by:

$$Y_{out}(z) = N_0 + STF_4(z).X_4 + STF_4(z).STF_3(z).X_3 + STF_4(z).STF_3(z).STF_2(z).X_2 + STF_4(z).STF_3(z).STF_2(z).STF_1(z).X_1 + NTF_4(z)Q_4(z) + STF_4(z).NTF_3(z).Q_3(z) + STF_4(z).STF_3(z).NTF_2(z).Q_2(z) + STF_4(z).STF_3(z).STF_2(z).NTF_1(z).Q_1(z) \quad (12)$$

where,

$$STF_4(z) = \frac{1}{M_4},\ STF_3(z) = \frac{1}{M_3},\ STF_2(z) = \frac{1}{M_2},\ STF_1(z) = \frac{1}{M_1},\ NTF_4(z) = (1-z^{-1})^4,\ NTF_3(z) = (1-z^{-1})^3,\ NTF_2(z) = (1-z^{-1})^2,\ \text{and}\ NTF_1(z) = (1-z^{-1}).$$

IV. Design Method

The DDSM quantization error power is distributed over a few tones that are specified by the period, leading to a tone spacing of $df[k] = \frac{f_s}{N}$, where f_s is the sampling frequency and N is the period. When the sequence length and, consequently, the number of tones is large, the Power Spectral Density (PSD) approaches the classical white noise approximation. The PSD of Y_2, Y_3, and Y_4 in the second-order LSB LFSR dither signal in the DDSM2, the multi-modulus DDSM3, and dithered DDSM4 are defined by [13]:

$$P_2(\Omega[k]) = \frac{1}{12}(|1-z^{-1}|)^4{}_{z=e^{j\Omega}} = \frac{1}{12}\left(2\sin\left(\frac{\Omega}{2}\right)\right)^4 \quad (13)$$

$$P_3(\Omega[k]) = \frac{1}{12}(|1-z^{-1}|)^6{}_{z=e^{j\Omega}} = \frac{1}{12}\left(2\sin\left(\frac{\Omega}{2}\right)\right)^6 \quad (14)$$

$$\Omega[k] = \frac{2\pi}{N}.k, \qquad k = 0,1,\dots,\frac{N}{2}$$

$$P_4(\Omega[k]) = \frac{1}{12}(|1-z^{-1}|)^8 + \frac{1}{12}\frac{1}{M_4{}^2}(|1-z^{-1}|)^4{}_{z=e^{j\Omega}} \quad (15)\ (16)$$

where Ω is the angular frequency of the oscillation and P is the density of the power spectrum. Also, at the output of the proposed hybrid modulator, since P_2 and P_3 are second-order and third-order shaped, respectively, while P_4 is fourth-order shaped, if the level of the lowest frequency tone in P_2 and P_3 is below that of P_4, the overall power of P_2 and P_3 should always be below the P_4 envelope. This can be expressed as:

$$P_2 < P_4, f = \frac{f_s.k}{N_2}, k = 1,2,\dots,\frac{N_2}{2} \quad (17)$$

$$P_3 < P_4, f = \frac{f_s.k}{N_3}, k = 1,2,\dots,\frac{N_3}{2} \quad (18)$$

Note that for a DDSM with an output period of *N*, the lowest frequency tone is at $\frac{f_s}{N}$.

Thus, at low frequencies:

$$|1-z^{-1}|^2 = \left|1-e^{\frac{-j2\pi f}{f_s}}\right|^2 = |2\sin\left(\frac{\pi f}{f_s}\right)|^2, \sin\left(\frac{\pi f}{f_s}\right) \approx \frac{\pi f}{f_s} \text{ for } f \ll f_s \quad (19)$$

We can approximate P_2, P_3, and P_4 at low frequencies by:

$$P_2 = \frac{1}{12}\left(\frac{1}{M_3.M_4}\right)^2 2^4.(\frac{\pi f}{f_s})^4 \quad (20)$$

$$P_3 = \frac{1}{12}\frac{1}{M_4{}^2}2^6.(\frac{\pi f}{f_s})^6 \quad (21)$$

$$P_4 = \frac{1}{12}2^8.(\frac{\pi f}{f_s})^8 + \frac{1}{12}\frac{1}{M_4{}^2}2^4.(\frac{\pi f}{f_s})^4 \quad (22)$$

Substituting Equs. (20)-(22) into the constraints Equs. (17) and (18), we have:

$$\frac{1}{12}2^8.(\frac{\pi f}{f_s})^8 + \frac{1}{12}\frac{1}{M_4{}^2}2^4.(\frac{\pi f}{f_s})^4 \approx \frac{1}{12}2^8(\frac{\pi f}{f_s})^8 \quad (23)$$

$$\left(\frac{1}{M_3.M_4}\right)^2 2^4.(\frac{\pi f}{f_s})^4 < 2^8.(\frac{\pi f}{f_s})^8, f = \frac{f_s}{M_2{}^2} \quad (24)$$

$$2^6.\frac{1}{M_4{}^2}(\frac{\pi f}{f_s})^6 < 2^8.(\frac{\pi f}{f_s})^8, f = \frac{f_s}{(M_3-\alpha)^3} \quad (25)$$

Therefore:

$$\left(\frac{1}{M_4}\right)^2 < \frac{2^2.\pi^2}{M_3{}^6} \quad (26)$$

$$M_3{}^3 < 2\pi.M_4 \rightarrow 2^{3n_3} < 2\pi.2^{n_4} \rightarrow 3n_3 < \log_2(2\pi) + n_4 \rightarrow n_3 < \frac{2.65+n_4}{3} \quad (27)$$

$$\left(\frac{1}{M_3.M_4}\right)^2 < \frac{2^4.\pi^4}{M_2{}^4} \quad (28)$$

$$M_2 < \frac{\sqrt{M_3.M_4}}{2\pi} \quad (29)$$

In the VM-EFM1 accumulator, the output Y_1 will be periodic with a cycle length between two and M_1. In the worst case, the quantization noise power of VM-EFM1 is spread over (M_1-1) tones. The power in the lowest tone, after passing through MASH 1-1, multi-modulus MASH 1-1-1, and dithered MASH 1-1-1-1, is obtained by:

$$P_{tone} = (\frac{1}{M_1.M_2.M_3.M_4})^2 = STF_1{}^2.STF_2{}^2.STF_3{}^2.STF_4{}^2 \quad (30)$$

Consequently, to mask the worst-case tone from VM-EFM1 at the output of dithered DDSM 1-1-1-1, it is required that:

$$\Omega_1[1] = \frac{2\pi}{M_1}, k = 1, N_1 = M_1 \quad (31)$$

$$P_4(\Omega_1[1]) \geq N_f.P_{tone} \quad (32)$$

where N_f is FFT length, which presents the frequencies at which the PSD is estimated.

Substituting Equs. (22) and (30) into the constraint Equ. (32), we obtain:

$$N_f(\frac{1}{M_1.M_2.M_3.M_4})^2 \leq \frac{1}{12}(\frac{2\pi}{M_1})^8 \rightarrow M_1 \leq \sqrt[6]{\frac{(2\pi)^8.M_2{}^2.M_3{}^2.M_4{}^2}{12N_f}} \quad (33)$$

A. Simulation Results

Given three design parameters of the reference frequency f_{ref}, the channel spacing f_s, and the output frequency f_{out}, we need to determine nine integers of $N_0, X_1, X_2, X_3, X_4, M_1, M_2, M_3$, and M_4. First, M_4 is obtained and then M_1, M_2, and M_3 are calculated.

Selecting the variable modulus EFM1, we compute:

$$p_1 = \gcd(f_{ref}, f_{out}, f_s) \quad (34)$$

$$p_2 = \frac{f_{pc}}{p_1} \quad (35)$$

where gcd(a,b,c) denotes the greatest common divisor of a, b, and c. Then, the modulus M_1 is calculated as follows:

$$M_1 = \frac{p_2}{\gcd(p_1,p_2)} \quad (36)$$

M_2 and M_3 obtain from Equs (27) and (29).

Next, the inputs $N_0, X_1, X_2, X_3,$ and X_4 can be determined.

$$I_1 = \frac{f_{out}}{f_{ref}} \quad (37)$$

The integer division number is obtained as:

$$N_0 = \text{floor}(I_1) \quad (38)$$

where floor(x) returns the largest integer less than x.

$$I_4 = M_4.(I_1 - N_0) \quad (39)$$

The input of dithered MASH 1-1-1-1 modulator is determined as:

$$X_4 = \text{floor}(I_4) \quad (40)$$

The input of multi-modulus MASH 1-1-1 modulator is determined as:

$$I_3 = M_3.(I_4 - X_4) \quad (41)$$

$$X_3 = \text{floor}(I_3) \quad (42)$$

The input of modified MASH 1-1 modulator is calculated as:

$$I_2 = M_2.(I_3 - X_3) \quad (43)$$

$$X_2 = \text{floor}(I_2) \quad (44)$$

The input integer number of VM-EFM1 is obtained by choosing:

$$X_1 = M_1.(I_2 - X_2) \quad (45)$$

In GSM 1800, consider the problem of synthesizing an output frequency of 1.800 GHz from a 13 MHz reference clocked. In this example, $f_{ref} = 13$ MHz, $f_s = 200$ KHz, $f_{out} = 1.80$ GHz yielding, $N_0 = 138$, $X_4 = 472, X_3 = 9$, $X_2 = 13$, $X_1 = 7$, $M_1 = 13, M_2 = 2^4, M_3 = 2^4$, and $M_4 = 2^{10}$.

In contrast, in the classical MASH 1-1-1-1, no approximation is implicated in the hybrid modulator. In particular,

$$f_{out} = \left(138 + \frac{472 + \frac{9 + \frac{13 + \frac{7}{13}}{2^4}}{2^4}}{2^{10}}\right).f_{ref} = 1.800\text{GHz} \quad (46)$$

In order to compare classical and hybrid modulators, we demonstrate simulation results. The initial states of the first stage registers are set to odd values to avoid short cycles. The simulated output power spectrum of the classical 23-bit MASH 1-1-1-1 DDSM is shown in Fig.9. The simulated output power spectral density (PSD) of the hybrid DDSM 1-2-3-4 is illustrated in Fig.10. As expected, the hybrid DDSM 1-2-3-4 achieves an almost identical PSD compared to the traditional 23-bit MASH 1-1-1-1.

B. Hardware Complexity

The proposed multi-stage Sigma-Delta modulator circuit has 4-4-4-10 bits, whose power consumption for different transistor models is presented in Table II. The clocked pulse signal frequency of 1 MHz is selected and the number of transistors in this circuit is 2503 complementary transistors. Table III compares the number of transistors and the power consumption of the conventional 1-1-1-1 MASH modulator with the proposed method. The waveform of time domain of the modulator is plotted in Fig.11 after simulation with different transistor models. Continuation of the conventional 1-1-1-1 23-bit multi-stage Sigma-Delta modulator for 3271665 input with initial conditions $e_1[0] = 1$, $e_2[0] = 0$, $e_3[0] = 0$ and $e_4[0] = 0$ with HSPICE software and manufacturing technology 0.18 micrometers are implemented.

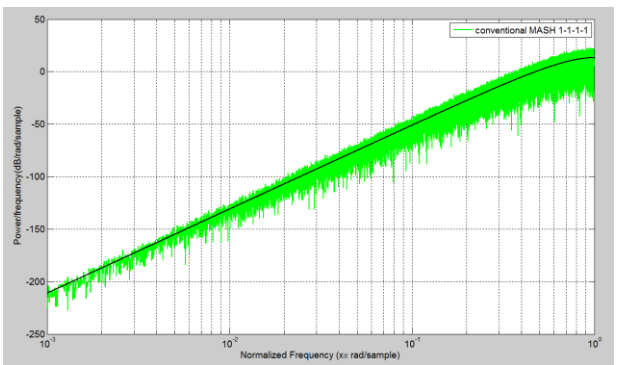

Fig.9: Simulated PSD at the output of a second-order dithered classical MASH 1-1-1-1 DDSM; the input is 3271665, $M = 2^{23}$. The solid black curve shows the PSD of the fourth-order shaped quantization noise of MASH 1-1-1-1 with second-order shaped additive LSB dither.

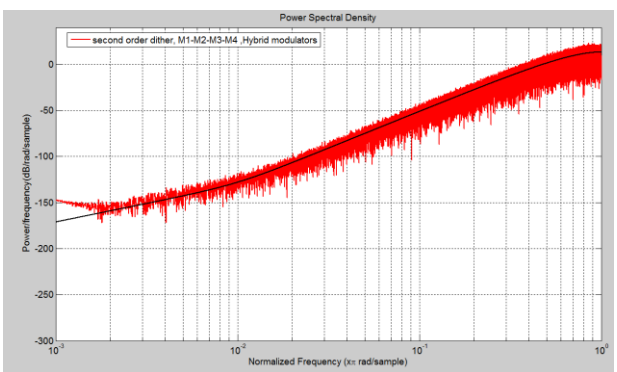

Fig.10: Simulated PSD at the output of a second-order dithered hybrid DDSM 1-2-3-4; the inputs are $X_4 = 472, X_3 = 9$, $X_2 = 13, X_1 = 7$, the modulus are $M_1 = 13$, $M_2 = 2^4, M_3 = 2^4$, and $M_4 = 2^{10}$. The FFT length is $N_f = 2^{18}$. The solid curves assume shaped white quantization noise including second-order shaped additive LSB dither.

TABLE II

COMPARISON OF POWER CONSUMPTION OF MULTI-STAGE MODULATOR STRUCTURE OF THE PROPOSED DESIGN 4-4-4-10 BITS WITH THE MODEL OF DIFFERENT TRANSISTORS N, P.

Transistor Type	Power Consumption
TT	14.06 nW
FF	75.36 nW
FS	71.09 nW
SF	16.75 nW
SS	110 nW

TABLE III
COMPARISON OF THE PROPOSED DESIGN WITH THE CONVENTIONAL 1-1-1-1 MASH SIGMA-DELTA MODULATOR.

Methods	Filip Flaps	Transistor Count	Power Consumption in TT mode
MASH 1-1-1 conventional 25-bit structure [17] (a)	78	2939	297.53 nW
Proposed DDSM4 4-4-4-10 bit (b)	74	2503	14.059 nW
a/b%	94%	85%	47 times

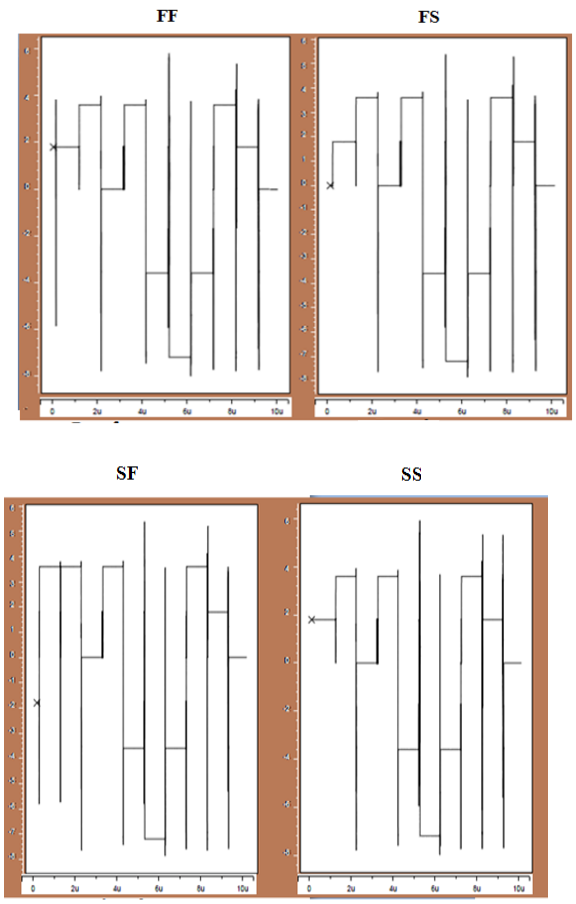

Fig .11. Time waves of the proposed Sigma-Delta modulator with manufacturing technology of 0.18 micrometers per input $X_1 = 7$, $X_2 = 13$, $X_3 = 9$, $X_4 = 472$ and modules $M_1 = 13$, $M_2 = 16$, $M_3 = 16$, $M_4 = 1024$ and the clocked pulse frequency is 1 MHz.

V. THE PROPOSED PLL CIRCUIT

In GSM450 telecommunication system, the synthesizer input frequency is 13 MHz and its output frequency is 450 MHz. In the following, the different parts of this PLL synthesizer circuit are designed.

A. *Phase /Frequency Detector (PFD)*

The PFD circuit is shown in Fig.12. The most important aspect of the phase detector (PD) design is the estimation of the reset path delay. One of the disadvantages of the phase / frequency detector circuit is the presence of a dead zone. In this case, the output pulses become so narrow that they cannot activate the charge pump circuit.

In this figure, four inverting gates are used to delay the reset path. Gates have also been used to connect the Up and Down signals to the charge pump. In this circuit, flip-flops in the Fig.13 are used. This flip-flop has normal and pulse-sensitive reversing gates. In a clocked pulse sensitive inverter gate, if the clocked pulse is equal to one, the gate is activated and if it is zero, the gate does not operate.

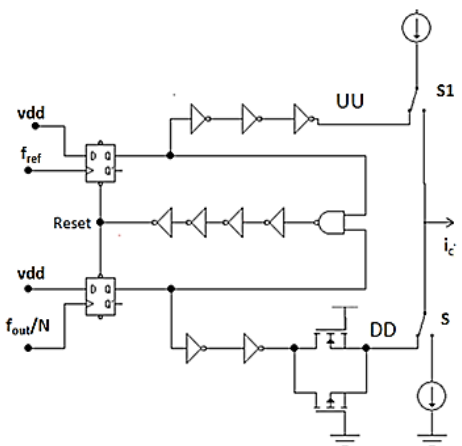

Fig. 12. PFD circuit selected in this synthesizer.

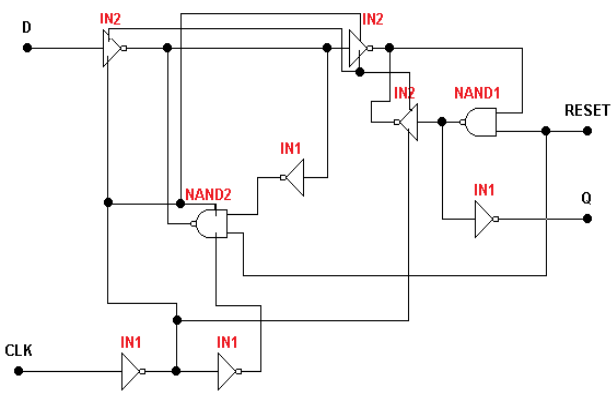

Fig. 13. The D flip-flop circuit with reset base and use of dynamic gates.

B. *Charge Pumping (CP)*

The CP circuit at the transistor level is shown in Fig.14. Transistors M_1, M_2 act as switches to reduce load injection error, undesirable reference tones, and current mismatch. Transistors M_1-M_4 perform the task of switching the charge pump. The rest of the transistors are current mirrors that repeat a certain amount of current at the output. In addition, the

current of the CP circuit is considered equal to 50 microamperes.

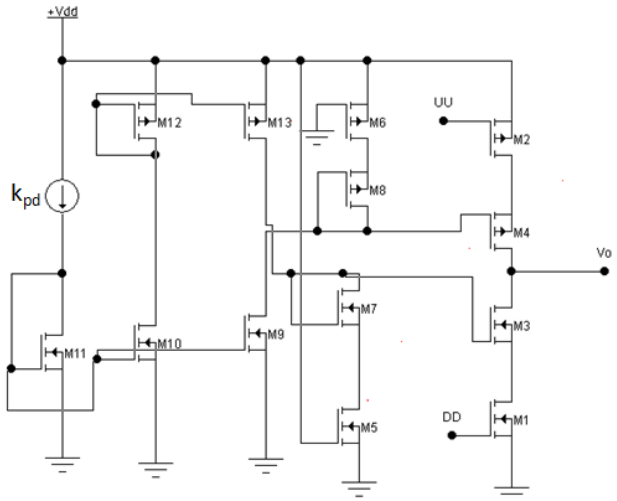

Fig. 14. CP circuit at the transistor level.

C. *Loop filter*

This synthesizer uses a third-order loop filter. This loop filter works in such a way that the response speed is reduced. The narrower the bandwidth of the filter, the lower the cut-off frequency of the filter, and consequently, the slower the loop response time to respond to changes. The circuit of this filter is shown in Fig15. The transfer function of this filter is Equ. (47). The values of the elements of this loop filter are shown in Table IV. Fig.16 shows the time domain waveforms of this PFD / CP / Loop filter.

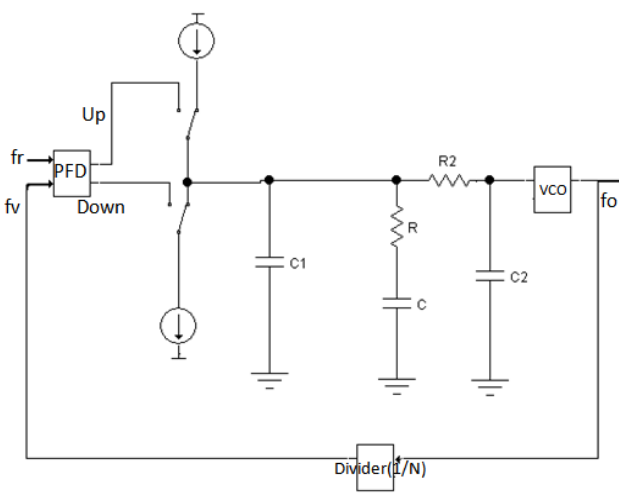

Fig. 15. The proposed CP phase locked loop circuit with a third-order filter.

$$F(s) = \frac{1+RCs}{R.R2.C.C1.C2s^3+((C1+C2)RC+R2.C2.(C+C1))s^2+(C+C1+C2)s} \quad (47)$$

D. *Divider into feedback path*

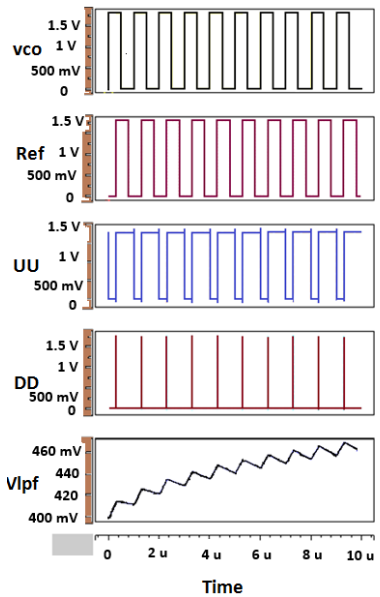

Fig. 16. Waveforms of PFD / CP / loop filter on transistor level.

TABLE IV
VALUES OF LOOP FILTER ELEMENTS IN THIS SYNTHESIZER.

Transistor Type	Power Consumption
N	30-38
f_{ref}	13 MHz
f_{out}	430-450 MHz
K_{pd}	50 µA
C_1	780 pF
C	3.4 nF
C_2	78 pF
R	3.9 KΩ
R_1	306 Ω

will use three counters, as shown in Fig17. In the proposed divider, there is a dual divider P / P + 1 (in this case 5, 6) which divides its input signal by 5, 6 according to the control input. The value of the fractional divider can be programmed as Equ. (48).

$$\mathbf{n_{frac} = 5 \times (6 + N_A) + N_B} \quad (48)$$

where N_A, N_B are the loaded numbers of counter A and B, respectively. These counters are static CMOS in full scale and operate at a frequency of 450 MHz. The time domain waveforms of this divider are shown in Fig.18.

E. *Voltage Control Oscillator (VCO)*

VCO circuits are divided into three categories. NMOS (N metal oxide semiconductor) category, PMOS (P metal oxide semiconductor) category and CMOS (Complementary metal

oxide semiconductor) category. The active circuit of the first type consists of a pair of transistors of type N, which are placed in a cross couple. The advantages of this structure are more simplicity, less noise. One of its disadvantages is its relatively high power consumption. Type P structures are made of PMOS transistors and their power consumption and noise performance are weaker. CMOS structures are made of a pair of N, P type transistors that have lower current consumption, but higher power consumption, noise, jamming capacitance, and complexity. Therefore, in this paper we use the N-type circuit. (Fig.19)

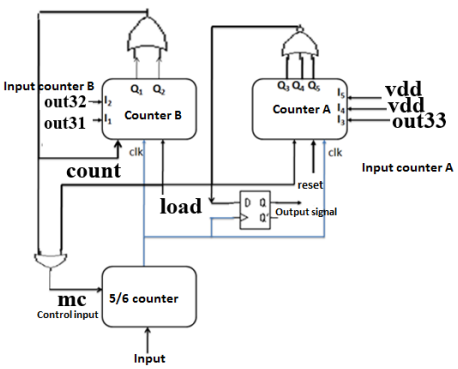

Fig. 17. Multi -module divider structure using 5,6 pre-divider and programmable counter.

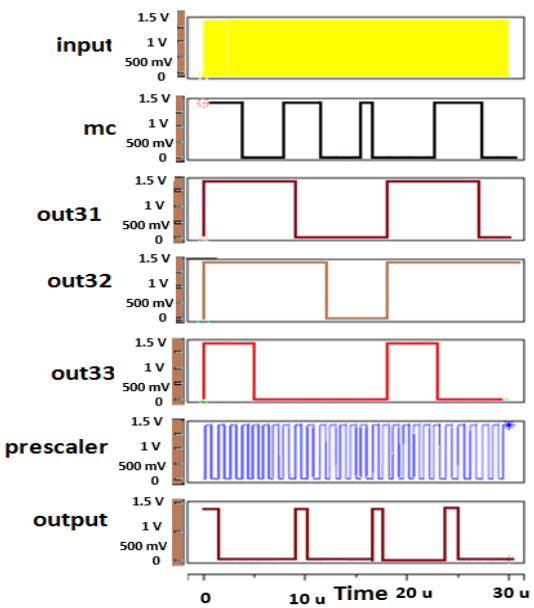

Fig. 18. The waveforms of multi modulus divider with three counters.

In the proposed phase locked loop circuit, the introduced fourth-order Sigma-Delta modulator is used.

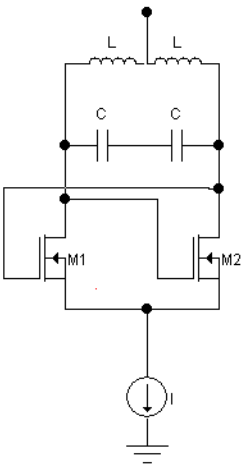

Fig. 19. The NMOS type differential tank circuit in this paper.

Table V compares the proposed method with other methods in terms of power consumption and number of transistors. As this table shows, the number of transistors in this modulator is less than other methods and has lower power consumption.

TABLE V
COMPARISON OF THE PROPOSED DESIGN WITH OTHER METHODS.

Methods	Power Consumption	Transistor Count
[4]	127 nW	2570
[18]	280 nW	2800
[22]	300 nW	2939
[28]	150 nW	2700
Proposed method	100 nW	2503

In this structure, the Carry Skip Adder (CSA) stages have been used as 1-2-3-3-5-3-3-2-1. CMOS transistors are used to make adder circuits. Each logic gate and flip flop is made by CMOS transistors and finally the number of transistors is counted. This configuration has 2939 CMOS transistors. Therefore, in total, the hardware consumption in the proposed method has reached 85% and has decreased by 15%. The total power consumption of a conventional 23-bit fourth-order structure with different transistor models is shown in Table VI, which is much higher than the proposed method.

VI. Conclusions

This paper presents a novel method for digital delta-sigma modulators (DDSMs) that can be used for precision frequency synthesizers. The hybrid DDSM 1-2-3-4 has four stages and the inputs of these stages are fixed numbers. The first stage of this modulator is programmable EFM1 and the module is not power of two. The second stage is a second-order modulator whose modulus of power of 2. The third stage is a third-order modulator with different modules and the fourth stage is a

fourth-order modulator with a dither signal. Optimal input signals are applied to each modulator to provide error masking. In this method, the input with high word length is divided into several optimal and smaller parts and each input is applied to a modulator. The proposed multi-stage Sigma-Delta modulator circuit has 4-4-4-10 bits, whose power consumption for normal transistor models is 14.08 nW. The clocked pulse signal frequency of 1 MHz is selected and the number of transistors in this circuit is 2503 complementary transistors. the conventional 1-1-1-1 MASH Sigma-Delta modulator has 2939 CMOS transistors. Therefore, in total, the hardware consumption in the proposed method has reached 85% and has decreased by 15%. It also simulates corner effects. A PLL circuit was also designed and implemented. In this PLL circuit, a frequency/ phase detector, a charge pump (CP) circuit, a third-order loop filter and a voltage-controlled oscillator (VCO) of the type NMOS are used. Meanwhile, in the feedback path of this PLL, a divider with three counters has been introduced and implemented. The waveforms of this PLL circuit were also plotted in the time domain.

TABLE VI

COMPARISON OF POWER CONSUMPTION OF CONVENTIONAL 1-1-1-1 23-BIT MULTI- STAGE MODULATOR STRUCTURE WITH DIFFERENT N, P TRANSISTOR MODELS.

Type of Transistors	Power Consumption
TT	297.53 µW
FF	355.3 µW
FS	482.3 µW
SF	339.14 µW
SS	248.42 µW

REFERENCES

[1] K. Hosseini and M.P. Kennedy, *Minimizing Spurious Tones in Digital Delta–Sigma Modulators*, Springer, pp. 100-150, New York, 2011.

[2] S. Pamarti, J. Welz and I. Galton, "Statistics of the quantization noise in 1-bit dithered single-quantizer digital delta–sigma modulators", *IEEE Trans. Circuits Syst.I, Regular Paper*, Vol. 54, No. 3, pp. 492–503, 2007.

[3] S. Pamarti and I. Galton, "LSB dithering in MASH delta-sigma D/A converters", *IEEE Trans. Circuits Syst. I, Regular Papers*, Vol. 54, No. 4, pp. 779–790, 2007.

[4] M.P. Kennedy, H. Mo and B. Fitzgibbon, "Spurious tones in digital delta-sigma modulators resulting from pseudorandom dither", *journal of the Franklin Institute*, pp. 1-20, 2015.

[5] M.P. Kennedy, B. Fitzgibbon and K. Dobmeier, "Spurious Tones in Digital Delta-Sigma Modulators with Pseudorandom Dither", *978-1-4673-5762-IEEE*, pp. 2747-2750, 2013.

[6] V.R. Gonzalez-Diaz, M.A. Garcia-Andrade, G.E, Flores-Verdad and F. Maloberti, "Efficient dithering in MASH sigma–delta modulators for fractional frequency synthesizers", *IEEE Trans. Circuits Syst.I, Regular Papers*, Vol. 57, No. 9, pp. 2394–2403, 2010.

[7] M. Borkowski and J. Kostamovaara, "Variable modulus delta–sigma modulation in fractional-N frequency synthesis", *Electronics Letters*, Vol. 43, No. 25, pp. 1399-1400, 2007.

[8] K. Hosseini and M.P. Kennedy, "Maximum sequence length MASH digital delta-sigma modulators", *IEEE Trans. Circuits Syst.I, Regul. Pap.* Vol. 54, No. 12, pp. 2628–2638 2007.

[9] K. Hosseini and M.P. Kennedy, "Architectures for maximum sequence length digital delta–sigma modulators", *IEEE Trans. Circuits Syst.II, Express Briefs*, Vol. 55, No. 10, pp. 1104–1108, 2008.

[10] K. Hosseini and M.P. Kennedy, "Mathematical analysis of a prime modulus quantizer MASH digital delta–sigma modulator", *IEEE Trans.Circuits Syst.II, Express Briefs*, Vol. 54, No. 12, pp. 1105–1109, 2007.

[11] J. Song and I.C. Park, "Spur-free MASH delta–sigma modulation", *IEEE Trans.CircuitsSyst.I, Regular Papers*, Vol. 57, No. 9, pp. 2426–2437, 2010.

[12] K.J. Wang, A. Swaminathan and I. Galton, "Spurious Tone Suppression Techniques Appliedto a Wide-Bandwidth 2.4 GHz Fractional-N PLL". *IEEE Journal on Solid-State Circuits*, Vol. 43, No. 12, pp. 2787–2797, 2008.

[13] M.P. Kennedy, H. Mo, B. Fitzgibbon, A. Harney, H. Shanan and M. Keaveney," 0.3–4.3 GHz Frequency-Accurate Fractional- Frequency Synthesizer With Integrated VCO and Nested Mixed-Radix Digital- Modulator-Based Divider Controller", *IEEE journal of solid state circuits*, Vol. 49, No. 7, pp. 1595-1605, 2014.

[14] S.A. Sadatnoori, E. Farshidi and S. Sadughi, "A novel structure of dithered nested digital delta-sigma modulator with low-complexity low-spur for fractional frequency synthesizers", *COMPEL - The international journal for computation and mathematics in electrical and electronic*, Vol. 35, No. 1, pp. 157-171, 2016.

[15] S.A. Sadatnoori, E. Farshidi and S. Sadughi, "A Novel Architecture of Pseudorandom Dithered MASH Digital Delta-Sigma Modulator with Lower Spur ", *Journal of Circuits, Systems and Computers*, Vol. 25, No. 7: pp. 1650072-1, 1650072-18, 2016.

[16] H. Mo and M.P. Kennedy, "Masked Dithering of MASH Digital Delta-Sigma Modulators With Constant Inputs Using Multiple Linear Feedback Shift Registers, *IEEE Transactions on Circuits and Systems I: Regular Papers*, 64(6) , 1390-1399, (2017).

[17] Y. Zhang, R. Wunderlich and S. Heinen, "A low-complexity low-spurs digital architecture for wideband PLL applications", *Microelectronics Journal*, Vol. 45, pp. 842–847, 2014.

[18] W.J. Lancioni, F.C. Dualibe, P. Petrashin, L. Toledo and L. Vazquez, "Continuous time full-feedforward MASH 2-2 architecture for sigma-delta modulators", *2018 IEEE 9th Latin American Symposium on Circuits & Systems (LASCAS)*, pp. 1-4, 2018.

[19] Y. Liao, X. Fan and Z. Hua, "Influence of LFSR Dither on the Periods of a MASH Digital Delta-Sigma Modulator", *IEEE Transactions on Circuits and Systems II: Express Briefs*, Vol. 66, No. 1, pp. 66-70, 2019.

[20] Z. Ye. and M.P. Kennedy, "Hardware reduction in digital delta-sigma modulators via error masking—Part I: MASH DDSM",*IEEE Trans. Circuits Syst. I, Reg. Papers*, Vol. 56, No. 4, pp. 714–726, 2009.

[21] Z. Ye. and M.P. Kennedy, "Hardware reduction in digital delta-sigma modulators via error masking—Part II: SQ-

DDSM", *IEEE Trans. CircuitsSyst. II, Exp. Briefs*, Vol. 56, No. 2, pp. 112–116, 2009.
[22] Y. Liao , X. Fan and Z. Hua, "Influence of LFSR Dither on the Periods of a MASH Digital Delta–Sigma Modulator", *IEEE Transactions on Circuits and Systems II: Express Briefs*, Vol. 66, No. 1, pp. 66-70, 2019.
[23] L. Le and G. Chen, "Designing and Optimizing of Sigma-Delta Modulator Using PSO Algorithm", *IEEE International Conference of Safety Produce Informatization (IICSPI)*, China, 2019.
[24] V. Mazzaro and M.P. Kennedy, "Mitigation of Horn Spurs in a MASH-Based Fractional-N CP-PLL"; *IEEE Transactions on Circuits and Systems II: Express Briefs*, Vol. 67, No. 5, pp. 821-825, 2020.
[25] D. Mai and M.P. Kennedy, "Analysis of Wandering Spur Patterns in a Fractional- *N* Frequency Synthesizer With a MASH-Based Divider Controller", IEEE Transactions on Circuits and Systems I: Regular Papers, Vol. 67, No. 3, pp. 729-742, 2020.
[26] A. Shamsi, "A new Mismatch cancelation for Quadrature Delta-Sigma Modulator"; *International Journal of Industrial Electronics Control and Optimization IECO*, Vol. 3, No. 2,pp. 196-204, 2020.
[27] D. Mai, Y. Donnelly, M.P. Kennedy,S. Tulisi, J. Breslin, P. Griffin, M. Connor, S. Brookes, B. Shelly and M. Keaveney, "Wandering Spur Suppression in a 4.9-GHz Fractional-N Frequency Synthesizer", *IEEE Journal of Solid-State Circuits* , Vo1. 1, No.1, 2022.
[28] A.M. Abdul and U.R. Nelakuditi, "A Linearized Charge Pump for Power and Phase Noise Efficient Fractional-N PLL Design", *2021 5th International Conference on Trends in Electronics and Informatics (ICOEI)*, 2021.

Leila Jahanpanah received the BSc degree in Electrical Engineering from the Islamic Azad University of Arak Branch in 2005, and the MSc degree in Electrical Engineering from the Islamic Azad University Arak Branch, Iran, in 2010.She is currently a PHD. student in Electrical Engineering at the Mahshahr Branch Islamic Azad University. Her research interests include circuit theory, analog circuit design, Analog to digital modulator.

Seyed Ali Sadatnoori received his Bsc degree in Electrical Engineering from the Islamic Azad University of Dezful Branch and Msc degree in Electrical Engineering from the central Tehran branch Islamic azad university, respectively, in 2001 and 2006. He received PHD degree in Electrical Engineering from the Tehran science and research branch Islamic Azad University, in 2016. He is also an Assistant Professor of Shoushtar Branch Islamic Azad University. His current research interests include mobile ad hoc networks, wireless networks, transmitter and receiver circuits, Analog to digital modulator, integrated circuits, and neural network.

Iman Chaharmahali received the BSc degree in Electrical Engineering from the Islamic Azad University of Borujerd in 2007, and the MSc degree (Hons) in Electronics Engineering from Islamic Azad University, Arak, Iran, in 2010, where he is currently working toward the PHD degree in Electronics Engineering. His research interests include circuit theory, analog circuit design, modelling, and simulation, artificial neural networks and nano electronic.

IECO

This page intentionally left blank.

International Journal of Industrial Electronics, Control and Optimization © 2022 IECO
Vol. 5, No. 2, pp. 189-204, April (2022)

Adaptive Delay Compensator Based H_2/H_∞ Wide-Area Controller to Improve Damping of Inter-Area Oscillations

Esmaeel Rokrok [1,†], Saman Dehghaninejad [2], Amir Hossein Poursaeed [3]

[1,2,3] Department of Electrical Engineering, Lorestan University, Khorramabad, Iran

ABSTRACT

Recent technical advances in Wide-Area Measurement Systems (WAMS) have made it possible to use a combination of measured signals from remote locations to design centralized control. However, the transmission delay of remote signals and changes in the power system operating point are significant issues in the operation of the Wide-Area Damping Controller (WADC). Regarding issues and uncertainties in the power system, mixed H_2/H_∞ synthesis has been proposed for wide-area robust controller design. In this paper, an adaptive wide-area robust controller for Thyristor Controlled Series Capacitors (TCSC) is presented to improve the inter-area oscillation damping in multi-machine power systems in which the time-varying delays in feedback signal time are taken into account. So, an Adaptive Delay Compensator (ADC) is used to compensate for the delay of receiving remote signals. Despite the nonlinearity of the power system, the changes in the operating point, and the presence of time-varying delays, the proposed scheme shows robust performance in damping the low-frequency oscillations. The efficiency of the proposed control system in the presence of TCSC is shown through simulation results that show its superiority over the conventional control system. The simulation of the paper is carried out on the Four-Machine Two-Area test system and 10-machine, 39-bus New England power system.

Article Info

Research Article

Keywords:

Adaptive Robust Controller , Inter-Area Oscillation Damping, Time-Varying Delay ,Wide-Area Damping Controller

Article History:

Received 2021-11-28
Accepted 2022-05-19

I. INTRODUCTION

Once Damping inter-area modes of oscillation depend on different factors such as the system load level, the optimal transmission system design, the severity of the fault, and the type of system load [1]. Economically, power systems need to be operated near the system stability limit to reduce inter-area oscillations damping.

Also, the critical conditions are generated once the number of industrial loads and power electronics devices have increased, primarily constant power and constant current loads. Therefore, increasing the damping of inter-area oscillations is necessary to increase the transferable power using a suitable control strategy [2]. With the emergence and development of WAMS, many various controllers have been proposed to improve the performance of the power system [3]. Wide-Area Controller System (WACS) is used to improve the damping of inter-area oscillations which is called the Wide-Area Damping Controller (WADC). WADC for inter-area oscillation damping was first introduced in [4] under a hierarchical control structure, while Power System Stabilizers (PSSs) are used to stabilize local modes. WADC design method using wide-area signals can make it possible to select the optimal feedback signals with high observability from the inter-area modes of oscillation. As a result, WADC is more effective in damping inter-area oscillations than local controllers [5].

There is a time delay in transmitting feedback signals by a telecommunications channel from one place to another as an inherent feature of the WAMS. The delay depends on various factors such as the type of telecommunication channel, distance, and signal transmission protocol [6]. If the delay is

[†]**Corresponding Author**: rokrok.e@lu.ac.ir
Tel: +98-9166671706, Fax: +9866-33120088, Lorestan University
Department of Electrical Engineering, Lorestan University, Khorramabad,Iran

not correctly considered in the controller design, it can affect WADC performance and system stability. The design method of conventional lead-lag compensators is presented to compensate for the phase change caused by the signal transmission delay in [7]. In [8] and [9], the methods based on Lyapunov stability theory are used to take the latency in the telecommunication channel into account. Also, the Smith Predictor is used to compensate for a certain amount of delay in [10]–[12], in which the linear model of the system is designed at an operating point. Therefore, the predictor may be ineffective in compensating for the delay once the system's operating point changes and leads to the production of an unstable signal.

Controllers designed using the aforementioned methods have constant parameters. So, these controllers will perform well only in small changes in latency. To ensure the optimal performance of the controller under abnormal operating conditions, it is necessary to compensate for the time-varying delay using adaptive approaches. Adaptive Delay Compensator (ADC) for wide-area robust damping controller design is presented in [13]–[16].

In [17], a robust multipurpose controller has been used to design the wide-area controller. For this purpose, the control scheme is based on the use of hierarchical control. Another limitation that poses a severe challenge to WADC implementation is the uncertainty in the system dynamic model. In [13]–[17], first, the structure which is used to implement WADC is introduced, then the multipurpose controller design method is investigated by mixed H_2/H_∞ synthesis and pole-placement using Linear Matrix Inequalities (LMI).

In this paper, an adaptive wide-area robust controller for TCSC is designed to improve the damping of inter-area oscillations in multi-machine power systems by considering the time-varying delay in the transmission of feedback signals. The structure of the topics of the article is as follows. Section II describes the modeling of different power system components, such as generator, excitation system, PSS, load, and TCSC. Section III introduces the design method of the robust inter-area controller. In section IV, the implementation of the proposed method for adaptive delay compensation is introduced. In section V, the results of the ADC-based wide-area controller for TCSC applied to the Four-Machine Two-Area test system and 39-bus New England power system are discussed. Finally, the conclusion is given in section VI.

II. MODELLING OF POWER SYSTEM COMPONENTS

performance as well as system stability. Power system dynamics and electrical relationships, which are described by differential equations, are nonlinear by nature. These equations represent the dynamical model of elements such as generators, excitation systems, governors, PSS, wind turbines, FACTS devices, etc. Generally, the power system can be expressed by a set of first-order differential and algebraic equations. With differential equations of power system components as well as the algebraic equations of the transmission network, the mathematical model of the whole system can be expressed by Eq. (1) [18], [19]:

$$\begin{cases} \dot{x_s} = f(x_s.d.u) \\ 0 \;\; = g(x_s.d.u) \\ y_s = h(x_s.d.u) \end{cases} \quad (1)$$

Where the vector function f defines the differential equations while g and h are the algebraic vector functions of the power system static equations. Also, x_s is the vector state variables of the system which is defined by Eq. (2).

$$\begin{aligned} x_s = [&\lambda_{1d1} \;\; \lambda_{1d2} \;\cdots\; \lambda_{1di} \,.\lambda_{2q1} \;\; \lambda_{2q2} \;\cdots \lambda_{2qi} \,. \\ &E'_{d1} \;\; E'_{d2} \cdots E'_{di}.E'_{q1} \;\; E'_{q2} \;\cdots E'_{qi}.\delta_1 \;\;\; \delta_2 \;\; . \\ &\omega_1 \;\; \omega_2 \;\; \cdots \;\; \omega_i. \;\; X_{1E1} \;\; X_{1E2} \;\; \cdots \;\; X_{1Ei}.X_{2E1} \;\; X_{2E2} \\ &X_{3E1} \;\; X_{3E2} \;\; \cdots \;\; X_{3Ei}.X_{tcsc}]^T \end{aligned} \quad (2)$$

Also, d is the vector of power system variables, as shown in Eq. (3).

$$\begin{aligned} &d \\ &= [\theta_1 \;\;\;\; \theta_2 \;\; \cdots \;\; \theta_{n_{bus}} \,.V_1 \;\;\;\; V_2 \;\;\; \cdots \;\;\; V_{n_{bus}} \,]^T \end{aligned} \quad (3)$$

Generally, the system inputs include governor reference, excitation system voltage, generator rotor speeds, and TCSC reference compensation percentage. In this paper, the reference voltage and rotor speed of the generators are considered the system's inputs, which are defined in Eq. (4).

$$u = [V_{WADCi} \;\;\; . \;\;\; X_{WADCi} \;]^T \;\;\; : i \in \{cg\} \quad (4)$$

cg refers to a set of controlled generators that damping of inter-area oscillations by applying control signals to their excitation system. Also, the static load model can be considered as Eqs. (5-6) [19]:

$$P_L(V) = \; P_0(A_1 + A_2\frac{V}{V_0} + A_3(\frac{V}{V_0})^2) \quad (5)$$

$$\mathrm{Q_L(V)} = \; \mathrm{Q_0(B_1 + B_2\frac{V}{V_0} + B_3(\frac{V}{V_0})^2)} \quad (6)$$

Where P_0 and Q_0 are the active and reactive load power at rated voltage V_0, respectively. Also, P_L and Q_L represent the active and reactive load power at V voltages, respectively. Also, the weighting factors $\mathrm{A_3}, \mathrm{A_2}, \mathrm{A_1(B_3}, \mathrm{B_2}, \mathrm{B_1})$ represent the share percentage of active (reactive) load of constant impedance, constant current, and constant power, respectively. It should be noted that constant impedance and constant power load models are used in the Four-Machine Two-Area and 39-bus New England test systems, respectively. The relationship between these weighting factors must be established, as shown in Eq. (7).

$$\mathrm{A_1 + A_2 + A_3} = B_1 + B_2 + B_3 = 1 \quad (7)$$

The sub-transient model is also used to model the synchronous generators which are shown in Eqs. (8)-(13) [1].

$$T'_{d0i}\dot{E}'_{qi} = -E'_{qi} - (x_{di} - x'_{di})\left[i_{di} - \frac{x'_{di} - x''_{di}}{(x'_{di} - x_{li})^2}(\lambda_{1di} + (x'_{di} - x_{li})i_{di}) - E'_{qi}\right] + E_{fdi} \quad (8)$$

$$T''_{d0i}\dot{\lambda}_{1di} = -\lambda_{1di} + E'_{qi} - (x'_{di} - x_{li})i_{di} \quad (9)$$

$$T'_{q0i}\dot{E}'_{di} = -E'_{di} + (x_{qi} - x'_{qi})\left[i_{qi} - \frac{x'_{qi} - x''_{qi}}{(x'_{qi} - x_{li})^2}(\lambda_{2qi} + (x'_{qi} - x_{li})i_{qi}) + E'_{di}\right] \quad (10)$$

$$T''_{q0i}\dot{\lambda}_{2qi} = -\lambda_{2qi} - E'_{di} - (x'_{qi} - x_{li})i_{qi} \quad (11)$$

$$\dot{\delta}_i = \omega_i - \omega_s \quad (12)$$

$$2H_i\dot{\omega}_i = P_{mi} - (i_{qi}\lambda_{di} - i_{di}\lambda_{qi}) - K_{Di}(\omega_i - 1) \quad (13)$$

The IEEE type AC4A excitation system model is used in this paper. The block diagram of the excitation system is shown in Fig. 1 [18]. Differential equations that show the dynamic behavior of this type of excitation system defined as Eqs. (14)-(17).

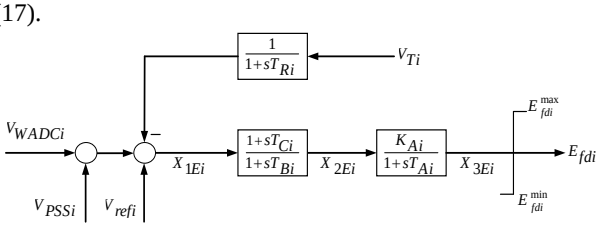

Fig. 1. IEEE type AC4A excitation system model

$$\dot{E}_{fdi} = \frac{K_{Ai}X_{2Ei}}{T_{Ai}} - \frac{1}{T_{Ai}}E_{fdi} \quad (14)$$

$$\dot{X}_{1Ei} = -\frac{1}{T_{Ri}}X_{1Ei} + \frac{1}{T_{Ri}}V_{Ti} \quad (15)$$

$$\dot{X}_{2Ei} = \frac{1}{T_{Bi}}\left(\frac{T_{Ci}}{T_{Ri}} - 1\right)X_{1Ei} - \frac{1}{T_{Bi}}X_{2Ei} - \frac{T_{Ci}}{T_{Bi}T_{Ri}}V_{Ti} + \frac{1}{T_{Bi}}(V_{WADCi} + V_{PSSi} + V_{refi}) \quad (16)$$

$$E_{fdi} = \begin{cases} E_{fdi}^{min} \\ X_{3Ei} \quad ; E_{fdi}^{min} \le X_{3Ei} \le E \\ E_{fdi}^{max} \end{cases} \quad (17)$$

The third-order model was used to design the PSS to stabilize the local modes of oscillations, as shown in Fig. 2. The rotor speed of the generator is used as an input signal to the PSS. So, Eqs. (18)-(20) represent the dynamic behavior of the PSS model.

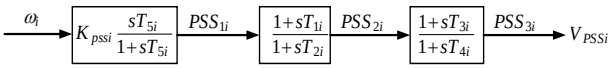

Fig. 2. Type PSS1A power system stabilizer model

$$P\dot{S}S_{1i} = -\frac{1}{T_{5i}}PSS_{1i} + K_{pssi}\frac{1}{120\pi}\dot{\omega}_i \quad (18)$$

$$P\dot{S}S_{2i} = -\frac{1}{T_{2i}}PSS_{2i} + \frac{1}{T_{2i}}PSS_{1i} + \frac{T_{1i}}{T_{2i}}P\dot{S}S_{1i} \quad (19)$$

$$P\dot{S}S_{3i} = -\frac{1}{T_{4i}}PSS_{3i} + \frac{1}{T_{4i}}PSS_{2i} + \frac{T_{3i}}{T_{4i}}P\dot{S}S_{2i} \quad (20)$$

Also, the dynamical model of TCSC considering the delay in thyristor firing angles is depicted by a lag compensator block in Fig. 3 [20]. Therefore, the output reactance changes can be expressed by Eqs. (21)-(24).

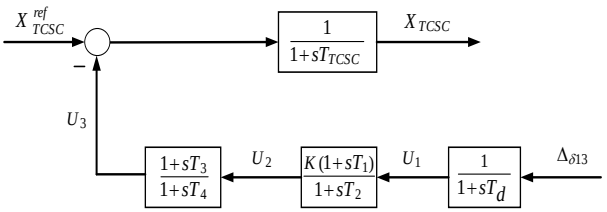

Fig. 3. TCSC block diagram

$$\dot{U}_0 = -\frac{1}{T_d}U_0 + \frac{1}{T_d}\Delta_{\delta 13} \quad (21)$$

$$\dot{U}_1 = -\frac{1}{T_2}U_1 + \frac{1}{T_2}KU_0 + \frac{T_1}{T_2}K\dot{U}_0 \quad (22)$$

$$\dot{U}_3 = -\frac{1}{T_4}U_3 + \frac{1}{T_4}U_1 + \frac{T_3}{T_4}\dot{U}_1 \quad (23)$$

$$\dot{X}_{tcsc} = -\frac{1}{T_{tcsc}}X_{tcsc} + \frac{1}{T_{tcsc}}X_{TCSC}^{ref} - \frac{1}{T_{tcsc}}U_3 \quad (24)$$

Where U_3 is a complementary control signal generated through a third-order dynamical model with generator rotor angle changes as its input. Also, the connection between the dynamic equations of the generators is established through the network admittance model. In the two-axis model of the synchronous generator, the dynamics of each machine are presented in a d-q reference frame that rotates at the speed of the machine rotor. To solve these equations, it is necessary to define a single reference frame for the whole system, called the system reference frame, and express all voltages and currents in that reference frame. The system reference frame rotates at synchronous speed. The voltage and current quantities of each machine can be expressed in the d-q reference frame of the machine or the system reference frame (R-I axes), as shown in Fig. 4. According to Fig.4, Eqs. (25) and (26) will be

established between the d-q and R-I quantities.

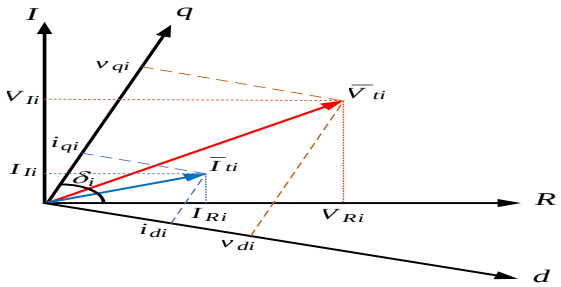

Fig. 4. The system reference frame and i^{th} generator reference frame

$$\bar{V}_{ti} = V_{Ri} + jV_{Ii} = (v_{di} + jv_{qi})e^{j(\delta_i - \frac{\pi}{2})} \quad (25)$$

$$\bar{I}_{ti} = I_{Ri} + jI_{Ii} = (i_{di} + ji_{qi})e^{j(\delta_i - \frac{\pi}{2})} \quad (26)$$

III. Wide-Area Damping Controller Design

This paper uses a robust multipurpose control based on [21] to design the wide-area controller. For this purpose, a two-level hierarchical control scheme is used with local controllers at the first level while the wide-area controller is implemented at the second stage. The hierarchical control scheme has minimum damping due to the performance of local controllers in the case of loss of telecommunications [3], [22]–[24].

The main goal of the multipurpose controller design is to use the combination of time and frequency domain performance of mixed H_2/H_∞ synthesis and defining the constraints of closed-loop poles placement in the desired location. In the design of the single-purpose H_∞ controller, robust stability, and elimination of output disturbance are achieved by H_∞ synthesis. In the multipurpose controller design of mixed H_2/H_∞ synthesis, the H_∞ synthesis is only used to obtain robust stability against model uncertainty, while the elimination of output disturbance with considered limitations is carried out by H_2 synthesis. So, the multipurpose controller has a better transient response than the single-purpose scheme. The block diagram of the closed-loop system with WADC utilizing the multipurpose design is shown in Fig. 5, where u_{wadc} and y_{wadc} represent the wide-area controller's input vector and output vector, respectively [25].

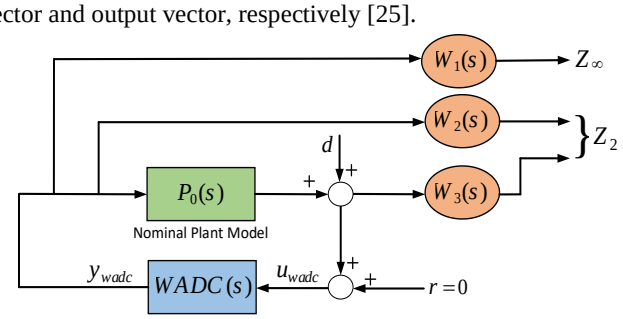

Fig. 5. Multipurpose controller design using weighting functions

In Fig. 5, the output channel z_∞ corresponds to optimizing the H_∞ performance while the output channel z_2 aims to improve the H_2 performance. Also, $W_3(s)$, $W_2(s)$ and $W_1(s)$ are the weighting functions in the frequency domain. The $W_3(s)$ function, which is in the z_2 channel, is a low-pass filter used to eliminate the disturbance effect on the output. Also, the weighting function $W_2(s)$ is a high-pass filter which usually is considered as a small constant number to minimize the disturbance effect on the controller output. Finally, the weighting function $W_1(s)$, which is in the output channel of Z_∞, is a high-pass filter used to robust stability against the model uncertainty. Furthermore, $P_0(s)$ is the nominal plant of the system which is obtained by the reduced model of the power system. The delay has been considered in this system linear model [15]. So, the system shown in Fig. 5 can be shown as a Linear Fractional Transformation (LFT) model in Fig. 6, where $\tilde{P}_0(s)$ represents the modified plant model with weighting functions.

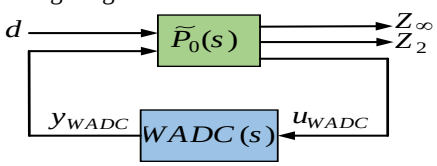

Fig. 6. LFT block diagram for the multipurpose design approach

$$\begin{cases} \dot{x}_P = A_P x_P + B_{Pd} d + B_P y_{wadc} \\ z_\infty = C_x x_P + D_{dx} d + D_x y_{wadc} \\ z_2 = C_2 x_P + D_{d2} d + D_2 y_{wadc} \\ y_s = u_{wadc} = C_P x_P + D_{pd} d \end{cases} \quad (27)$$

$$\begin{cases} \dot{x}_k = A_k x_k + B_k u_{wadc} \\ y_{wadc} = C_k x_k + D_k u_{wadc} \end{cases} \quad (28)$$

So, state-space equations of the closed-loop system can be expressed in Eq. (29).

$$\begin{cases} \dot{x}_{cl} = A_{cl} x_{cl} + B_{cl} d \\ z_\infty = C_{cl1} x_{cl} + D_{cl1} d \\ z_2 = C_{cl2} x_{cl} + D_{cl2} d \end{cases} \quad (29)$$

Where x_{cl}, C_{cl1}, and C_{cl2} are defined as Eqs. (30)-(32), respectively.

$$x_{cl} = \begin{pmatrix} x_p \\ x_k \end{pmatrix} . A_{cl} = \begin{pmatrix} A_P + B_P D_K C_P & B_P C_K \\ B_K C_P & A_K \end{pmatrix} . \begin{pmatrix} B_{pd} + B_p D_k D_{pd} \\ B_k D_{pd} \end{pmatrix} \quad (30)$$

$$C_{cl1} = \begin{pmatrix} C_\infty + D_\infty D_k C_p & D_\infty C_k \end{pmatrix} . \quad D_{cl1} = D_{d\infty} + D_\infty D_k D_{pd} \quad (31)$$

$$C_{cl2} = \begin{pmatrix} C_2 + D_2 D_k C_p & D_2 C_k \end{pmatrix} . \quad D_{cl2} = D_{d2} + D_2 D_k D_{pd} \quad (32)$$

According to Fig. 5, the main objectives of WADC design are as follows. 1) Improve H_∞ synthesis performance to controller robustness against system uncertainties, 2) Improve H_2 synthesis performance to improve controller performance

once the system is subjected to large disturbances, 3) Placement of the closed-loop poles in a specific location on the left-half plane to achieve a desired transient response. In mathematical terms, multipurpose controller design can be expressed as an optimization problem that minimizes mixed H_2/H_∞ synthesis, which is displayed as Eq. (33).

$$\begin{aligned} &Minimize\ \ a_\infty \left\| T_{dz_\infty}(s) \right\|_\infty^2 + a_2 \left\| T_{dz_2}(s) \right\|_2^2 \\ &subject\ \ to: \\ &poles\ \ \in region \end{aligned} \tag{33}$$

Where $T_{dz_\infty}(s)$ and $T_{dz_2}(s)$ are the closed-loop transfer functions of the disturbance d to the outputs z_∞ and z_2, respectively. $\left\| T_{dz_\infty}(s) \right\|_\infty$ and $\left\| T_{dz_2}(s) \right\|_2$ represent the H_∞ and H_2 norms of the $T_{dz_\infty}(s)$ and $T_{dz_2}(s)$ transfer functions, respectively. Also, a_∞ and a_2 weighting factors. To achieve the desired transient response, it is necessary to place the closed-loop poles in the left-half plane. This specific location for the placement of closed-loop poles is considered according to Fig. 7. Therefore, the maximum settling time and the minimum inter-area oscillation damping ratio will be limited to $4/a$ and $\cos(\beta)$, respectively.

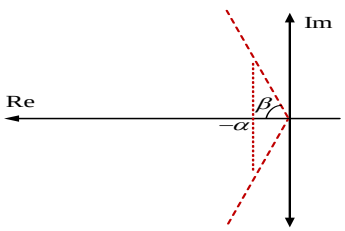

Fig. 7. The region of interest for the pole-placement of the closed-loop system

IV. Adaptive Delay Compensator for Wide-Area Robust Controller Design

An ADC for the robust controller system to dampen the inter-area oscillations has been presented. The implementation of the proposed method contains two main steps: 1) To design an ADC, First, ADC is defined as the weighted sum of several phase compensators with the consideration of the delay variation range. Then, the weighting factors are adjusted in real-time according to the measured delay value to compensate for the time-varying delay. 2) To design the robust controller, the delay compensator is considered as a part of the controlled system, and the WADC controller is designed using the method as mentioned above described in Section III to improve the damping of inter-area oscillations.

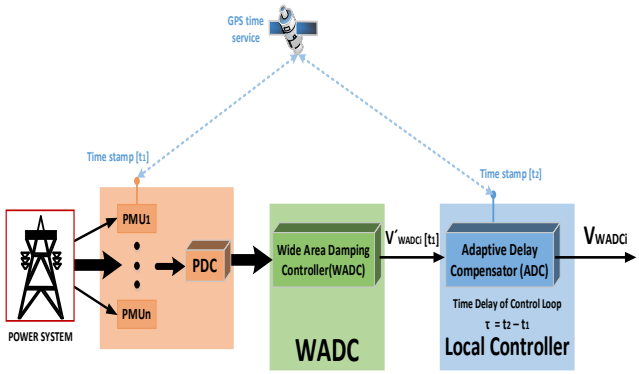

Fig. 8. Control structure based on generator excitation system with ADC

The most crucial point to remember about continuous-time delay compensation is the robustness of WADC against delay changes. However, the ADC can easily extract the delay model and use it to design WADC and its robustness against delay changes. The delay caused by signal transmission becomes even more critical once the used control scheme is the wide-area controller [26]. The structure of the wide-area control system with the ADC is shown in Fig. 8. PMU measurements are collected at t_1 and synchronized in Phasor Data Concentrator (PDC) [27]. When one or more telecommunications links become overloaded, the PDC waits until it receives all the signals with timestamp t_1 and sends feedback signals to the WADC after the measured signals are synchronized. After receiving the feedback signals, WADC calculates the control signal V'_{WADC_i} with the timestamp t_1 and sends it to the ADC located at the control center. When ADC receives control signal V'_{WADC_i} (corresponds to timestamp t_1), the control loop delay is calculated as $\tau = t_2 - t_1$, where t_2 represents the new timestamp currently that the control signal reaches the delay compensator. Also, it is determined in real-time by the Global Positioning System (GPS). So, the ADC generates the appropriate phase value to compensate for the measured delay. Then, the compensated signal V_{WADCi} is applied to the Automatic Voltage Regulator (AVR) input mounted on the synchronous generator excitation system or FACTS compensator to achieve desirable dynamical performance. In this paper, the ADC performance is evaluated in a wide-area control system on the TCSC. Also, it is assumed that the WADC is located near of the TCSC installed location. So, the proposed control scheme is shown in Fig. 9. In the presented scheme, ADC receives the feedback signal M (corresponds to timestamp t_1) from the data center. ADC performs the phase compensation concerning measured delay and applies the compensated signal to the WADC input. So, WADC calculates the control signal X_{WADC} and apply it to TCSC to improve the damping of inter-area oscillations.

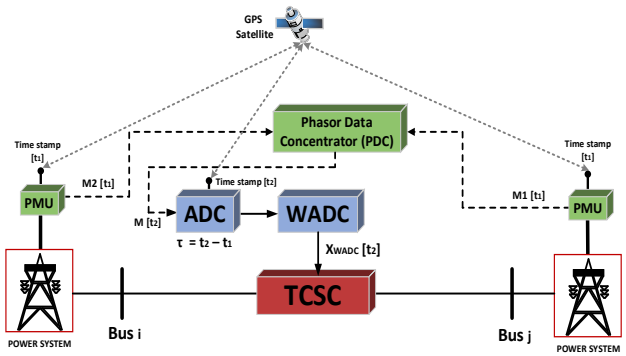

Fig. 9. The proposed control scheme based on TCSC usage with ADC

A. *The delay of the WAMS communication network*

The delays in the WAMS communication network are caused by the measurements' processing time, synchronization, sending of measurement signals, calculation of control signals, and sending them. Therefore, the total delay is equal to the time it takes to send a measured signal by the PMU to the control center. Conventional telecommunication lines in the WAMS are generally divided into two categories; wired links and wireless links. Satellite and digital microwave links are the most used wireless links, while fiber-optic lines, Power Line Carriers (PLCs), and telephone lines are among the most common wired links. The delay for these conventional telecommunication lines is shown in Table I[28], [29].

TABLE I
DELAY FOR VARIOUS TELECOMMUNICATION LINES IN THE WAMS SYSTEM [30]

Telecommunication line type	Delay (milliseconds)
Fiber optic lines	100-150
Digital microwaves	100-150
Power line carrier	150-350
Telephone lines	200-300
Satellite	500-700

B. *Delay modeling*

The most widely used approach of delay modeling is to approximate it with a transfer function in a specific frequency range. The delay transfer function is generally defined as Eq. (34). A common approach used for delay modeling is the Pade Approximation of order n of the delay, which is presented as Eq. (35) [15].

$$G_d(s) = e^{-\tau s} \tag{34}$$

$$G_d^n(s) = \frac{\sum_{k=0}^{n} \frac{(-1)^k (2n-k)!\,n!}{2n!\,k!\,(n-k)!} \tau^k s^k}{\sum_{k=0}^{n} \frac{(2n-k)!\,n!}{2n!\,k!\,(n-k)!} \tau^k s^k} \tag{35}$$

The approximated delay model is obtained by Eq. (36).

$$G_D(s) = \frac{(1-\frac{s\tau}{2n})^n}{(1+\frac{s\tau}{2n})^n} \tag{36}$$

C. *Adaptive Delay Compensation Design*

The proposed ADC is a weighted sum of several compensators in which the weighting factor corresponds to each compensator is updated in continuous time according to the measured delay. To describe the ADC process, $\bar{G}_D(s)$ considered as a minimum phase transfer function, as shown in Eq. (37).

$$\bar{G}_D(s) = \frac{1}{(1+\frac{s\tau}{2n})^{2n}} \tag{37}$$

The phase of the $\bar{G}_D(s)$ the transfer function is the same as the approximate delay model phase expressed by the Eq. (36). Therefore, the transfer function of each compensator using $\bar{G}_D(s)$ is defined by Eq. (38).

$$DC_i(s) = K(T_i)\frac{\left(1+\frac{sT_i}{2n}\right)^{2n}}{(1+sT_c)^{2n}} \qquad i = 1,2,\cdots,m \tag{38}$$

Where $DC_i(s)$ represents the i^{th} compensator transfer function, m shows the number of compensators, T_i and T_c are the phase lead (numerator) and phase lag (denominator) time constants of the are i^{th} compensator, respectively. Also, K is the Gain Correction Factor (GCF), a function of the delay. So, the state-space equations of the compensators can be expressed using controllable canonical realization. The i^{th} compensator state-space equations will be defined as Eqs. (39) and (40).

$$\dot{x}_{ADC}(t) = A_{ADC}x_{ADC}(t) + B_{ADC}u_{ADC}(t) \tag{39}$$

$$y_{DC_i}(t) = C_{DC_i}x_{ADC}(t) + D_{DC_i}u_{ADC}(t) \tag{40}$$

Where A_{ADC} and B_{ADC} are state matrices and delay compensator inputs, respectively. Also, C_{DC_i} and D_{DC_i} are the output and direct supply matrices of the i^{th} compensator, respectively. x_{ADC} is the state variable vector of delay compensator, u_{ADC} represents the remote signal applied to the compensator input, and finally, y_{DC_i} represents the output of the i^{th} compensator. The proposed ADC is considered as a weighted sum of a small number of compensators where its transfer function is indicated in Eq. (41).

$$ADC(s) = \frac{N(s)}{D(s)} = \sum_{i=1}^{m} \beta_i(\tau) DC_i(s) \tag{41}$$

Where $N(s)$ and $D(s)$ are the polynomials of the numerator and denominator of ADC, respectively. Also, $\beta_i(\tau)$ is the weighting factor of the i^{th} compensator. If m is the number of compensators, then the weighting factors used in Eq. (41) can be obtained by Eq. (42).

$$\bar{\beta}(\tau) = \bar{T}^{-1}\bar{T}_\tau \tag{42}$$

Where $\bar{\beta}(\tau)$, $\bar{T}$, and $\bar{T}_\tau$ are expressed as Eqs. (43)-(45).

$$\bar{\beta}(\tau) = [\beta_1(\tau) \quad \beta_2(\tau) \quad \cdots \quad \beta_m(\tau)]^{\mathrm{T}} \tag{43}$$

$$\bar{T} = \begin{pmatrix} 1 & 1 & \cdots & 1 \\ T_1 & T_1 & \cdots & T_m \\ T_1^{\,2} & T_2^{\,2} & \cdots & T_m^{\,2} \\ \vdots & \vdots & \ddots & \vdots \\ T_1^{\,m-1} & T_2^{\,m-1} & \cdots & T_m^{\,m-1} \end{pmatrix} \tag{44}$$

$$\bar{T}_\tau = \begin{pmatrix} 1 \\ \tau \\ \tau^2 \\ \vdots \\ \tau^{m-1} \end{pmatrix} \tag{45}$$

The implementation of the proposed ADC is shown in Fig. 10, where matrices $\bar{C}_{ADC}$ and $\bar{D}_{ADC}$ are defined as Eqs. (46) and (47), respectively.

$$\bar{\mathrm{C}}_{\mathrm{ADC}} = [\mathrm{C_{DC1}}^{\mathrm{T}} \quad \mathrm{C_{DC2}}^{\mathrm{T}} \quad \cdots \quad \mathrm{C_{DCm}}^{\mathrm{T}}]^{\mathrm{T}} \tag{46}$$

$$\bar{\mathrm{D}}_{\mathrm{ADC}} = [\mathrm{D_{DC1}}^{\mathrm{T}} \quad \mathrm{D_{DC2}}^{\mathrm{T}} \quad \cdots \quad \mathrm{D_{DCm}}^{\mathrm{T}}]^{\mathrm{T}} \tag{47}$$

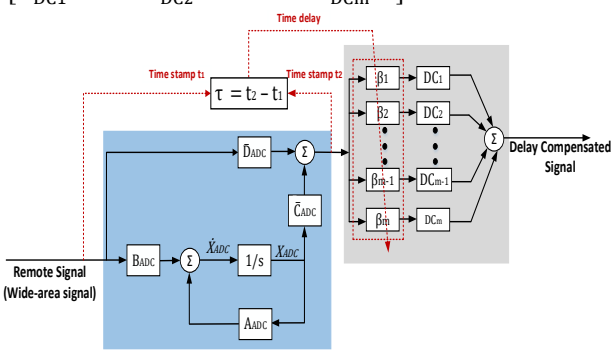

Fig. 10. The proposed ADC

The block diagram of the closed-loop system by considering WADC and ADC is depicted in Fig. 11. In this figure, $G_0(s)$ represents the linearized model of the power system, and the compensated delay model is represented by $CDM_t(s)$. To implement the ADC using Eq. (41), the compensated delay model will be represented as Eq. (48) [27].

$$\mathrm{CDM_\tau(s) = ADC(s)G_D(s)} = \frac{\sum_{i=1}^{m}\beta_i(\tau)\mathrm{K(T_i)}\left(1+\frac{\mathrm{sT_i}}{2n}\right)^{2n}}{(1+\mathrm{sT_c})^{2n}}\frac{(1-\frac{s\tau}{2n})^{n}}{(1+\frac{s\tau}{2n})^{n}} \tag{48}$$

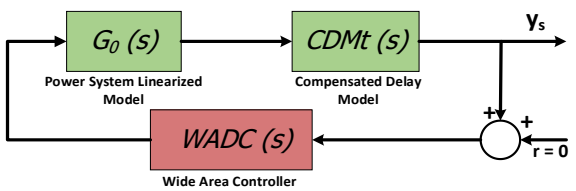

Fig. 11. Closed-loop system block diagram considering WADC and ADC

By considering the ADC, the common point of the system linearized and compensated delay models are considered the plant that the WADC is designed. The plant for the above-mentioned system displayed in Fig. 11 is defined as Eq. (49).

$$\mathrm{P(s) = G_0(s)CDM_\tau(s)} \tag{49}$$

V. Simulation Results

A. Case Study I: Four-Machine Two-Area Test System

To show the advantages of TCSC-based WADC performance, the proposed control scheme was applied to the Four-Machine Two-Area test system, which is shown in Fig. 12. It should be noted that PSSs are only installed on G1 and G3 generators, while PSSs for G2 and G4 generators have not been considered. The transfer function of the PSSs as mentioned earlier and the conventional wide-area controller are shown in Eqs. (50) and (51), respectively.

$$H_{PSS}(s) = 8\frac{7s}{1+8s}\left(\frac{1+008s}{1+003s}\right)^2 \tag{50}$$

$$H_{WADC}(s) = K_a\frac{7s}{1+8s}\left(\frac{1+0.08s}{1+0.03s}\right)^2 \tag{51}$$

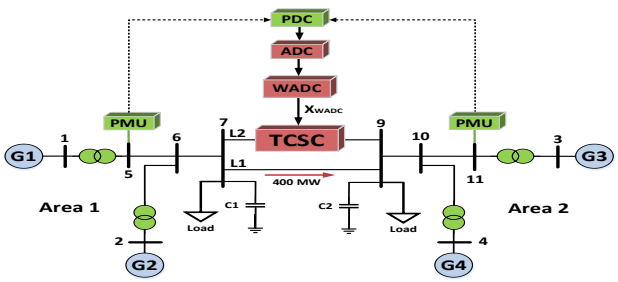

Fig. 12. Single line diagram of two area four machine system with TCSC

TABLE II
TIME-VARYING DELAY CONSIDERED

Time Interval (s)	Time Delay (ms)
$0 \le t < 7$	$470 \pm \theta_\tau$
$7 \le t < 10$	$150 \pm \theta_\tau$
$10 \le t \le 20$	$290 \pm \theta_\tau$

Where K_a is selected based on a trade-off between the delay margin and the damping performance. The time-domain simulations are carried out to show the performance of the proposed WADC in the presence and absence of TCSC once the system is subjected to a large disturbance. The simulation results for the three-phase fault that occurred on the L2 line for different delay values are shown in Fig. 13. The three-phase to fault occurs at 0.1 s while it is cleared after 0.1 s. Also, the assumed time-varying delay is considered in Table II, where θ_τ is a random value between zero and 30 ms. As shown in Fig. 13, the adaptive wide-area robust controller has a great performance in damping inter-area oscillations against the different values delay compared to the other methods. When the delay is 100 ms, the ADC is equal to the DC1 compensator, and the performance of the lead-lag controller with $K_a = 4$ is approximately similar to the performance of the proposed method. However, the performance of the conventional

controller completely deteriorates with an increase in delay value and time-varying delay. On the other hand, the controller with $K_a = 2$ gain can withstand a more extensive range of delay changes because its delay margin is 358 ms. As can be seen, this enhancement in the delay margin is obtained by weakening the controller damping performance where damping of the oscillations is last more than 20 s with different values of time delay. Although this gain provides an enhanced damping ratio for the lead-lag controller compared to the open-loop system, the desirable damping is not preserved in either low or high values of delay.

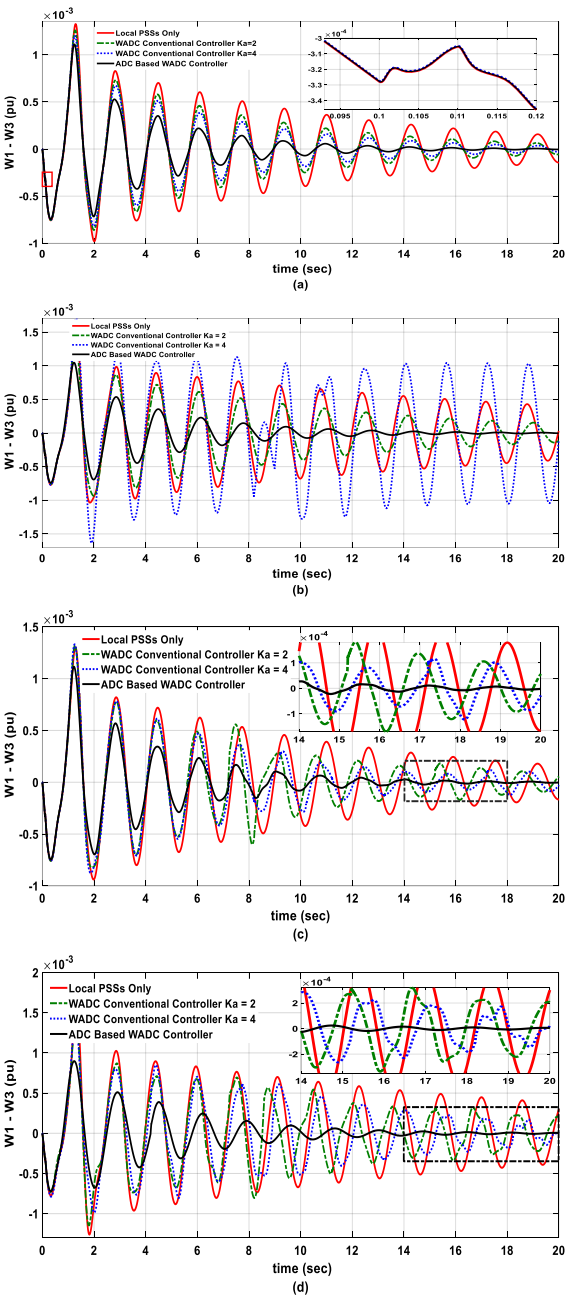

Fig. 13. The rotor speed changes of the G1 and G3 subjected to a 3-phase fault on the L2 line (a) delay =100 ms (b) delay =300 ms, (c) delay =500 ms, (d) time-varying delay.

Also, Fig. 14 shows the simulation results of the G1 and G3 generators' speed changes caused by different delays with ADC-based centralized controller and PSS. As can be seen, the ADC-based WADC has appropriate damping at different time delays than the fixed-delay compensators (DC1, DC3, and DC5) and PSS.

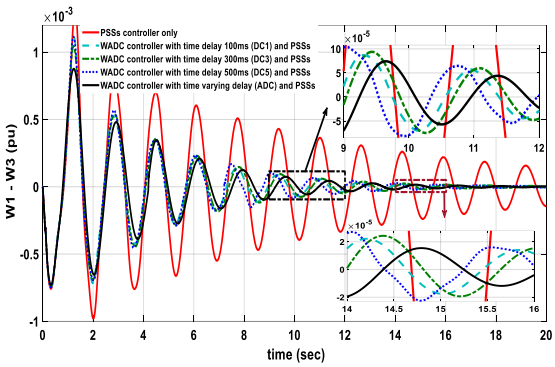

Fig. 14. Different delays with ADC-based centralized controller caused the rotor speed changes of the G1 and G3

Small signal analysis for the Two-Area test system in the presence and absence of TCSC shows that the system has three oscillatory modes. The participation of each generator in these oscillatory modes is shown in Tables III and IV. As can be seen, the damping ratio of all electromechanical modes as well as the frequency of local modes has changed. However, the inter-area mode frequency increased from 0.7344 Hz to 0.7515 Hz. This mode has a settling time of 30 s because of its damping ratio and low oscillation frequency. So, it is essential to improve the damping ratio of this oscillatory mode.

TABLE III
ELECTROMECHANICAL MODES OF TWO-AREA SYSTEM WITHOUT TCSC

Local and inter-area modes value	Mode shape	Damping ratio (%)	Frequency (Hz)	Mode
$-0.6467 \pm 4.6711i$	G1, G2 VS. G3, G4	13.71	0.7344	1
$-5.8336 \pm 12.298i$	G3 VS. G4	42.86	1.9573	2
$-4.7517 \pm 13.7841i$	G1 VS. G2	32.59	2.1938	3

TABLE IV
ELECTROMECHANICAL MODES OF TWO-AREA SYSTEM WITH TCSC

Local and inter-area modes value	Mode shape	Damping ratio (%)	Frequency (Hz)	Mode
$-0.7349 \pm 4.7116i$	G1, G2 VS.G3,G4	15.41	0.7515	1
$-5.8698 \pm 12.4025i$	G3 VS. G4	42.78	1.9739	2
$-4.7804 \pm 13.9393i$	G1 VS. G2	32.44	2.2185	3

The considered feedback signals are the speed changes of the generators in the system. The inter-area mode damping is done by applying a control signal to the generator excitation system. The relative values of the inter-area mode for different feedback signals and control locations are shown in Table V. According to the results, the G1 generator is considered the control location, and the speed changes between the G1 and G3 generators, which have the highest visibility of the inter-area mode, are selected as the feedback signal. In this work, the WADC is located near the TCSC while ADC is installed to compensate for the delay in the feedback signal.

TABLE V

FEEDBACK SIGNALS AND CONTROL LOCATIONS

		Feedback Signal					
		$\omega_1 - \omega_2$	$\boldsymbol{\omega_1 - \omega_3}$	$\omega_1 - \omega_4$	$\omega_2 - \omega_3$	$\omega_2 - \omega_4$	$\boldsymbol{\omega_3 - \omega_4}$
Control Location	G1	0.0561	**1.0000**	0.9038	0.8175	0.8178	0.0409
	G2	0.0506	0.8148	0.7984	0.7138	0.7581	0.0385
	G3	0.0423	0.8506	0.6417	0.5163	0.5896	0.0289
	G4	0.0473	0.7124	0.7064	0.6791	0.6302	0.0353

The order of the linearized model obtained by MATLAB software is 55, which is reduced to 10 using the Schur model order reduction method [31]. The bode diagram for the original model and reduced model are shown in Fig. 15 (a). As can be seen, the reduced model in the frequency range of the electromechanical oscillations has the same dynamic behavior as the original model. The delay variation is considered between 100 ms and 500 ms. Also, the time constants of these compensators are considered as T_1 =0.1, T_2 =0.2, T_3 =0.3, T_4 = 0.4, T_5 = 0.5. The variations in the delay will cause uncertainty in the compensated delay model. The main part of this uncertainty is due to the variation in the gain value of this model, which if GCF is not used, the gain increases with increasing of the delay value and decreases with decreasing of the delay value. Therefore, using an appropriate gain factor can reduce the caused uncertainty by delay variations. The MSV diagram of the designed plant considering the uncertainty is shown in Fig.15 (b).

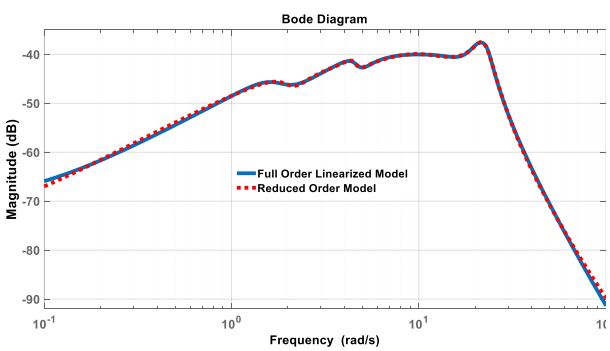

(a)

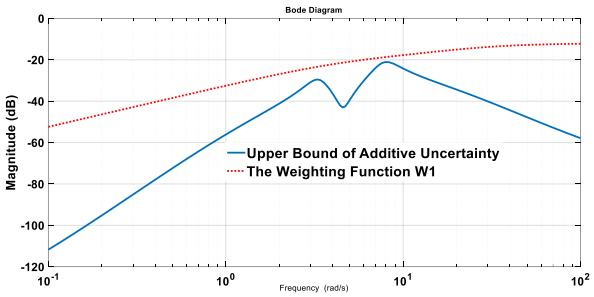

(b)

Fig. 15. (a) Bode plot of the linearized model and reduced model (b) MSV diagram for $W_1(s)$ weighting function and plant uncertainty

Also, the weighting functions $W_1(s)$,$W_2(s)$,$W_3(s)$ are considered as Eqs. (52) - (54) [32].

$$W_2(s) = 02 \tag{52}$$

$$W_3(s) = \frac{10}{s+20} \tag{53}$$

$$W_1(s) = 8s/(s+90) \tag{54}$$

The weighting factors of H_∞ and H_2 are assumed 0.5. The results of the controller design are presented in Table VI.

TABLE VI

THE DESIGNED CONTROLLER WITH TCSC BY CONSIDERING $a = 0.49$ AND $\beta = 87$ FOR THE LMI REGION

Designed controller with TCSC	
$\|\|T_{dz_\infty}\|\|_\infty$	$\|\|T_{dz_2}\|\|_2$
0.786	0.244

The time-varying delay, the weighting factors of compensators, and the ADC output signal applied to the AVR input of the G1 generator are shown in Fig. 16. This figure shows the ADC output variations between the outputs of other compensators when a large latency variation occurs.

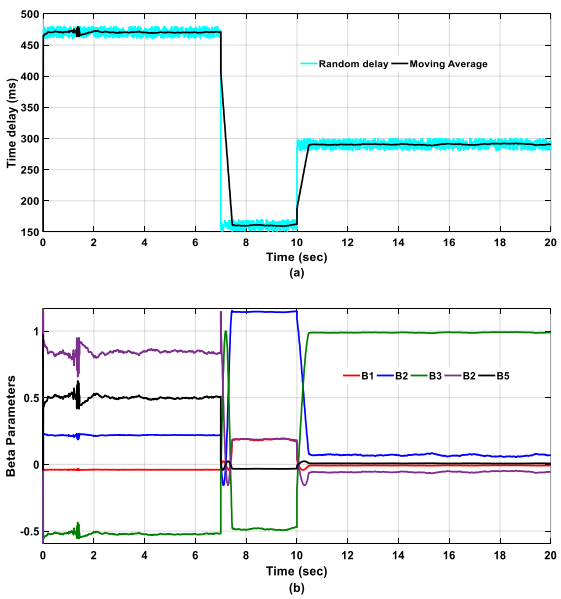

Fig.16 . Continued

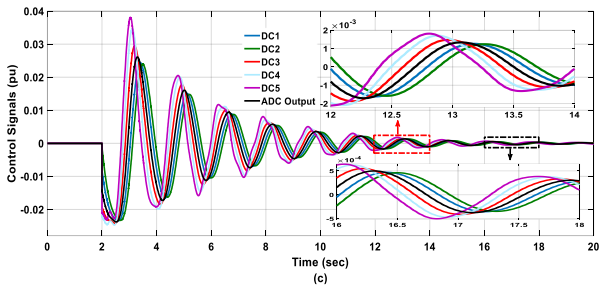

Fig. 16. Vertex compensator weights and control signals. (a) Time-varying delay, (b) Weight of vertex compensators, (c) the output of vertex compensators and ADC

Also, Fig. 17 shows the rotor speed changes of the G1 and G3 caused by different delays with ADC-based centralized controller and TCSC. As can be seen, the ADC-based WADC with TCSC has suitable damping at different time delays than the fixed-delay compensators (DC1, DC3, and DC5).

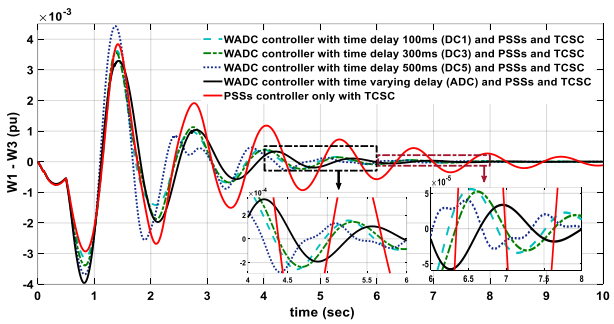

Fig. 17. The rotor speed changes of the G1 and G3 were caused by different delays with an ADC-based centralized controller and TCSC

Fig. 18 shows the active power from bus 7 to bus 9 with fault levels and different operating conditions. A three-phase to fault occurs at 1 s on the L2 line, and it is cleared after 0.1 s. Fig. 18 (a) shows the active power from bus 7 to bus 9 considering 80% of the load, Fig. 18 (b) shows 100% of the load, and Fig. 18 (c) shows 120% of the loads. As can be seen, WADC based ADC with TCSC compared to WADC with 300 ms fixed-delay compensator and PSSs have better performance.

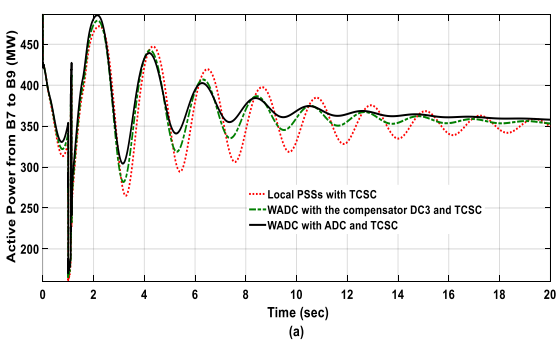

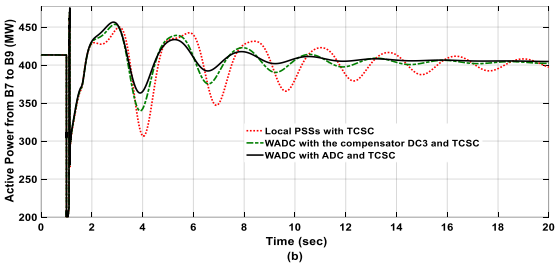

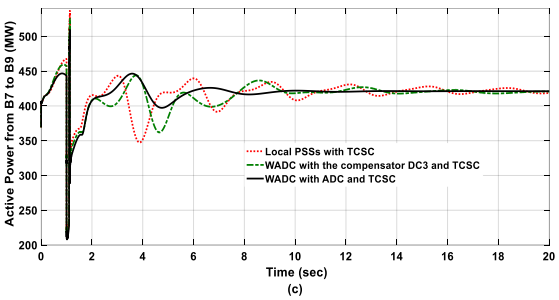

Fig. 18. The occurrence of 3-phase to fault on the L2 line at different operating points with the presence of TCSC (a) 80% load (b) 100% load (c) 120% load

B. Case Study II: 39-Bus 10-Machine Power System

The IEEE 39-bus 10-machine system with TCSC is chosen to evaluate the performance of the proposed method in a wide-area controller based on the use of FACTS devices. The single-line diagram of the network is shown in Fig. 19. This system consists of 10 synchronous generators, in which the G1 generator represents the dynamic model of the external grid. To impose the stress on the system, the load level and the generation have been increased. The local PSSs are installed only on generators G2, G3, G5, G8, and G9, while other generators are not equipped with PSS. The PSS transfer function installed on the aforementioned generators is displayed in Table VII [33], [34].

Small signal analysis of the linearized model of the system, according to Table (8), shows that the system has four oscillatory modes with a frequency of less than one Hz. Since, in each of these oscillatory modes, several generators oscillate against each other, they can be considered inter-area oscillation modes. Corresponding generators that produce these oscillatory modes include five groups of coherent generators. As shown in Table VIII, the groups mentioned above of coherent generators consist of G9, (G2 and G3), (G4, G5, G6, and G7), (G8 and G10), and G1.

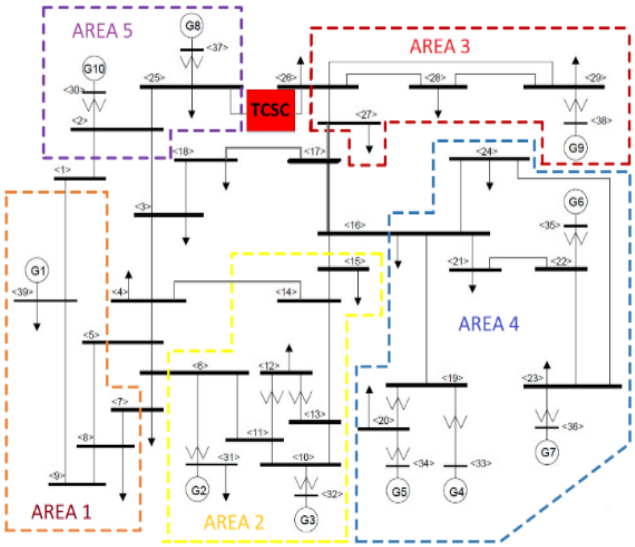

Fig. 19. 39-Bus 10-Machine Power System

TABLE VII
THE INSTALLED PSS ON 39-BUS TEST SYSTEM GENERATORS

Generator	The Installed PSS
G2, G3	$5\frac{8s}{1+8s}\left(\frac{1+0.06s}{1+0.01s}\right)^2$
G9, G8, G5	$7\frac{8s}{1+8s}\left(\frac{1+0.06s}{1+0.01s}\right)^2\left(\frac{1+005s}{1+0.01s}\right)$

TABLE VIII
INTER-AREA MODES OF OSCILLATION OF THE 39-BUS TEST SYSTEM WITH TCSC

Local and inter-area modes value	Mode shape	Damping ratio	Frequency	Mode
$-0.58 \pm 1.76i$	G1 VS. the others	31.29	0.2801	1
$-2.21 \pm 2.52i$	(G3, G2) VS. G9 and (G8,G10)	65.93	0.4010	2
$-1.81 \pm 2.74i$	G9 VS. (G4, G7) and (G8, G10)	55.11	0.4361	3
$-1.64 \pm 4.67i$	(G7, G4) VS. (G2, G3) and (G8,G10)	33.13	0.7432	4

Controllability and observability methods are used to determine the appropriate control location and control signal. One of these methods is the Residue Value which is based on model analysis [30]. This value is calculated for the lines of the case study system, as shown in Table IX. As shown in Table IX, the maximum value of the residues is related to the line (26-25). According to this controllability index, line (26-25) is the best place to install TCSC in this system. The measured signals are the speed of synchronous generators, and the feedback signals are considered the speed difference between the two generators. Also, for a comparative study without TCSC, a wide-area control signal is applied to the input of the AVR system installed on the excitation of some synchronous generators. The selection of the appropriate feedback signal and control location is made independently according to the maximum Geometric Measure of Controllability (GMC) and the maximum Geometric Measure of Controllability (GMO) for that mode to damp the inter-area oscillations. The details of these measures are not discussed here and can be found in [35], while the effectiveness of this method has been confirmed in [32]. Table X shows each mode's control location and selected feedback signal based on the maximum GMC and GMO indices. For example, according to Table 8, the first mode shows the oscillation of the G1 generator compared to the rest of the system generators. It can be effectively controlled by measuring the speed difference between the G1 and G9 generators and applying a control signal to the G9 generator. Therefore, G2, G4, and G9 are the selected control locations to improve the damping of inter-area oscillations. It is also assumed that the bus connected to generators G1, G2, G3, G5, G9, and G10 are equipped with PMUs to obtain feedback signals.

TABLE IX
TCSC RESIDUE COEFFICIENT IN THE 39-BUS TEST SYSTEM

TCSC Placement	
The Normalized Residue	Line
0.34	9 – 39
0.59	17 – 27
0.28	15 – 16
0.91	16 – 21
0.26	14 – 15
0. 58	21 – 22
0.41	16 – 17
0.53	2 – 3
0.13	3 – 4
0.68	2 – 25
0.28	7 – 8
1.00	**25 – 26**
0.52	26 – 28
0.64	28 – 29
0.45	17 – 18

TABLE X
FEEDBACK SIGNALS AND THE SELECTED CONTROL LOCATIONS TO IMPROVE THE DAMPING OF INTER-AREA OSCILLATIONS

Mode Number	1	2	3	4
Control Location Based on Maximum GMC	G9	G2	G9	G4
Feedback Signal Based on Maximum GMO	$\omega_1 - \omega_9$	$\omega_2 - \omega_9$	$\omega_9 - \omega_{10}$	$\omega_3 - \omega_5$

The linearized model of the case study system is obtained at the nominal operating point using MATLAB software. The order of the obtained linear model is equal to 116. To facilitate the design of the WADC, the order of the system is reduced to

10 using the Schur model order reduction method in the robust control toolbox of MATLAB software. The frequency response of the full-order and the reduced model are shown in Fig. 20 (a). According to this figure, the reduced model has the dynamic behavior of the full-order system with reasonable accuracy in the frequency range of electromechanical modes.

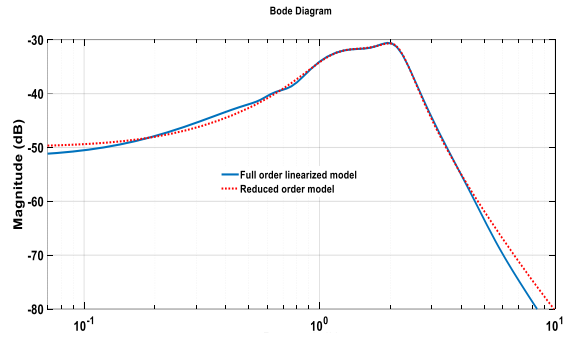

(a)

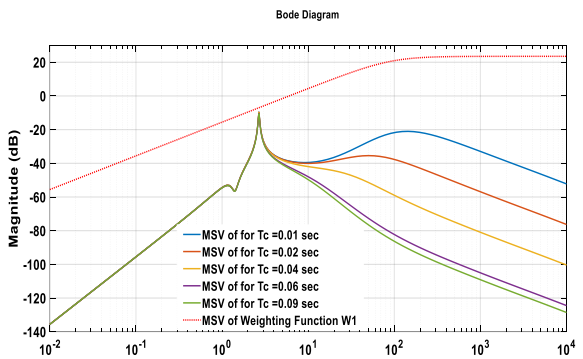

(b)

Fig. 20. (a) Bode plot of the linearized model and reduced model (b) MSV plot of plant model uncertainty and the corresponding weighting function

As mentioned before, changes in the delay will cause uncertainty in the compensated delay model. The main contribution of the uncertainty is due to the change in the gain of this model. If the GCF is not used to modify the gain value, the gain increases with increasing delay and decreases with decreasing delay. So, the resulted uncertainty can be significantly reduced using an appropriate gain factor. The MSV diagram of the designed plant uncertainty is shown in Fig. 20 (b). The time-varying delay is considered according to Table XI, where θ_τ is a random value between zero and 30ms.

TABLE XI

THE CONSIDERED TIME-VARYING DELAY

Time Interval (s)	Time Delay (ms)
$0 \le t < 7$	$120 \pm \theta_\tau$
$7 \le t < 13$	$300 \pm \theta_\tau$
$13 \le t \le 20$	$480 \pm \theta_\tau$

The maximum and minimum value of the delay for the system is considered 100 ms and 500 ms, respectively. Then, ADCs are designed to compensate for delayed changes adaptively. Therefore, the ADC is installed in the control location, close to the TCSC installation site, to compensate for the delay. The lead-phase time constants of the delay compensator are selected as $T_1 = 01$, $T_2 = 02$, $T_3 = 03$, $T_4 = 04$, $T_5 = 0.5$. Also, the selection of optimal weighting functions $W_1(s)$, $W_2(s)$, and $W_3(s)$ to design the centralized WADC for the 39-bus test system are considered as Eqs. (55)-(57) [32].

$$W_1(s) = \frac{10s}{s+60} \tag{55}$$

$$W_1(s) = \frac{10s}{s+60} \tag{56}$$

$$W_3(s) = \frac{5}{s+10} \tag{57}$$

To design the central controller, the relative weighting factors of a_∞ and a_2 are considered to 0.5 to consider the robustness and efficiency of the controller. In this study, the value of $T_C = 004$ is selected as the ADC lag-phase time constant, and the performance of the designed controller is evaluated. Using small signal analysis for the closed-loop system, the designed controller performance is examined in the face of various delay values and system operating point changes. To define the new operating points, it is assumed that the load of the area containing the G9 and busbars 26, 27, 28, and 29 will change from 60% of the nominal load to 140%. Given that the G9 is involved in all the first three modes, the main purpose of the changes in load and generation is to change the power exchange between the adjacent areas. As shown in Figs. 13 and 14, the proposed WADC improves the damping of inter-area oscillations while its performance does not weaken when confronted with the change in delay value or the operating points.

Time-domain simulations confirm the effectiveness of the presented ADC in the presence of the TCSC. For this purpose, nonlinear simulations are performed for 20 s, and the performance of the proposed method in the face of different values of delay, nonlinear nature of the power system, large disturbances, and changes in operating conditions are evaluated. The proposed method shows excellent damping in different operating conditions and different scenarios of delay changes. Fig. 21 shows the simulation results of a three-phase fault that occurs in 0.1 s between busbars 17 and 18 and clears after 0.1 s. To illustrate the advantage of having a TCSC with an ADC, comparisons are made between WADC with ADC, a DC_5 constant compensator designed for a fixed delay value of 500 ms, and a robust controller provided in [21]. In conventional controllers, the coefficients of the controllers must be changed to keep the system stable by changing the system's operating point, but the ADC and TCSC-based wide-area controller, which is shown in Fig. 22, is robust against load level changes of the system.

According to the time-varying delay scenario presented in Table 10, the moving average of the delay, the weighting factors of the compensators, and control signals with compensated delay (the output of each ADC) applied to the AVR of G2, G4, and G9, which is depicted in Fig. 23. As shown in Fig. 23, the proposed method maintains the desired performance in damping oscillations, and ADC effectively compensates for the time-varying delay. In $0 \leq t < 7$, the average delay is 120 ms and DC_1 can compensate for 100 ms. Therefore, the delay can be partially compensated, and as a result, the performance of DC_1 and ADC is almost the same. As the delay increases during the $t \geq 7$, the uncompensated delay increases significantly, leading to a deterioration in WADC performance.

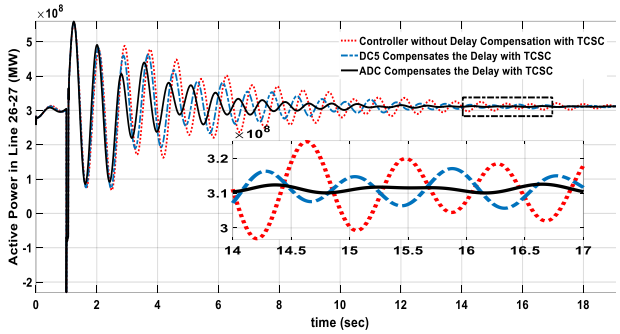

Fig. 21. The occurrence of three-phase fault on line 18-17 and the presence of TCSC between buses 26-25: with ADC - with fixed delay compensator 500ms (DC_5)- No delay compensator

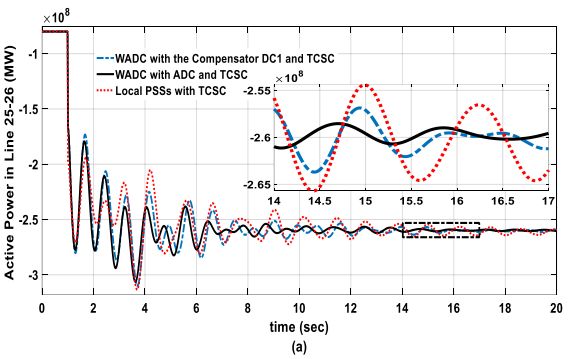

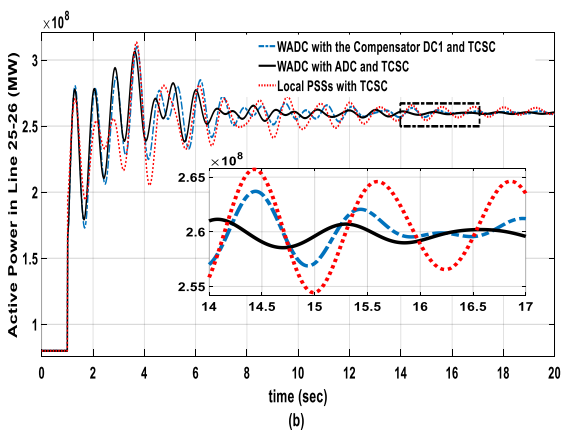

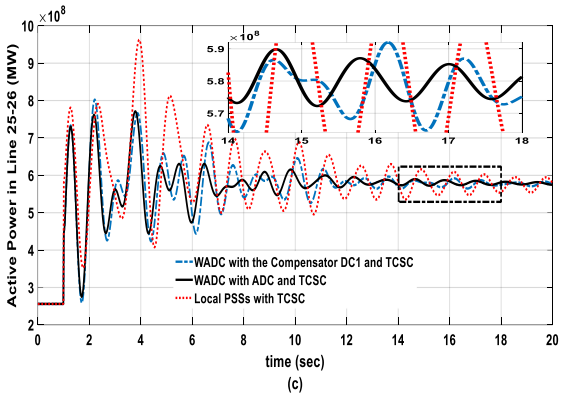

Fig. 22. The occurrence of 3-phase to fault on line 27-17 at different operating points with the presence of TCSC (a) 60% load (b) 100% load (c) 140% load

Also, in Figs. 25 and 26, a comparison of the two cases without TCSC and with TCSC with ADC is considered. When TCSC is used, the wide-area robust control of the system is done in a centralized way (i.e., all feedback signals from the speed difference of the generators are in the same place with WADC and applied to TCSC). Also, when TCSC is not used, the wide-area robust control can be applied semi-centralized, which means at the location of G9, G4, and G2 with PSS signal is applied to the excitation system. Fig. 24 shows the controller analysis against delay changes, while in Fig. 25, the controller is analyzed against load changes.

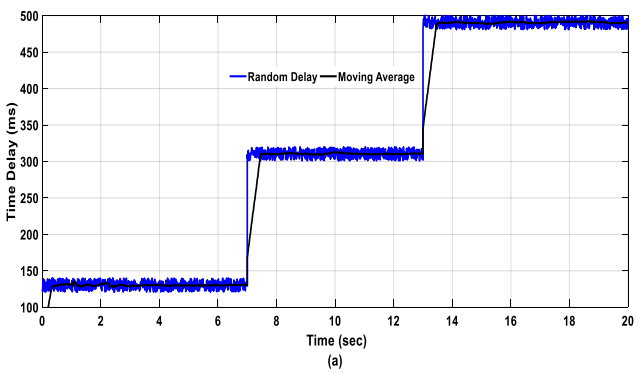

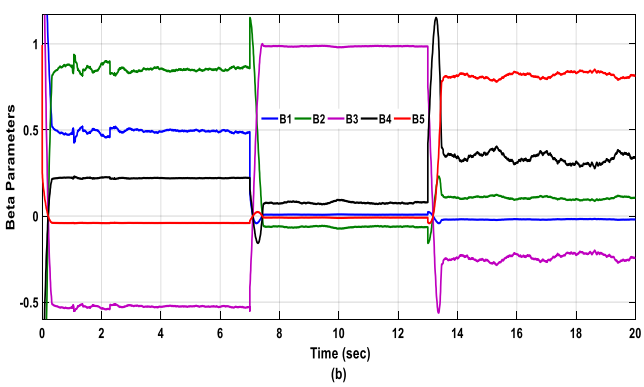

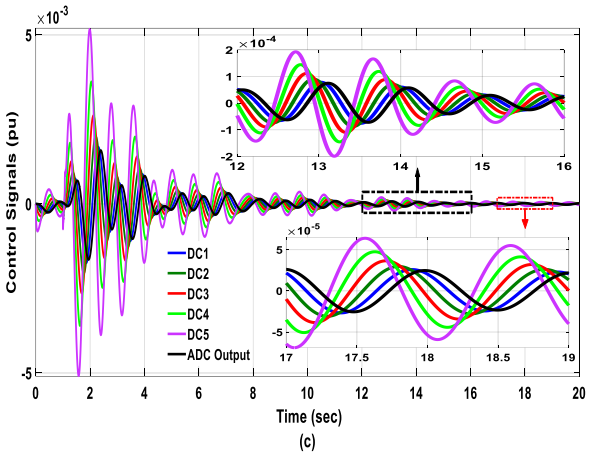

(c)

Fig. 23. (a) Moving average delay, (b) Changes in compensator weighting factors, and (c) ADC output in the presented scenario in Table IV

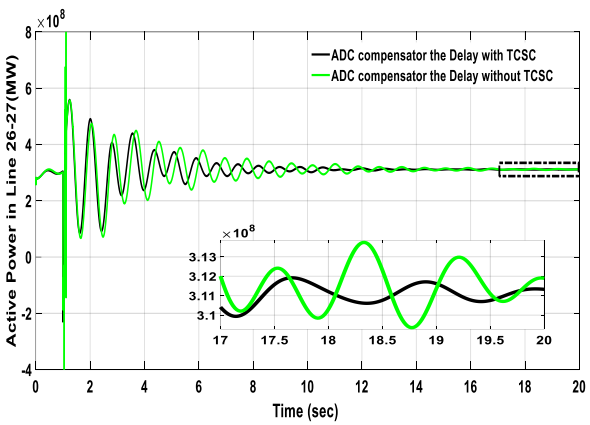

Fig. 24. Comparison of two modes without TCSC and with TCSC considering ADC and delay at different times for 10-machine system and creating three-phase short-circuit fault on line 17-18

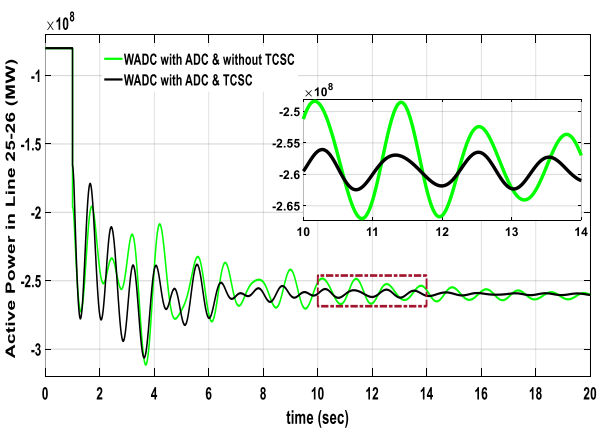

(a)

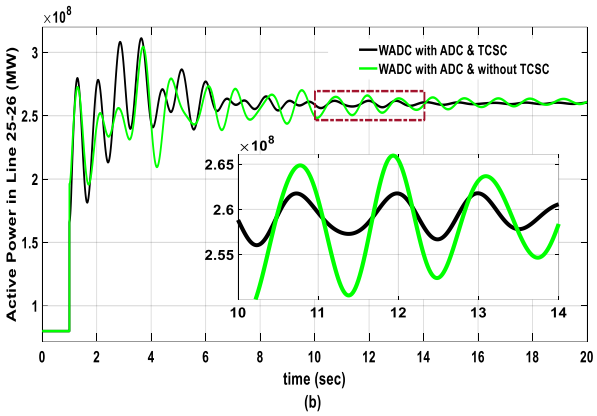

(b)

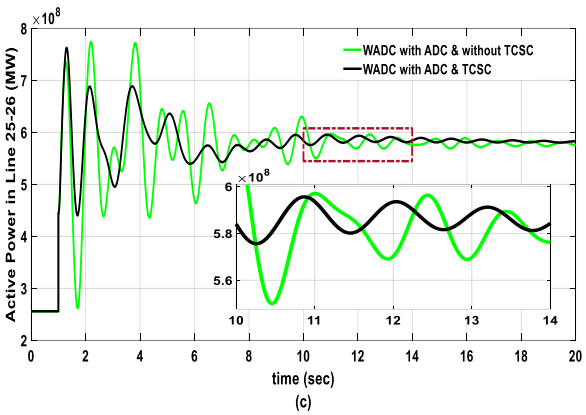

(c)

Fig. 25. Comparison of two modes without TCSC and with TCSC considering ADC for 39-bus test system and three-phase fault on line 17-27 at different operating points (a) 60% load, (b) 100% load, (c) 140% load

VI. CONCLUSION

This paper presents an ADC to compensate for the time-varying delay in a wide-area robust controller. The proposed adaptive compensator is implemented as the weighted sum of several compensators which each of them has a weighting factor according to the measured delay. Consequently, with the delay variations and compensating for it, these weighting factors are continuously updated. Using this compensator, a model for the compensated delay is presented, which can be easily applied to the system nominal plant to design WADC by the mixed H_2/H_∞ synthesis. Also, the uncertainties in the compensated delay model, caused by delay value variations, have been considered in designing a wide-area controller to ensure its robust stability. Using the simulations carried out on the Two-Area Four-Machine power system, and 39-bus New England test system, the efficiency of the proposed method was investigated by implementing two control schemes based on the use of voltage control loops synchronous generators and the TCSC for damping of the inter-area oscillations. The simulation results confirm the effectiveness of the presented method in compensation for time-varying delay and its robustness against changes in the operating point of the system.

REFERENCES

[1] P. W. Sauer, M.A. Pai, J. H. Chow, *Power System Dynamics and Stability: With Synchro phasor Measurement and Power System Toolbox*, 2th ed., Wiley-IEEE Press, pp. 71-231, 2017.

[2] M. M. Rizi, S. Abazari and N. Mahdian "Dynamic Stability Improvement of Power System with Simultaneous and Coordinated Control of DFIG and UPFC using LMI," *Int. J. Industrial Electronics, Control and Optimization, IECO*, Vol. 4, No.3, pp. 341-353, July. 2021.

[3] P. Agnihotri, A. M. Kulkarni, A. M. Gole, B. A. Archer, and T. Weekes, "A robust wide-area measurement-based damping controller for networks with embedded multiterminal and multi-infeed HVDC links," *IEEE Trans. Power Syst*., vol. 32, no. 5, pp. 3884–3892, 2017.

[4] A. Patel, S. Ghosh, and K. A. Folly, "Inter-area oscillation damping with non-synchronized wide-area power system stabilizer," *IET Gener. Transm. Distrib.*, vol. 12, no. 12, 2018.

[5] G. Tzounas, M. Liu, M. A. Adib Murad, and F. Milano, "Stability Analysis of Wide Area Damping Controllers with Multiple Time Delays," *IFAC-Papers Online*, vol. 51, no. 28, 2018.

[6] M. Mokhtari and F. Aminifar, "Toward wide-area oscillation control through doubly-fed induction generator wind farms," *IEEE Trans. Power Syst.*, vol. 29, no. 6, 2014.

[7] P. Zhang, D. Y. Yang, K. W. Chan, and G. W. Cai, "Adaptive wide-area damping control scheme with stochastic subspace identification and signal time delay compensation," *IET Gener. Transm. Distrib.*, vol. 6, no. 9, 2012.

[8] Y. Li, Y. Zhou, F. Liu, Y. Cao, and C. Rehtanz, "Design and Implementation of Delay-Dependent Wide-Area Damping Control for Stability Enhancement of Power Systems," *IEEE Trans. Smart Grid*, vol. 8, no. 4, 2017.

[9] Y. Li, C. Rehtanz, D. Yang, S. Rüberg, and U. Häger, "Robust high-voltage direct current stabilizing control using wide-area measurement and taking transmission time delay into consideration," *IET Gener. Transm. Distrib.*, vol. 5, no. 3, pp. 289–297, 2011.

[10] D. Dotta, A. S. e Silva, and I. C. Decker, "Wide-area measurements-based two-level control design considering signal transmission delay," *IEEE Trans. Power Syst.*, vol. 24, no. 1, 2009.

[11] W. Yao, L. Jiang, J. Wen, Q. Wu, and S. Cheng, "Wide-area damping controller for power system interarea oscillations: A networked predictive control approach," *IEEE Trans. Control Syst. Technol.*, vol. 23, no. 1, 2015.

[12] H. Ye and Y. Liu, "Design of model predictive controllers for adaptive damping of inter-area oscillations," *Int. J. Electr. Power Energy Syst.*, vol. 45, no. 1, 2013.

[13] L. Cheng, G. Chen, W. Gao, F. Zhang, and G. Li, "Adaptive time delay compensator (ATDC) design for wide-area power system stabilizer," *IEEE Trans. Smart Grid*, vol. 5, no. 6, 2014.

[14] Y. Shen, W. Yao, J. Wen, and H. He, "Adaptive wide-area power oscillation damper design for photovoltaic plant considering delay compensation," *IET Gener. Transm. Distrib.*, vol. 11, no. 18, 2017.

[15] M. Beiraghi and A. M. Ranjbar, "Adaptive Delay Compensator for the Robust Wide-Area Damping Controller Design," *IEEE Trans. Power Syst.*, vol. 31, 2016.

[16] Y. Li, D. Yang, F. Liu, Y. Cao, and C. Rehtanz, *Interconnected Power Systems*, Springer-Verlag Berlin Heidelberg, pp. 93-223, 2016.

[17] R. Fan, S. Wang, R. Huang, J. Lian, and Z. Huang, "Wide-area measurement-based modal decoupling for power system oscillation damping," *Electr. Power Syst. Res.*, vol. 178, 2020.

[18] S. Liu, "Assessing placement of controllers and nonlinear behavior of electrical power system using normal form information," Ph.D. Dissertation, Iowa State University, U.S.A, 2006.

[19] P. Kundur, "*Power system stability and control," Power System Stability and Control*, 3th ed., Wiley-IEEE Press, 2019.

[20] A. Movahedi, A. H. Niasar, and G. B. Gharehpetian, "Designing SSSC, TCSC, and STATCOM controllers using AVURPSO, GSA, and GA for transient stability improvement of a multi-machine power system with PV and wind farms," *Int. J. Electr. Power Energy Syst.*, vol. 106, 2019.

[21] W. Yao, L. Jiang, J. Wen, Q. H. Wu, and S. Cheng, "Wide-area damping controller of Facts devices for inter-area oscillations considering communication time delays," *IEEE Trans. Power Syst.*, vol. 29, no. 1, 2014.

[22] V. V. G. Krishnan, S. C. Srivastava, and S. Chakrabarti, "A robust decentralized wide area damping controller for wind generators and facts controllers considering load model uncertainties," *IEEE Trans. Smart Grid*, vol. 9, no. 1, 2018.

[23] J. Deng, C. Li, and X. P. Zhang, "Coordinated Design of Multiple Robust FACTS Damping Controllers: A BMI-Based Sequential Approach with Multi-Model Systems," *IEEE Trans. Power Syst.*, vol. 30, no. 6, 2015.

[24] I. Abdulrahman, R. Belkacemi, and G. Radman, "Power oscillations damping using wide-area-based solar plant considering adaptive time-delay compensation," *Energy Syst.*, 2019.

[25] S. Ghosh, K. A. Folly, and A. Patel, "Synchronized Versus Non-Synchronized Feedback for Speed-Based Wide-Area PSS: Effect of Time-Delay," *IEEE Trans. Smart Grid*, vol. 9, no. 5, 2018.

[26] N. R. Chaudhuri, S. Ray, R. Majumder, and B. Chaudhuri, "A new approach to continuous latency compensation with adaptive phasor power oscillation damping controller (POD)," *IEEE Trans. Power Syst.*, vol. 25, no. 2, 2010.

[27] X. Zhang, C. Lu, S. Liu, and X. Wang, "A review on wide-area damping control to restrain inter-area low frequency oscillation for large-scale power systems with increasing renewable generation," *Renewable and Sustainable Energy Reviews*, vol. 57. 2016.

[28] M. J. Alinezhad, M. Radmehr, and S. Ranjbar, "Adaptive wide area damping controller for damping inter-area oscillations considering high penetration of wind farms," *Int. Trans. Electr. Energy Syst.*, vol. 30, no. 6, 2020.

[29] M. Mokhtari, F. Aminifar, D. Nazarpour, and S. Golshannavaz, "Wide-area power oscillation damping with a fuzzy controller compensating the continuous communication delays," *IEEE Trans. Power Syst.*, vol. 28, no. 2, 2013.

[30] I. Zenelis and X. Wang, "Wide-area damping control for interarea oscillations in power grids based on PMU measurements," *IEEE Control Syst. Lett.*, vol. 2, 2018.

[31] M. Rydel, R. Stanisławski, and K. J. Latawiec, "Balanced truncation model order reduction in limited frequency and time intervals for discrete-time commensurate fractional-order systems," *Symmetry (Basel).*, vol. 11, no. 2, 2019.

[32] Y. Wang, Q. Wu, W. Gong, and M. P. S. Gryning, "H∞ Robust Current Control for DFIG-Based Wind Turbine Subject to Grid Voltage Distortions," *IEEE Trans. Sustain. Energy*, vol. 8, no. 2, 2017.
[33] Z. Zhang, W. Qiao, and Q. Hui, "Power System Stabilization Using Energy-Dissipating Hybrid Control," *IEEE Trans. Power Syst.*, vol. 34, no. 1, 2019.
[34] Y. Li, C. Rehtanz, S. Rüberg, L. Luo, and Y. Cao, "Wide-area robust coordination approach of HVDC and FACTS controllers for damping multiple interarea oscillations," *IEEE Trans. Power Deliv.*, vol. 27, no. 3, 2012.
[35] M. Li and Y. Chen, "A Wide-Area Dynamic Damping Controller Based on Robust H∞ Control for Wide-Area Power Systems with Random Delay and Packet Dropout," *IEEE Trans. Power Syst*., vol. 33, no. 4, 2018.

Esmaeel Rokrok was born in Khorramabad, Iran, in 1972. He received his B.Sc., M.Sc., and Ph.D. degree in Electrical Engineering from Isfahan University of Technology, in 1985, 1997 and 2010, respectively. He is an associate professor in the Department of Electrical Engineering, Lorestan University. His major research interests lie in the area of power system control and dynamics, dispersed generation, microgrid and robust control.

Saman Dehghaninejad was born in Khorramabad, Iran, in 1995. He received his B.Sc. degree in Electrical Engineering from Semnan University, Semnan, Iran, in 2016, and his M.Sc. in Electrical Engineering from Lorestan University (LU), Khorramabad, Iran, in 2019. He is currently a Ph.D. Student at Lorestan University, Khorramabad, Iran. His research interests include power system control and dynamics, energy management, smart grids.

Amir Hossein Poursaeed was born in Khorramabad, Iran, in 1993. He received B.Sc. and M.Sc. degrees from Lorestan University (LU), Khorramabad, Iran in 2015 and 2018, respectively. He is currently a Ph.D. Student at Lorestan University, Khorramabad, Iran. His research interests include power system protection, stability, electromagnetic transients, and machine learning applications in power systems.